

University of Alberta

Empowering the Base Metals: Rational Design of Homogeneous Catalysts for Hydrotreatment, and Reduction of Organic Unsaturates

by

Jeffrey Camacho Bunquin

A thesis submitted to the Faculty of Graduate Studies and Research
in partial fulfillment of the requirements for the degree of

Doctor of Philosophy

Department of Chemistry

©Jeffrey Camacho Bunquin

Fall 2013
Edmonton, Alberta

Permission is hereby granted to the University of Alberta Libraries to reproduce single copies of this thesis and to lend or sell such copies for private, scholarly or scientific research purposes only. Where the thesis is converted to, or otherwise made available in digital form, the University of Alberta will advise potential users of the thesis of these terms.

The author reserves all other publication and other rights in association with the copyright in the thesis and, except as herein before provided, neither the thesis nor any substantial portion thereof may be printed or otherwise reproduced in any material form whatsoever without the author's prior written permission.

For Inay Linda and Tatay Kari

Abstract

Hydrocarbon-soluble, low-coordinate, phosphoranimide-supported complexes of the base metals (iron, cobalt and nickel) were developed and evaluated for a range of stoichiometric and catalytic bond-forming and bond-breaking transformations. An unprecedented family of tetrametallic clusters of Co(I) and Ni(I), with formula $[M(NP^tBu_3)_4]$, was synthesized in high yields and characterized by single crystal X-ray analysis and by solution-phase magnetic susceptibility measurements. These *ancillary-ligand-free* clusters exhibit high room-temperature magnetic susceptibility and are structurally unique; each metal center in the coplanar, tetranuclear core is linear, two-coordinate. A rare homoleptic, mononuclear, three-coordinate Co(III) d⁶ complex $[Co(NP^tBu_3)_3]$ was also synthesized in high yield and characterized using NMR spectroscopy and single crystal X-ray analysis.

The ancillary ligand-free “surface-mimetic” clusters constitute a new class of high-activity homogeneous catalysts for room-temperature hydrogenation and hydrosilylation of polar and nonpolar unsaturates. Both clusters hydrogenate unactivated and sterically hindered alkenes and alkynes to the corresponding alkanes (1 atm H₂). These clusters also hydrosilylate a range of functionalized aldehydes and ketones, utilizing a diverse scope of organosilyl hydride reagents. Radical clock

hydrosilylation studies revealed differences in the mechanistic behavior of the isostructural Co(I) and Ni(I) clusters: the cobalt catalyst functions through a non-radical mechanism while nickel catalyst shows contributions from radical-type pathway(s).

More importantly, both Co(I) and Ni(I) clusters are high-activity catalysts for the hydrogenolysis of carbon-heteroatom bonds under remarkably mild conditions (90-150 °C, 1 atm H₂). Both clusters constitute the very first set of homogeneous, first-row transition metal catalysts for the mild-condition hydrodesulfurization of dibenzothiophene derivatives. The tetranuclear clusters also activate C-O bonds in symmetrical and unsymmetrical aryl ethers and dibenzofuran-type substrates, producing aromatic hydrocarbons and phenols. In some preliminary experiments, the Ni(I) cluster and the mononuclear Co(III) complex were shown active for the hydrogenolysis of C-N bond in neutral and basic aromatic nitrogenous substrates. Results of hydrogenolysis studies show catalyst selectivity for the direct hydrogenolysis of C_{aryl}-X bonds (X = S, O, N) with complete suppression of aromatic ring hydrogenation pathways. Lastly, the both Co(I) and Ni(I) clusters effect the deoxygenation of a range of functionalized carbonyl substrates, producing unique mixtures of hydrocarbons under mild hydrosilylation conditions.

Acknowledgements

I would like to express my sincerest gratitude to the following people for their invaluable contribution and support in the past five years. This academic journey would not have been this eventful, fun and fulfilling without each of you.

I would like to thank my research supervisor, Professor Jeffrey Stryker, for the mentorship and for giving me the opportunity to work on this project. I will always be grateful for the trust and freedom that you have given me in exploring this body of research. I would also like to thank Prof. Todd Lowary, Prof. Jillian Buriak, Prof. Frederick West, Prof. Murray Gray, Dr. Mainak Ghosh and Mr. Wayne Moffat for their guidance, support and constant encouragement. Special mention is given to Prof. Kevin Smith (UBC-O) for his insightful suggestions that paved way to pivotal advances in this research. I would like to thank the past and present members of the Stryker group who, in one way or another, have contributed to my training and professional maturity.

I would like to express my sincerest gratitude to the Herrera-Lim family (Kuya Tito, Ate Rita, Ate Weng, Missy and Pao) for always welcoming me to your family. I would also like to thank my friends for being my stronghold. Special mention to Verner Lofstrand, Christine Dunbar, Mike Deo, Jason Brandt, Yonghoon Kwon, Yen-Ku Wu, Adam Malcolm, Alice Chan, Nada Djokic, Shaohui Yu, Kuya Ronnie Perez, Stan Stoyanov, Kuya John Villegas, Kuya Ivan Sy, Ate Michelle Sy and Dr. Hayley Wan.

Lastly, I will always be thankful to my family for their immeasurable support and unconditional love. To my constant sources of inspiration, love and courage, Tatay, Inay, Kuya Eric, Ate Bing, Kent and Lana, thank you and I love you. This is all for you.

Table of Contents

Chapter 1: Phosphoranimide-Supported Clusters of the Base Metals

1.1 Introduction	2
1.2 Project Background	13
1.3 Results and Discussion	17
1.4 Summary and Conclusions	59

Chapter 2: Tetrametallic Cobalt and Nickel Clusters for Homogeneous Catalytic Hydrogenation

2.1 Introduction	63
2.2 Results and Discussion	66
2.3 Conclusions	92

Chapter 3: Base Metal-Catalyzed Hydrosilylation of Carbonyl Compounds

3.1 Introduction	95
3.2 Results and Discussion	97
3.3 Conclusions	119

Chapter 4: High-Activity Base Metal Catalysts for Hydrodesulfurization

4.1 Introduction	122
4.2 Organometallic Modeling of Hydrodesulfurization Catalyst Active Sites	127
4.3 Results and Discussion	140

4.4 Summary and conclusions	183
Chapter 5: Base Metal-Catalyzed Hydrogenolysis of C–O and C–N Bonds	
5.1 Introduction to Catalytic C–O Bond Reduction	187
5.2 Results and Discussion: C–O Hydrogenolysis	194
5.3 Review of Homogeneous Models for C–N bond Activation	213
5.4 Conclusions	234
Chapter 6: Base Metal-Catalyzed Deoxygenation of Carbonyl Compounds	
6.1 Introduction	237
6.2 Results and Discussion	240
6.3 Conclusions	269
Chapter 7: Experimental Details	279
References	393
Appendix	409

Table of Figures

Figure 1.1 Representative examples of ligand-supported transition metal clusters	6
Figure 1.2 <i>Trans</i> -olefin selective, bimetallic rhodium-catalyzed hydrogenation of internal alkynes	8
Figure 1.3 Representative examples of ligand-supported transition metal clusters for metal-metal cooperativity studies	12
Figure 1.4 Comparative illustration of phosphoranimide steric pressure with traditional organometallic support ligands	14
Figure 1.5 Binding modes of anionic trialkylphosphoranimide ligands	15
Figure 1.6 Solid-state structure of $[\text{Co}_3(\text{CH}_3\text{COO})_6(\text{HNPPh}_3)_2]$ 13	19
Figure 1.7 Solid-state structure of $[\text{Co}(\text{HNP}^t\text{Bu}_3)_2(\text{NC}_{12}\text{H}_8)_2]$ 17	27
Figure 1.8 Solid-state structure of $[^t\text{Bu}_3\text{PNH}_2]^+[\text{Co}(\text{HNP}^t\text{Bu}_3)_2(\text{SPh})_3]^-$ 18	30
Figure 1.9 Solid-state structure of $[\text{CoCl}(\mu_2-\text{NP}^t\text{Bu}_3)(\text{THF})]_2$ 24	38
Figure 1.10 Representative structure of trialkylphosphoranimidometal(I) metal clusters	41
Figure 1.11 Representative examples of two-coordinate complexes stabilized by bulky ligands	42
Figure 1.12 Solid-state structure of $[\text{Co}(\mu_2-\text{NP}^t\text{Bu}_3)]_4$ 26a	46
Figure 1.13 Solid-state structure of $[\text{Ni}(\mu_2-\text{NP}^t\text{Bu}_3)]_4$ 26b	49
Figure 1.14 d-orbital splitting diagram for linear, two-coordinate complexes	50
Figure 1.15 d-orbital splitting diagram for trigonal planar, three-coordinate complexes	55
Figure 1.16 Solid-state structure of $[\text{Co}(\text{NP}^t\text{Bu}_3)_3]$ 22	56
Figure 2.1 Illustration of modes of alkyne coordination to metal complexes	74
Figure 2.2 FT-IR spectra of 26b in C_6D_6 upon exposure to H_2	78
Figure 2.3 Proposed mechanism for alkyne hydrogenation	81
Figure 2.4 Proposed mechanism for linear dimerization of terminal alkynes	88
Figure 2.5 Alternative mechanism for linear dimerization of terminal alkynes	90
Figure 2.6 Alternative mechanism for linear dimerization of terminal alkynes	91
Figure 3.1 Proposed mechanism for aldehyde dimerization catalyzed by 26b	114
Figure 3.2 Proposed mechanism for C–C bond breaking in cyclopropyl phenyl ketone catalyzed by 26b	117
Figure 3.3 Proposed mechanism for carbonyl hydrosilylation	119

Figure 4.1 Volcano plot of HDS activity of transition metal sulfides	125
Figure 4.2 Mechanism for HDS – Proposal	170
Figure 4.3 Mechanism for KH-induced <i>ortho</i> -metallation of DBT	180
Figure 4.4 Mechanism for desulfurization of thiolate intermediates	181
Figure 5.1 Representative structure of lignin	190
Figure 5.2 Mechanism for HDO – Proposal	212
Figure 5.3 Coordination modes of benzofuran-type substrates	212
Figure 5.4 Illustration of classes of nitrogenous compounds in petroleum feedstocks	215
Figure 5.5 Mechanism of hydrodenitrogenation of benzoquinoline substrates	216

Table of Tables

Table 1.1	Pertinent bond distances in 13	19
Table 1.2	Pertinent bond distances in 17	27
Table 1.3	Pertinent bond distances in 18	30
Table 1.4	Selected bond distances and bond angles in 26a	47
Table 1.5	Selected bond distances and bond angles in 26b	48
Table 2.1	Summary of hydrogenation results	93
Table 3.1	Catalytic hydrosilylation of cyclohexanone	98
Table 3.2	Hydrosilylation of aliphatic aldehydes and ketones	101
Table 3.3	Hydrosilylation of aryl aldehydes and ketones	102
Table 3.4	Hydrosilylation of aldehydes and ketones with tertiary silanes	107
Table 3.5	Hydrosilylation of allylbenzene	110
Table 4.1	Basic scavenger screening for silane-promoted hydrodesulfurization of dibenzothiophene	144
Table 4.2	Basic scavenger screening for hydrogen-promoted hydrodesulfurization of dibenzothiophene	149
Table 4.3	Catalytic hydrodesulfurization of DBT	153
Table 4.4	Catalytic hydrodesulfurization of DBT in THF	155
Table 4.5	Catalytic hydrodesulfurization of 4,6-diethylDBT	158
Table 4.6	Catalytic hydrodesulfurization of diphenyl sulfide	160
Table 4.7	Catalytic hydrodesulfurization of DBT in the presence of nitrogenous inhibitors	165
Table 4.8	Catalytic hydrodesulfurization of DBT: Control experiments	177
Table 4.9	Summary of hydrodesulfurization results	185
Table 5.1	Catalytic hydrogenolysis of 4-phenylanisole	201

Table 5.2	Catalytic hydrogenolysis of 2-methoxynaphthalene	203
Table 6.1	Catalytic deoxygenation of 2-cyclohexen-1-one	242
Table 6.2	Catalytic deoxygenation of (+)-Carvone	250
Table 6.3	Catalytic deoxygenation of 89	258
Table 6.4	Catalytic deoxygenation of 312	261
Table 6.5	Catalytic deoxygenation of 99	262
Table 6.6	Catalytic deoxygenation of 87	264
Table 6.7	Catalytic deoxygenation of 91	266
Table 6.8	Summary of enone deoxygenation	271
Table 6.9	Summary of aryl ketone deoxygenation	272
Table 6.10	Summary of aryl aldehyde deoxygenation	274

List of Abbreviations

atm	Atmospheres
°C	Degrees Celsius
DBF	Dibenzofuran
DBT	Dibenzothiophene
DFT	Density Functional Theory
dme	1,2-dimethoxyethane
Et	Ethyl group
eq.	equivalents
η	Eta (hapticity)
GC-MS	Gas Chromatography – Mass Spectrometry
h	Hours
[H]	Reducing agent
HDN	Hydrodenitrogenation
HDO	Hydrodeoxygenation
HDS	Hydrodesulfurization
HOMO	Highest Occupied Molecular Orbital
Hz	Hertz
IR	Infrared
LDA	Lithium diisopropylamide
L _n	Ligand(s)
LUMO	Lowest Unoccupied Molecular Orbital
M	Metal

μ	Mu (bridging)
me	Methyl group
mg	Milligrams
MHz	Megahertz
min	Minutes
mL	Millilitres
mmol	Millimoles
MS	Mass Spectrometry
<i>n</i> -	Linear chain
NMR	Nuclear Magnetic Resonance
[O]	Oxidizing agent
OAc	Acetate
ORTEP	Oak Ridge Thermal Ellipsoid Plot
Ph	Phenyl
psi	Pounds per square inch
PY	Pyridine
Q	Quinoline
<i>t</i> Bu	<i>tert</i> -Butyl
THF	Tetrahydrofuran
TMEDA	Tetramethylethylenediamine
TMS	Trimethylsilyl
TOF	Turnover Frequency
TON	Turnover Number

Chapter 1

Phosphoranimide-Supported Complexes of the Base Metals

1.1 Introduction and Background

Heterogeneous catalysis is a key enabling tool that sustains major industries and shapes world economies.^{1,2} Petroleum processing, fine chemicals synthesis, and polymer production, among many others, are industries largely dependent on heterogeneous catalysis. Societal modernization drives the demand to sustain these industries and, at the same time, satisfy ever more stringent environmental policies and regulation. The development of more efficient and practical catalysts thus continues to be an area of enormous research attention. Current research efforts are dedicated to addressing two principal challenges in metal catalysis: (1) a non-sustainable dependence on the precious metals and (2) the rational design of heterogeneous catalysts.

Among pressing concerns in industrial catalysis is the depletive use of non-abundant second- and third-row transition metals. The use of precious metal catalysts contributes significantly to processing costs and, in some cases, results in serious environmental and waste-management issues.³ The current dependency on semi-precious and precious metal catalysis is mainly due to the belief that the more abundant and significantly less toxic base metals are intrinsically much less active.⁴ To address this, the field has and continues to exert aggressive research efforts to elicit and harness the *precious metal-like reactivity* of the inexpensive and terrestrially abundant base metals.

The field of catalysis remains challenged in the rational design and synthesis of practical and efficient heterogeneous catalysts. Industrial catalysts are mostly surface catalysts. Spectroscopic and mechanistic studies on traditional heterogeneous catalysts reveal that coordinatively unsaturated metal centers, also called *surface vacancies*, act as the catalyst active sites.⁵⁻⁷ Thorough understanding of the nature of these low-coordinate active sites situated in a polynuclear coordination environment is crucial in understanding the mechanisms involved in of heterogeneous catalysis.

The high insolubility and structural complexity of heterogeneous catalysts makes rational design and mechanistic investigations difficult.^{5,8} Interestingly, several studies on industrial heterogeneous catalysts suggest that high activity may be a consequence of cooperativity among neighboring metal ions in proposed active sites.⁹⁻¹³ Hence, understanding metal–metal interactions provides important insights into how polynuclear active sites in heterogeneous catalysts function *in concert* during bond-forming and bond–breaking transformations.^{14,15}

The areas of heterogeneous catalysis and organometallic chemistry are evolving to become ever more common territory. The development of mononuclear and polynuclear complexes immobilized on inert inorganic supports has produced some of today's most active and efficient industrial

solid-state catalysts.^{12,16-18} Organometallic chemistry remains instrumental in the molecular modeling of heterogeneous catalyst active sites. However, rational design of soluble surrogates for heterogeneous catalyst active sites remains extremely challenging. In particular, the modeling of *surface vacancies* present on solid state catalysts remains difficult due to the challenges in nucleating low-coordinate metal centers and supporting these open-shell centers in a polynuclear coordination environment.^{14,19,20}

1.1.1 Ligand-Supported Transition Metal Clusters as Models for Heterogeneous Catalyst Active Sites

More than three decades ago, the use of molecular metal clusters as soluble models for heterogeneous catalyst active sites was introduced, a theme that continues to be fertile ground for research in catalysis.^{12,16,21-}

²³ Interestingly, the term “molecular cluster” has become loosely used in the literature to describe two considerably different families of polynuclear coordination complexes: (1) *molecular metal clusters* and (2) *polymetallic complexes*. In 1965, F. A. Cotton described molecular metal clusters as “those containing a finite group of metal atoms which are held together entirely, mainly, or at least to a significant extent, by bonds directly between the metal atoms even though some non-metal atoms may be associated intimately with the cluster,” while polymetallic complexes are those without metal-metal bonds, whether the metals are interacting or

non-interacting.^{12b} For our purposes, we consider all polymetallic assemblies to be clusters, without regard to metal-metal interactions.

Ligand-supported clusters can exhibit physical and chemical properties similar to active sites on active metal surfaces. This family of compounds consists of coordination complexes with polynuclear arrays of two or more metal centers stabilized by a sandwich of ligands. Ligand-supported clusters are classified mainly according metal oxidation states.^{16,23,24} Low valent clusters, with metal oxidation states ranging from +1 to the higher negative states, are often used as models for bulk metal active sites.^{23,25} Metal carbonyl clusters constitute the largest group of low-valent molecular clusters, with reported cluster nuclearities ranging from 2 to 38.²⁶⁻²⁸ On the other hand, high-valent clusters, commonly supported by polyfunctional and/or polyanionic ligands, are models for active sites on high-valent solid state catalysts such as transition metal oxides and sulfides.^{10,29,30}

Figure 1 shows examples of molecular transition metal clusters with metals at various oxidation states. Clusters **1** and **2** are representatives of homopolymetallic and heteropolymetallic metal carbonyl clusters, respectively. Cluster **1** had been used as catalyst for a few organic transformations.^{31,32} Cluster **2**, developed by Curtis and coworkers, is a monumental accomplishment, a discrete, molecular cluster that models CoMoS₂-type hydrodesulfurization catalyst active sites.³⁰ On the other

hand, clusters **3** and **4** represent ligand-supported base metal and precious metal hydrides. Cluster **3** was initially reported as a homogeneous model for the study of carbon-hydrogen bond activation³³ while **4**, a putative model for hydrodesulfurization active sites, was demonstrated capable of multimetal activation of carbon-sulfur bonds in thiophene-type substrates.³⁴ The activity of clusters **2** and **4** will be presented in greater detail in Chapter 4.

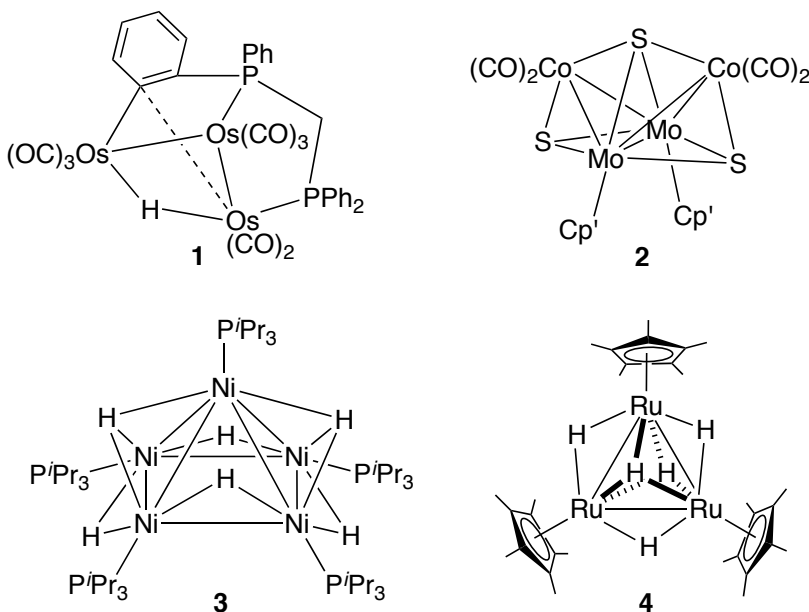


Figure 1.1. Representative examples of ligand-supported transition metal clusters.

1.1.2 Reactivity of Ligand-supported Clusters

Ligand-supported transition metal clusters exhibit stoichiometric and catalytic reactivity that is atypical of their mononuclear congeners and

occasionally similar to heterogeneous catalyst.^{16,23} In 1975, Muetterties predicted that ligand-supported clusters would be demonstrated to be active for organic and inorganic transformations that cannot be achieved using mononuclear complexes.^{16,23} Metal carbonyl clusters, the most diverse group of molecular clusters, have been extensively studied for a range of catalytic processes, including hydrogenation/isomerization of unsaturated compounds,³⁵ hydroformylation,³⁶ reduction of nitroaryls,³⁷ and the water-gas shift reaction.³⁸

The increasing interest in catalysis research using ligand-supported clusters is attributed to the advantages of a polynuclear metallic core. These discrete, polymetallic coordination arrays are (1) capable of multimetal substrate activation, also known as *cooperativity effects*; (2) provide a range of accessible core redox states, and (3) act as “*molecular containers*” for high-reactivity inorganic/organometallic fragments.^{16,23,39,40}

Metal-metal cooperativity effects are proposed to be responsible for some unique transformations mediated by ligand-supported clusters. In a handful of examples, unique stereoselectivities and chemoselectivities have been observed.^{23,40} The presence of two or more metal centers within mutual bonding distances translates to a greater number of closely spaced molecular orbitals, hence, a smaller HOMO-LUMO gap.^{23,41}

The unique selectivity is attributed to multimetal substrate binding, allowing for multi-center substrate activation.⁴² One pertinent example features the selective bimetallic rhodium-catalyzed hydrogenation of internal alkynes, exclusively forming the *trans*-olefin product (Figure 2).²³ The results demonstrate unusual stereoselectivity as internal alkyne hydrogenation invariably produces *cis*-alkenes as the predominant isomer when catalyzed by mononuclear complexes. Structural elucidation of a reactive intermediate **6** (Figure 2) shows that the low-valent, bimetallic rhodium catalyst **5** reacts with the internal alkyne to form a vinyl-bridged dirhodium complex **6** where the vinyl moiety adopts the *trans*-stereochemistry. Hydrogenation of **6** forms the *trans*-alkene product.^{43,44}

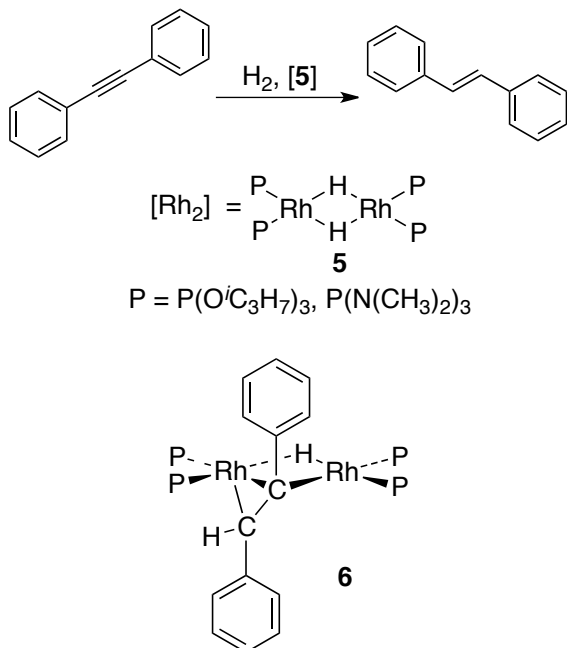


Figure 1.2. *Trans*-olefin selective, bimetallic rhodium-catalyzed hydrogenation of internal alkynes.

Another advantage of ligand-supported transition metal clusters in catalysis involves their ability to act as efficient electron reservoirs. These polynuclear assemblies can transform into several redox states that are not accessible to monometallic species. Thorough investigation of these extended redox transformations is important in understanding multi-electron processes related to biologically important systems and a range of industrial processes.^{23,41}

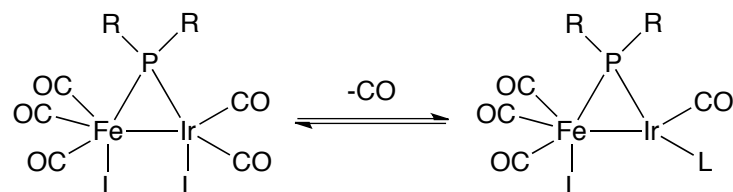
Ligand-supported transition metal clusters can function as “molecular containers” for storing and releasing reactive inorganic/organometallic fragments. The generation of reactive fragments is commonly achieved through the scission of metal-metal and/or metal-ligand bonds, forming low-coordinate metal centers that can bind with incoming substrate molecules.^{12,14,41,45}

Largely varied sets of process conditions have been employed in cluster-catalyzed transformations, with most examples requiring harsh temperatures and pressures. The inherent reactivity of transition metal clusters is a function of the metals’ degree of coordinative saturation.^{12,23,41} Coordinatively saturated clusters are generally less reactive, commonly requiring activation under harsh reaction conditions. This lower activity is a consequence of large HOMO-LUMO gaps and occupancy of all low-lying molecular orbitals, hence, inhibiting or forbidding substrate ligation.⁴¹

Several strategies have been developed to activate saturated clusters through the more facile generation of vacant coordination site. One involves the replacement of one of the strong field ligands with a weak field donor molecule that can more readily dissociate to generate a vacant metal binding site. In most cases however, this strategy results in a loss of catalytic activity.^{23,46}

Other strategies involve the activation of metal-metal bonds. This strategy is commonly employed in first row transition metal clusters as first row metal-metal bonds are significantly weaker than their second- and third-row congeners.⁴¹ Cleavage of a M–M bond results in the formation of two (or more) low coordinate metal centers; however, the strategy poses a certain risk of complete cluster decomposition. Decomposition is often suppressed or prevented entirely by installing anionic or dianionic O, S, RP and R₂P-type ligating atoms to keep the metallic core intact (Equation 1.1).⁴⁶ This strategy however, has never led to the successful generation of high-activity molecular catalysts.

Equation 1.1



The field has more recently set its focus on the rational synthesis of coordinatively unsaturated transition metal clusters. Coordinatively unsaturated metal clusters are more active due to the presence of at least one metal center with at least one vacant coordination site.^{23,26,41} Unfortunately, rational synthesis of low-coordinate transition metal clusters remains difficult and the field has not progressed rapidly.^{12,23}

Low-coordinate transition metal clusters nonetheless provide facile entry into catalytic cycles because low-coordinate assemblies possess structural and electronic properties similar to key reactive intermediates.^{23,41} In this pursuit, the ultimate goal of the field is to nucleate coordinatively unsaturated clusters where each metal center has a vacant coordination site.

1.1.3 Rational Synthesis of Low-Coordinate, Ligand-Supported Transition Metal Clusters. Model Compounds for Metal-Metal Cooperativity Studies

The rational synthesis of discrete, molecular, low-coordinate transition metal clusters is generally plagued by challenges related to redox instability and lack of control over the metal coordination environment. In most literature examples, the polynuclear core is sterically encumbered by the ligands, the metals are coordinatively saturated, or both.⁴⁷⁻⁴⁹ These properties limit the utility of soluble polynuclear assemblies in catalysis or as model systems for studying metal–metal

cooperativity, both of which, require the generation of an array of coordinatively unsaturated metal centers.^{47,48,49}

Recent investigations have demonstrated that ligand architecture plays a crucial role in controlling the metal coordination environment in these soluble polymetallic assemblies.^{47,48} Cleverly designed ligand scaffolds stabilize multiple transition metal ions within metal-metal bonding distance(s) while maintaining metal coordinative unsaturation, allowing for metal-metal cooperativity (**7-8**, Figure 1.3).^{14,50} The very limited number of catalytically active ligand-supported clusters highlights the great need to develop novel cluster design strategies that will nucleate polynuclear metal cores while maintaining low metal coordination.^{14,50}

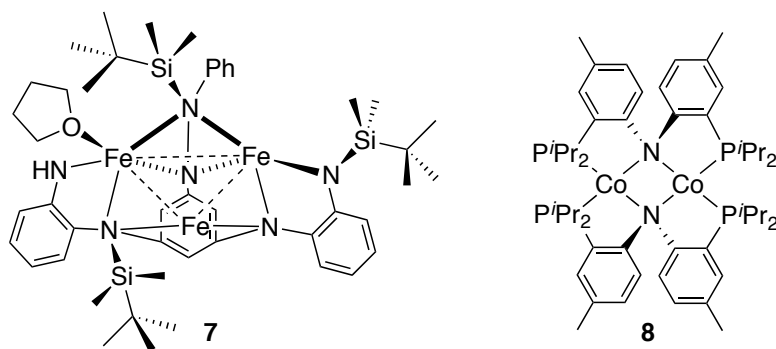


Figure 1.3. Polyfunctional ligand-supported molecular models for metal-metal cooperativity studies.^{14,50} Dotted lines depict intermetallic separation within bonding range.

We have developed a new approach to the design and synthesis of low-coordinate molecular transition metal clusters of the first-row transition elements, envisaging the assembly of soluble, structural analogues of the

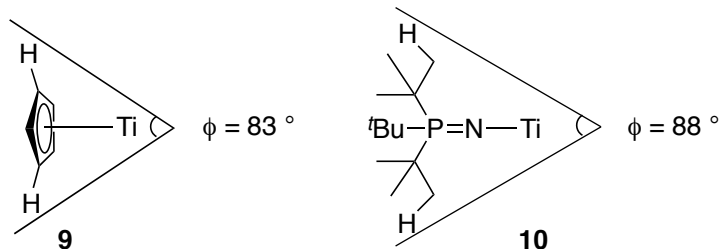
proposed active sites that power heterogeneous catalysts. This effort is focused on the rational synthesis of discrete molecular arrays of low valent, *terminally* low-coordinate metal ions. Our approach arises, essentially, from merging atomic-level supramolecular design with leading theories in inorganic coordination chemistry.⁵¹ To amplify the inherent reactivity of the resultant “active site”, *ancillary ligand-free* low-coordinate clusters were targeted. A strongly basic, *strongly bridging* anionic ligand system was employed to encourage intermetallic bridging through “single-atom” nitrogen centers. This would, at least in principle, nucleate a structurally robust polymetallic coordination array with surface-like structure(s) and catalytic reactivity.

1.2 Project Background: Cluster Design Strategy

Anionic trialkylphosphoranimide ligands bearing sterically bulky alkyl groups were selected to nucleate the low-coordinate first-row transition metal clusters. Bulky trialkylphosphoranimides are known to impose steric protection at the metal comparable to traditional organometallic supporting ligands (**9-10**, Figure 1.4). Computational modeling studies suggest that anionic trialkylphosphoranimides ligands are isolobal with cyclopentadienyl ligands; both systems use a σ and two π -type orbitals for metal coordination. When bound to a metal, the bulky phosphoranimide substituents allow for efficient kinetic isolation of the metal centers, keeping them low-coordinate. A unique advantage of inorganic

phosphoranimides over traditional organic ligands is the displacement of steric pressure away from the metal center(s) by the “extra” nitrogen atom in the phosphoranimide P=N functionality.^{52,53} This structural motif permits more facile coordination of incoming substrates or reagents to the unsaturated metal(s). In addition, the strongly basic and strongly bridging anionic nitrogen centers in sterically bulky electron-rich trialkylphosphoranimides are envisaged to be incapable of bridging more than two metal centers, imposing lower dimensionality on the resulting clusters.

Figure 1.4



Aside from imparting considerable steric protection at a distance, trialkylphosphoranimide ligands are nearly ideal supporting ligands, with characteristic thermal and oxidative stability, strong internal bonds, and tunable electronic character, the latter a function of the three phosphorus substituents.^{52,54-57}

Trialkyl- and triarylphosphoranimides are versatile supports for organometallic intermediates undergoing multi-electron redox transformations as these ligands can adopt various modes of coordination in response to electronic and steric factors at the metal center(s). Trialkylphosphoranimides coordinate in doubly-bridging (I), triply-bridging (II) or terminal (III) modes (Figure 1.5).^{52,53,58} When terminally bound, the phosphoranimide can donate up to a total of six electrons (I) to the metal *while occupying only one coordination site per metal* (Figure 1.5). A series of comprehensive reviews covering the synthesis and characterization of a range of transition metal phosphoranimide complexes has been published.^{52,56,59-63}

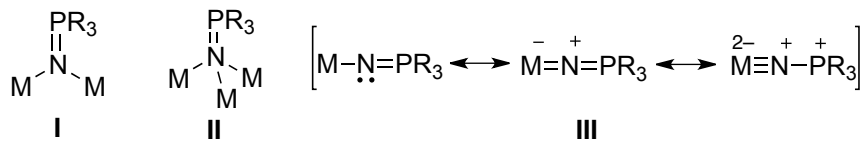
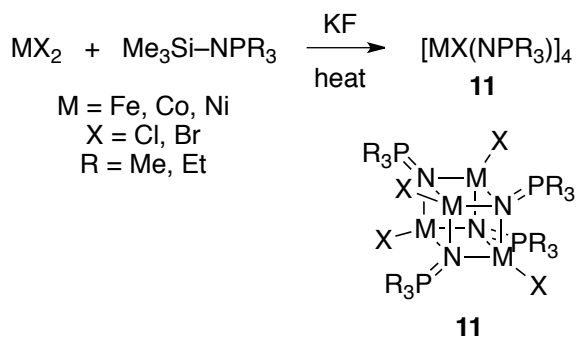


Figure 1.5. Binding modes of anionic trialkylphosphoranimide ligands.

Pioneering studies from the groups of Dehnicke^{56,57,61,64} and Stephan^{52-54,59,62,63,65-67} on the synthesis of phosphoranimide-supported clusters inspired us to pursue this cluster design paradigm. Dehnicke and coworkers demonstrated convincingly that sterically small

trialkylphosphoranimide anions ($R = Me, Et$) nucleate three-dimensional tetrametallic “heterocubane” clusters **11** from late first row metals, maintained by triply-bridging nitrogen centers (Equation 1.2). These clusters were synthesized via high-temperature molten-phase σ -bond metathesis reactions between various M(II) halide precursors and the corresponding N-trimethylsilyltrialkylphosphoranimide reagent in the presence of stoichiometric or excess quantities of Group I fluoride salts such as NaF and KF.^{57,64}

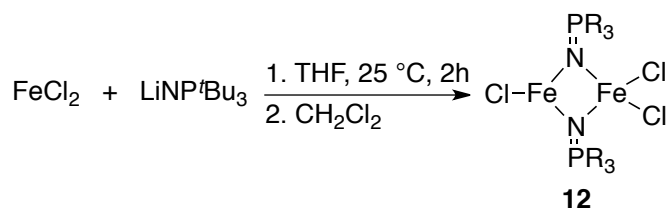
Equation 1.2



The Stephan group made an important contribution to the synthesis and understanding of phosphoranimide transition metal clusters by demonstrating that the *dimensionality*, nuclearity, and metal coordinative saturation could be manipulated by varying the phosphoranimide steric pressure. Anionic metathesis reaction between $FeCl_2$ and tri-*tert*-butylphosphoranimide, followed by metal oxidation resulted in the formation of a two-dimensional, mixed-valent, bimetallic $Fe(II)/Fe(III)$

cluster **12** where the ligands now adopt doubly bridging coordination (Equation 1.3).⁶⁶

Equation 1.3



1.3 Results and Discussion

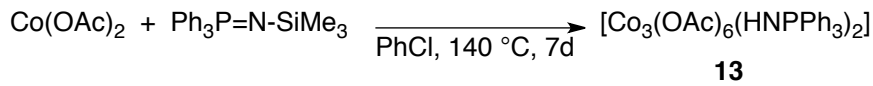
The succeeding sections tackle the synthesis, isolation, and characterization of a series of phosphoranimide-supported complexes of the first row transition metals. Methodology for preparation of mononuclear and polynuclear phosphoranimide complexes of the base metals at various oxidation states is described, using a range of different synthetic approaches. A series of structurally novel base metal phosphoranimide clusters has thus been successfully developed, many exhibiting unusual cluster nuclearity and dimensionality.

1.3.1 Cobalt (II) phosphoranimide clusters from σ -bond metathesis reactions –limitations of the Dehnicke Method

The synthesis of base metal clusters supported by bulky phosphoranimide ligands with general formula $[\text{M}(\text{NPR}_3)\text{OAc}]_n$ was initially approached using a modification of the high-temperature procedure

developed by Dehnicke and coworkers.^{57,64} Dehnicke and coworkers reported the successful synthesis of tetrametallic heterocubane clusters, $[M(NPR_3)X]_4$ (where R = Me, Et; and X = Cl, Br) through a high-temperature reaction between the solid M(II) halide precursor and the liquid $R_3N=P-SiMe_3$ reagent (Equation 1.2). The efficiency of the Dehnicke procedure decreases when higher molecular weight phosphoranimide ligands are used. These precursors are typically solid at room temperature and have dramatically higher boiling points. In order to ensure efficient contact between the M(II) salt and phosphoranimide precursors, the high-temperature synthesis was conducted in solution phase using high-boiling solvents such as chlorobenzene. The solution phase reaction between the solid N-trimethylsilyltriphenylphosphoranimine and stoichiometric cobalt (II) acetate in chlorobenzene at 140 °C afforded two fractions of products. The trimetallic cluster **13** was extracted as a dark blue, toluene-soluble solid that recrystallizes from a concentrated toluene solution at -35 °C in 30 % yield (Equation 1.4). Structural and compositional characterization of the toluene-insoluble fraction was not pursued since recrystallization was unsuccessful.

Equation 1.4



The solid-state structure of **13** shows a linear trimer of cobalt (II) acetate units with each terminal cobalt center capped with a neutral triphenylphosphoranimine ligand, $[\text{Co}_3(\text{CH}_3\text{COO})_6(\text{HNPPPh}_3)_2]$ (Figure 1.6). The ORTEP diagram further shows that all three metal centers are coordinatively saturated, while exhibiting two different Co(II) coordination numbers. The central cobalt ion, bound to six acetate residues, adapts an octahedral geometry while the two terminal cobalt centers are tetrahedral. Interestingly, four of the six acetate ions act as *three-atom bridges* while the remaining two serve as *single atom bridges*.

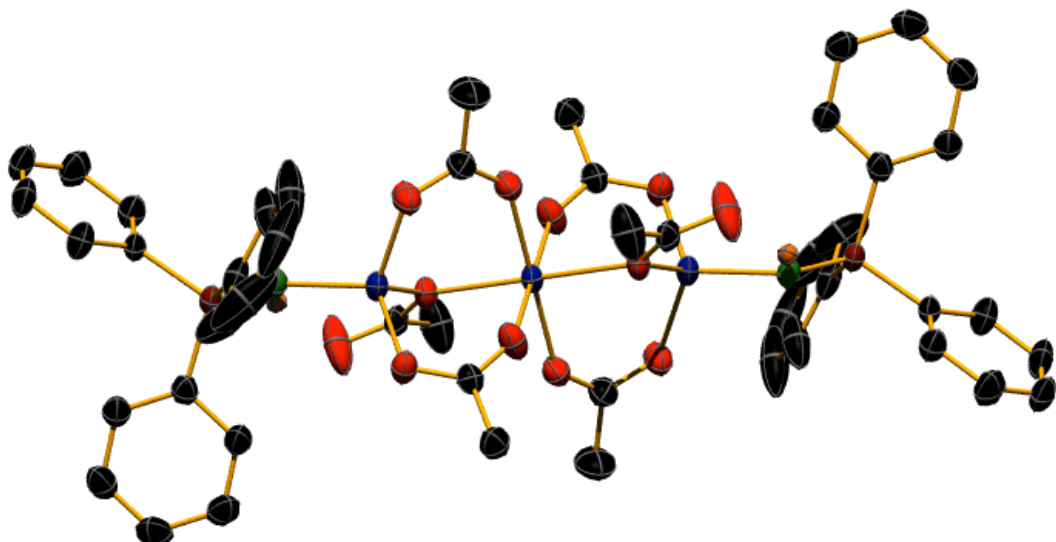


Figure 1.6. Solid-state structure of $[\text{Co}_3(\text{CH}_3\text{COO})_6(\text{HNPPPh}_3)_2]$ **13**. The thermal ellipsoids are shown at 50% probability. Hydrogen atoms have been omitted for clarity. $R1 = 0.0520$, $R(w) = 0.1516$.

Table 1.1. Pertinent bond distances in **13**.

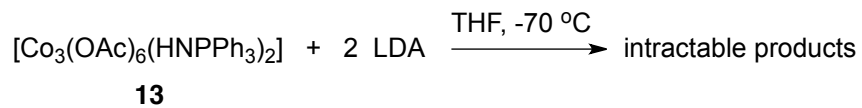
Bonded Atoms	Distance (\AA)
$\text{Co}_{\text{terminal}}-\text{O}$ (ave)	1.975(2)
$\text{Co}_{\text{terminal}}-\text{N}$ (ave)	1.979(3)
P–N	1.591(3)
$\text{Co}_{\text{central}}-\text{O}$ (ave)	2.103(2)
NH ······ O	2.11

The observed dative Co-N bond distance, 1.979(3) Å (Table 1), is shorter than the Co-N distances reported by Dehnicke and coworkers in the tetrametallic heterocubane clusters comprised of ionic Co-N bonds.^{57,64} This suggests a Co-N bond order greater than one and further suggests partial donation of the P-N π-electron density to a d-orbital on cobalt. This hypothesis is supported by the observed longer P-N bond in **13**, 1.591(3) Å, compared to the P-N length in the free Ph₃P=NH molecule, 1.524(3) Å.⁵⁶

The synthesis did not produce the target [Co(NPPh₃)(OAc)]_n oligomer(s). Displacement of acetate anions to achieve the 1 : 1 cobalt-to-acetate ion ratio in the product failed presumably due to the competitive protonation of the anionic triphenylphosphoranimide ligand, forming Ph₃PNH – a weaker donor compared to its anionic counterpart. A probable protonation pathway that can occur under the conditions described in Equation 1.4 involves the acid-base reaction between the strongly basic anionic triphenylphosphoranimide ligand and the acidic α-proton(s) of a metal-bound acetate ion.

The deprotonation of the phosphoranimine N-H bonds in **13** was then conducted to promote intermetallic bridging through the anionic nitrogen centers. Treatment of **13** with stoichiometric amounts of LDA at -70 °C in THF, however, afforded intractable dark-green products (Equation 1.5).

Equation 1.5



The high-temperature synthetic approach was also employed in an attempt to synthesize the corresponding tri-*tert*-butylphosphoranimine version of **13**. Minimal substrate conversion was observed, however, because $^t\text{Bu}_3\text{PN-SiMe}_3$ sublimes from the reaction mixture at temperatures above 90°C . This result highlights some of the limitations of Dehnicke's high temperature and melt-phase methodologies.

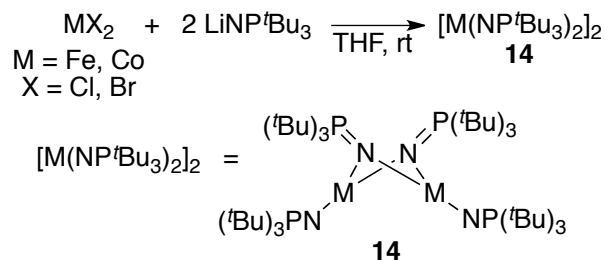
The synthesis of transition metal-phosphoranimide clusters presented highlights the limitations of metathetical exchange of the polydentate acetate ion. The protonation of the phosphoranimide nitrogen is presumably a result of an acid-base reaction with the acidic α -hydrogens of the acetate ligands. The formation of dative phosphoranimine-cobalt bonds instead of the expected anionic ligand necessitates selective deprotonation to impose intermetallic bridging through anionic phosphoranimide nitrogen centers

1.2.2 Phosphoranimide-Supported Cobalt Complexes – Anionic Ligand Metathesis

The ineffectiveness of Dehnicke's high-temperature synthetic strategy prompted us to adapt, modify, and enhance existing⁶⁶ strategies focused on anionic ligand metathesis, which is operationally straightforward and proceeds under mild conditions. Stephan and coworkers were among the first to demonstrate the utility of anionic ligand methathesis for the synthesis of a wide range of early to late transition metal phosphoranimide complexes.^{65,66} This synthetic approach has enabled the Stryker group to develop unprecedented classes of phosphoranimide-supported clusters of iron, cobalt and nickel.

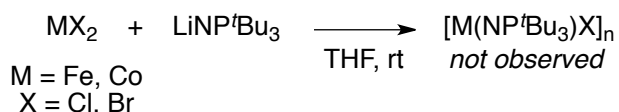
The synthetic utility of the anionic ligand metathesis was first established in the group by Dominique Hebert in the synthesis of a homoleptic, bimetallic cluster **14**, $[M(NP^tBu_3)_2]_2$ ($M = Fe, Co$), from the reaction between a M(II) halide precursor with two equivalents of LiNP^tBu₃ (Equation 1.6).

Equation 1.6



The anionic metathesis is highly sensitive to reaction conditions. Under the conditions described in Hebert's synthesis, attempts to synthesize oligomeric monohalide monophosphoranimido metal(II) complexes, $[M(NPR_3)X]_n$ ($n = 2$ to 4), employing a $1 : 1$ ratio between the M(II) halide precursor and $LiNP^tBu_3$, were unsuccessful (Equation 1.7). Hebert's pentane-soluble dimers, $[M(NP^tBu_3)_2]_2$, were obtained instead.

Equation 1.7



Since the metathesis approach is highly sensitive to reaction conditions, the synthesis of monophosphoranimidometal complexes was addressed using two complementary approaches: (1) starting from monohalide metal precursors and (2) identifying reaction conditions for the metal dihalide that disfavor the second metathesis step, which leads to the Stryker-Hebert dimers.

1.2.2.1 Synthesis of Co Phosphoranimide Complexes from Monomeric Co(I) Precursors

Our initial approach involved the use of metal(I) precursors, L_nMX , to ensure that the metathesis product maintains a $1 : 1$ metal-to-phosphoranimide ratio (Equation 1.8). In addition, we hypothesized that

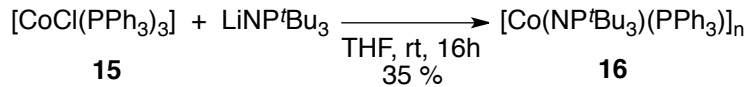
low valent metal phosphoranimide complexes would be amenable to oxidative functionalization, allowing access to a range of functionalized metal-phosphoranimide complexes.

Equation 1.8



Room temperature metathesis between the known Co(I) monohalide complex **20** and LiNP^tBu₃ returned a brown, pentane-soluble product (Equation 1.9). Repetitive fractional recrystallization was conducted using pentane to selectively precipitate out the dissociated PPh₃ fraction. In the end, a compound that nearly passes elemental analysis for the empirical formula [Co(NP^tBu₃)(PPh₃)] **21** was obtained in 35 % yield after 10 recrystallizations.

Equation 1.9



Considering the empirical formula of **16** and the dimeric structure of [M(NP^tBu₃)₂]₂ in the solid state, it is proposed that **16** is also dimeric. Recrystallization of **16** did not produce single crystals. This cobalt(I)-phosphoranimide derivative was nonetheless subjected to a series of

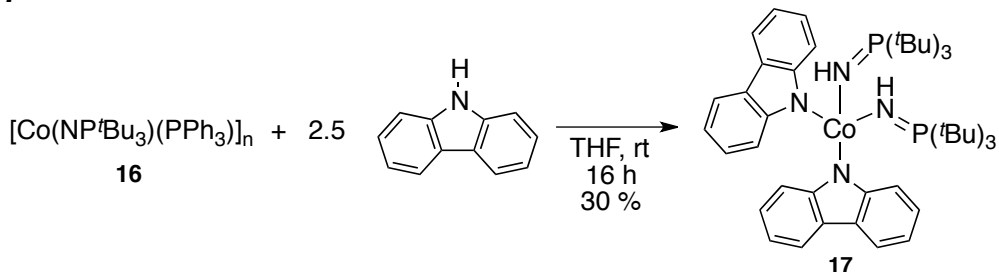
derivatization experiments, one approach to synthesize heteroleptic, high oxidation state metal-phosphoranimide complexes.

1.2.2.1.1 *Reactivity of $[Co(NP^tBu_3)(PPh_3)]_n$: Activation of Acidic X–H Bonds*

Complex **16** was subjected to anionic ligand protonolysis using reagents with acidic X-H (X = S, N) bonds, with the intention of preparing phosphoranimidometal complexes in a heteroatom-rich environment. Nitrogen- and sulfur-rich metal-phosphoranimide complexes could model organometallic intermediates involved in hydrodesulfurization and hydrodenitrogenation catalysis.

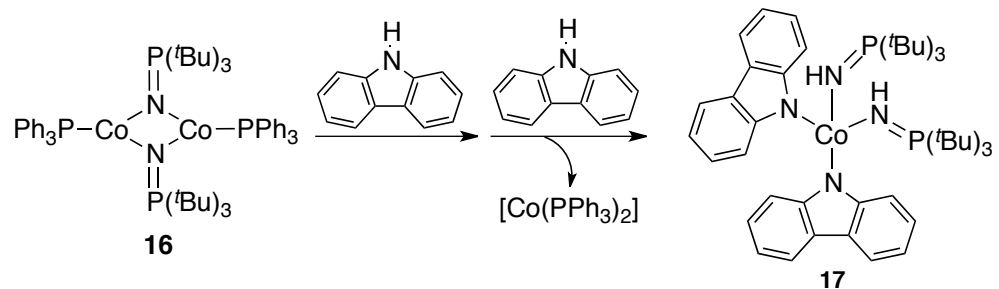
Treatment of **16** with excess carbazole afforded a dark blue, THF-soluble product that was crystallographically identified as the mononuclear bis(N-carbazolido)-bis(tri-*tert*-butyl)phosphoraniminecobalt(II) complex **17**. This mononuclear species presumably forms as a result of a redox conproportionation reaction and, since the Co(I) precursor was limiting, a maximum of 50 % yield was anticipated (Equation 1.10). Product **17** was obtained in 30 % yield.

Equation 1.10



The formation of the Co(II) complex **17** is presumably a result of acid-base reaction between the anionic phosphoranimide ligands with the N-H bonds of two incoming carbazole molecules and a one-electron transfer from the nitrogen-bound Co(I) center to the second Co(I) center of **16**. The electron transfer hypothetically forms the neutral cobalt fragment $[\text{Co}(\text{PPh}_3)_2]$ that eventually dissociates from the dimer, liberating the mononuclear product **17** (Equation 1.11).

Equation 1.11



The solid state structure of **17** (Figure 1.7) features a tetrahedral cobalt geometry with the two tricyclic carbazolide moieties perpendicularly oriented to one another. The measured Co–N_P bond distances are in the range of Co–N bond measurements reported by Dehnicke.^{57,64} The P–N

bond (1.6176(15) Å) is shorter than the P–N distance for a free $t\text{Bu}_3\text{P}=\text{NH}$ molecule. These structural data suggest partial donation of metal electron density to the polarized P–N bond and further indicate the π –acceptor property of the $t\text{Bu}_3\text{PNH}$ ligand.

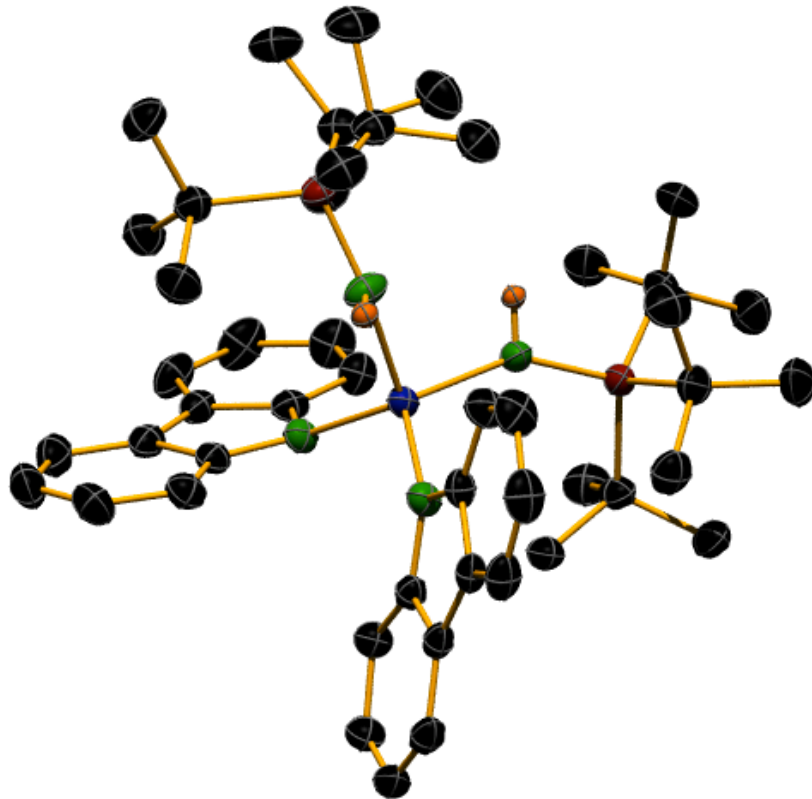


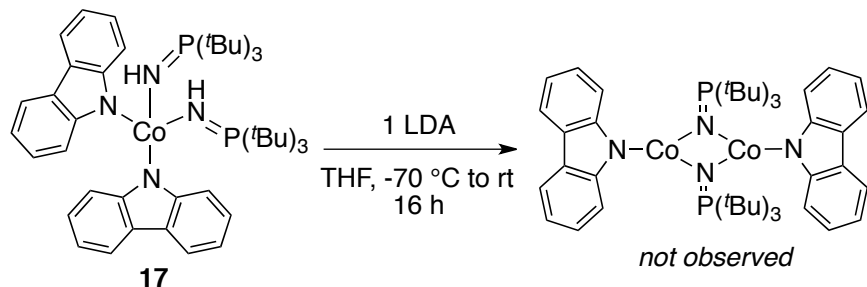
Figure 1.7. Solid-state structure of $[\text{Co}(\text{HNP}^t\text{Bu}_3)_2(\text{NC}_{12}\text{H}_8)_2]$ **17**. The thermal ellipsoids are shown at 50% probability. Hydrogen atoms have been omitted for clarity. $R1 = 0.0359$, $R(w) = 0.0957$.

Table 1.2. Pertinent structure parameters in **17**.

Bonded Atoms	Distance (Å)
Co–NP	2.0439(14), 2.0659(15)
Co–N _{carbazolide}	2.0337(15), 2.0159(14)
P–N	1.6176(15)

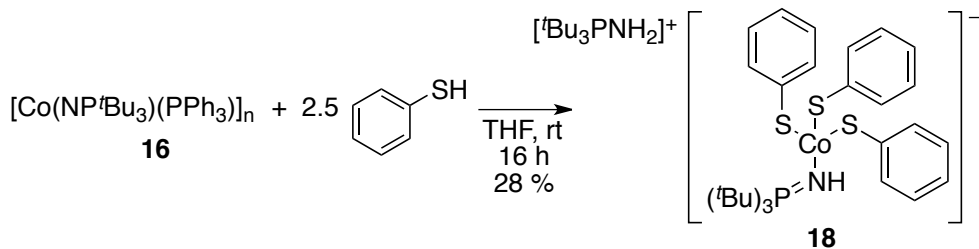
The mononuclear carbazolide-derivative **17** was treated with stoichiometric LDA in THF at $-70\text{ }^{\circ}\text{C}$ to promote intermetallic bridging through the anionic phosphoranimide nitrogen centers (Equation 1.12). The reaction, however, afforded an intractable product mixture.

Equation 1.12



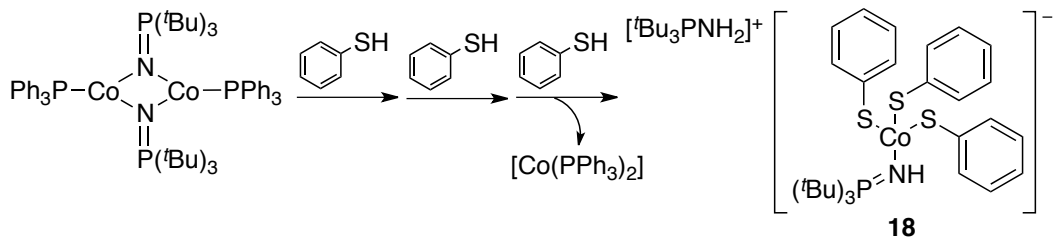
The Co(I) precursor **16** was also treated with excess thiophenol at $-70\text{ }^{\circ}\text{C}$ (Equation 1.13). The reaction produced the mononuclear complex salt, $[^{\prime}\text{Bu}_3\text{PNH}_2]^+[\text{Co}(\text{HNPO}^{\prime}\text{Bu}_3)(\text{SPh})_3]^-$ **18**. The 1 : 3 cobalt-to-thiophenolate ion ratio in **18** makes thiophenol (PhSH) the limiting reagent in the reaction described (Equation 1.13). With the complex stoichiometry taken into consideration, **18** was isolated in 28% yield.

Equation 1.13



Mechanistically, the formation of **18** can be envisaged as the result of a series of three acid-base reactions between the S-H bonds of three thiophenol and two equivalents of $^t\text{Bu}_3\text{PN}^-$, generating the metal-bound neutral $^t\text{Bu}_3\text{PNH}$ molecule and a cationic $^t\text{Bu}_3\text{PNH}_2^+$. The formation of the trithiophenolatocobalt(II) complex **18** occurs from single electron transfer from the sulfur-bound Co(I) center to the second Co(I) atom or the dimeric precursor **16**. Similar to the formation of **17** the electron transfer forms a neutral cobalt fragment $[\text{Co}(\text{PPh}_3)_2]$ that eventually deaggregates from the dimer to generate **18** (Equation 1.14). Despite its dubious origin, complex **18** is nonetheless the first crystallographically characterized sulfur-functionalized cobalt-phosphoranimine complex isolated in the Stryker group.

Equation 1.14



The X-ray crystallographic data for **18** (Table 1.3; Figure 1.8) show a 2.013(2) Å Co-N distance. This measurement is in the range of Co–N distances reported by Dehncke in a series of tetrametallic heterocubane Co(II) phosphoranimide complexes.^{57,61,64} The measured P–N distance of 1.594 Å is again shorter than the P–N bond in a free $^t\text{Bu}_3\text{P}=\text{NH}$ molecule.

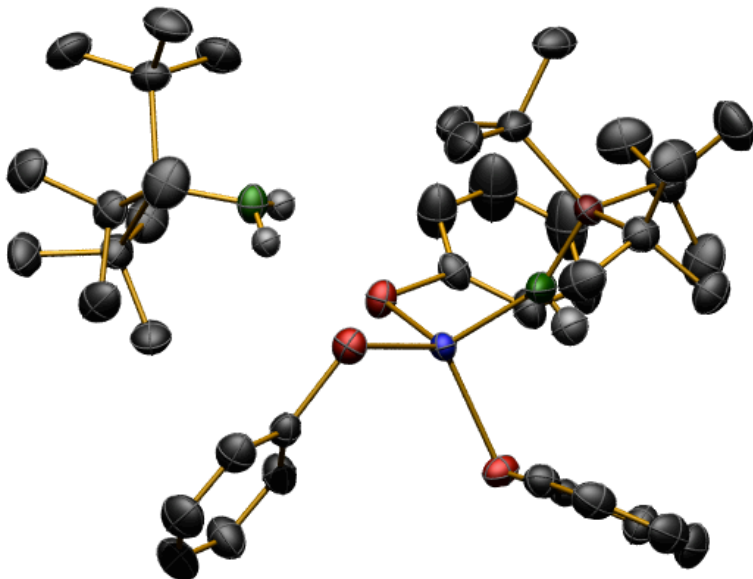


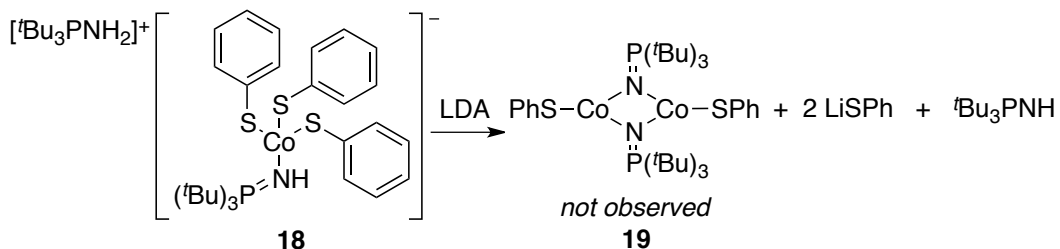
Figure 1.8. Solid-state structure of $[^t\text{Bu}_3\text{PNH}_2]^+[\text{Co}(\text{HNP}^t\text{Bu}_3)_2(\text{SPh})_3]^- \mathbf{18}$. The thermal ellipsoids are shown at 50% probability. Hydrogen atoms have been omitted for clarity. $R1 = 0.0399$, $R(w) = 0.0983$.

Table 1.3. Pertinent bond distances in **18**.

Bonded Atoms	Distance (Å)
Co–N	2.013(2)
Co–S	2.3248(7), 2.3260(7), 2.3388(7)
P–N	1.594(2)

Anionic thiolate complex **18** presents some of the structural properties desired for an organometallic model of the putative intermediates involved in catalytic hydrodesulfurization: *a soluble cobalt complex supported by a sulfur-rich coordination environment*. Conversion of **18** into a neutral oligomeric derivative **19** was attempted via stoichiometric deprotonation using LDA (Equation 1.15). The deprotonation unfortunately afforded intractable product mixtures under a range of reaction conditions.

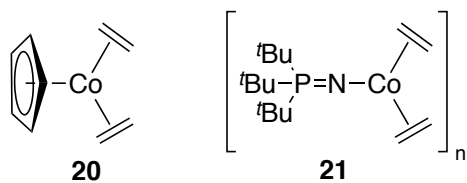
Equation 1.15



Mechanistic studies pertinent to the formation of complexes **17** and **18** were not pursued, as structural characterization of precursor **16** remains ambiguous and the deprotonation reactions uniformly unsuccessful.

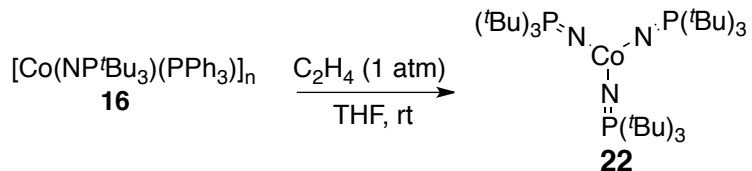
1.2.2.1.2 Organometallic Cobalt-Phosphoranimide Derivatives

The synthesis of organometallic derivatives of phosphine-stabilized **16** was conducted as an indirect alternative to structural characterization. Since the tri-*tert*-butylphosphoranimide ligand imposes steric protection comparable to a cyclopentadienyl anion,⁶² the preparation of the phosphoranimide version of the well-known Co(I) bis(ethylene) complex, $[\text{CpCo}(\text{C}_2\text{H}_4)_2]$ (**20**)⁶⁸ was attempted.

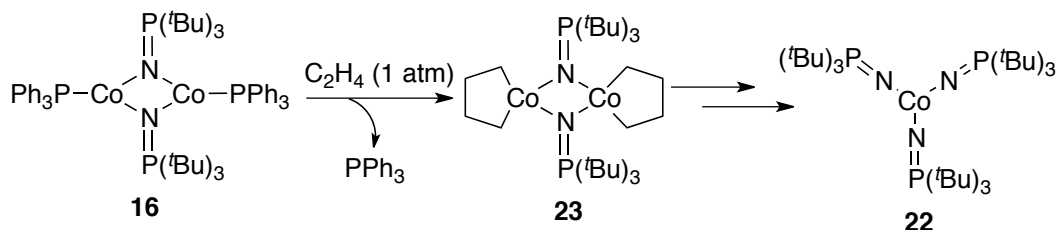


Exposure of a THF solution of **16** to a stream of prepurified ethylene gas at room temperature resulted in an abrupt color change from brown to cherry red. The resulting pentane-soluble crude product deposits single crystals from a concentrated THF solution (Equation 1.16). Surprisingly, the solid state structure of the product revealed the formation of a homoleptic Co(III) species, $[\text{Co}(\text{NP}^t\text{Bu}_3)_3]$ **22**. The mechanism for the formation of this high oxidation state phosphoranimide complex remains highly speculative. This species could form from the oxidative cyclometallation of a Co(I)-phosphoranimide fragment with two equivalents of ethylene molecules followed by ligand redistribution (Equation 1.17). The other cobalt coordination byproducts of this reaction were uncharacterized. Studies on the mechanism of this reaction were not pursued, although the reaction is a good subject for further investigation. A rational high-yielding synthesis and structural characterization of **22** are presented in the latter part of this chapter.

Equation 1.16



Equation 1.17



The anionic metathesis between LiNP^tBu_3 and $(\text{Ph}_3\text{P})_3\text{CoCl}$ afforded a pentane-soluble product $[\text{Co}(\text{NP}^t\text{Bu}_3)(\text{PPh}_3)]_n$ **16**. Upon treatment of reagents with acidic X–H bonds, complex **16** is a precursor for the synthesis of heteroleptic cobalt(II)-phosphoranimine complexes $[\text{Co}(\text{HNP}^t\text{Bu}_3)_2(\text{NC}_{12}\text{H}_8)_2]$ **17** and $[^t\text{Bu}_3\text{PNH}_2]^+[\text{Co}(\text{HNP}^t\text{Bu}_3)(\text{SPh})_3]^-$ **18** rather than maintain the phosphoranimide ligand in anionic form. The results demonstrate the difficulty in controlling the oxidative functionalization of low valent metal phosphoranimide precursors.

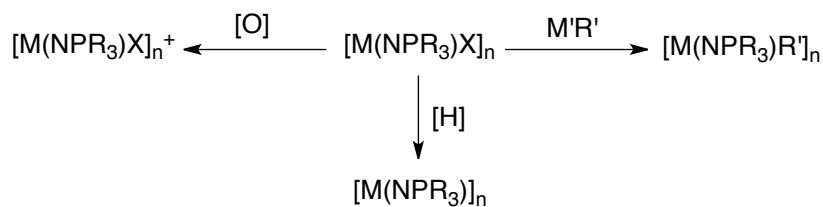
1.2.2.2 Synthesis of $[\text{M}(\text{NP}^t\text{Bu}_3)\text{X}]_2$ Dimers. Versatile Metal (II) Phosphoranimide Precursors

Oligomeric monophosphoranimidometal(II) complexes are simple, highly promising precursors to clusters with varying nuclearity and metals at different oxidation states, as illustrated in Scheme 1.

Dehnicke and coworkers demonstrated that the halide residues on the tetrametallic heterocubane clusters $[\text{M}(\text{NPR}_3)\text{X}]_4$ (where M = Fe, Co, Ni; X = Cl, Br; R = Me, Et) can be displaced by a range of strongly

nucleophilic reagents, to form heteroleptic phosphoranimidometal(II) clusters (Scheme 1). Treatment of $[M(NPMe_3)Cl]_4$ with alkyl transfer reagents ($M = Fe, Mn; R = -Me, -C\equiv CC_6H_5$) formed organometallic heterocubanes $[M(NPMe_3)R]_4$.^{57c,61,64}

Scheme 1



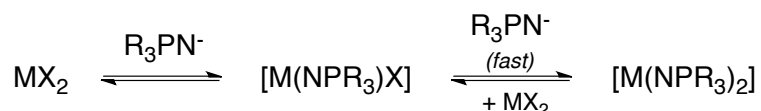
On the other hand, Stephan and coworkers initially attempted the synthesis and isolation of the $[M(NP^tBu_3)X]_n$ oligomers from the metathesis reaction between a M(II) halide and $LiNP^tBu_3$ in a 1 : 1 stoichiometry. The isolation and purification of the monophosphoranimidometal(II) derivative(s) was unsuccessful. Interestingly, however, the formation of $[M(NP^tBu_3)X]_2$ was confirmed by the ultimate isolation of the mixed-valent metal-phosphoranimide dimer $[M(NP^tBu_3)_2X_3]$ when the metathesis was conducted in dichloromethane, an oxidizing solvent (Equation 1.3).⁶⁶ The *in-situ* synthesis of $[M(NPR_3)X]_n$ ($M = Fe, Co; R = Cy, ^tBu$) precursors followed by chemical oxidation provided an efficient route to high oxidation state M(III)-phosphoranimide dimers $[M(NP^tBu_3)X_2]_2$ (Scheme 1) for these researchers.^{66,69}

Furthermore, we hypothesized that $[M(NPR_3)X]_n$ clusters supported by sterically bulky trialkylphosphoranimide ligands could be reduced to form ancillary ligand-free monophosphoranimidometal(I) oligomers, $[M(NPR_3)]_n$, where the metals are envisaged to remain low coordinate due to the steric protection provided by the bulky phosphorus substituents (Scheme 1). Although we were uncertain as to the precise structure that such oligomeric or polymeric materials might take, it was clear that such highly unsaturated clusters would be exceptionally reactive.

The high sensitivity of the anionic phosphoranimide metathesis to reaction conditions makes the synthesis of oligomeric $[M(NPR_3)X]_n$ precursors extremely challenging.⁶⁶ Room temperature metathesis experiments, where a 1 : 1 ratio between the metal(II) halide precursor and the anionic phosphoranimide reagent was employed, afforded only the corresponding Stryker-Hebert dimers, accompanied by half equivalent of the starting dihalide. This suggests fast rates for the metathesis of the second M-Cl bond relative to the first or, at least equally probable, rapid ligand redistribution of the desired mono(phosphoranimide) product to produce an equilibrium mixture of all three compounds, from which the metal dihalide precipitates selectively, leaving the bis(phosphoranimide) metal complex in solution. To address this, a series of experiments was undertaken to identify conditions that inhibit the second metathesis step.

It was assumed that maintaining low concentration of the anionic phosphoranimide would inhibit the formation of the Stryker-Hebert dimers. Maintaining a large excess of MX_2 makes the first metathesis step kinetically competitive with the second metathesis step (Equation 1.18). If the formation $[\text{M}(\text{NPR}_3)_2]$ is an equilibrium, a large excess of MX_2 could induce ligand redistribution, converting $[\text{M}(\text{NPR}_3)_2]$ back to the $[\text{M}(\text{NPR}_3)\text{X}]$ precursor. Furthermore, it was anticipated that the metathesis reaction would be slower and more selective at lower temperatures.

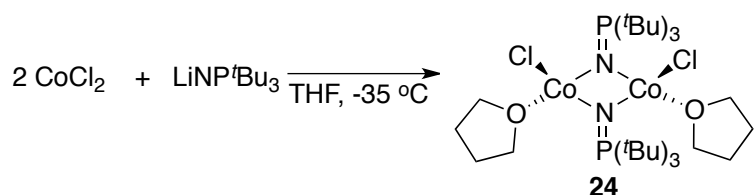
Equation 1.18



The utility of this low-temperature anionic ligand metathesis strategy was first demonstrated by the high-yield synthesis of a tri(*tert*-butyl)phosphoranimide-bridged dimer, $[\text{CoCl}(\mu_2\text{-NP}^t\text{Bu}_3)(\text{THF})]_2$ **24** (Equation 1.19), from the reaction between LiNP^tBu_3 and excess CoCl_2 (1 : 2) in THF at -35 °C. The dark blue, THF-soluble dimer **24** was readily isolated and purified by recrystallization from a cold, concentrated THF solution in 87 % yield. When in solution, complex **24** shows temperature sensitivity; a cold THF solution of the pentane-insoluble **24** decomposed into a dark green, pentane soluble product when warmed. The color and

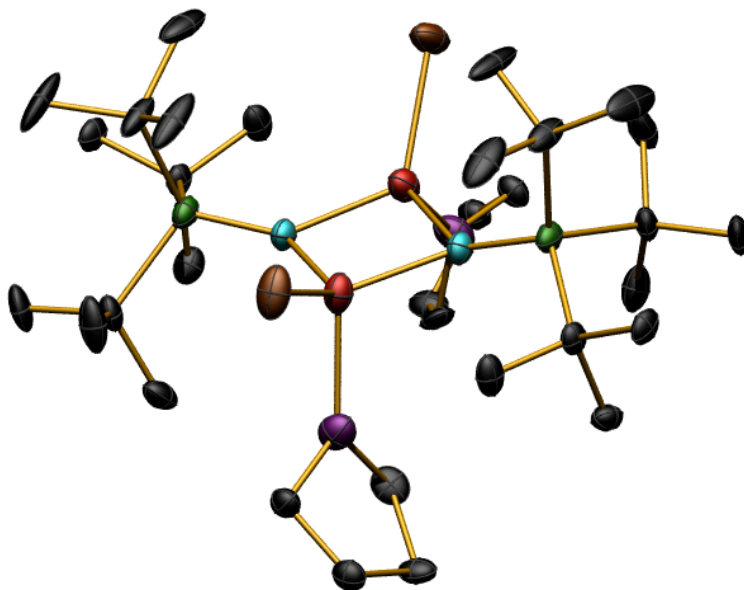
solubility of the decomposition product is similar to the Stryker-Hebert cobalt(II) dimer.

Equation 1.19



The solid state structure of dimer **24** features a dinuclear cobalt(II) core with doubly-bridging phosphoranimide ligands, one per metal (Figure 1.9). Each metal center is solvated by a THF molecule and decorated with a residual chloride. Interestingly and oddly, the halide functionality adopts a *cis*-orientation with respect to the planar Co_2N_2 core. Average $\text{Co}-\text{N}-\text{Co}$ and $\text{N}-\text{Co}-\text{N}$ bond angles of $84.38(6)^\circ$ and $95.56(6)^\circ$ were measured, respectively, representing a diamond-shaped Co_2N_2 core. Both cobalt(II) centers adopt a pseudo-tetrahedral geometry as evidenced by bond angles centered at cobalt that deviate from the ideal 109.5° . Magnetic susceptibility measurements on dimer **24** have not been conducted at this point; hence, the presence of a $\text{Co}-\text{Co}$ bond remains inconclusive despite the intermetallic distance of $2.6718(7)$ Å. The observed $\text{Co}-\text{N}$ bond distances are similar to Dehnicke's measurements in his tetrametallic heterocubane clusters $[\text{Co}(\text{NPR}_3)\text{Cl}]_4$, where $\text{R} = \text{Me}$, Et.^{57,64} Partial donation of Co(II) electrons to the polarized P–N bond is

suggested by the shortened P–N bond length in the dimer. This interaction is supported by the nearly planar geometry around the nitrogen centers, allowing for more effective alignment of the metal d-orbitals and ligand π orbitals involved in the back donation.



Bonded Atoms	Distance (\AA)	Bonded Atoms	Bond Angle ($^{\circ}$)
Co•••Co	2.6718(7)	Co–N–Co	84.38(6)
Co–Cl	2.2916(6)	Co–N–P	134.97(10)
Co–O	2.1033(16)		137.31(10)
Co–N	1.9861(16) 1.9924(16)	N–Co–N	95.56(6)
P–N	1.5829(16)	O–Co–Cl	95.40(5)
		Co–Co–N	47.91(5) 47.71(5)
		N–Co–Cl	123.21(5) 122.66(5)

Figure 1.9. ORTEP diagram of compound 3, $[\text{CoCl}(\mu_2\text{-NP}'\text{Bu}_3)(\text{THF})]_2$ **24**. The thermal ellipsoids are shown at 50% probability. Hydrogen atoms have been omitted for clarity. $R1 = 0.0305$, $R(w) = 0.0820$.

The generality of this synthetic strategy was demonstrated by the successful synthesis and isolation of a range of other $[M(NPR_3)X]_n$ congeners. In the Stryker group, H. Brown and D. Hebert adapted this approach for the large-scale high-yield synthesis of the Dehnicke tetramer $[Co(NPEt_3)Cl]_4^{70}$ and the previously unknown low-coordinate dimer $[Fe(NP^tBu_3)Br]_2^{70}$, respectively. For example, treatment of excess $FeBr_2(dme)$ with substoichiometric amounts of $LiNP^tBu_3$ allow for Hebert's synthesis of $[Fe(NP^tBu_3)Br]_2^{70}$ in 41 % yield.

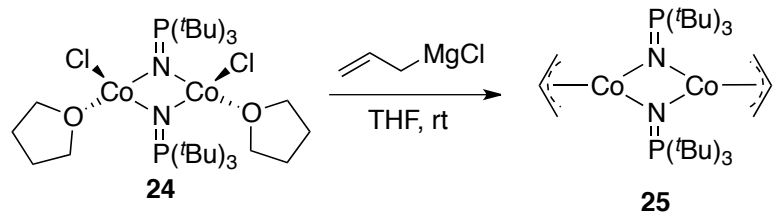
Isolation and structural characterization of the Ni(II) dimer analogous to precursor **24** was unsuccessful. Treatment of excess $NiBr_2(dme)$ with substoichiometric amounts of $LiNP^tBu_3$ forms a dark-green, THF-soluble product. The solids obtained did not pass elemental analysis for $[Ni(\mu_2-NP^tBu_3)Br]_2$ and recrystallization to obtain X-ray quality crystals was unsuccessful.

This strategy effectively addresses the limitations associated with Dehnicke's high temperature synthesis. The facile access to oligomeric monophosphoranimidometal(II) complexes has provided a diverse set of simple, well-characterized precursors for the synthesis of metal-phosphoranimide clusters of various metal oxidation states (Figure 9).

1.2.2.2.1 Synthesis of Allyl-functionalized Monophosphoranimidometal(II) Complexes

Treatment of dimer **24** with excess allylmagnesium chloride in THF resulted in the formation of a green, pentane-soluble species that was isolated and purified by pentane extraction and crystallization from a concentrated solution in THF at $-35\text{ }^{\circ}\text{C}$. The resulting microcrystalline solids nearly passed elemental analysis, as calculated for the allyl-substituted phosphoranimidometal(II) complex **25**, depicted as the expected dimer (Equation 1.20).

Equation 1.20

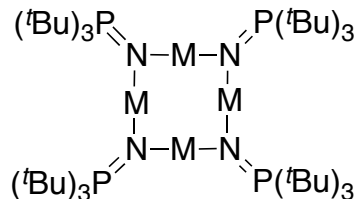


Highly air-sensitive complex **25** reluctantly crystallizes out of THF solution after concentration and cooling to $-35\text{ }^{\circ}\text{C}$. The synthesis, however, is irreproducible and highly dependent on the quality of the allyl transfer reagent. A dimeric structure for **25** is proposed, based on the X-ray structure of the corresponding allylnickel(II) complex recently obtained by Zhao in the Stryker group.⁷⁰ Exhaustive efforts to isolate and

structurally characterize **25** were deferred – this class of organometallic compounds has become the research focus of another member of the Stryker group.

1.2.3 Phosphoranimide-Supported Metal (I) Clusters $[M(NP^tBu_3)]_4$ – Tetrametallic Coordination Arrays with Linear, Two-coordinate Metal Centers

In this section is described the preparation and characterization of discrete *homoleptic trialkylphosphoranimide clusters of Co(I) and Ni(I)*, $[M(NP^tBu_3)]_4$ (**26a** and **26b**, Figure 1.10), in which the four metal centers are coplanar and extremely low-coordinate.



26a, M = Co; **26b**, M = Ni

Figure 1.10. Tetrametallic trialkylphosphoranimidometal(I) complexes.

Complexes **26a** and **26b** constitute the first polymetallic d^8 and d^9 coordination compounds in which each of the metal centers is linear and two-coordinate. Coordinatively-unsaturated transition metal complexes remain synthetically challenging inorganic constructs. There is, however,

an increasing interest in such compounds, which are both structurally unusual and widely anticipated to show enhanced reactivity toward a range of catalytic transformations. Two-coordinate complexes of later first-row transition metals are particularly difficult targets; only a few relevant compounds have been reported. The groups of Power, Arduengo, and Hillhouse have all developed successful approaches to monomeric, neutral, two-coordinate complexes of iron, cobalt and nickel.⁷¹⁻⁷⁶ The syntheses of these open-shell compounds adhere to a common design strategy: (1) the incorporation of bulky ligands (bulky carbanions, N-heterocyclic carbenes, arylthiolates and arylamides) to kinetically stabilize the low-coordinate metal center (**a** and **b** in Figure 1.11), and (2) the use of pendant Lewis acid groups (e.g. boryl, **c** in Figure 1.11) to reduce nitrogen basicity and discourage intermetallic ligand bridging. The use of bulky ligands however, necessarily renders the metal center sterically less accessible, limiting reactivity and scope.

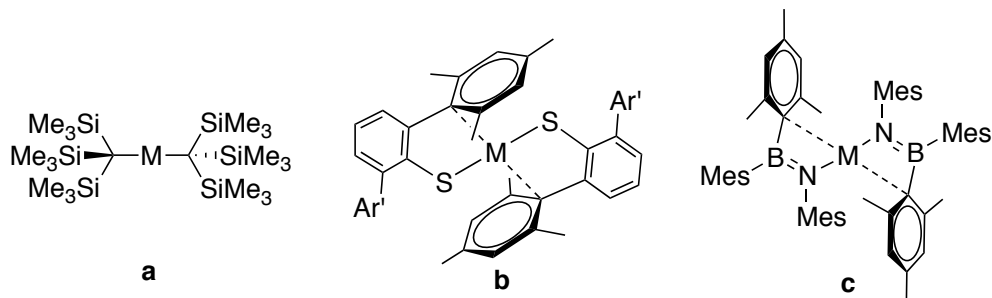
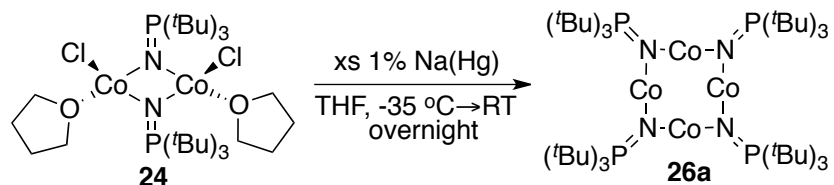


Figure 1.11. Representative two-coordinate complexes stabilized by bulky: (**a**) a bulky carbanionic ligand; (**b**) a bulky thiolato ligand; (**c**) a bulky amido ligand with pendant Lewis acidic group. $M = \text{Mn, Fe or Co}$.⁷⁶ Dotted lines represent weak metal–donor group interactions.

1.2.3.1 Synthetic Routes to $[M(NP^tBu_3)]_4$

Tetrametallic cobalt cluster **26a** was synthesized by the reduction of dimer **24**, $[\text{Co}(\text{NP}^t\text{Bu}_3)\text{Cl}(\text{THF})]_2$, with Na/Hg at room temperature for 16 hours (Equation 1.21). The reduction returned dark brown, pentane-soluble material, which crystallized only reluctantly and then, surprisingly, from THF at -35 °C. No yield was determined for this reaction since a more straightforward strategy, one that does not require the isolation of **24**, was also developed. Complex **26a** was characterized in the solid state by X-ray crystallography, in solution by magnetic susceptibility measurements, and by elemental analysis.

Equation 1.21



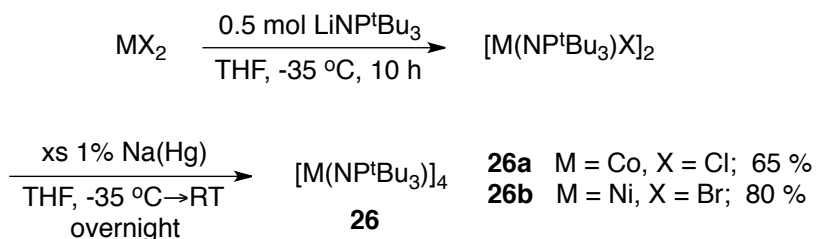
The reduction of **24** is sensitive to the choice of chemical reducing agent. Reduction with KC_8 results in the exchange of three $\text{Co}(\text{I})$ ions for three K^+ ions, but retains a tetrametallic core. The red-brown, pentane-soluble solid obtained from excess KC_8 readily forms prismatic single crystals from concentrated THF at -35 °C. Repeated X-ray crystallographic analysis of different single crystals revealed a

heteropolymetallic cluster, $[K_3Co(NP^tBu_3)_4]$, which is isostructural with cluster **26a**. The potassium ion exchange presumably proceeds through non-selective over-reduction of the cobalt(II) centers to elemental cobalt. This then results in the aggregation of a $[Co(NP^tBu_3)]$ monomer with three equivalents of KNP^tBu_3 , producing $[K_3Co(NP^tBu_3)_4]$. Overreduction and cation exchange was prevented when a weaker reducing agent (1% Na/Hg) was used. The product obtained from the reduction of **24** with 1% (wt/wt) Na/Hg passes elemental analysis for **26a** however, the diffraction data set for single crystals suggests partial substitution of the Co(I) centers for Na cations ($Co_{3.34}Na_{0.66}$).⁷⁰ The mechanism of cation substitution in the cobalt tetramer was not extensively studied; however, the results obtained from using the milder reductant (Na/Hg) suggest that further screening of alternative reducing agents may significantly enhance the efficiency and selectivity of reduction. The identification of potential chemical reducing agents awaits electrochemical measurements of the potential required to reduce the dimeric precursor **24** to **26a**.

Since the isolation of pure $[NiBr(\mu_2-NP^tBu_3)]_2$ was unsuccessful, the synthesis of the analogous nickel(I) tetramer **26b** was conducted using a two-step one-pot procedure involving (1) salt metathesis between excess $NiBr_2(dme)$ and substoichiometric amounts of $LiNP^tBu_3$ followed by (2) in situ reduction with 1 % (wt/wt) Na/Hg reagent (Scheme 2). The reduction step produced a dark green, pentane-soluble product, from which X-ray

quality crystals could be obtained easily via recrystallization in THF at -35 °C.⁷⁷ Cluster **26b** was obtained in high purity and 80% yield. Interestingly, the solid-state structure for **26b** shows no sign of partial exchange of the nickel centers for Na⁺ ions. The two-step synthesis of the corresponding tetrametallic cobalt cluster from CoCl₂ gratifyingly afforded **26a** in an overall 65 % yield (Scheme 2).

Scheme 2



1.2.3.2 Structural Characterization of [M(NP^tBu₃)]₄

The solid state structure of **26a** shows an aggregate of four tri-*tert*-butylphosphoranimidocobalt(I) monomers forming a tetrametallic cluster, where each Co(I) center is bonded to two doubly-bridging phosphoranimide ligands (**26a**, Figure 12). Interestingly, each of the four coplanar metal centers is monovalent and linearly two-coordinate. Figure 1.12 and Table 1.4 show the ORTEP diagram and summarize pertinent structural parameters for the Co₄N₄ cluster core, respectively. The measured Co–N bond distances range from 1.840(4) Å to 1.863(4) Å.

These bond lengths are shorter than the Co–N distances reported by Dehnicke in a series of tetrametallic Co(II) heterocubanes (1.953(6) to 2.370(1) Å).^{57,64} The significantly shorter Co–N distances suggest partial donation of the P–N bond π-electrons to half-filled metal d-orbitals. This suggestion of ligand-to-metal donation, however, is not supported by the shortened P–N bond 1.562(4) Å in the phosphoranimide ligand. *In lieu*, the relatively shorter Co–N bond could mainly be imposed by the doubly-bridging phosphoranimide ligands.

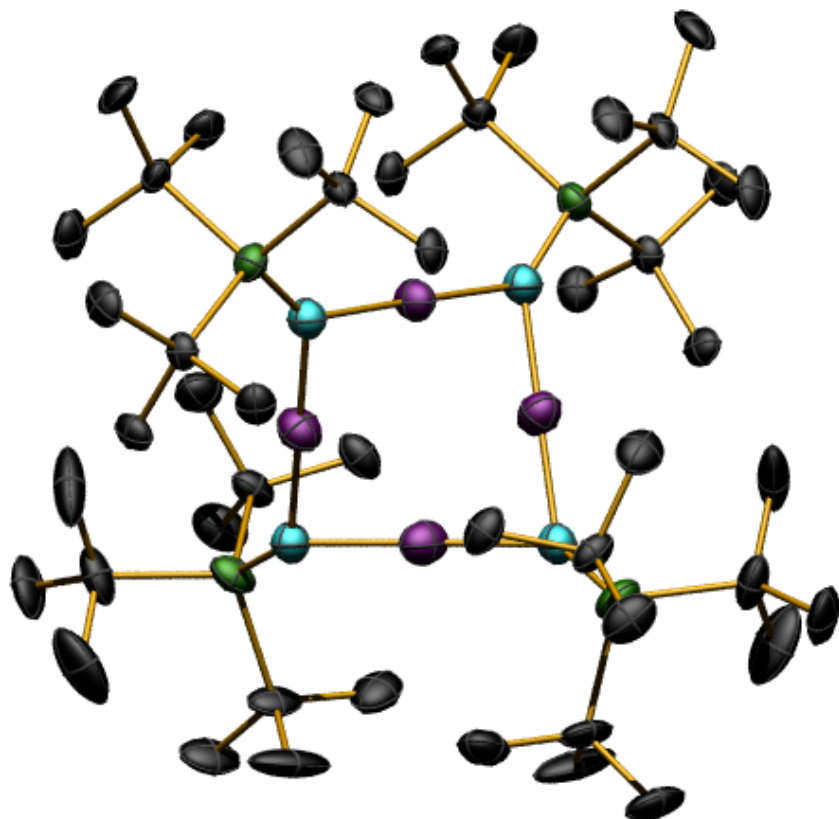


Figure 1.12. ORTEP diagram of compound $[\text{Co}(\mu_2\text{-NP}^t\text{Bu}_3)]_4$ **26a**. The thermal ellipsoids are shown at 50% probability. Hydrogen atoms have been omitted for clarity. $R1 = 0.0540$, $R(w) = 0.1445$.

Table 1.4. Selected bond distances and bond angles for **26a**.

Bonded Atoms	Distance (Å)	Bonded Atoms	Bond Angle (°)
Co $\cdots\cdots$ Co	2.41	N–Co–N	176.0(3), 177.9(3) 179.3(3)
Co–N	1.857(4), 1.840(4) 1.866(4), 1.863(4)	Co–N–P	136.9(3), 141.1(3) 134.1(3), 132.8(3)
P–N	1.562(4)	Co–N–Co	81.53(16), 80.64(16)

The N–Co–N bond angles range from 176.0(3)° to 179.3(3)°. These very slightly bent bond angles fall in the range of L–M–L angles reported for a series of two-coordinate and quasi-two-coordinate Co(II) complexes.^{75,76} Linear, two-coordinate Co(I) complexes are extremely rare. The slight deviation from perfect linearity could be a consequence of solid state crystal packing forces or, equally probable, due to weak bonding interactions between each pair of adjacent cobalt(I) centers. The presence of significant Co–Co bonding is inconsistent with the results of solution magnetic susceptibility measurements, as presented in the succeeding section.

The structure parameters for the Ni₄N₄ core (Table 1.5) and ORTEP diagram of **26b** (Figure 1.13) reveal an assembly isostructural to the tetrametallic cluster **26a**. This cluster has a Ni₄N₄ core composed of four 13-electron Ni(I) centers bridged by doubly-bridging anionic tri-*tert*–

butylphosphoranimide ligands. Compared to **26a**, the bond angles in **26b**, ranging from 178.39(18)° to 179.6(3)°, are nearer to perfect linearity. The Ni–N distances in **26b** range from 1.864(4) to 1.876(4) Å, surprisingly longer than the Co–N distances measured in **26a**. The longer M–N bond in **26b** could be due to the partial delocalization of metal electrons into the polarized P–N bond. The occurrence of nickel-to-ligand electron donation is supported by the shorter P–N bond distance 1.561(4) Å compared to the P–N distance in a free tri-*tert*-butylphosphoranimide anion.^{57,66} The metal–N distances measured in **26b** are comparable to the measurements reported in the first mononuclear Ni(I) amido complex, reported by Hillhouse and coworkers [1.865(2) Å].⁷¹

Table 1.5. Selected bond distances and bond angles for **26b**.

Bonded Atoms	Distance (Å)	Bonded Atoms	Bond Angle (°)
Ni•••Ni	2.38	N–Ni–N	178.9(3), 179.6(3) 178.31(18)
Ni–N	1.864(4), 1.864(4) 1.876(4), 1.876(4)	Ni–N–P	142.6(3), 138.8(3) 133.0(3), 135.5(3)
P–N	1.561(4)	Ni–N–Ni	79.29(15), 78.88(16)

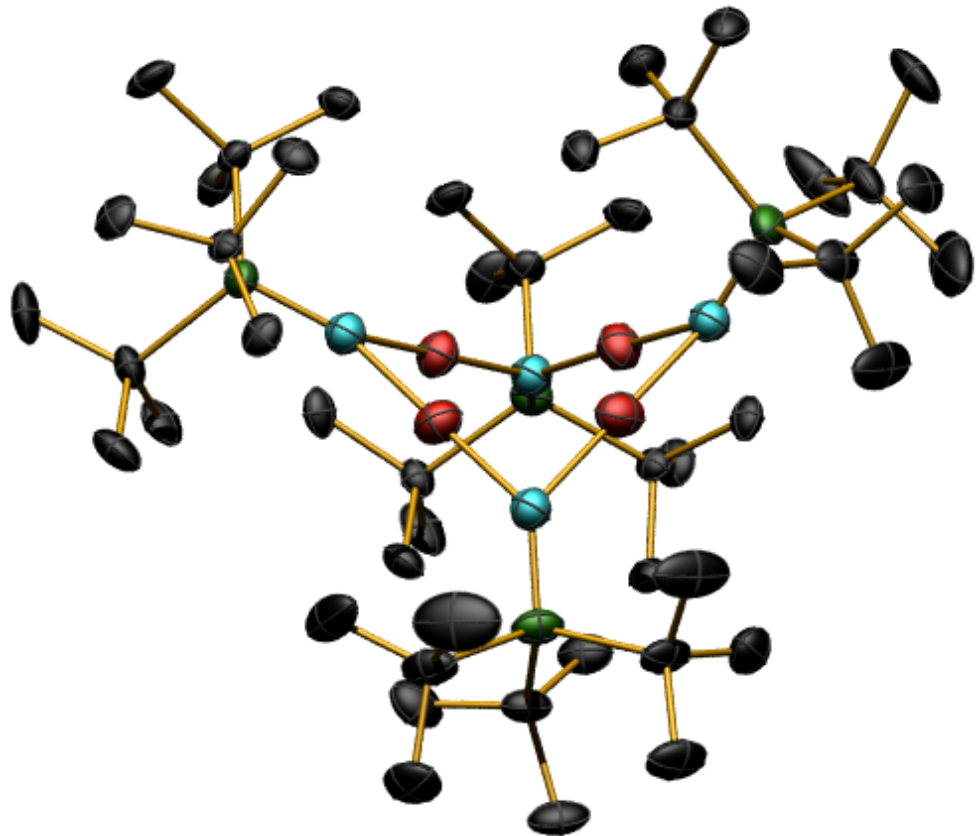


Figure 1.13. ORTEP diagram of compound **26b**, $[\text{Ni}(\mu_2\text{-NP}^t\text{Bu}_3)]_4$. The thermal ellipsoids are shown at 50% probability. Hydrogen atoms have been omitted for clarity. $R1 = 0.0649$, $R(w) = 0.1838$.

1.2.3.2 Preliminary Magnetic Susceptibility Studies on $[M(\text{NP}^t\text{Bu}_3)]_4$

Clusters **26a** and **26b** were each subjected to room temperature solution-phase magnetic susceptibility measurements using the Evan's method. Assuming that the tetrametallic cluster remains intact in cyclohexane at 27 °C, cobalt cluster **26a** exhibits eight-electron paramagnetism ($\mu_{\text{eff}} = 8.98 \mu_{\text{Bo}}$). This suggests a high-spin d⁸ configuration for each cobalt center in the cluster (a, Figure 1.14). The triplet spin-only magnetic state of **26a** suggests the absence of significant

Co–Co bonding despite the short Co–Co distances (2.41 Å) imposed by the single-atom nitrogen bridges.⁷⁰ The solid state structural data, coupled with the results of the magnetic susceptibility measurements, confers an effective electron count of 12 at each Co(I) center. This, in turn, validates our group’s design principle for the synthesis of polynuclear, ligand-supported assemblies with terminally low-coordinate – *open shell* – metal centers.

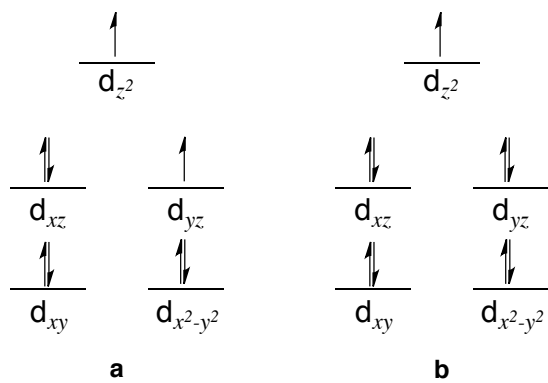


Figure 1.14. Orbital splitting diagram for a linear, two-coordinate metal complex. (a) high spin d^8 -configuration; (b) d^9 configuration.

Room-temperature solution magnetic susceptibility measurements revealed that nickel congener **26b**, again assuming an intact cluster in cyclohexane at 27 °C, behaves as a 3.5-electron paramagnet (4.40 μ_{Bo} , 0.85 of an unpaired electron per Ni center). This suggests a high-spin d^9 configuration for each Ni(I) center (**b** in Figure 1.14). The partial quenching of the magnetic spin could be due to weak bonding interactions among the adjacent nickel centers (Ni–Ni distance of 2.38 Å). Variable temperature

NMR experiments on **26b** in toluene-D₈ revealed that the cluster is paramagnetic at temperatures ranging from -80 to 60 °C.

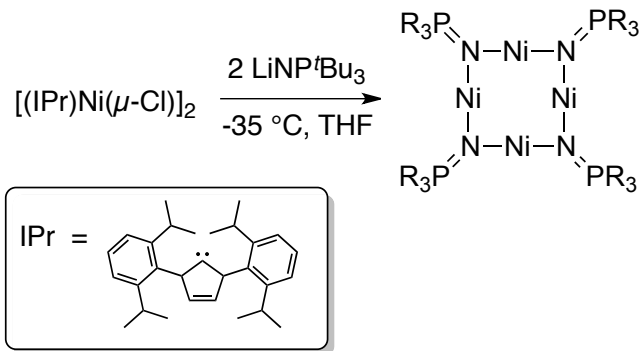
Both tetrametallic clusters **26a** and **26b** have thus been rigorously characterized. The solid-state structures of both clusters revealed bond angles near perfect linearity (176.0(3)–179.6(3) Å). The paramagnetic Co(I) and Ni(I) clusters exhibit high solution magnetic susceptibility, making them highly attractive candidates for studies of single molecule magnetism. In addition, the results of the magnetic susceptibility measurements do not support the presence of M–M bonding despite the close proximity of Co(I) and Ni(I) centers in the M₄N₄ cluster core. To this point, studies of the electrochemical properties of clusters **26a** and **26b** have not been conducted. Thorough investigation of the magnetic and electronic properties, both in solution and in the solid state, is warranted to assess the potential for applications of these compounds in materials chemistry.

1.2.3.3 Synthesis of Phosphoranimidonickel(I) Complexes with Ancillary Donor Ligands

The synthesis of an N-heterocyclic carbene-functionalized monophosphoranimidonickel(I) complex was attempted via low-temperature anionic metathesis reaction between LiNP^tBu₃ and [(IPr)Ni(μ₂-

$\text{Cl})_2$, Ni(I) precursor that Hillhouse and coworkers⁷¹ used for the synthesis of mononuclear, heteroleptic, two-coordinate d^9 complexes (Equation 1.22). Surprisingly, the pentane-soluble fraction of the resulting mixture returned the tetrametallic Ni(I) cluster **26b** upon recrystallization from a cold, concentrated THF solution. At this point, the yield of **26b** was not quantitatively measured. This result indicates the inherent robustness of the tetrametallic core toward ligand-induced deaggregation in the presence of excess strong donor ligands. Quantification of the products of the reaction is ideal to confirm the possibility of reversible solution-phase cluster deaggregation in the presence of excess quantities of exogenous donor molecules.

Equation 1.22

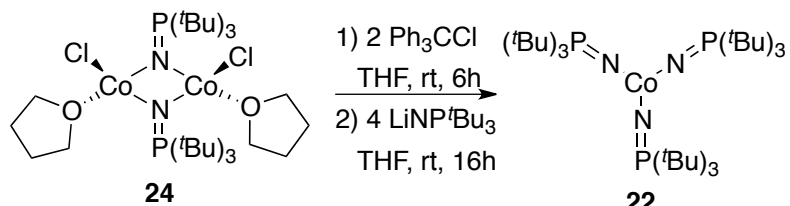


1.2.4 Synthesis of Homoleptic, Mononuclear Co(III) Phosphoranimide Complex $[\text{Co}(\text{NP}^t\text{Bu}_3)_3]$

An efficient and straightforward synthesis of $[\text{Co}(\text{NP}^t\text{Bu}_3)_3]$ **22** was achieved using two related anionic metathesis strategies, both starting

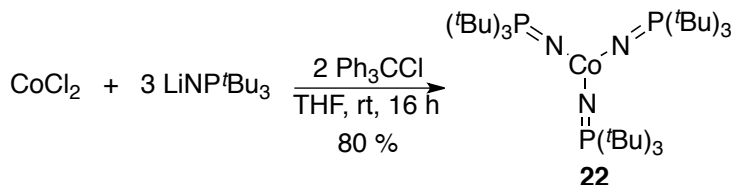
with metal(II) precursors. In the first approach, the oxidation of $[\text{Co}(\text{NP}^t\text{Bu}_3)\text{Cl}(\text{THF})]_2$ **24** with two equivalents of Ph_3CCl was performed, followed by addition of four equivalents of LiNP^tBu_3 at room temperature (Equation 1.23). The cherry red, pentane-soluble product deposits X-ray quality single crystals from a concentrated THF solution at -35°C . The product exhibits identical unit cell parameters to that obtained from complex **27** obtained serendipitously from a redox disproportionation (Section 1.2.2.1.2). A reliable yield for this procedure was not determined since a more straightforward and more efficient two-step synthesis was developed starting directly from CoCl_2 .

Equation 1.23



In the second approach, the treatment of CoCl_2 with three equivalents of LiNP^tBu_3 in THF was followed by in situ oxidation of the Co(II) center with one equivalent of an oxidizing agent, optimally Ph_3CCl . The pentane-soluble product **22** was selectively recrystallized from a cold, concentrated THF solution and obtained in 80% yield (Equation 1.24). This material did not pass elemental analysis presumably due to minimal contamination from residual oxidant, Ph_3CCl .

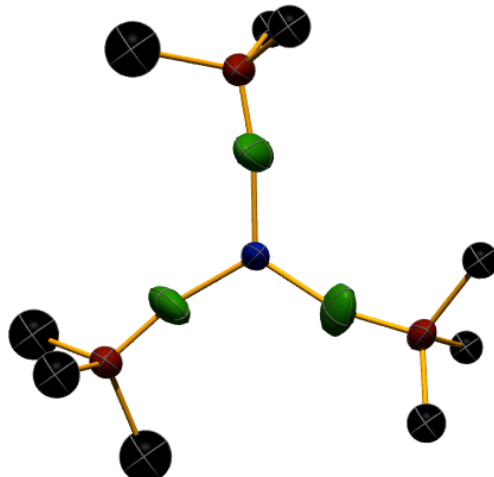
Equation 1.24



The complex, however, is surprisingly diamagnetic. The product shows a single ^{31}P -NMR chemical shift at -41 ppm in C_6D_6 . The synthesis of other tris(trialkylphosphoranimido)metal(III) complexes and the screening of optimum chemical oxidants was designated a low priority and is now the responsibility of other coworkers. Nonetheless, this synthetic approach is preferred since it can be done at ambient temperatures and does not require the preparation and isolation of the temperature-sensitive Co(II) precursor **24**.

The solid-state structure of **22** revealed the trigonal planar cobalt coordination geometry, but the data set obtained from crystallographic analysis suffered from serious thermal disorder arising from the forced coplanarity of the three bulky tri-*tert*-butylphosphoranimide ligands (Figure 1.15). The N-Co-N bond angles range from 119 to 122° while Co-N distances range from 1.78 to 1.84 Å, typical of single Co–N bonds. The trigonal planar metal geometry, coupled with the strong donor tendency of the anionic phosphoranimide ligands, allows for a low-spin d^6 configuration (Figure 1.16) of **22**, confirmed by the observed diamagnetic behavior in C_6D_6 . As noted, ^{31}P -NMR experiments in C_6D_6 revealed a single chemical

shift at -41 ppm, consistent with a highly symmetrical structure and trigonal planar metal coordination around a three-fold axis of rotation. The low spin d⁶ configuration in **22** is in retrospect not surprising for a three-coordinate complex supported by very strong field ligands. The lone pair orbitals on the anionic nitrogen centers can mix with higher energy metal-based molecular orbitals (dxy, dx²-y²), forcing the six metal d-electrons to pair up and occupy the low lying d orbitals (dxz, dyz, dz²).^{14,78-82}



Bond	Distance (Å)	Bond	Angles (°)
Co-N	1.777	N-Co-N	122.04
	1.836		118.99
	1.812		118.94
P-N	1.549	P-N-Co	163.00
	1.482		163.58
	1.508		164.16

Figure 1.15. ORTEP diagram of [Co(NP^tBu₃)₃] **27**. The data set obtained is not of publishable quality, attributable to severe thermal disorder of the phosphoranimide *tert*-butyl groups. The highly disordered methyl groups have been omitted for clarity. The CoN₃ core shows a trigonal planar Co(III) geometry.

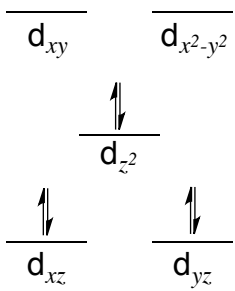


Figure 1.16. Orbital splitting diagram for a trigonal planar metal complex.

Tris(phosphoranimide complex **22** is an important addition to the small family of monometallic d^6 trigonal planar transition metal complexes supported by simple, monodentate ligands.⁸² Homoleptic, mononuclear non-d¹⁰ first row metal(III) complexes are extremely rare. Among the first row transition metals, iron and manganese have the most diverse examples of three-coordinate complexes.⁸² The rarity of three-coordinate complexes of d^0 to d^9 transition metals has been attributed to a kinetic instability resulting from the coordinative unsaturation. The preparation of three-coordinate transition metal complexes thus requires similar strategies to those used in the synthesis of two-coordinate complexes. These compounds are generally stabilized by sterically bulky and, in most cases, polydentate ligands.⁸²

Three-coordinate coordination complexes are interesting subjects in the study of organometallic reaction mechanisms.⁸² The formation of three-coordinate metal ions plays a crucial role in mapping out the mechanism of cation migration between trigonal and tetrahedral positions

in strongly conducting solid ionic matrices. In addition, it is proposed that three-coordinate intermediates play important roles in some rhodium-catalyzed reaction processes.⁸²

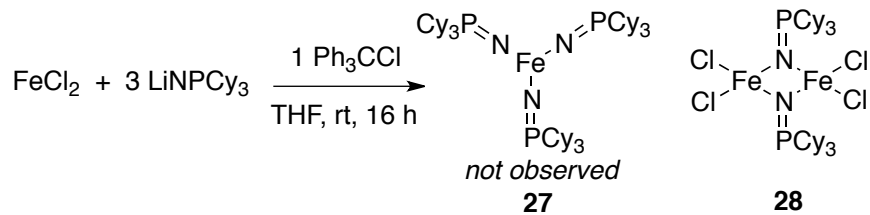
In terms of reactivity, a range of unprecedented organic transformations has been reported using three-coordinate transition metal complexes. The stoichiometric and catalytic transformations reported by the groups of Wolczanski^{78,83} and Cummins⁸⁴ feature the activation a range of strong bonds (C-H bonds in alkanes, N-N bonds in nitrous oxides, triple bonds in CO, CN⁻ and N₂) mediated by three-coordinate second- and third-row transition metal complexes. The high reactivity of these complexes is attributed to several consequences of low metal coordination:⁸² (1) a small HOMO-LUMO gap and (2) a large binding affinity to an incoming fourth donor molecule, which together explain the rich coordination chemistry reported for these open-shell systems; In addition, the presence of adjacent electrophilic (metal) and nucleophilic (ligand) sites in the complex allows for heterolytic bond activation and other cooperative effects.⁸²

The cherry-red complex **22** immediately reacts upon treatment with Lewis acids such as AlMe₃ forming intensely dark, uncharacterizable compounds. This is presumably due to the formation of an adduct between the Lewis acidic aluminum center with the Lewis basic, terminally

bound tri-*tert*-butylphosphoranimide nitrogen centers in **22**. Studies on the potentially rich coordination chemistry of **22** and related mononuclear complexes will be conducted by others in the group. The activity of this homoleptic, high-valent complex for the reductive activation of C–X bonds (X = S, N) will be briefly discussed in Chapters **4** and **5**.

The synthesis of a three-coordinate Fe(III) complex **31** was attempted using the anionic tricyclohexylphosphoranimido ligand (Equation 1.25). Treatment of FeCl_2 with excess LiNPCy_3 and one equivalent of an oxidant resulted in the formation of a red-orange product mixture. A red-orange, pentane-soluble fraction, presumably complex **27**, was isolated via solvent extraction. Crystallization of this fraction, however, was unsuccessful, suggesting that it may contain more than one compound. On the other hand, the dark orange, THF-soluble fraction deposits X-ray quality crystals from a concentrated THF solution at -35 °C. X-ray crystallographic analysis revealed a structure corresponding to the known dimeric dichloromono(tricyclohexylphosphoranimido)iron(III) complex **28**, first reported by the Stephan group.⁶⁶

Equation 1.25



1.4 Summary and Conclusions

The synthesis of phosphoranimide-supported, polynuclear clusters of Fe, Co and Ni was attempted using several synthetic strategies. The solution-phase version of Dehnicke's high-temperature cluster synthesis starting from $\text{Co}(\text{OAc})_2$ and $\text{Ph}_3\text{P}=\text{N}-\text{SiMe}_3$ unexpectedly afforded a trimetallic cluster $[\text{Co}_3(\text{CH}_3\text{COO})_6(\text{HNPPh}_3)_2]$ **13** where the phosphoranimide ligands were protonated to give undesired imine complexes. Deprotonation of **13** to eliminate acetate ions and promote intermetallic bridging through anionic phosphoranimide nitrogen centers afforded intractable products. The results further suggest that polydentate anions such as acetate only reluctantly undergo substitution during the metathesis reaction.

A series of alternative approaches were explored for the synthesis of metal phosphoranimide complexes where a 1 : 1 metal-to-phosphoranimide ratio is maintained. The synthesis of oligomeric monohalo-monophosphoranimidometal(II) complexes $[\text{M}(\text{NPR}_3)\text{X}]_n$ ($n = 2$ to 4) has been accomplished under mild conditions. The dimeric complex $[\text{Co}(\text{NP}^t\text{Bu}_3)\text{Cl}(\text{THF})]_2$ **24** with an empirical formula similar to Dehnicke's clusters was best synthesized via low-temperature metathesis maintaining a constantly low concentration of the anionic phosphoranimide reagent. Complex **24** proved to be a useful precursor to a range of unsaturated

mononuclear and polynuclear phosphoranimidometal complexes with metal oxidation states ranging from +1 to +3.

Chemical reduction of M(II) monohalide complexes **24** afforded an unprecedented class of tetrametallic, ancillary-ligand-free clusters of cobalt and nickel (**26a,b**) wherein each of the four metal centers is monovalent, structurally linear, and coplanar with the other metals. Each metal center is supported exclusively by two doubly-bridging anionic phosphoranimide ligands. The M(I) clusters were optimally synthesized via a two-step procedure starting directly from the M(II) dihalide and trialkylphosphoranimide salt. The isostructural tetrametallic clusters **26a** and **26b** were completely characterized in the solid state and in solution. Cluster **26a** and **26b** comprise the first examples of tetrametallic d⁸ and d⁹ systems where the four metal centers are linear two-coordinate. Both clusters exhibit high room-temperature magnetic susceptibility, highlighting the potential for observing single molecule magnetism and developing applications to materials chemistry.^{75,76} The low-valent and open-shell nature of the metal centers is anticipated to activate these base metal cluster catalysts for a range of challenging and unprecedented catalytic transformations. Documenting the diverse catalytic reactivity of clusters **26a** and **26b** is the principle focus of Chapters 2 through 6.

A straightforward and efficient synthesis of the homoleptic, mononuclear, three-coordinate d⁶ complex [Co(NP^tBu₃)₃] **22** was developed. The trigonal planar coordination geometry afforded a low-spin, diamagnetic complex that constitutes a unique addition to the limited family of non-d¹⁰ three-coordinate transition metal complexes. The catalytic activity of monomeric **22** will be briefly discussed in Chapters **4** and **5**.

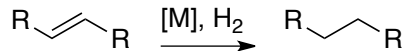
Chapter 2

Tetrametallic Cobalt and Nickel Clusters for Homogeneous Catalytic Hydrogenation

2.1 Introduction

Hydrogenation, the addition of a hydrogen molecule across an unsaturated functional group, remains a key-enabling process that sustains a diverse set of chemical industries.⁸⁵⁻⁸⁷ The transition metal-catalyzed activation and addition of the mild and cheap reductant hydrogen (H_2) to saturate organic compounds has been among the most active areas of research in homogeneous catalysis (Equation 2.1).⁸⁸

Equation 2.1



Transition metal-catalyzed hydrogenation is dominated by catalysts compromising the expensive, scarce, and in most cases, toxic precious metals such as rhodium,^{43,89-91} iridium,⁹²⁻⁹⁵ and ruthenium.^{96,97} Current industrial dependence on semi-precious and precious metal catalysts necessitates resource-intensive catalyst separation and recovery strategies,⁹⁸⁻¹⁰⁰ which contribute significantly to manufacturing costs and environmental footprint. This, coupled with the ever-increasing demand for commodity and fine chemicals derived by catalytic hydrogenation highlights the need for cost-effective hydrogenation catalyst technologies to ensure long-term process and environmental sustainability.

Significant advances have been made over the last two decades in the development of cost-efficient, high activity, non-precious metal hydrogenation catalysts. Main-group¹⁰¹⁻¹⁰³ and first row transition metal¹⁰⁴⁻¹⁰⁷ catalysts have been developed, effecting hydrogenation under mild conditions and, in some cases, mediating highly selective reductions of unsaturated bonds.

The Earth-abundant and significantly less toxic first row transition metals, particularly iron, cobalt and nickel comprise a set of promising alternative catalysts.¹⁰⁸ However, this area of catalysis remains plagued with challenges to the development of high-activity base metal catalysts that manifest practical conversion rates, good functional group tolerance, and desirable selectivity. Among the base metals, cobalt has been most extensively studied for homogeneous hydrogenation.¹⁰⁹⁻¹¹³ On the other hand, there has recently been an increase in momentum in the development and use of homogeneous iron coordination complexes¹⁰⁴ as the most promising and most cost-effective base metal catalysts, addressing both costs and environmental toxicity issues. Meanwhile, thoroughly characterized, homogeneous nickel hydrogenation catalysts remain extremely rare.^{33,114,115}

The catalyst design strategy developed by the Stryker group in developing low-coordinate, phosphoranimide-supported base metal

clusters draws inspiration from the proposed low-coordinate nature of the active sites (*surface vacancies*) essential to industrial hydrotreatment catalysts – heterogeneous (solid-state) catalysts active for hydrogenation and hydrogenolysis of a range of unsaturated organic substrates.¹³ In addition, from the perspective of structure-reactivity relationships, clusters **26a** and **26b** could be considered the simplest homogeneous representations of hydrogenation-active metal surfaces such as Raney cobalt/nickel.^{47-49,116-121} Furthermore, the low-valent and terminally low-coordinate metal centers in both clusters are envisaged to confer enhanced reactivity toward substrate ligation and the oxidative activation of H₂.⁷⁷

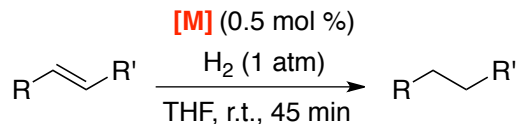
The soluble polynuclear active sites, **26a** and **26b**, were envisaged to mimic the activity of heterogeneous hydrotreatment catalysts; hence we decided to use the catalytic hydrogenation of alkenes and alkynes, representative of unsaturated petroleum constituents, as initial test of cluster reactivity. Since the focus of this graduate work is on the development of catalytic strategies for hydrogenolysis of carbon-heteroatom bonds under mild conditions, we elected to only briefly pursue the investigation of the hydrogenation activity of **26a** and **26b**. Several catalytic carbon-carbon bond forming transformations have been discovered during the study of catalytic hydrogenation; these were

optimized, providing synthetically useful *homogeneous* base metal-catalyzed organic transformations.

2.2 Results and Discussion

The succeeding sections present a series of 40-minute cobalt- and nickel-catalyzed hydrogenations of a range of unactivated alkenes and alkynes, conducted in THF under exceptionally mild conditions: room temperature and one atm H₂. Low catalyst loadings ranging from 0.4 to 1.0 mol% were used (Equation 2.2). In the entirety of this chapter, the term “turnover frequency” corresponds to the *moles of substrate reduced per mole of catalyst per hour* under the reaction conditions provided. Since we elected to focus our efforts on the study of catalytic carbon-heteroatom bond hydrogenolysis, extensive investigation of the kinetics and mechanism(s) of the catalytic alkene/alkyne hydrogenation reactions were not pursued. At this point, the variability of hydrogenation rates as a function of time remains undetermined. The hydrogenation rates presented in the succeeding sections were obtained from fixed-duration experiments representative of single points in a hypothetical turnover frequency versus reaction time plot.

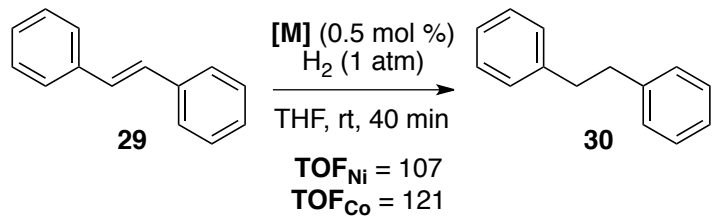
Equation 2.2



2.2.1 Hydrogenation of Trans-Stilbene

Tetrametallic clusters **26a** and **26b** were active catalysts for the hydrogenation of *trans*-stilbene **29**, conjugated internal alkyne, to 1,2-diphenylethane **30** in THF under very mild reaction conditions: 0.5 mol % catalyst loading at room temperature under one atm H₂ (Equation 2.3). The cobalt catalyst **26a** exhibits faster turnover in comparison to nickel cluster **26b**, 62 and 55 h⁻¹, respectively. Experiments designed to probe the observed difference in hydrogenation activities of clusters **26a** and **26b** are presented in the succeeding sections.

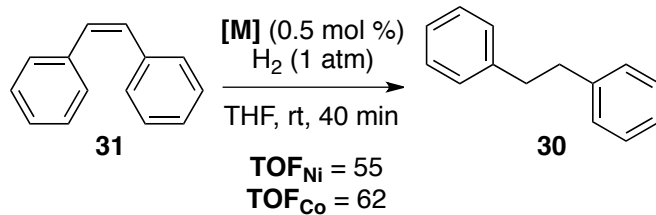
Equation 2.3



2.2.2 Hydrogenation of Cis-Stilbene

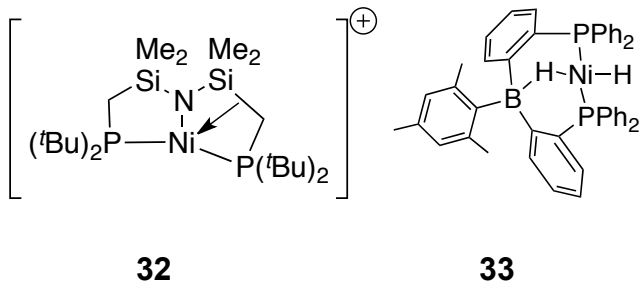
Under reaction conditions identical to the hydrogenation of *trans*-stilbene, *cis*-stilbene **31** was efficiently reduced to 1,2-diphenylethane **30** (Equation 2.4). Consistently, the cobalt catalyst showed a higher hydrogenation rate (121 hour^{-1}) compared to the nickel catalyst (107 hour^{-1}). The surprisingly slower rate of *cis*-alkene hydrogenation is suspected to arise from competitive alkene isomerization to produce the corresponding *trans*-alkene. In both experiments, trace amounts of *trans*-stilbene, resulting from isomerization to *cis*-olefin, were detected.

Equation 2.4



The efficient hydrogenation of these deactivated hindered alkenes under exceptionally mild conditions demonstrates the high activity of clusters **26a** and **26b** for the reduction of unactivated unsaturated organic substrates. Both tetrametallic, phosphoranimide-supported clusters of Co(I) and Ni(I) thus comprise a unique set of robust, thoroughly characterized base metal hydrogenation catalysts. In particular, **26b** is a

unique addition to the small family of fully characterized homogeneous nickel hydrogenation catalysts. Most nickel hydrogenation catalysts are in heterogeneous in nature, including Raney nickel¹¹⁶⁻¹²⁰ and Ziegler-type systems.^{112,122-124} The family of thoroughly characterized, discrete, molecular nickel hydrogenation precatalysts includes only a set of bis(phosphine)nickel(II) halides^{115,120,125-127} and the recently reported mononuclear complexes such as **32**¹¹⁵ and **33**,¹¹⁴ both supported by polyfunctional ligands. These homogeneous hydrogenation catalysts, however, are low activity, generally requiring harsher conditions of pressure and temperature.



32

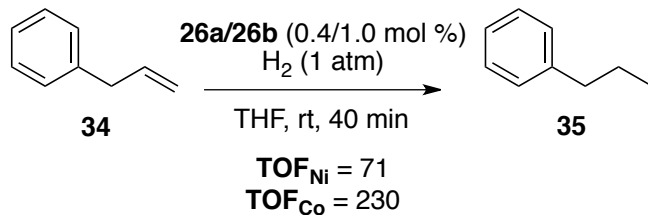
33

A handful of discrete, molecular nickel clusters have been reported as catalyst precursors (precatalysts) for hydrogenation. For example, the tetranuclear isocyanide cluster $[\text{Ni}_4\{\mu-\eta^2\text{-CNC(CH}_3)_3\}_3\{\text{CNC(CH}_3)_3\}_4]^{128}$ and the bimetallic complex $[\{\eta^4\text{-1,5-cyclooctadiene}\}\text{Ni}]_2\{\mu-\eta^2\text{-C}_2\text{Ph}_2\}]^{128}$ were used as precatalysts for alkyne hydrogenation, mainly forming *cis*-alkenes. These catalysts only reluctantly reduce alkenes to the corresponding saturated hydrocarbons.²³

2.2.3 Hydrogenation of Allylbenzene

To gain insight into the mechanism of olefin hydrogenation, the reduction of allylbenzene **34**, an alkene that is prone to isomerization, was conducted (Equation 2.5). Both tetrametallic catalysts **26a** and **26b** effected the hydrogenation, giving n-propylbenzene **35** quantitatively. Interestingly, a faster rate of hydrogenation was observed in the cobalt-catalyzed hydrogenation ($\text{TOF} = 230 \text{ h}^{-1}$, 0.4 mol %), despite the higher catalyst loading used in the nickel-catalyzed reduction ($\text{TOF} = 71 \text{ h}^{-1}$, 1.0 mol %).

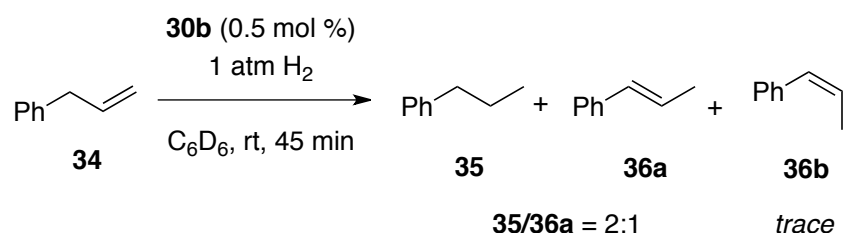
Equation 2.5



The composition of the mixture prior to reaction completion was studied to determine the competitiveness of alkene isomerization. A room temperature, nickel-catalyzed hydrogenation of allylbenzene **34** quenched prior to completion offered important mechanistic implications (Equation 2.6). The slower rate of allylbenzene reduction was confirmed to result from the strong tendency of nickel cluster **26b** to isomerize carbon-carbon double bonds, mainly rapidly producing the more stable *trans*-1-

phenylpropene **36a**. At 75% conversion, the reaction mixture consists of n-propylbenzene **35** and *trans*-1-phenylpropene **36a** in a ratio of 2 : 1, accompanied by a trace amount of the corresponding *cis*-isomer **36b**. The competitive alkene isomerization thus obscures the determination of the actual rate of carbon-carbon double bond hydrogenation.

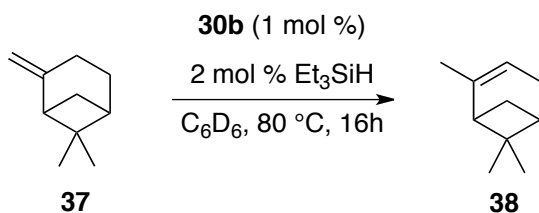
Equation 2.6



2.2.3.1 Hydrogenation / Isomerization

Alkene isomerization only reluctantly proceeds in the absence of a hydride source. The catalytic isomerization was then conducted under conditions of substoichiometric hydride. In the event, β -pinene **37** was converted quantitatively to α -pinene **38** in the presence of catalytic amounts of triethylsilane, Et_3SiH (Equation 2.7).

Equation 2.7



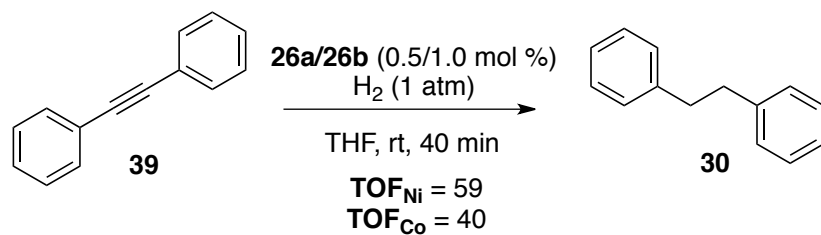
The catalytic alkene isomerization can proceed through two possible mechanisms: (1) allylic C–H activation or (2) hydride insertion. Since catalytic isomerization was only observed under H₂ atmosphere or in the presence of an organosilyl hydride, the latter is the more probable mechanism. Catalytic alkene isomerization has a range of commercial applications; both homogeneous and heterogeneous nickel catalysts for alkene isomerization are known.^{129,130}

2.2.4 Hydrogenation of Diphenylacetylene

The exhaustive, room-temperature hydrogenation of diphenylacetylene **39** proceeds quantitatively to 1,2-diphenylethane **30** (1 atm H₂, 10 h, 100% conversion). The observed rate of internal alkyne hydrogenation is obscured by three competitive events: (1) reduction to mixtures of the *cis*- and *trans*-stilbene, (2) *cis* to *trans*-stilbene isomerization and (3) hydrogenation to 1,2-diphenylethane. Using the nickel catalyst **26b**, selective partial hydrogenation to a mixture of *cis*- and *trans*-stilbenes **29** : **31** (2.7 : 1) is obtained over short reaction periods (Equation 2.8). The corresponding cobalt-catalyzed reaction afforded a mixture of products where the *cis*-to-*trans*-alkene ratio is higher but still only 6 : 1. The high proportion of *trans*-isomer in the nickel-catalyzed hydrogenation is unusual for hydrogenation catalysis, but it is presumed to

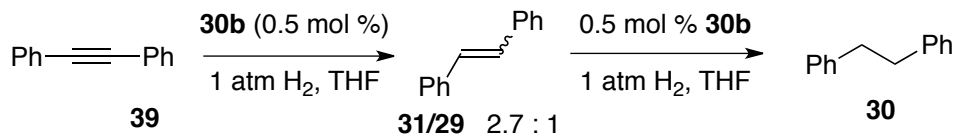
arise from fast nickel-catalyzed *cis* to *trans* isomerization relative to the reduction of the stilbene to diphenylethane.

Equation 2.8



Comparison of the observed hydrogenation rates of substrates **29**, **31** and **39** also reveals important mechanistic details. The nickel-catalyzed partial conversion of diphenylacetylene **39** to stilbene proceeds at a turnover frequency of 59 h^{-1} (Equation 2.9). In separate experiments presented earlier using the pure alkene isomers, the hydrogenation of *cis*- and *trans*-stilbene to 1,2-diphenylethane **30** proceeds at TOF's of 108 and 54 h^{-1} , respectively. The partial reduction of diphenylacetylene to stilbene proceeds more slowly than the reduction of stilbene to diphenylethane. This strongly suggests that the alkyne acts as a competitive inhibitor for alkene hydrogenation, binding more strongly to the catalyst but, unsurprisingly, hydrogenating more slowly.

Equation 2.9



No detectable precipitation or change in the color of the solution is observed throughout the course of the hydrogenation reaction. The rate of hydrogenation of **29** is unaffected by the presence of a large excess of metallic mercury ($\text{TOF} = 60 \text{ h}^{-1}$). These observations are consistent, though inconclusively, with a homogeneous active nickel catalyst (Equation 2.10).^{91,131-135}

Equation 2.10

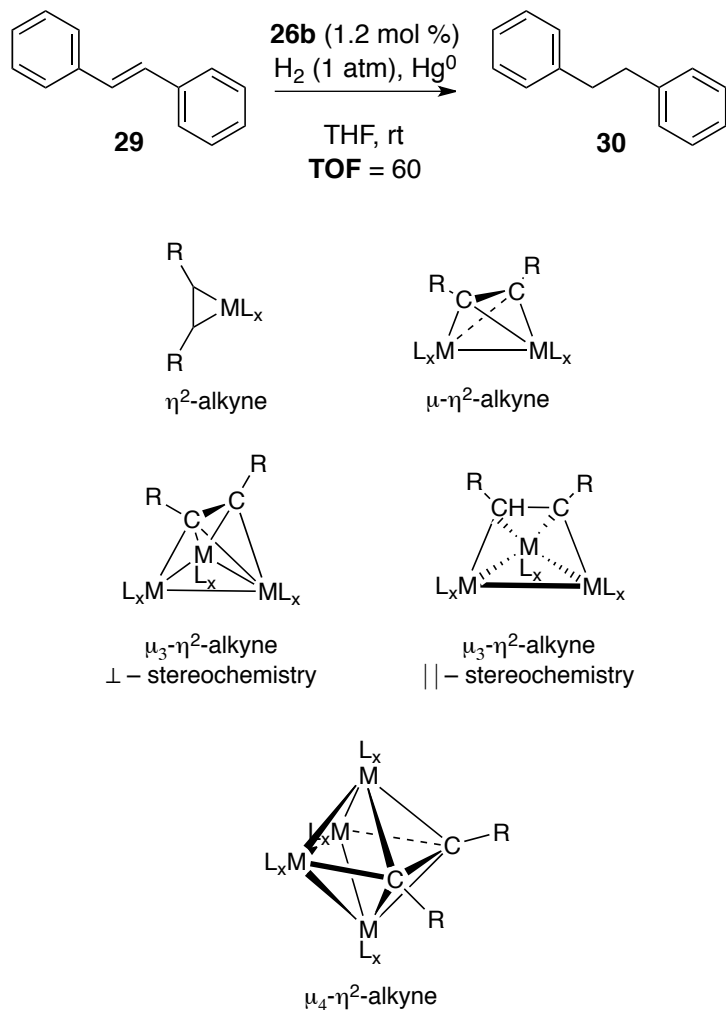


Figure 2.1. Modes of alkyne coordination to metal complexes.²³

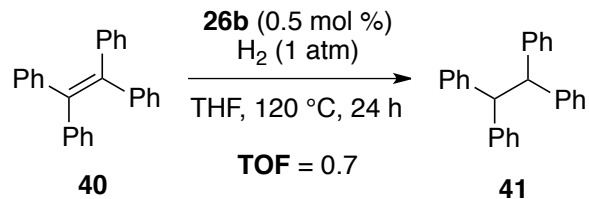
The hydrogenation of alkynes, in some cases, reveals mechanistic details that cannot be obtained from alkene hydrogenation experiments.²³ The observed selectivity in polynuclear catalysts, leading to the formation of *cis*- and/or *trans*-stilbene, may result from a *concerted or pseudo-concerted* bimetallic alkyne activation.²³ There are precedents for the ability of bimetallic complexes to selectively hydrogenate internal alkynes to *trans*-alkenes via bimetallic substrate activation (Figure 1.2, Chapter 1).²³ Alkynes are capable of adapting various modes of ligation to metal complexes with varying metal nuclearity, leading to different stereochemical configurations of the alkyne–metal adducts (Figure 2.1). At this point, however, there is insufficient experimental data to propose multimetal substrate activation. Isolation of reactive intermediates and kinetic investigations are warranted to determine the nuclearity of the active cobalt and nickel hydrogenation catalysts.

2.2.5 Hydrogenation of Hindered Olefins

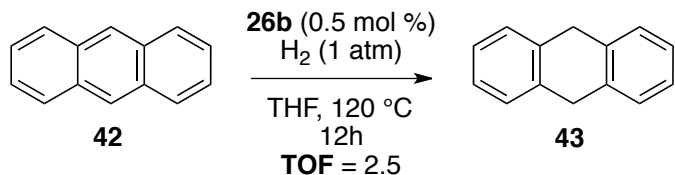
Catalytic hydrogenation of tetrasubstituted alkenes is rare. Using the nickel catalyst, the catalytic hydrogenation of 1,1,2,2-tetraphenylethylene **40** and the modestly aromatic anthracene **42** was observed, albeit at elevated temperatures. Tetraphenylethylene **40** was converted to 1,1,2,2-tetraphenylethane at a turnover of 0.7 h^{-1} at $120\text{ }^\circ\text{C}$ (Equation 2.11). Under identical reaction conditions, the central ring of

anthracene **42** underwent catalytic hydrogenation at a turnover of 2.5 h^{-1} (Equation 2.12). The catalysis only proceeds at elevated reaction temperatures, possibly due to the necessity for cluster deaggregation, generating organometallic fragments of lower nuclearity (e.g. a dimer) that can more readily bind with extremely hindered alkenes. In the case of 1,1,2,2-tetraphenylethylene **40**, catalyst decomposition was observed over three hours at $120\text{ }^\circ\text{C}$ under one atmosphere of hydrogen. The observed reduction of these hindered aryl alkenes can proceed via single-electron transfer followed by protonation of the resulting benzylic radical anion.

Equation 2.11



Equation 2.12



2.2.5.1 Mechanism of Hydrogenation

The reaction between the nickel catalyst **26b** and hydrogen in the absence of substrate takes place instantly, resulting in the immediate

darkening of the solution without precipitate formation. The reaction of **26b** with a continuous stream of H₂ at one atmosphere was monitored using IR spectrometry. New IR stretches in the range of 2400-1600 cm⁻¹, strongly suggestive of terminal and bridging metal hydrides, were observed within twenty minutes after H₂ exposure (Figure 2.2). The potential of heterolytic activation of hydrogen across Ni–N bond(s) is not supported by the absence of IR bands corresponding to N–H bond stretching. The dark solid recovered from this reaction does not crystallize under conditions that result in the crystallization of **26b**. This further suggests that the reaction between **26b** and hydrogen is irreversible. Paramagnetic ¹H-NMR experiments in C₆D₆ did not reveal conclusive information on the formation of active metal hydrides and/or metal-dihydrogen complexes.

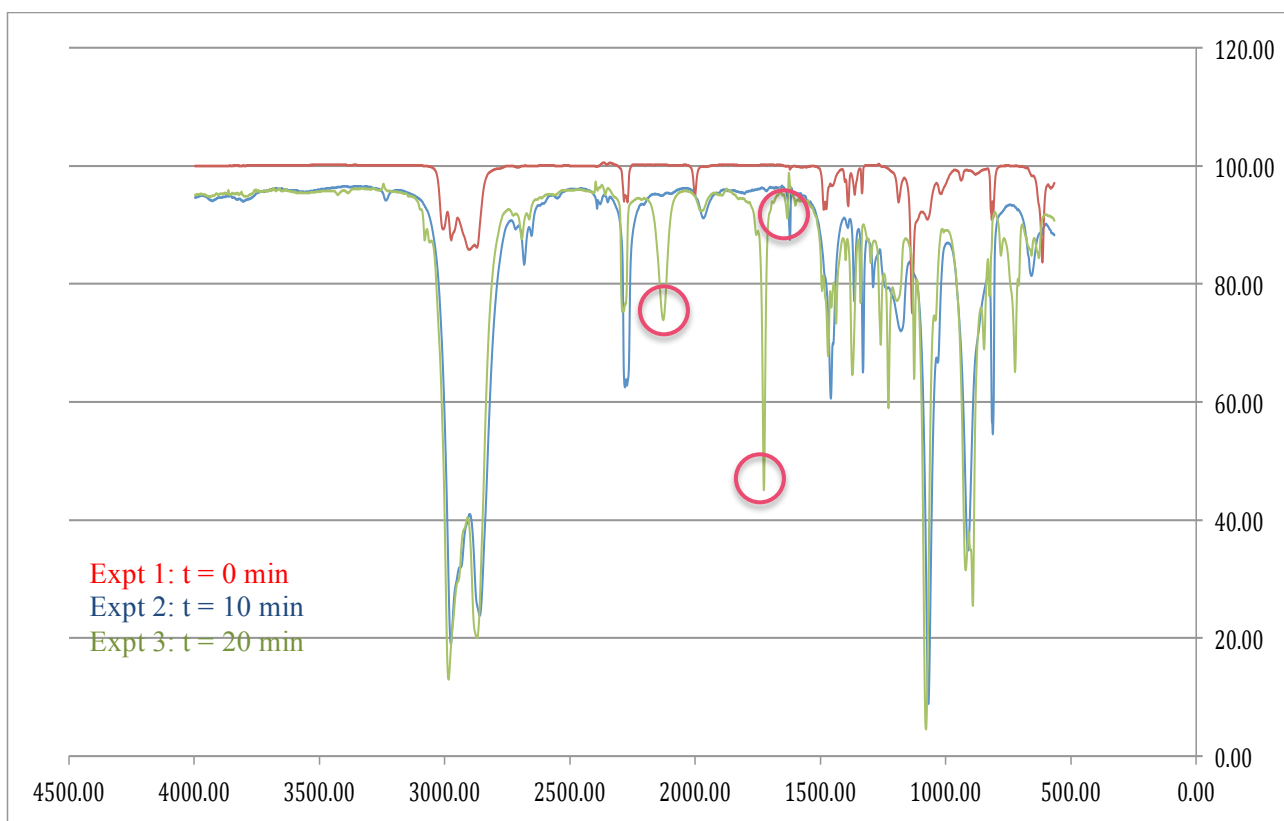


Figure 2.2. FT-IR spectra of $[\text{Ni}(\text{NP}^t\text{Bu}_3)_4]_{\text{26b}}$ in C_6D_6 upon exposure to H_2 .

The nature of the active cobalt and nickel hydrogenation catalysts remains poorly understood at this point. Systematic kinetic and mechanistic investigations are necessary to determine the nuclearity of the active catalyst(s) and to understand the mechanism of the hydrogenation catalysis. Kovalenko and coworkers are currently working on DFT simulations of the mechanism of the hydrogenation catalysis. Preliminary results of DFT calculations revealed that the reaction between the tetrametallic precursor **26b** with two molecules of hydrogen proceeds without energy barrier, producing a tetrahydridonickel(II) complex **45** (Equation 2.13),¹³⁶ where three of the four hydrides are terminally bound and one is doubly bridging.^A

Equation 2.13

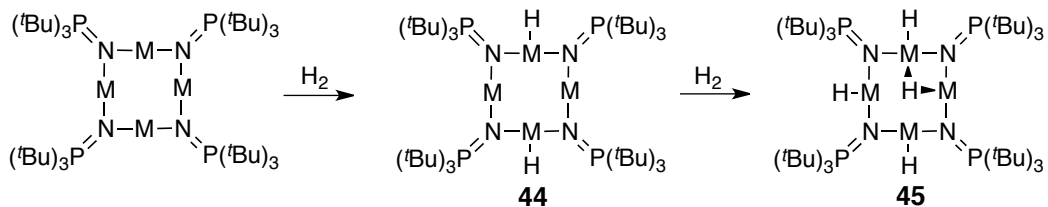


Figure 2.3 shows a highly tentative mechanistic outline of the cobalt- and nickel-catalyzed hydrogenation. The tetrametallic cluster irreversibly reacts twice with H₂ to form a tetrameric hydride-functionalized active catalyst. Considering the lack of concrete mechanistic information,

^A A detailed discussion of the ongoing theoretical simulation of this reaction will be reported in due course.

we elected to use intermediate **45** as a temporary representation of the active hydrogenation catalyst - a tetrametallic system with three terminal hydrides and one doubly bridging hydride ion; one of the metal centers in this cluster is more coordinatively unsaturated, hence, providing a *vacancy* for initial substrate precoordination. Intermediate **45** then reacts with an incoming alkyne, forming a substituted *cis*- and *trans*-vinyl intermediate **47**. The *cis*-vinyl intermediate **47** can then undergo beta-hydride elimination, followed by alkyne reinsertion into the M–H bond to give rise to the *trans*-vinyl-functionalized intermediate **48**. The bimetallic reductive elimination of the vinyl fragment and a hydride in **47** and **48** results in the liberation of the hydrogenated product. The resulting mixed-valent species **49** then undergoes reaction with H₂ to reform the active species **45**.

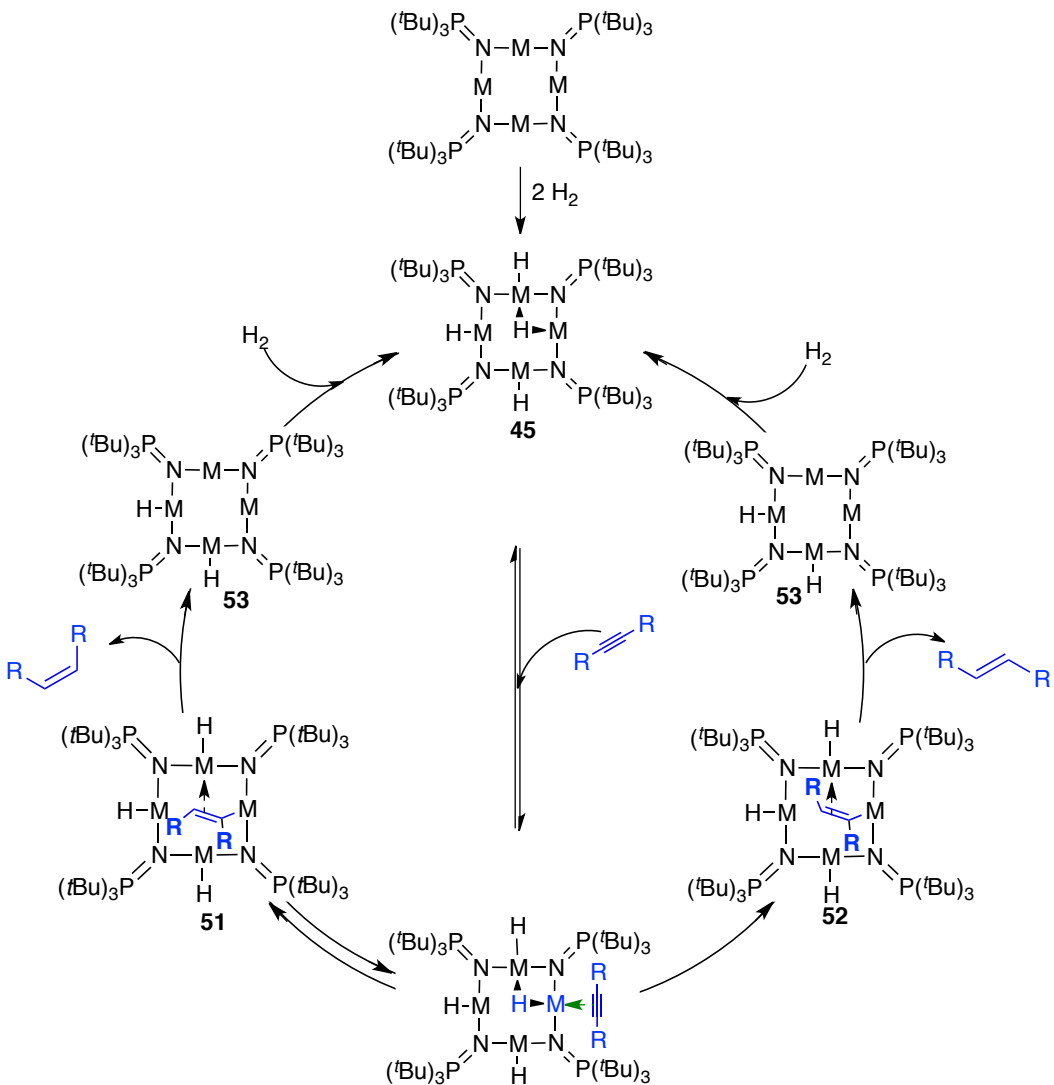


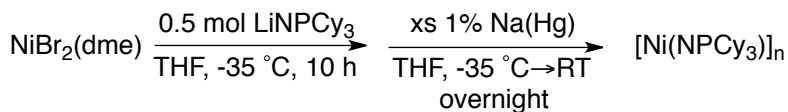
Figure 2.3. Proposed mechanism of alkyne hydrogenation.

2.2.6 In-Situ Synthesis and Reactivity of other M(I) Hydrogenation

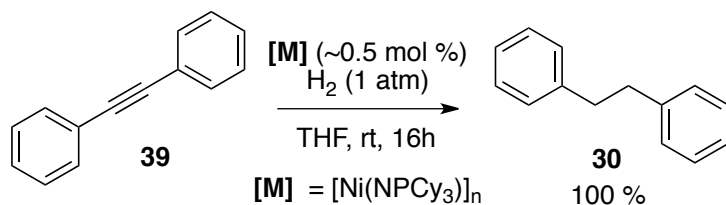
Catalysts

The synthesis of the tricyclohexylphosphoranimide version of catalyst **26b** was attempted using the same procedure employed and presented in Chapter 1 (Equation 2.14). Thus, (dme) NiBr_2 was treated with substoichiometric quantities of LiNPCy_3 in THF at -35 and stirred for 10 hours. The reaction mixture was then treated with excess 1 % (wt/wt) Na/Hg amalgam at room temperature overnight. The reduction produced a brownish-green, pentane-soluble product that quantitatively hydrogenates of diphenylacetylene **39** to 1,2-diphenylethane **30** in less than 16 hours under one atmosphere of hydrogen (Equation 2.15). In this case, the rate of hydrogenation is undetermined since the catalyst used is not rigorously characterized.

Equation 2.14

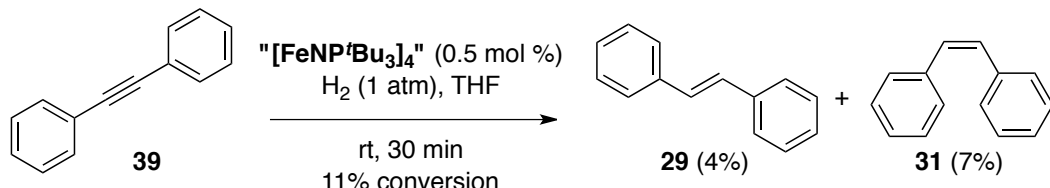


Equation 2.15



The *in situ* synthesis of a phosphoranimido iron(I) catalyst $[\text{Fe}(\text{NPR}_3)]_n$ was conducted using the same synthetic procedure, substituting $\text{FeBr}_2(\text{dme})$ and LiNP^tBu_3 in place of the previous reagents.⁷⁷ The brown, pentane-soluble solid obtained from the synthesis does not recrystallize, at least under conditions employed for the purification of **26a** and **26b**. Importantly, a catalytic amount of the uncharacterized iron derivative effected the catalytic hydrogenation of diphenylacetylene at modest turnover, giving a mixture of *cis*- and *trans*-stilbene (Equation 2.16).

Equation 2.16

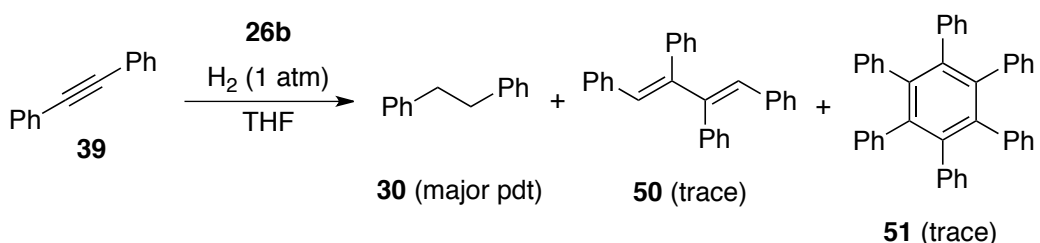


2.2.6.1 Carbon-Carbon Bond-Forming Side Reactions

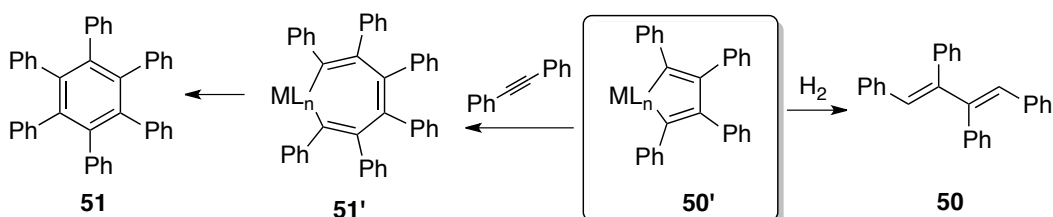
Trace amounts of alkyne dimerization and [2+2+2] cycloaddition products were detected in the alkyne hydrogenation experiments. The hydrogenation of diphenylacetylene **39** (1 atm H_2 , room temperature) resulted in the formation of the hydrogenated linear dimer **50** in trace amount, along with a similar trace of hexaphenylbenzene, the product of alkyne trimerization. (Equation 2.17). The dimer presumably forms from

the hydrogenation of a tetrasubstituted metallocyclopentadiene intermediate **50'** that also leads to the cyclotrimerized product **51** during [2+2+2] cycloaddition reaction (Equation 2.18).

Equation 2.17



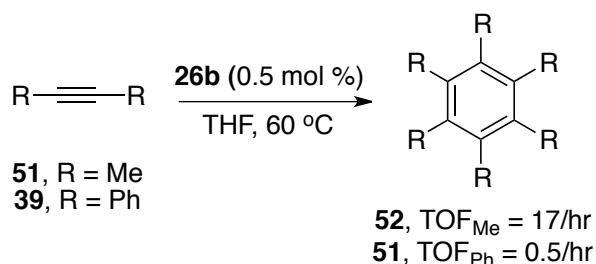
Equation 2.18



Since metal-catalyzed [2+2+2] cycloaddition is important in organic synthesis, nickel catalyst **26b** was purposefully evaluated for its activity towards alkyne cyclotrimerization. The internal alkyne, 2-butyne **52**, indeed undergoes [2+2+2] cycloaddition upon heating in THF at 60 °C, forming 1,2,3,4,5,6-hexamethylbenzene **53** with a turnover frequency of 17 h⁻¹ (Equation 2.19). Under identical reaction conditions, diphenylacetylene **39**, a significantly more hindered substrate, undergoes cyclotrimerization to 1,2,3,4,5,6-hexaphenylbenzene **51** at the much

slower rate of 0.5 h^{-1} . The scope and selectivity of internal alkyne cyclotrimerization has not been explored as of yet.

Equation 2.19

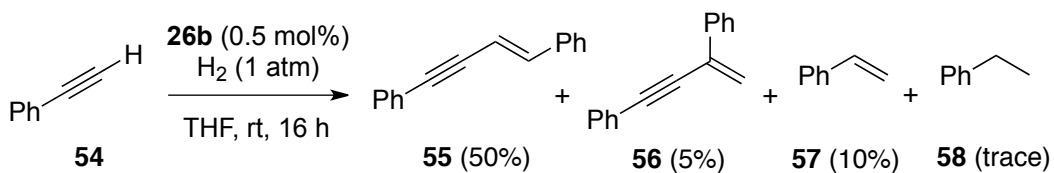


The requirement for elevated reaction temperatures may be due to the necessity for the cluster to breakdown into lower nuclearity active species, where the metal centers are more sterically accessible for alkyne binding. There is, however, insufficient mechanistic information to propose a either monometallic or polynuclear mechanism for the catalytic alkyne [2+2+2] cycloaddition.

2.2.7 Linear Dimerization of Phenylacetylene

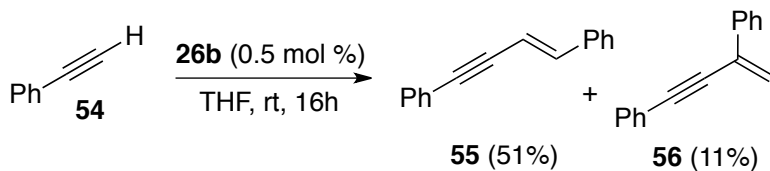
The hydrogenation of terminal alkynes was evaluated using phenylacetylene **54** (Equation 2.20). The catalysis surprisingly formed styrene **57** and ethylbenzene **58** as minor products, while 55% of the substrate was converted into a 10 : 1 mixture of the head-to-head and head-to-tail linear dimers **55** and **56**, respectively.

Equation 2.20



Catalytic linear dimerization of alkynes has been instrumental to the synthesis of conjugated enynes. Enynes, particularly when polyarylated, are known to have diverse applications in materials chemistry.¹³⁷⁻¹³⁹ The dimerization of **54** was conducted in the absence of H₂. Treatment of **54** with a catalytic quantity of **26b** at room temperature resulted in a dark brown reaction mixture. The catalyst effected a 70% substrate conversion into a 5 : 1 mixture of dimers **55** and **56** (Equation 2.21). The remaining 30 % of the substrate was converted into a mixture of triphenylbenzenes, which form by competitive catalytic [2+2+2] cycloaddition. Interestingly, the yields observed from this experiment are comparable to reported yields in alkyne dimerizations catalyzed by homogeneous second- and third-row transition metal complexes.¹⁴⁰⁻¹⁴²

Equation 2.21



Since kinetic and mechanistic information on the nickel-catalyzed linear dimerization of terminal alkynes is not yet available, only highly tentative mechanistic proposals can be drawn at this point. There are three logical mechanistic pathways that could explain the catalytic linear dimerization of phenylacetylene.^{140,142,143} Assuming that the tetrametallic cluster remains intact during the catalysis, one mechanism involves the bimetallic oxidative activation of the terminal C-H bond in phenylacetylene. This results in the formation of a higher oxidation state species **59** (Figure 2.4). An incoming phenylacetylene molecule then precoordinates with **59** in two possible orientations **60a** and **60b**. Each terminal alkyne molecule in the isomeric species **60** then undergoes insertion into the M-C bond forming either the sterically favored intermediate **61a** or the less stable isomer **61b**. Bimetallic reductive elimination then leads to the formation of the two isomeric products **55** and **56** and the regeneration of **26**.

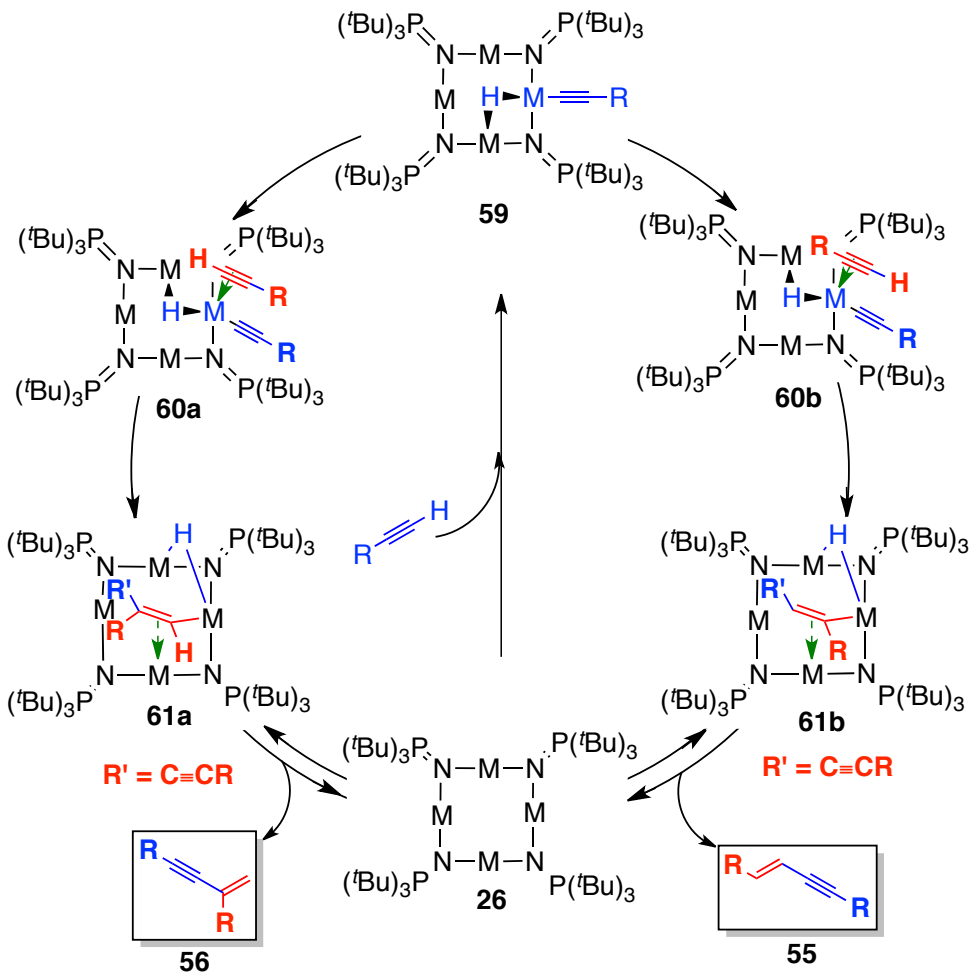


Figure 2.4. Proposed mechanism for the linear dimerization of terminal alkynes.

Intermediate **59** which forms from the bimetallic oxidative C–H activation in phenylacetylene by **26** can also undergo hydrogen transfer from the metal center to the basic nitrogen center of the phosphoranimide ligand (Figure 2.4). This rearrangement results in the formation of an acetylidic-substituted metal(I)-phosphoranimine intermediate **62** (Figure 2.5). On the other hand, an equally probable route for the formation of **62** proceeds through the direct deprotonation of the terminal C–H bond in

phenylacetylene by the basic nitrogen center of the phosphoranimide ligand. An incoming phenylacetylene molecule can then bind to **62** and insert into the M–C bond, forming either of the two isomeric enyne-substituted nickel phosphoranimine intermediate **64a** and **64b**. The syn addition of the M–C bond across the carbon–carbon triple bond of the precoordinated phenylacetylene molecule in **63b** selectively forms the (*E*)-enye that eventually forms the major dimerization product. The linear dimerization products **55** and **56** can then be generated from protonation of the metal-bound enye by an incoming phenylacetylene molecule, regenerating the active catalyst **62**.

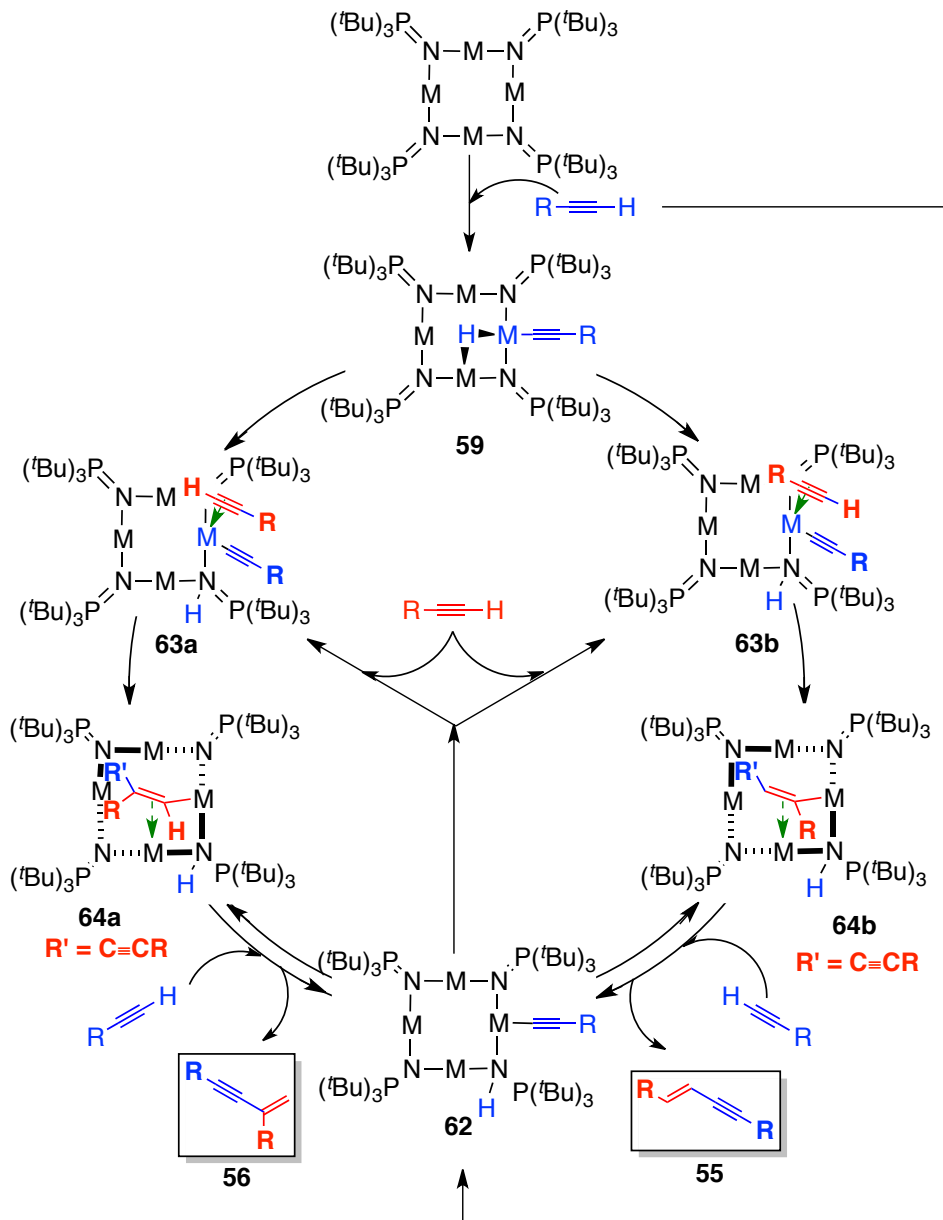


Figure 2.5. Mechanism of terminal alkyne linear dimerization.

The third probable pathway that produces enynes involves the isomerization of **59** to the vinylidene intermediate **65** (Figure 2.6). The tetrametallic cluster **65** can then undergo another bimetallic oxidative C–H activation forming intermediate **66**. Intramolecular migration of the

acetylide molecule then occurs to form the enyne-substituted complex **67**.

This mode of acetylide migration has been preceded to selective form the *cis* head-to-head dimer due to steric considerations.¹⁴² The experiment, however, gives the *trans*-dimer as major product.

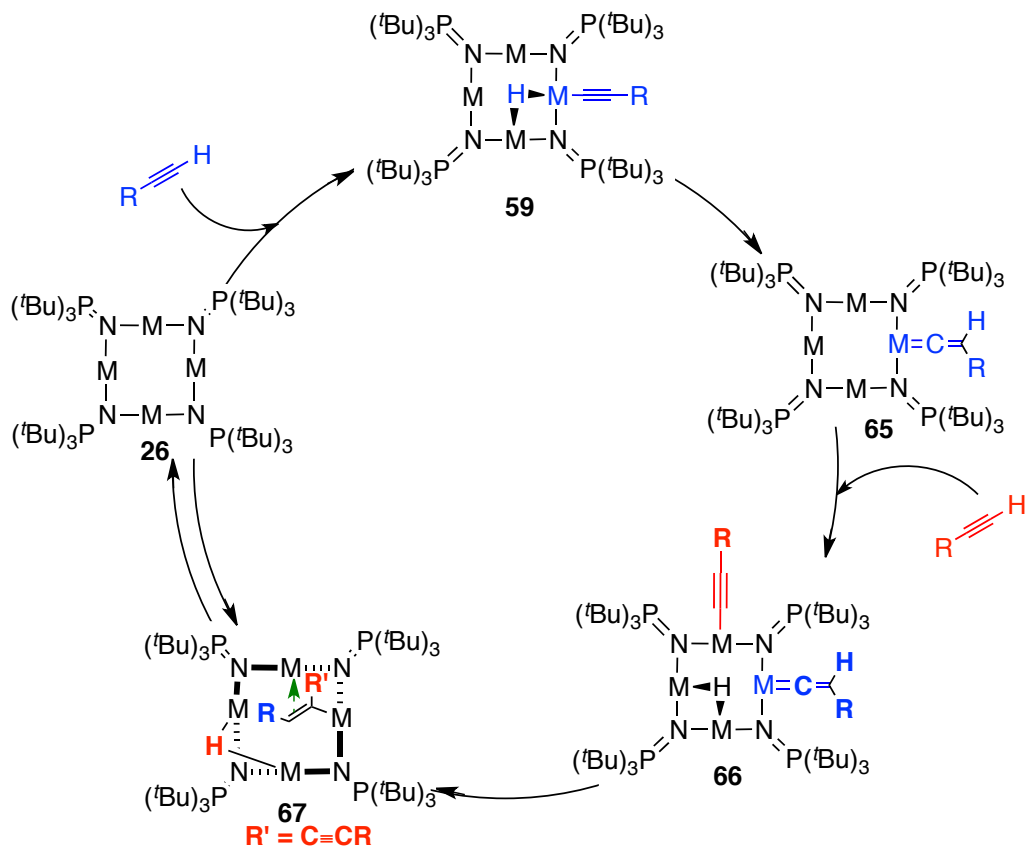


Figure 2.6. Mechanism of terminal alkyne linear dimerization.

2.3 Conclusion

Both the cobalt **26a** and nickel **26b** clusters demonstrated activity for the hydrogenation of a range of unactivated alkenes and alkynes under exceptionally mild reaction conditions. Partial internal alkyne hydrogenation results in the formation of mixtures of the *cis*- and *trans*-alkenes, although both are hydrogenated further. Allylic alkenes undergo catalytic isomerization, providing new catalysts for applications in alkene isomerization. To the best of our knowledge, the turnover rates of the hydrogenation reactions presented above make cluster **26a** and **26b** among the most active homogeneous base metal hydrogenation precatalysts reported in the literature. Thorough investigation of the mechanism of alkene and alkyne reduction was not pursued, but will be important if we are to gain critical insights into the nature of the active catalyst(s).

Lastly, both catalysts also demonstrated activity for carbon-carbon bond-forming reactions involving alkynes. The nickel catalyst was active for [2 + 2 + 2] cycloaddition of internal alkynes and the linear dimerization of terminal alkynes, affording mixtures of head-to-head and head-to-tail dimers. Systematic investigations of the kinetics of the catalytic bond-forming transformations are ideal for future work to determine the nature and nuclearity of the active catalytic species.

Table 2.1. Summary of hydrogenation results.

Entry	Substrate	Cat	mol%	T (°C)	Product	%Conv	TOF (h ⁻¹)
1		26a	0.4	25		54	230
2		26b	1.0	25		49	71
3		26a	0.5	25		23	62
4		26b	0.5	25		18	55
5		26a	0.5	25		39	121
6		26b	0.5	25		35	107
7		26a	0.5	25	Mixtures of <i>cis</i> - and <i>trans</i> - stilbene	11	40
8		26b	1.0	25		13	59

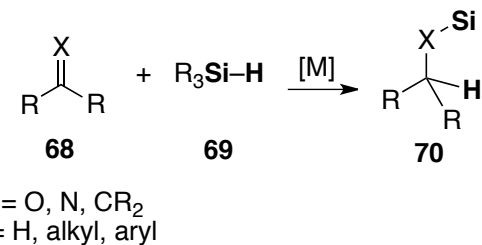
Chapter 3

Base Metal-Catalyzed Hydrosilylation of Carbonyl Compounds

3.1 Introduction

The catalytic reduction of unsaturated bonds remains an active area of research in both academic and industrial research as these processes are vital to the production of commodity and value-added chemicals.¹⁴⁴⁻¹⁴⁷ Transition metal-catalyzed hydrosilylation is a highly atom-economical approach to the reduction of unsaturated organic substrates into synthetically useful organosilanes.¹⁴⁸⁻¹⁵² The catalytic addition of a Si–H bond across a C=X (X = C, N, O) double bond is mainly dominated by expensive and mostly toxic precious transition metals (Equation 3.1), including platinum,¹⁵³⁻¹⁵⁷ ruthenium,¹⁵⁸⁻¹⁶⁰ rhodium¹⁶¹⁻¹⁶⁵ and iridium.^{166,167}

Equation 3.1

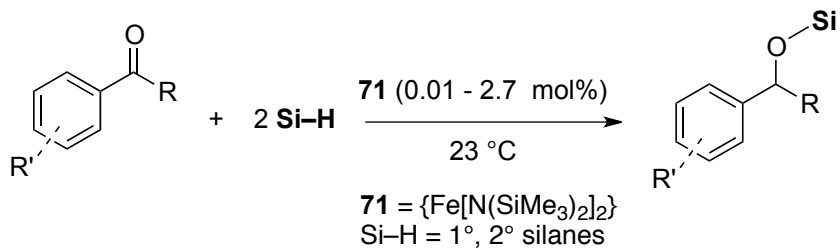


The field continues to develop high-activity and cost-effective hydrosilylation catalyst technologies by developing metal-free strategies¹⁶⁸ and alternative catalysts utilizing the less expensive, abundant, and significantly less toxic first-row transition metals.¹⁰⁸ Several homogeneous hydrosilylation catalysts have been developed using early to late first row metals. Coordination complexes of titanium,^{169,170} iron,¹⁷¹⁻¹⁷⁴ copper^{108,175-}

¹⁷⁹ and zinc¹⁸⁰⁻¹⁸³ have been reported active for the reduction of a range of polar and nonpolar unsaturated functional groups. Most of these catalysts are supported by polyfunctional ligand scaffolds, which in some cases, attenuate catalyst activity and consequently require co-catalysts and other additives. On the other hand, the use of cobalt¹⁸⁴⁻¹⁸⁹ and nickel¹⁹⁰⁻¹⁹⁴ for catalytic hydrosilylation remains underdeveloped.

A common hydrosilylation catalyst design strategy involves the synthesis of low-valent metal complexes, generating highly active metal center(s) toward oxidative activation of a Si–H bond – the key step in the catalytic cycle.¹⁹⁵ Tilley and coworkers reported the efficient hydrosilylation of a broad range of carbonyl compounds under remarkably mild conditions, catalyzed by a two-coordinate mononuclear iron (II) catalyst, {Fe[N(SiMe₃)₂]}, supported only by simple amido ligands (Equation 3.2).¹⁹⁶ The low coordinate and low valent metal centers in clusters **26a** and **26b**, coupled with their high hydrogenation activity, prompted us to optimize both tetrametallic clusters for the catalytic hydrosilylation of a range of unsaturated functional groups.

Equation 3.2



3.2 Results and Discussion

This chapter tackles the hydrosilylation of a range of unsaturated organic substrates catalyzed by **26a** and **26b** under exceptionally mild conditions. The results (*vide infra*) suggest that relative to reported homogeneous base metal catalysts, both clusters exhibit enhanced activity, covering a diverse set of functionalized carbonyl substrates and useful organosilyl hydrides.

Throughout this chapter, the catalyst turnover number (**TON**) corresponds to the moles of C=O double bond reduced to a C–O single bond. Catalyst turnover frequency, on the other hand, is the ratio of **TON** to the reaction period (hours).

3.2.1 Preliminary Hydrosilylation Experiments

The catalytic activities of both **26a** and **26b** were initially evaluated in the hydrosilylation of cyclohexanone **72** using phenylsilane PhSiH₃ as reductant (Table 3.1; Equation 3.3). Both clusters effected the hydrosilylation of **72** under remarkably mild conditions: room temperature and low catalyst loading (0.4 mol %). The catalytic hydrosilylation with the polyhydridic reductant PhSiH₃ is surprisingly non-selective; in both cases

(Entries **1-2**), mixtures of (cyclohexyloxy)phenylsilane **73** and bis(cyclohexyloxy)phenylsilane **74** were obtained.

Equation 3.3

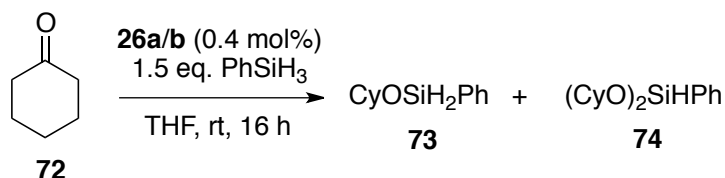


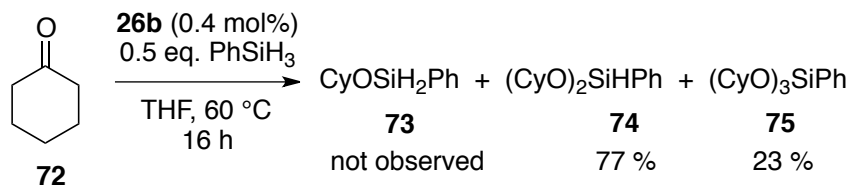
Table 3.1. Catalytic hydrosilylation of cyclohexanone **67**.

Entry	Catalyst	Yield of 73 (%) ^a	Yield of 74 (%) ^a	TON
1	26a	34	17	145
2	26b	22	73	238

^aPercentage conversion is based on GC-MS analyses.

The Ni(I) catalyst **26b** showed higher activity and after 16 hours resulted in near quantitative (95 %) substrate conversion (238 turnovers) to a 1 : 3.5 mixture of PhSiH₂(OCy) **73** and PhSiH(OCy)₂ **74**. This product distribution suggests that PhSiH₂(OCy) **73**, a secondary organosilyl hydride, is more reactive than PhSiH₃. This hypothesis was confirmed in an experiment where a 2 : 1 PhSiH₃-to-cyclohexanone stoichiometric ratio was purposefully employed. The catalysis returned a mixture comprising mainly of **74** (75 %) and tris(cyclohexyloxy)phenylsilane **75** (23 %) (Equation 3.4). Under the given conditions, PhSiH₂(OCy) **73** was not detected.¹²

Equation 3.4

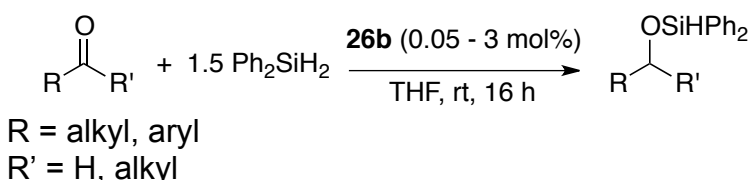


The observed difference in hydrosilylation activities of the Co(I) and Ni(I) catalysts prompted further research to explore the scope of carbonyl substrates and organosilyl hydrides, using the more active nickel catalyst **26b**. At room temperature, catalyst **26b** reacts with primary, secondary and tertiary silanes, affording the corresponding alkoxy silane derivatives for a range of functionalized aldehydes and ketones. The efficiency of tertiary organosilyl hydrides, however, varies with substrate type.

3.2.2 Hydrosilylation Substrate Scope

The generality of the catalysis was evaluated through a series of 16-hour experiments under a range of conditions summarized in Equation 3.5. Diphenylsilane, a secondary organosilyl hydride Ph_2SiH_2 , was used as reductant since it showed high selectivity for the monoalkoxy silane derivatives.

Equation 3.5



3.2.2.1 Hydrosilylation of Aliphatic Carbonyl Compounds

Catalyst **26b** efficiently hydrosilylates aliphatic aldehydes and ketones (Table 3.2, Equation 3.6). Aldehydes are unsurprisingly more reactive toward hydrosilylation than are ketones. Isovaleraldehyde **76** was reduced quantitatively to a 3 : 2 mixture of monoalkoxydiphenylsilane **77** and dialkoxydiphenylsilane **78**, respectively (TON = 250, Entry 1, Table 3.2). Cyclohexanone **72** undergoes hydrosilylation at a relatively attenuated rate, mainly forming (cyclohexyloxy)diphenylsilane **79** with a 55 % conversion (TON = 140, Entry 2; Table 3.2). Interestingly, **26b** exhibits high propensity to reduce polar unsaturated groups over non-polar unsaturated functionalities when both present in a non-conjugated form. The selectivity is presumably due to the stronger affinity of the open-shell M(I) centers in **26a/b** to the polar unsaturated groups thus, kinetically favoring carbonyl ligation and the subsequent reduction. For example, the isolated carbon-carbon double bond in 3-cyclohexene-1-carboxaldehyde **81** selectively form the organosilanes derivative **82** (Entry 3, Table 3.2).

Equation 3.6

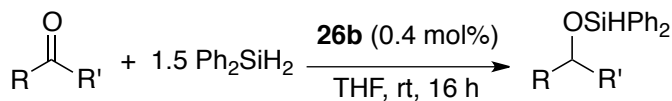
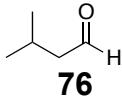
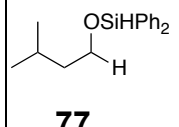
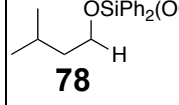
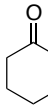
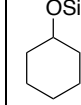
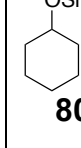
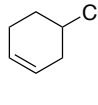
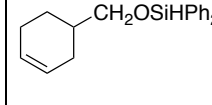


Table 3.2. Hydrosilylation of aldehydes and ketones catalyzed by **26b**.

Entry	26b [mol %]	Substrate	Conv. [%] ^[a]	TON	Product(s)
1	0.4		59 41	250	 
2	0.4		55 2	140	 
3	0.4		91	228	

3.2.3 Hydrosilylation of Aromatic Aldehydes and Ketones

Aromatic aldehydes and ketones are selectively reduced to the corresponding monoalkoxydiphenylsilane derivatives under equally mild reaction conditions (Equation 3.7). *Para*-ethylacetophenone **83** is transformed to the monoalkoxydiphenylsilane product **84** at a slow rate (**TON** = 96, Entry 1; Table 3.3). Interestingly, the electron-rich *para*-methoxyacetophenone **85** is reduced at a comparable rate (**TON** = 90; Entry 2, Table 3.3). Quantitative hydrosilylation of **85** was achieved at a

higher catalyst loading (**TON** = 200, Entry 3). At this point, the apparent indifference of catalyst **26b** to more electron rich substrates remains poorly understood and requires systematic mechanistic investigations.

Equation 3.7

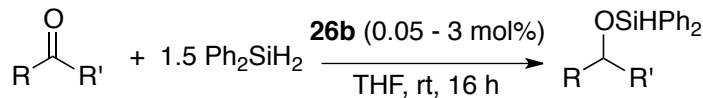
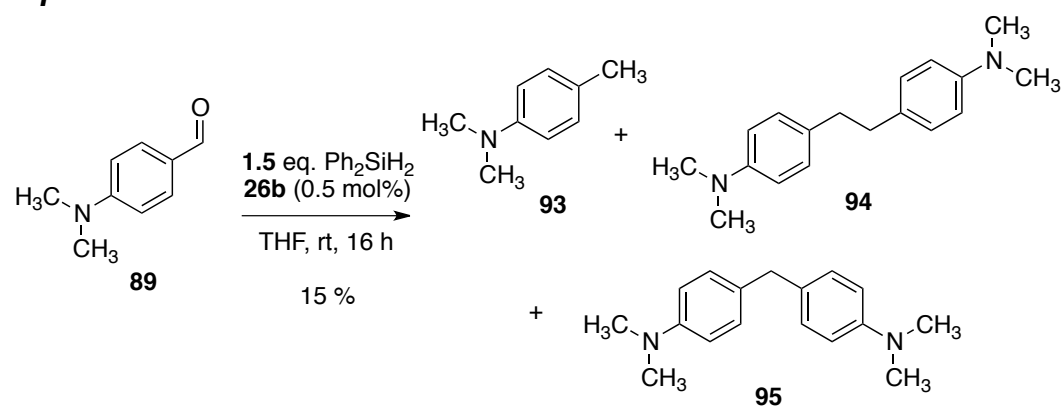


Table 3.3. Hydrosilylation of aryl aldehydes and aryl ketones catalyzed by **26b**.

Entry	26b [mol %]	Substrate	Conv. [%] ^[a] / (TON)	Product(s)
1	0.5		48 (96)	
2	0.5		45 (90)	
3	3.0		>98 (200)	
4	0.5		97 (194)	
5	0.5		85 (170)	
6	0.5		90 (180)	

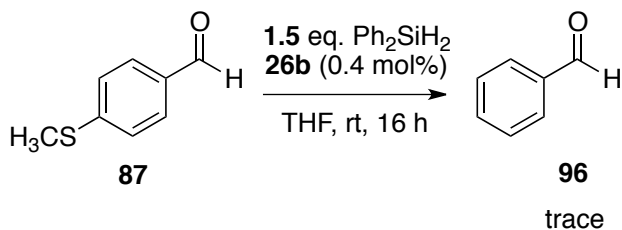
Aromatic aldehydes are expectedly hydrosilylated at faster rates. Electron-rich aryl aldehydes 4-(methylthio)benzaldehyde **87** and 4-(*N,N'*-dimethylamino)benzaldehyde **89** underwent near quantitative reduction (85-97 %) to monoaryloxydiphenylsilane derivatives under mild conditions with turnover numbers of 194 and 170, respectively (Entries **4-5**, Table **3.3**). The relatively lower yield of the hydrosilylation derivative of **89** is due to the competitive, catalytic deoxygenation of C=O double bonds. The remaining 15 % of the starting material **89** was converted into a mixture of deoxygenation products (**93-94**, Equation **3.8**) and bis(4-(*N,N'*-dimethylaminophenyl)methane **95**, presumably formed from the coupling of a deoxygenated molecule of **89** with a decarbonylated substrate. Interestingly, all aromatic carbonyl substrates presented formed trace amounts corresponding deoxygenated products (Entries **1-6**, Table **3.3**). This catalytic side reaction, to the best knowledge, is unprecedented for the base metals under the given conditions. An extensive study of the scope of catalytic carbonyl deoxygenation is the focus of Chapter **6**.

Equation 3.8



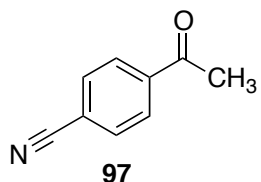
The tendency of **26b** to reductively cleave C–S bonds was also observed in the room-temperature reduction of 4-(methylthio)benzaldehyde **87**. The reduction is dominantly selective for the carbon-oxygen double bond hydrosilylation (Entry 4, Table 3.3) however, trace amounts of benzaldehyde **96**, the product carbon-sulfur bond activation, was also detected at room temperature (Equation 3.9). Interestingly, catalyst deactivation was not observed considering the formation of a potential inhibitor methyl sulfide (CH_3S^-) formed from the C–S bond hydrogenolysis. Low-valent organometallic complexes have been used as models for metal active sites on industrial hydrodesulfurization catalysts (CoMoS_2 and NiWS_2). These modeling studies are crucial to understand the active role(s) of cobalt and nickel promoter ions in the industrial activation of carbon-sulfur bonds in petroleum constituents. The utility of both Co(I) and Ni(I) tetrametallic clusters **26a** and **26b** for stoichiometric and catalytic reductive carbon-sulfur bond activation will be discussed in Chapter 4.

Equation 3.9



The catalyst chemoselectivity was evaluated in the hydrosilylation of carbonyl substrates with other polar unsaturated functionalities. The

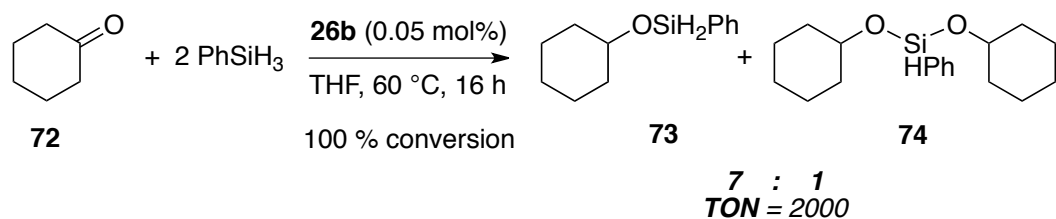
electron-deficient methyl 4-formylbenzoate **91** underwent highly selective aldehyde C=O double bond hydrosilylation to the corresponding aryloxydiphenylsilane derivative **92** at room temperature, leaving the ester group unaffected (Entry **6**, Table **3.3**). On the other hand, the catalytic reduction of 4-cyanoacetophenone **97** gave a complex mixture of products, suggesting the competitive reduction with the carbon–nitrogen triple bond.



3.2.4 Solvent-Free Hydrosilylation

The efficiency of the hydrosilylation catalysis was demonstrated in the quantitative reduction of liquid substrates without added solvents under mild conditions. Neat cyclohexanone **72** underwent quantitative reduction using PhSiH₃ at 0.05 mol% loading of **26b** at 60 °C. The 16-hour reduction gave a 7 : 1 mixture comprising of PhSiH₂(OCy) **73** and PhSiH(OCy)₂ **74** (TON = 2000, Equation **3.10**) and no signs of catalyst decomposition or precipitate formation was observed over the course of the solvent-free catalysis.

Equation 3.10



3.2.5 Carbonyl Substrate Scope with Tertiary Organosilyl Hydride as Reductant

The catalysis proceeds efficiently with primary and secondary organosilyl hydrides (PhSiH₃ and Ph₂SiH₂, respectively). Surprisingly, the scope of carbonyl substrates that undergo catalytic reduction varies with the type of tertiary organosilyl hydride. The most limited scope of carbonyl substrates was observed using unactivated trialkylsilanes. Triethylsilane (Et₃SiH) is only effective in the hydrosilylation of non-enolizable carbonyl substrates. Non-enolizable substrates underwent clean hydrosilylation albeit at remarkably slower rates (Entries 1-4, Table 3.4; Equation 3.11). The inability of Et₃SiH to hydrosilylate enolizable substrates is attributed to catalyst decomposition. The addition of isovaleraldehyde **76** or cyclohexanone **72** to a solution of the Ni(I) catalyst **26b** and Et₃SiH causes immediate catalyst decomposition as evidenced by solution decolorization (dark green to pale pink) and precipitate formation. The decomposition is presumably due to competitive deprotonation of the acidic α-hydrogen(s) of the carbonyl substrates.

Equation 3.11

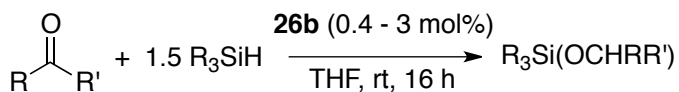
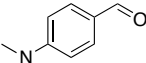
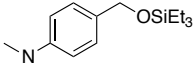
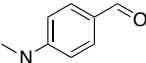
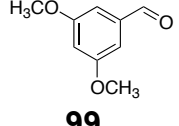
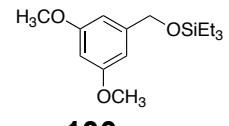
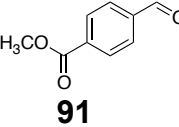
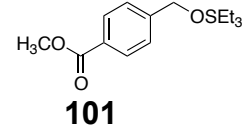
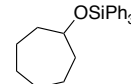


Table 3.4. Hydrosilylation of aldehydes and ketones with tertiary silanes.

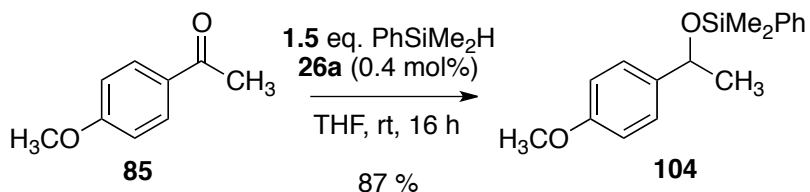
Entry	26b [mol %]	Substrate	Conv. [%] ^a (TON)	Product
1	0.9		19 (21)	
2	3.0	 89	55 (18)	 98
3	0.8	 99	62 (78)	 100
4	0.7	 91	48 (69)	 101
5	0.5 ^[b]	 102	12 (24)	 103

^a Conversion was determined by GC-MS [b] Ph₃SiH was used at 60°C.

The purported competitive deprotonation of enolizable substrates is suppressed by using more reactive tertiary silanes. Cycloheptanone **102** undergoes slow but clean reduction to **103** using excess quantities of the sterically hindered triphenylsilane at 60 °C (Entry 5, Table 3.4). Interestingly, the reactivity of a monoarylated organosilyl hydride seems

insufficient to effect the hydrosilylation of enolizable substrates. Even though no signs of catalyst decomposition were observed, the nickel-mediated reduction of *p*-methoxyacetophenone **85** with PhSiMe₂H proceeds stoichiometric. Surprisingly, the cobalt catalyst **26a** efficiently reduces **85** with PhSiMe₂H to the corresponding monoalkoxysilane derivative **104** at 87 % substrate conversion (**TON** = 218; Equation 3.12). The observed difference in the activities of the Co(I) and Ni(I) clusters potentially reflects the greater stability of the nickel-alkoxide complex that forms from the initial substrate reduction.

Equation 3.12



The observed turnover frequencies are slow relative to the rates reported by Tilley and coworkers.¹⁹⁶ We tentatively attribute the slower rates to steric factors. Assuming the clusters remain intact during the course of the catalysis, the tetrametallic cores could be considerably hindered compared to Tilley's monomeric active Fe(II) catalyst. The morphology of metal centers in catalysts **26a** and **26b** bestows enhanced activity toward Si–H activation. To the best of our knowledge, this additive/activator-free, base metal-catalyzed carbonyl hydrosilylation covers the broadest scope of applicable organosilyl hydrides.^{195,196}

3.2.6 Catalytic Hydrosilylation of Nonpolar Unsaturates

The demonstrated hydrosilylation activities of **26a** and **26b** prompted us to evaluate both catalysts for hydrosilylation of nonpolar unsaturates. By comparison, both catalysts are surprisingly ineffective for hydrosilylation of nonpolar unsaturated functionalities. Catalytic hydrosilylation of allylbenzene **34**, for example, affords an unimpressive mixture of hydrogenation, isomerization, and hydrosilylation products, with the latter detected in trace quantities (Equation 3.13, Table 3.5). For each catalyst, all three products were obtained at attenuated rates relative to catalytic hydrogenation using H₂. The cobalt-catalyzed reaction afforded n-propylbenzene **35** as the major product. On the other hand, the nickel reduction catalysis produced *trans*-1-phenyl-propene **36a**, product of alkene isomerization, as the dominant species. This variation in catalyst selectivity is consistent with the observed greater tendency of the nickel catalyst to isomerize alkenes (Chapter 2) thus, inhibiting the hydrogenation rate.

Equation 3.13

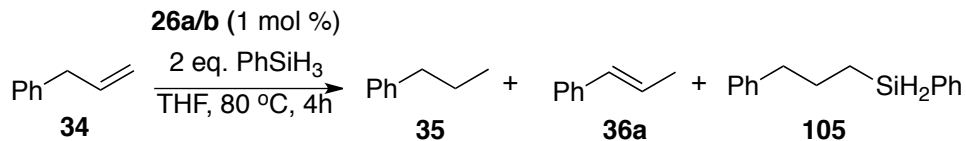
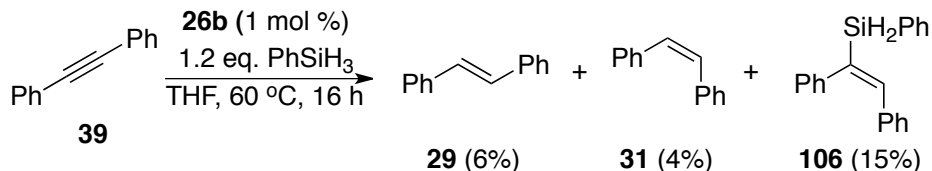


Table 3.5. Catalytic hydrosilylation of allylbenzene.

Catalyst	Conversion to 34 (%)	Conversion to 36a (%)	Conversion to 105 (%)
26a	28	70	2
26b	74	24	2

Internal alkynes under catalytic hydrosilylation, producing vinylsilanes as the major products. Under the conditions described in Equation 3.14, the hydrosilylation of diphenylacetylene **39** resulted in an overall 25 % substrate conversion to a 2 : 1 : 5 mixture of *trans*-stilbene **29**, *cis*-stilbene **31** and (1,2-diphenylvinyl)phenylsilane **106**. The given product distribution, however, shows that hydrogenation remains highly competitive.

Equation 3.14



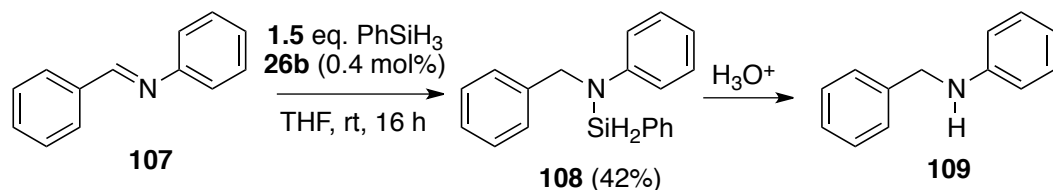
The selectivity of **26a** and **26b** for alkene hydrogenation/isomerization is, again, tentatively attributed to steric factors, which disfavor coordination of the larger silane fragment. These results also suggest, though inconclusively, that the tetrametallic catalyst functions as the intact tetramer throughout the catalytic process.

Systematic kinetic and mechanistic investigations are thus needed to understand the mechanism and variations in catalyst selectivities.

3.2.7 Imine hydrosilylation catalysis

The nickel catalyst **26b** is also active toward imine hydrosilylation. *N*-benzylideneaniline **107** was efficiently hydrosilylated to the corresponding aminophenylsilane derivative **108** (42 %; TON = 105) at room temperature (Equation 3.15). Hydrolysis of the product mixture afforded the expected secondary amine, benzyl phenyl amine **109**. This demonstrates the potential utility of the catalysts for the mild condition reduction of unsaturated C–N bonds. Optimization and exploration of the generality of catalysts **26a** and **26b** would be an important topic for further studies.

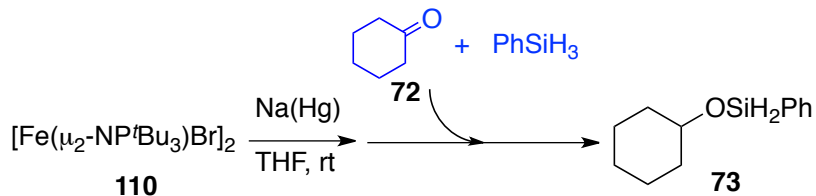
Equation 3.15



3.2.8 Iron-Catalyzed Hydrosilylation of Cyclohexanone

An active iron hydrosilylation catalyst can be synthesized from the reduction of monobromomono-(tris-*tert*-butyl)phosphoranimidoiron(II) $[\text{Fe}(\text{NP}^t\text{Bu}_3)\text{Br}]_2$ **110**. The brown, pentane soluble solid, expected to be $[\text{Fe}(\text{NP}^t\text{Bu}_3)]_4$, catalytically hydrosilylates cyclohexanone **72** into monocyclohexyloxyphenylsilane **73** (Equation 3.16). The precatalyst, however, is structurally uncharacterized.

Equation 3.16

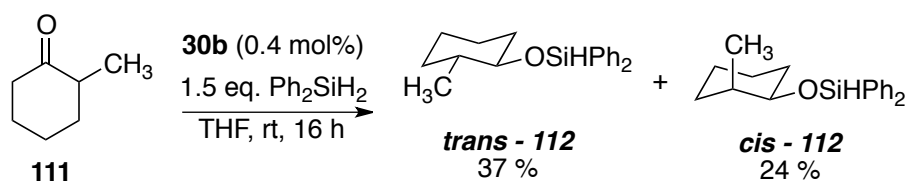


3.2.9 Stereoselectivity of Hydrosilylation

The relatively slow hydrosilylation rates and the observed catalyst selectivity for hydrogenation-isomerization of nonpolar unsaturated bonds lead us to propose an intact tetrametallic catalyst. *In lieu*, we evaluated the stereoselectivity of the C=O double bond hydrosilylation. We hypothesized that an intact tetranuclear catalyst with two identical reactive surfaces could induce diastereoselectivity in the reduction of unsymmetrical substrates. Interestingly, the catalyst exhibits low diastereoselectivity for hydrosilylation. The room temperature hydrosilylation of 2-

methylcyclohexanone **111** with Ph₂SiH₂, afforded a 1.5:1 mixture of the *trans*- and *cis*-product **112** (Equation 3.16). This product distribution, however, does not provide confirmative information on the nuclearity of the active catalyst.

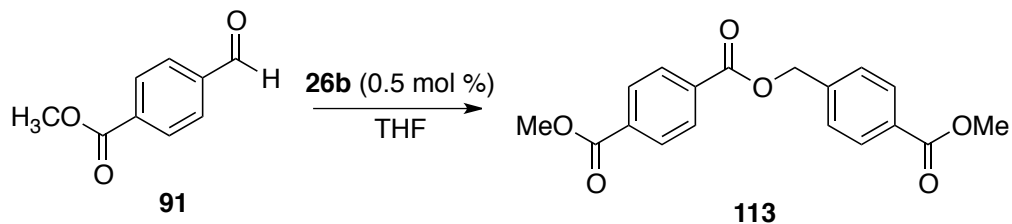
Equation 3.17



3.2.10 Control Experiments

The hydrosilylation catalysis does not proceed in the absence of the Co(I) or Ni(I) catalyst. In the absence of an organosilyl hydride reductant, aldehydes such as methyl 4-formylbenzoate **91** undergoes slow but catalytic dimerization – *Tishchenko Reaction* – to the corresponding ester **113** (13 %, **TON** = 26; Equation 3.18).

Equation 3.18



The dimerization is presumably initiated by a radical species **115** (Figure 3.1). Intermediate **107** transforms into an alkoxide-substituted active nickel catalyst **116** via single-electron transfer. Complex **116** then metathetically transfers the alkoxide fragment to an incoming aldehyde **114**, forming an acetal-functionalized intermediate **117**. Intermediate **117** undergoes β -hydride elimination, liberating the ester product **118** and forming an active nickel hydride **119**. Intermediate **119** then reacts with an aldehyde molecule to reform **114**.

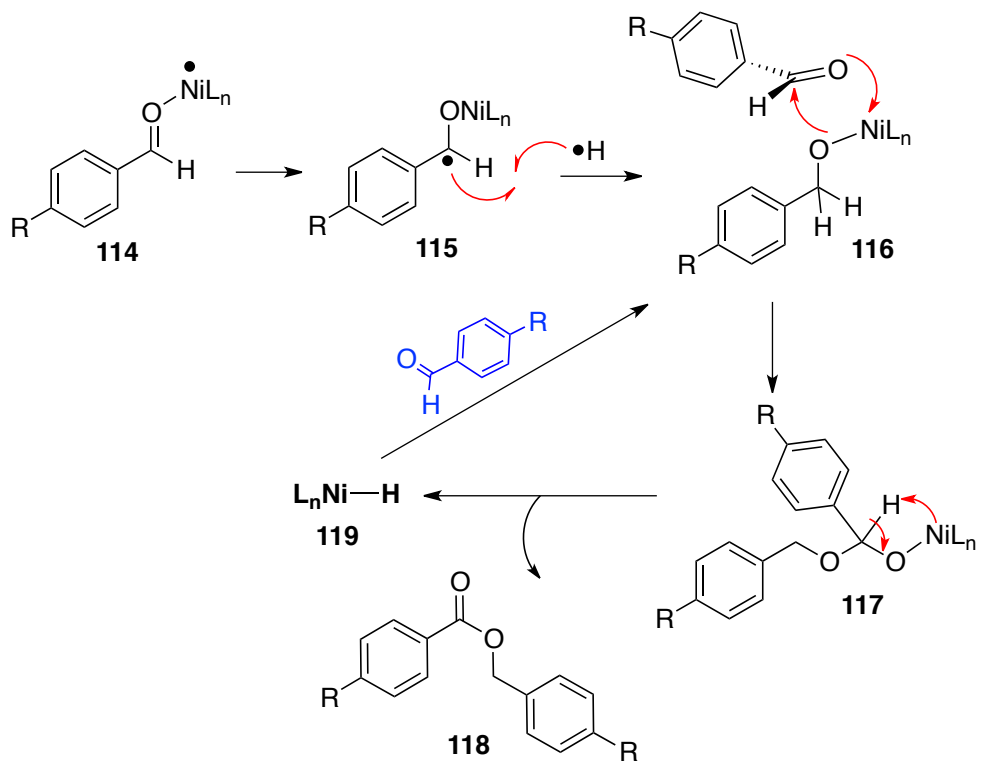


Figure 3.1

This result, though preliminary, suggests the potential utility of the catalysts for mild condition, catalytic carbon-oxygen bond forming transformations.

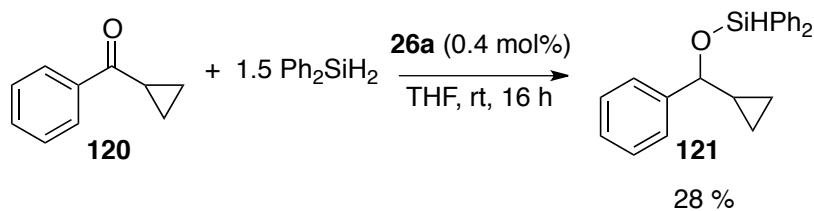
3.2.11 Test of Catalyst Homogeneity

Successful hydrosilylation reactions show no visible signs of color change or precipitate formation. Large excess of metallic mercury does not attenuate the rates of hydrosilylation. The room temperature hydrosilylation of isovaleraldehyde in C₆D₆ (0.8 mol % **26b**; TON = 68/h) is unaffected even in the presence of large quantities of metallic mercury (> 250 equivalents). These observations are suggestive, though inconclusively, of a homogeneous active catalyst.^{131-135,197}

3.2.12 Hydrosilylation of a Radical Clock: A Mechanistic Probe

As a preliminary mechanistic probe for the cobalt- and nickel-catalyzed hydrosilylation, the reduction of a radical clock, cyclopropyl phenyl ketone **120** was carried out (Equation 3.19). The cobalt-catalyzed hydrosilylation resulted in exclusive formation of the expected alkoxy silane derivative **121**. This suggests a non-radical mechanism for the reduction.

Equation 3.19



On the other hand, the nickel-catalyzed reaction afforded a mixture comprised of the carbon-oxygen double bond hydrosilylation product **121** and phenyl propyl ketone **122**, the product of catalytic carbon-carbon bond activation of the cyclopropyl ring (Equation 3.20). The formation of the ring-opened product **122** suggests the possible contribution of a radical mechanism, proceeding via a cyclopropyl methyl radical intermediate **123** (Figure 3.2). Intermediate **123** undergoes homolytic cyclopropyl ring opening to form an enolate radical **124** that eventually undergoes hydrogen radical abstraction, producing enol **125**. Keto-enol tautomerism then gives the observed ring-opened product **122**. The apparent radical mechanism for the nickel-mediated catalysis is not surprising as the intact Ni(I) tetramer **26b** exhibits 3.5-electron paramagnetism, a doublet magnetic spin state for each Ni(I) center. In the same regard, the observed non-radical mechanism for the cobalt-catalyzed reduction raises mechanistic insights since the Co(I) tetrametallic cluster **26a** behaves as an eight-electron paramagnet (two unpaired electrons per cobalt center).⁷⁷

Equation 3.20

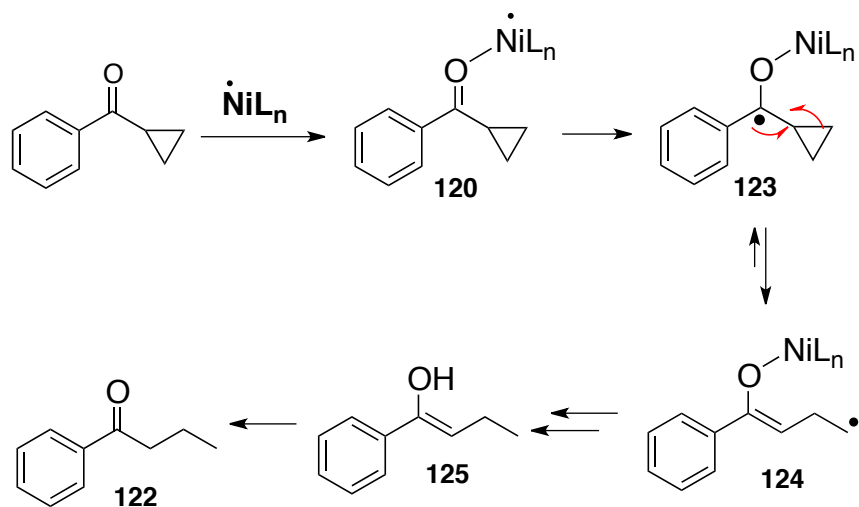
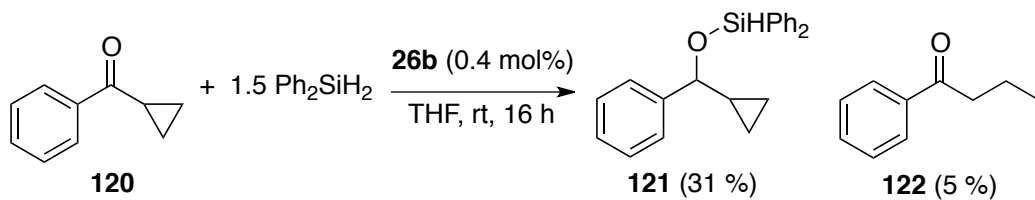


Figure 3.2. Potential mechanism for C-C bond breaking in **96**.

The apparent contribution of a radical mechanism for the nickel-catalyzed reduction is further supported, though inconclusively, by the observed substituent redistribution at silicon.¹⁹⁸⁻²⁰¹ Detectable levels of diphenylsilane Ph_2SiH_2 and alkoxydiphenylsilanes were observed in nickel-catalyzed reactions using PhSiH_3 . These mechanistic observations further raise mechanistic issues as distinct reactivities were observed using the two isostructural catalysts. These results suggest that *the observed variation in chemical behavior in these ancillary ligand-free metal*

clusters is, inherently, a function of the metal itself. A more thorough mechanistic investigation, however, is still needed to better understand the observed difference in chemical reactivity between the Co(I) and Ni(I) clusters.

3.2.13 Mechanism of Hydrosilylation

With the assumption that the tetrametallic cluster remains intact during the course of the catalysis, the bimetallic catalytic cycle presented in Figure 3.3 is proposed for the non-radical carbonyl hydrosilylation. The oxidative cleavage of a Si–H bond is proposed since both Co(I) and Ni(I) clusters **26** spontaneously react upon treatment with organosilyl hydride reagents. This results in the formation of a silyl- and hydride-functionalized organometallic intermediate **126**. Intermediate **126** delivers a hydride to an incoming carbonyl substrate through transition state **127**, affording an alkoxy-substituted organometallic intermediate **128**. Regeneration of the active catalyst **126** proceeds via two possible pathways. First, the bimetallic reductive elimination of the alkoxy and silyl fragments in **128** can liberate the alkoxy silane product and regenerate the M(I) cluster **26**. The second probable pathway involves the sigma-bond metathesis between the M–O bond of **127** and the Si–H bond of an incoming organosilyl hydride, regenerating intermediate **126**.

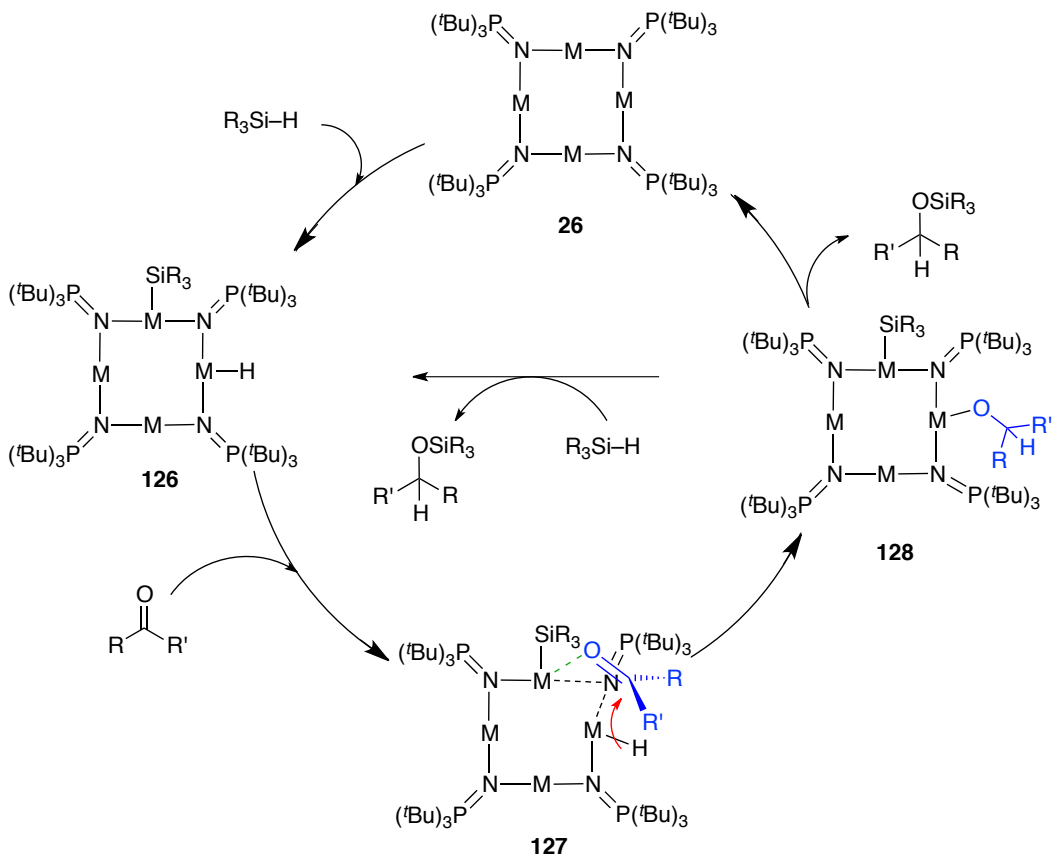


Figure 3.3. Mechanism of nickel-catalyzed hydrosilylation.

3. 3 Conclusion

Both tetrametallic clusters **26a** and **26b** were demonstrated highly active for the catalytic hydrosilylation of a range of carbonyl substrates under exceptionally mild reaction conditions. The additive/activator-free catalytic hydrosilylation of polar unsaturates proceeds efficiently under mild conditions. The catalysis efficiently works with a diverse scope of organosilyl hydride reagents. Primary, secondary and tertiary silanes are

efficiently converted into alkoxy silanes, and the catalysts tolerate a wide range of functional groups including isolated alkenes, tertiary amines, esters, ethers and thioethers.

Both catalysts reluctantly hydrosilylate nonpolar unsaturates (alkenes and alkynes), producing mixtures composed mainly of hydrogenation and isomerization products. In addition, the catalysis was also shown to be effective in the reduction of other polar unsaturated functional groups such as carbon-nitrogen double bonds in imines. Systematic investigation of the hydrosilylation mechanism is highly warranted to further define the mechanistic differences between the cobalt- and nickel-catalyzed reduction.

Chapter 4

High-Activity Base Metal Catalysts for Hydrodesulfurization.

4.1 Introduction and background.

The ever increasing demand for transportation fuels and the highly restrictive environmental policies on toxic gas (SO_x and NO_x) emissions raise barriers to the sustainability of petroleum-based industries.^{15,202,203} Significant industrial research attention is currently dedicated to the development of practical petroleum upgrading technologies that will produce high energy-density and environmentally safe – *zero-sulfur* and *zero-nitrogen* – fuels and commodity petrochemicals. The complete removal of sulfur and nitrogen during industrial hydrotreatment (hydrodesulfurization and hydrodenitrogenation) currently requires resource-intensive process conditions; high temperatures and high hydrogen pressures that together contribute significantly to processing costs and the sacrifice of key process efficiencies.^{15,203-206}

Industrial hydrotreatment is commonly catalyzed by sulfided second- and third-row transition metals promoted by other transition metal ions such as cobalt, nickel, tungsten, and ruthenium (e.g. CoMoS_2 and NiWS_2).^{11,15,202-207} These solid-state oxide or sulfide precatalysts are thermodynamically very stable, requiring costly and energy intensive activation and operation. These bulk metal sulfides are supported and subjected to high temperatures (300 to 650 °C) and high hydrogen pressures (10 to 120 atm) in order to reductively extrude surface sulfide

ions as H₂S gas, generating coordinatively unsaturated metal centers – *surface vacancies* – for substrate binding and reaction.^{15,203}

The rational design of practical and efficient transition metal hydrotreatment catalysts is largely dependent on understanding the nature of the coordinatively unsaturated catalyst active sites. Even though industrial hydrotreatment research, particularly that directed toward hydrodesulfurization, already spans more than half a century, the field's understanding of the mechanism of bulk metal-catalyzed hydrodesulfurization remains nebulous.^{15,203,205} The complex surface features and non-uniform composition of heterogeneous hydrotreatment catalysts make mechanistic investigations extremely difficult. Hence, despite the abundant literature on hydrotreatment, there remains a dearth of meaningful investigations of common catalyst reactivity patterns and optimum process conditions. This problem might be addressed if rigorous mechanistic and kinetic investigations could be done using discrete, preferably *single-site*, platform compounds that mimic purported heterogeneous catalyst active sites.

The discovery of stoichiometric desulfurization by heterogeneous Raney nickel raised controversies on the actual role of the first-row transition metal “promoter” used ubiquitously in industrial hydrotreatment catalysts.²⁰⁸⁻²¹¹ Nonetheless, industrial research on hydrodesulfurization continues to be dominated by precious and semi-precious transition metal

catalysts (e.g. Mo, W, Pt).^{203,212} The cheap and earth-abundant first-row transition metals have received profoundly little attention from the research community, due to the perception that the base metals are of intrinsically low reactivity.^{13,15,30,203,204,213} Studies comparing the activities of various heterogeneous transition metal sulfide catalysts supports this notion of low activity for first row transition metals.²⁰² Figure 4.1 shows the standard “volcano plot” depicting the trend in activity for dibenzothiophene (DBT) hydrodesulfurization as a function of the transition metal sulfide catalysts’ position in the periodic table.²⁰² The plot highlights the great disparity in the activity of first row transition metals from second- and third-row metals.

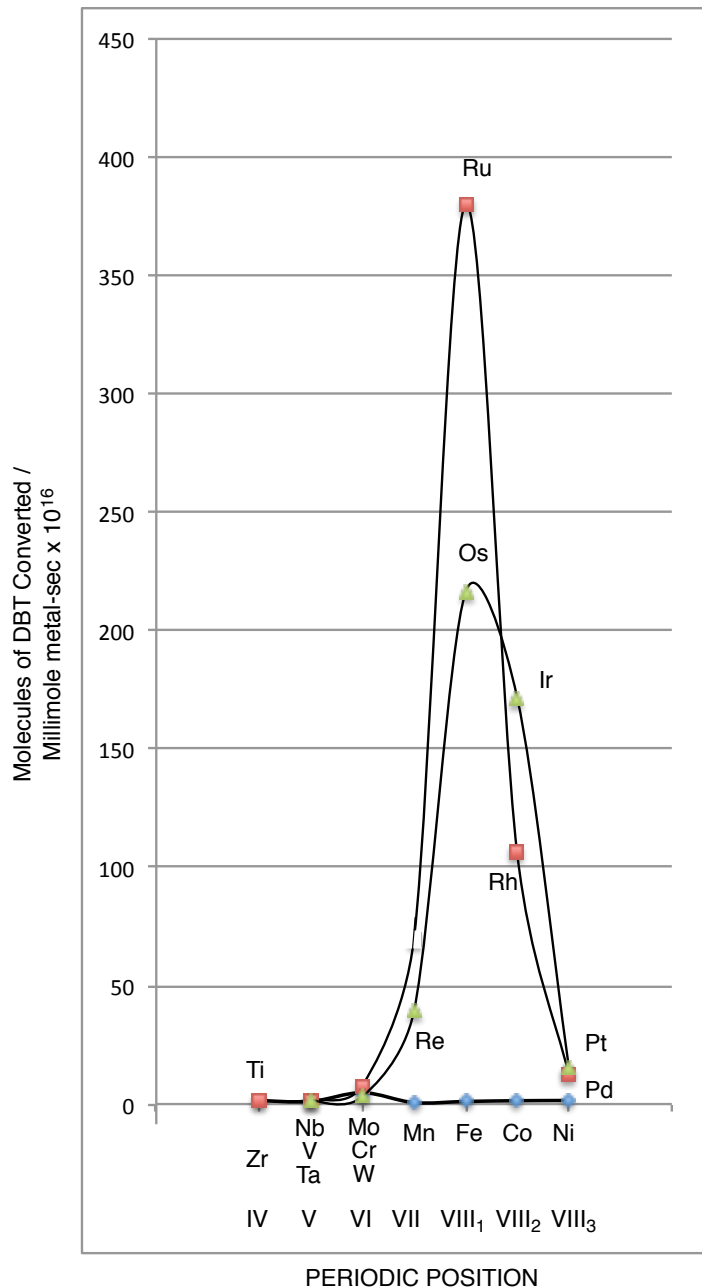


Figure 4.1. Hydrodesulfurization activity of transition metal sulfides as a function of their periodic position.²⁰²

Interestingly, several recent reports on the effects of catalyst dispersion²¹⁴ and nature of the inorganic support^{198,215,216} can be interpreted to suggest that the *active metal sites on industrial CoMoS₂*

catalysts directly involve the promoter ion, typically cobalt, rather than the more abundant molybdenum. These findings supported the Stryker group's hypothesis that high-activity molecular catalysts derived from cheap and naturally abundant first row transition metals, particularly iron, cobalt and nickel, could be developed as models for heterogeneous hydrotreatment catalyst active sites. However, crucial to this endeavor is the identification of an enabling coordination environment that would unleash *precious metal-like* hydrotreatment activity from the base metals.

The tetrametallic Co(I) and Ni(I) clusters **26a** and **26b** provide a nearly ideal platform for the organometallic modeling of heterogeneous HDS catalyst active sites. These hydrocarbon-soluble “*single-site*” clusters possess a tetrametallic core that combines the high coordinative unsaturation (i.e., “surface vacancies”) and polymetallic essence of the heterogeneous catalyst active sites. In addition, these clusters provide the advantage of high solubility in hydrocarbon solvents, rendering them amenable to spectroscopic studies and solution characterization. These structural properties, coupled with the demonstrated activity of these catalysts for reducing unsaturated organic compounds under exceptionally mild conditions, prompted us to study the utility of these clusters for the stoichiometric and catalytic hydrogenolysis of carbon-heteroatom bonds, starting with catalytic hydrodesulfurization.

This chapter begins with a brief survey of the literature on inorganic and organometallic models for the active sites of heterogeneous hydrotreatment catalysts. More importantly, in this chapter is reported the surprisingly general utility of clusters **26a** and **26b** in the activation and hydrogenolysis of carbon-sulfur bonds under mild conditions.

4.2 Organometallic Modeling of Hydrodesulfurization Catalyst Active Sites

The use of transition metal coordination complexes to model HDS active sites has provided many pertinent insights into the most probable mechanisms of hydrodesulfurization. Three classes of homogeneous HDS models have been developed over the past three decades: (1) low-valent metal coordination complexes,^{120,217,218} (2) molecular transition metal hydrides^{34,219,220} and (3) ligand-supported transition metal clusters.²²¹⁻²²³ These modeling strategies have produced a range of mononuclear and polynuclear precious and non-precious metal transition metal complexes that, generally, effect the stoichiometric activation of carbon-sulfur bonds, confirming that many first row metal coordination environments support a C–S bond activation mechanism for metal-mediated HDS.

Precious transition metals have been at the forefront in terms of demonstrated reactivity toward a wide range of catalytic transformations. Interestingly, however, and disappointingly similar to the first row metals,

homogeneous precious metal systems, are, with one notable exception, also limited to stoichiometric desulfurization.^{15,203,224}

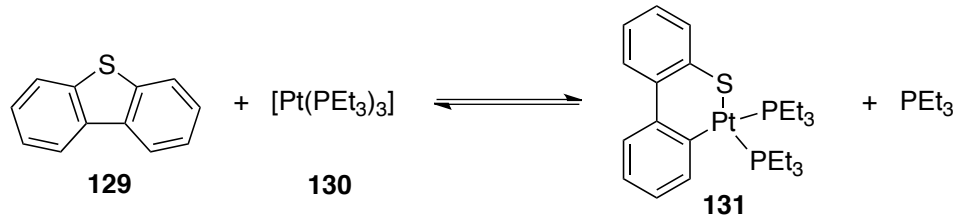
4.2.1 Low-valent, Transition Metal Coordination Complexes as Models for Stoichiometric C-S Bond Activation

Low-valent mononuclear transition metal complexes have been used as model systems for studies of metal-sulfur substrate binding and the mechanism of carbon-sulfur bond scission. These complexes, with characteristically low metal oxidation states, are highly active toward the oxidative cleavage of strong carbon-sulfur bonds in a range of thioethers.

Mononuclear, zero-valent platinum complexes of the formula $[\text{Pt}(\text{PR}_3)_3]$ **130** are capable of stoichiometric carbon-sulfur bond activation of dibenzothiophene (DBT) **129**, the benchmark substrate for deep hydrodesulfurization.^{225,226} The platinum undergoes reversible insertion into a carbon-sulfur bond in **129**, affording the six-membered metallacycle **131** (Equation 4.1). Variations in the phosphorus substituents revealed that the facility of the carbon-sulfur bond scission is a function of the donor/acceptor properties of the ancillary phosphine ligands. Furthermore, it was reported that the addition of alumina to the product induces the reversal of the C–S bond insertion. These results parallel the behavior of platinum active sites on alumina-supported hydrotreatment catalysts. Interestingly, the organometallic intermediate(s) **131** undergo(es) complete

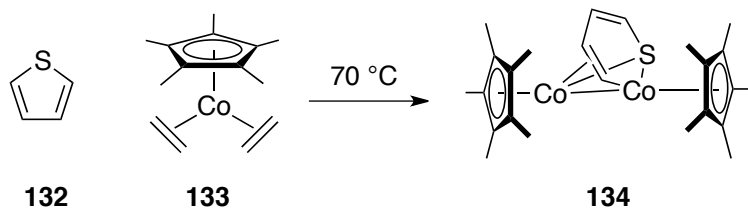
desulfurization to the corresponding hydrocarbons upon treatment with stoichiometric amounts of Group 1 and other main group metal hydride reagents.^{225,226}

Equation 4.1



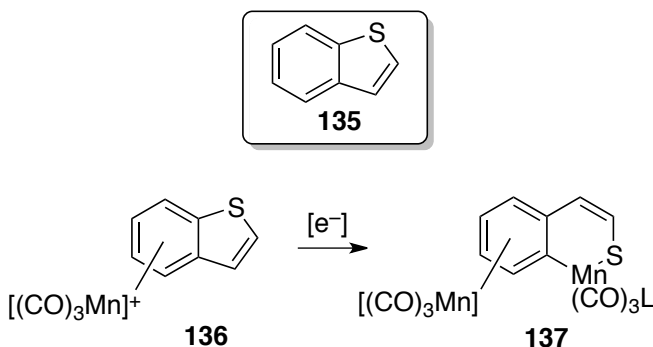
Low-valent base metal complexes have also proved useful in the modeling of organometallic HDS catalysts. W. D. Jones and coworkers reported the substoichiometric cleavage of a carbon-sulfur bond in thiophene **132** using the low-valent cobalt complex **133** under mild thermolysis (Equation 4.2).²²⁷ The reaction produces a mixed-valent, bimetallic insertion product **134**, where the ring-opened thiophene remnant bridges two cobalt centers (Equation 4.2). The bridging thiol shows dynamic binding behavior, alternating between the two cobalt centers and providing insights into how thiophenic substrates and related intermediates bind with polynuclear catalyst surface sites.

Equation 4.2



Other low-valent base metal complexes have been instrumental in the study of metal-mediated C–S bond activation. Benzothiophene **135** binds with manganese carbonyl complexes in an η^6 -fashion to the phenyl ring. Reduction of the manganese-benzothiophene complex **136** with cobaltacene resulted in the insertion of a manganese fragment into a C_{aryl}–S bond **137** (Equation 4.3).^{228,229}

Equation 4.3

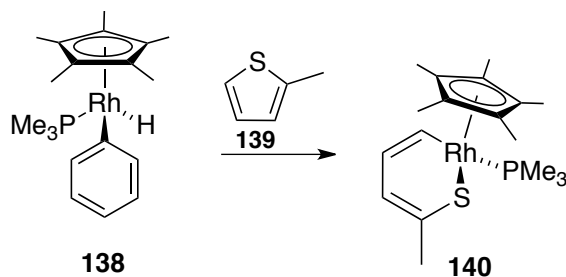


4.2.2 Transition Metal Hydride Complexes

Isolable mononuclear transition metal hydrides are also active for the cleavage of carbon-sulfur bond under thermolytic conditions. Hydrido-

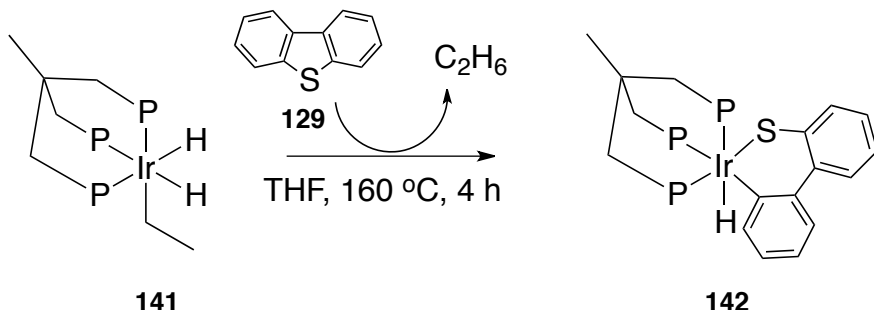
rhodium complex **138** cleaves the more sterically accessible C–S bond in 2-methylthiophene **139** to give the analogous insertion product **140** (Equation 4.4). The formation of this adduct proceeds in a stepwise manner starting with reversible C–H activation followed by oxidative insertion into the carbon-sulfur bond.²³⁰

Equation 4.4

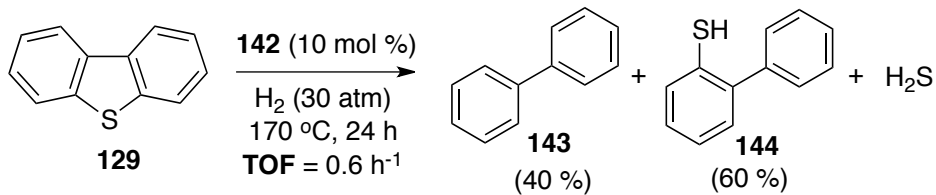


The only previously reported homogeneous HDS catalyst is another precious metal hydride. The group of Bianchini reported the phosphine-supported hydrido-iridium complex **142** (Equation 4.5) and the subsequent reductive cleavage of the C–S bond in DBT **129** (Equation 4.6). High catalyst loading (10 mol%) effected the hydrodesulfurization of **129** under relatively mild process conditions: 30 atm H_2 and 170 °C. The catalysts afford a mixture of biphenyl **143**, 2-phenylthiophenol **144** and hydrogen sulfide gas. The iridium catalyst activates slowly C–S bonds at a rate of 0.6 per hour at this temperature.²³¹ Since the catalysis involves iridium, large-scale application for hydrotreatment is not possible.

Equation 4.5



Equation 4.6



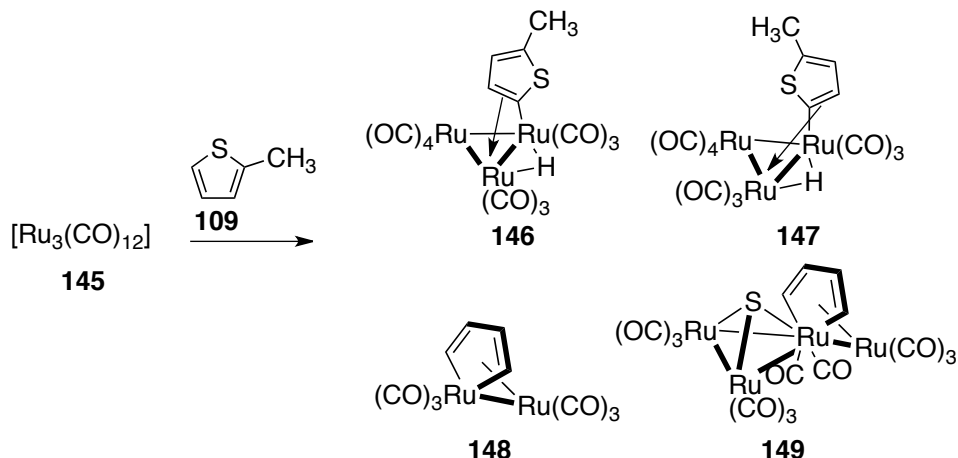
4.2.3 Discrete Polynuclear Transition Metal Coordination Complexes as Models for Stoichiometric C-S Activation

The use of ligand-supported transition metal clusters as soluble surrogates for heterogeneous HDS catalyst active sites has produced the most diverse set of soluble organometallic model systems. This approach combines the advantages of metal–metal cooperativity arising from the polynuclear cluster core with the reactivity of low-valent metal centers and/or metal-hydride functionality.

4.2.3.1 Homopolymetallic Precious Metal Clusters for Stoichiometric C-S Activation

Ruthenium is one of the most extensively studied precious metals for organometallic modeling of HDS catalyst active sites, arising from its established role as a “promoter ion” in a range of solid-state catalysts. Under thermolytic conditions, the low-valent triruthenium carbonyl cluster **145** reacts with 2-methylthiophene **139**, affording a mixture of products from C-H bond activation (**146-147**) and C–S bond insertion (**148-149**, Equation 4.7).¹⁵

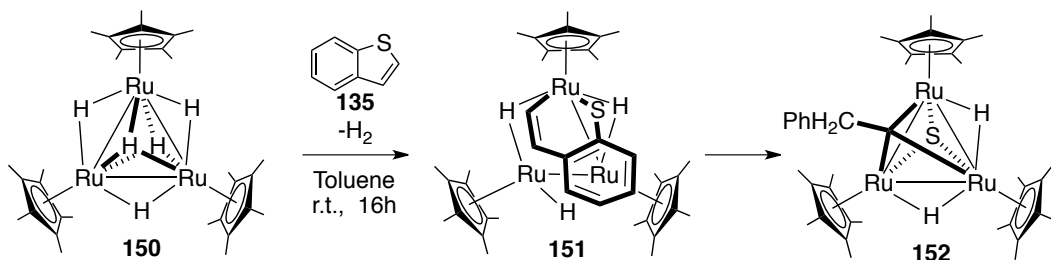
Equation 4.7



Precious metal hydride clusters are also capable of carbon-sulfur bond scission in thiophenic substrates. Suzuki and coworkers developed a discrete trimetallic ruthenium hydride cluster **150** that stoichiometrically cleaves both C–S bonds in benzothiophene **135** at room temperature. The reaction ultimately affords a sulfided triruthenium derivative **152** in good

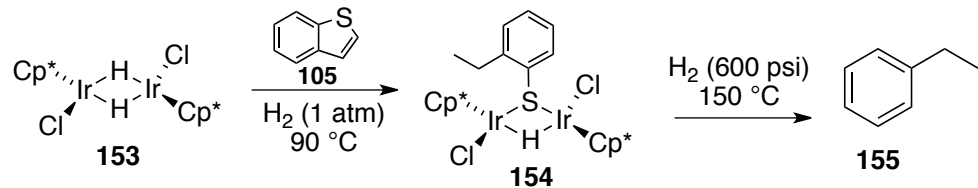
yield (Equation 4.8). Cluster **150** stoichiometrically desulfurizes DBT at a much slower rate (eight days at 110 °C).³⁴

Equation 4.8



In addition, cooperative bimetallic C–S bond activation was demonstrated by Jones and coworkers in the stepwise desulfurization of benzothiophene using the dimeric iridium hydride complex **153** (Equation 4.9). The first C–S activation step results in the formation of a 2-μ₂-ethylthiophenolato-bridged iridium dimer **154**. Thermolysis at 150 °C under high hydrogen pressure (600 psi) resulted in complete desulfurization to ethylbenzene **155**, stoichiometrically.²²⁰

Equation 4.9



The clusters reported by Suzuki and Jones are important demonstrations of the ability of polymetallic assemblies to mediate

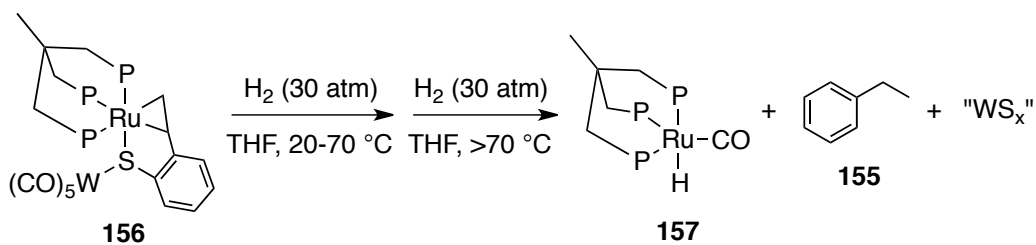
multimetal substrate activation under exceptionally mild conditions – *metal-metal cooperativity*. Furthermore, these model studies have identified various modes of substrate binding on polynuclear active sites.

4.2.3.2 Heteropolymetallic Clusters as Models for Promoted HDS Catalysts

Discrete, heteropolymetallic cluster complexes are ideal models for “promoted” heterogeneous HDS catalysts. This approach has provided a number of platform compounds that can be used to delineate the role of the promoter ions in modern HDS catalysts.

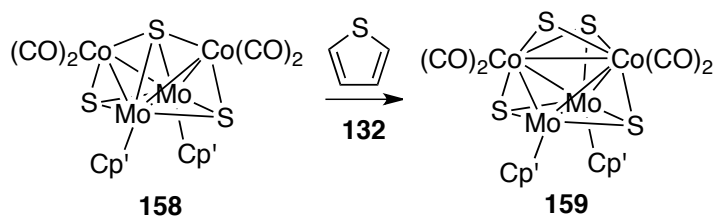
Bianchini and coworkers demonstrated the facile desulfurization of the bimetallic, thiolate-functionalized ruthenium-tungsten complex **156**, where the sulfur center bridges the two metal centers (Equation 4.10). Their findings suggest that the hydrogenolysis probably occurs at the ruthenium center – the promoter ion. Furthermore, assistance from the second component metal (W) was necessary for optimal reactivity, since a more facile desulfurization occurs when the thiolate sulfur bridges the two metal centers.²²¹

Equation 4.10



Curtis and coworkers reported a groundbreaking contribution to the organometallic modeling of CoMoS₂-type heterogeneous HDS catalysts and offered unprecedented mechanistic insight into C–S bond cleavage using the tetrametallic, mixed-valent, cyclopentadienyl-supported cobalt-molybdenum sulfide cluster **158** (Equation 4.11).³⁰ The mechanism of C–S bond scission deduced from this investigation is consistent with cooperative substrate binding and initial sulfur coordination at the cobalt center. This mode of substrate coordination is fluxional, as evidenced by the concerted “walking” of the thiolate ligand between the Co and Mo centers. Homolytic C–S bond activation was proposed to be involved, since the desulfurization of thiophene-type substrates produced the tetrasulfido cobalt-molybdenum cluster **159** together with products logically derived from alkyl and phenyl radicals. These mechanistic insights provide among the most detailed evidence of the role of metal-metal cooperativity in the HDS activity of CoMoS₂-type catalysts. These clusters, however, are not competent for catalytic HDS.

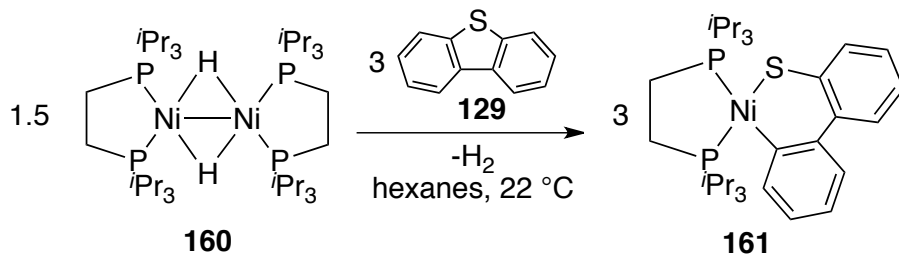
Equation 4.11



4.2.3.3 Base Metal Clusters for Stoichiometric C-S Activation

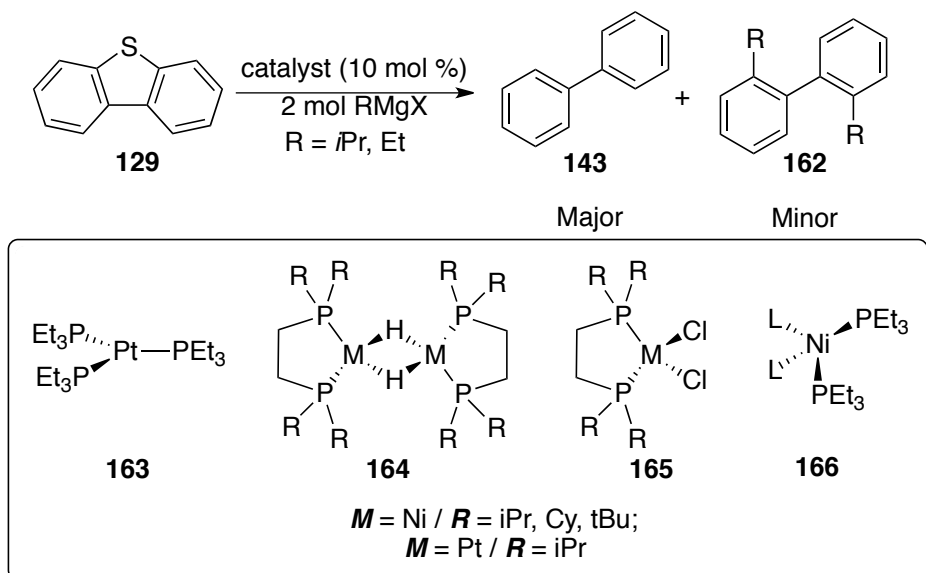
Ligand-supported clusters of first row transition metals have also been used to model the role of cobalt and nickel promoter ions in CoMoS₂/NiWS₂ catalysts. Jones and coworkers reported the stoichiometric desulfurization of thiophene **132**, benzothiophene **135** and dibenzothiophene **129** using the bimetallic phosphine-substituted Ni(I) hydride **160** under mild conditions. The nickel-mediated C–S bond activation produced mixtures of mononuclear complexes, such as **161** in Equation **4.12**. In this report, the active organometallic species was proposed to be a monometallic Ni(0) complex formed upon reductive elimination of hydrogen from **160**.^{9,217,232}

Equation 4.12

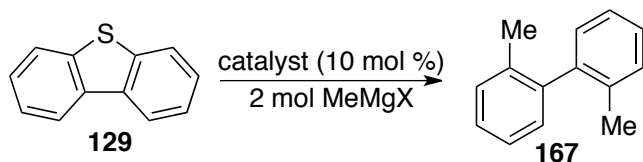


In a recent publication, J. Garcia, *et al.*, reported that clusters of the formula **164**, together with mononuclear Ni and Pt complexes **163-166** (Equation 4.13) are capable of *catalytic deep* desulfurization using alkyl magnesium reagents as stoichiometric reducing agents.²²² Prior to our discoveries, this was the only report of the use first-row transition metal catalysts for desulfurization. This process is *not* hydrodesulfurization per se, since hydrogen is not used as the hydride source. The carbon-sulfur bond activation is believed to proceed via a Kumada-like cross coupling mechanism. This was confirmed by the formation of 2,2'-dimethyldiphenyl **167** from methylmagnesium chloride, a reagent that cannot undergo β -hydride elimination (Equation 4.14).²²²

Equation 4.13

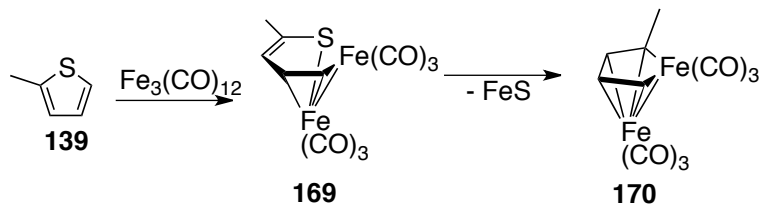


Equation 4.14



Rauchfuss and coworkers explored the utility of cheap, nontoxic iron clusters for hydrodesulfurization.²³³ They reported that the low valent, trimetallic iron carbonyl cluster **168** activates the less hindered C-S bond in 2-methylthiophene to form thiolate complex **169** (Equation 4.15). Subsequent thermolysis resulted in the elimination of colloidal FeS and the formation of the desulfurized bimetallic organometallic species **170**.

Equation 4.15



The literature thus reveals a range of approaches to organometallic modeling of heterogeneous HDS catalyst active sites. Some of these approaches use low-valent metal complexes for the facile oxidative scission of carbon-sulfur bonds, while other strategies involve the use of molecular transition metal hydrides to mediate carbon-sulfur bond hydrogenolysis following C–S bond cleavage. Interestingly, the largest set

of organometallic models has been developed using ligand-supported transition metal clusters, echoing our general strategy for catalyst design.

4.3 Results and Discussion

From the perspective of structure-reactivity relationships, molecular clusters **26a** and **26b** can be considered the simplest irreducible representation of an active metal surface. Clusters of this type can potentially model HDS-active metal surfaces, including Raney cobalt/nickel catalysts.^{208-211,234} The low valent, terminally low-coordinate metal centers, coupled with the high activity demonstrated in the catalytic hydrogenation of alkenes and alkynes,⁷⁷ prompted us to investigate the utility of these homoleptic tetrametallic clusters for the catalytic hydrodesulfurization of a range of thioether substrates under mild conditions. This work represents *the discovery of the first high-activity base metal catalysts for HDS, homogeneous or heterogeneous.*

4.3.1 Deep Hydrodesulfurization

Our investigation of catalytic hydrodesulfurization is mainly focused on the hydrodesulfurization of dibenzothiophene derivatives, coined *deep hydrodesulfurization*. Dibenzothiophene compounds comprise the most hydrotreatment-resistant constituents of heavy petroleum feedstocks.^{15,213} The inherently strong carbon-sulfur bonds in DBT, coupled with the

sterically encumbered thioether center, render it poorly reactive toward traditional HDS catalysts, unless operated under extremely harsh process conditions, effectively near-combustion.

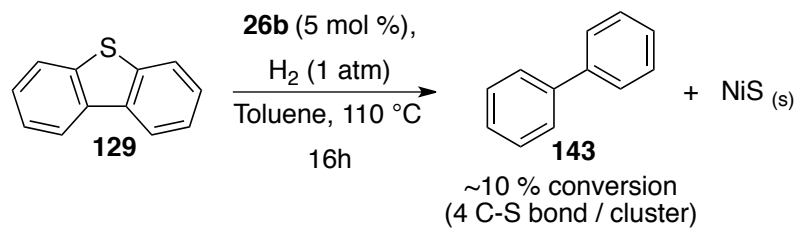
The succeeding sections tackle the strategies we adopted for the optimization of catalytic deep hydrodesulfurization using clusters **26a** and **26b**, ultimately identifying exceptionally mild reaction conditions. Toluene was selected as the reaction medium for most of this work, allowing us to determine the behavior of these catalysts in an inert, purely hydrocarbon environment.

4.3.1.1 *Preliminary HDS Experiments: Stoichiometric Deep Hydrodesulfurization*

Treatment of dibenzothiophene **129** with catalytic Ni(I) cluster **26b** (5 mol %) in toluene at 100 °C under 1 atm H₂ (Equation 4.16) resulted in near stoichiometric desulfurization of DBT to biphenyl **143** (10% conversion). The observed conversion translates to the activation of ~4 C–S bonds per cluster (one C–S bond per nickel center). The dark-green reaction mixture completely decolorized after 16 hours and a black, toluene-insoluble solid, presumably nickel sulfide, was deposited. The non-catalytic nature of this desulfurization is unsurprising, since it is well-established that under such mild conditions, the thermodynamic resting state of HDS catalysts is in the sulfided form. In addition, assuming that

H_2S gas is indeed generated during the course of the reaction, catalyst decomposition resulting from eventual acid-base reaction of the hydrogen sulfide with the basic phosphoranimide nitrogens is also highly probable.

Equation 4.16



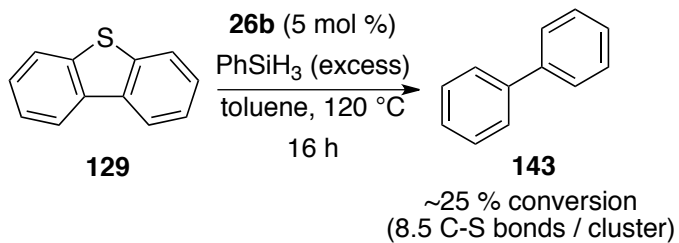
4.3.1.2 Catalytic Deep Hydrodesulfurization

From the non-catalytic desulfurization of DBT and the assumed formation of a bulk metal sulfide, we hypothesized that catalytic hydrodesulfurization could be achieved under conditions where (1) the sulfide anion produced in the reaction can be sequestered from the active metal catalyst, or (2) the H_2S can be irreversibly scavenged from the reaction medium. This goal is most readily accomplished through the addition of stoichiometric strongly basic scavengers and/or electrophilic reagents that react with metal sulfides or thiols to regenerate vacant metal binding sites for substrate ligation.

4.3.1.2.1 Organosilyl Hydride-Promoted Catalytic Deep HDS

Organosilyl hydrides are a promising set of additives that can simultaneously act as the reductant (hydrogen surrogate) and capture sulfide anions and/or thiols to form inert bis-silyl sulfides. This strategy allowed for the first catalytic hydrodesulfurization of DBT **129** under mild conditions. The reaction between DBT and two equivalents of PhSiH₃ in the presence of catalytic **26b** (5 mol%) in toluene at 120 °C resulted in 25% desulfurization to biphenyl (Equation 4.17). This conversion translates to 8.5 C–S bonds activated per cluster (~two C–S bond cleavages per nickel center) over the course of 16 hours, slowly but cleanly producing biphenyl.

Equation 4.17



Under the assumption that catalyst decomposition due to protic impurities/contaminants might be prevented by the presence of base, the hydrodesulfurization of DBT using PhSiH₃ was repeated in the presence of stoichiometric amounts of various basic scavengers. Group 1 *tert*-butoxide salts were initially screened as scavenger candidates (Equation 4.18, Table 1). Dibenzothiophene was treated with 2 equivalents of PhSiH₃,

catalytic quantities of **26b** (1.7 mol%) and two equivalents of the base in THF. An ethereal solvent was used to better solubilize the basic scavenger. No significant increase in the desulfurization rate was observed using LiO^tBu and NaO^tBu as basic scavengers. Interestingly, however, the nickel-catalyzed HDS in the presence of KO^tBu proceeds at a much faster rate (~38 C–S bond cleaved per cluster over 16 h) relative to the basic-scavenger-free experiment. The reaction resulted in an overall conversion of 56%, producing a 1 : 6 mixture of biphenyl **143** and 2-phenylthiophenol **144**, respectively (Entry 3, Table 4.1).

Equation 4.18

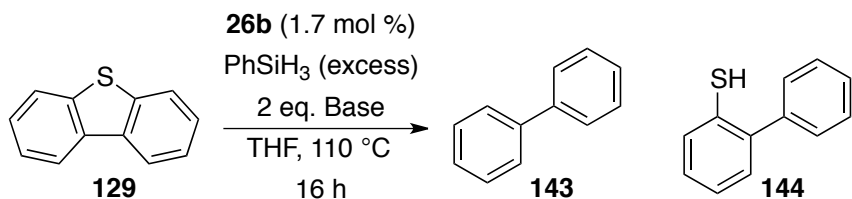
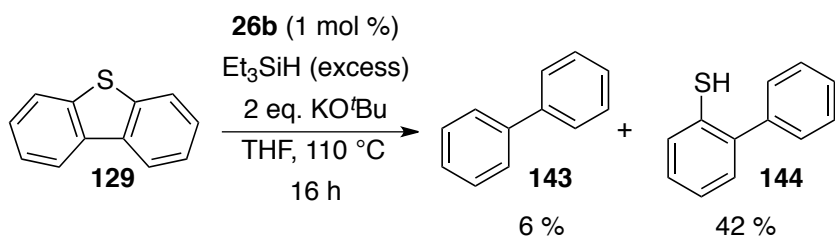


Table 4.1. Basic scavenger screening for silane-promoted HDS of DBT **99**.

Entry	Base	% Conversion	
		113	114
1	LiO ^t Bu	6	0
2	NaO ^t Bu	6	0
3	KO ^t Bu	8	48

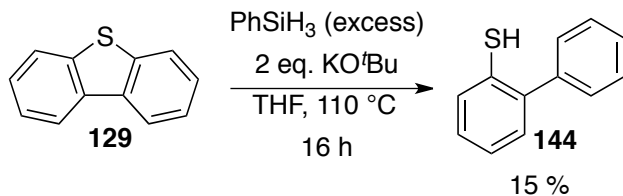
This desulfurization strategy promises to be useful for a wide scope of organosilyl hydrides. Under identical conditions, DBT undergoes a 48% conversion to a 1 : 8 mixture **113** and **114** using instead the unactivated tertiary organosilyl hydride, Et₃SiH (Equation 4.19).

Equation 4.19



Surprisingly, slow hydrogenolysis of the first carbon-sulfur bond in dibenzothiophene to give 2-phenylthiophenol **114** (15%), was also observed in a control experiment where DBT was treated with excess PhSiH₃ and KO^tBu in the absence of the nickel catalyst **26b** (Equation 4.20). This observation, to the best of our knowledge, is the first demonstration of a metal-free hydrogenolysis of sulfide ethers.

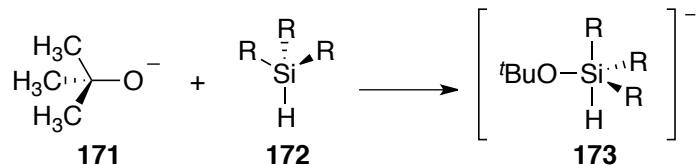
Equation 4.20



Metal-free C–S bond hydrogenolysis is presumably mediated by the hypervalent organosilyl hydride **173**, which forms from the reaction of organosilyl hydride **172** with the *tert*-butoxide ion (Equation 4.21).^{235,236} The addition of KO^tBu to PhSiH₃ in THF results in the abrupt development of a pink color prior to the reduction. The active hypervalent silicon hydride species, however, remains structurally uncharacterized. Interestingly, Grubbs and coworkers recently demonstrated the metal-free

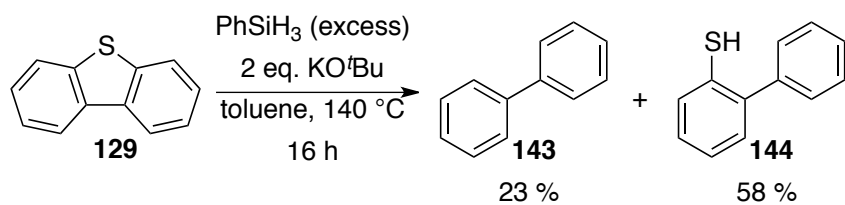
hydrogenolysis of dibenzofuran-type substrates using mixtures of organosilyl hydrides in the presence of potassium salts.²³⁷

Equation 4.21



The observed differences in rate and conversion to C–S cleavage products using different Group 1 *tert*-butoxide salts is attributed to a standard cation effect.²³⁸ The larger cation (K^+) creates a more ionic metal–oxygen bond and a much more strongly nucleophilic alkoxide anion, which in turn leads to faster formation and higher concentration of the active hypervalent silylate compound **173**. Faster conversion is observed at increased temperatures. The metal-free desulfurization of DBT at 140 °C resulted in an 81% conversion to a 1 : 2.5 mixture of **143** and **144**, respectively (Equation 4.22). To this point, however, the scope of thioether substrates and reactive organosilyl hydrides in the metal-free process has not been extensively studied. Interestingly, preliminary experiments show that *metal-free deep hydrodesulfurization* also proceeds at temperatures as low as 90 °C. At this point, insufficient mechanistic information has been obtained to draw a tentative mechanism for the metal-free desulfurization of HDS.

Equation 4.22



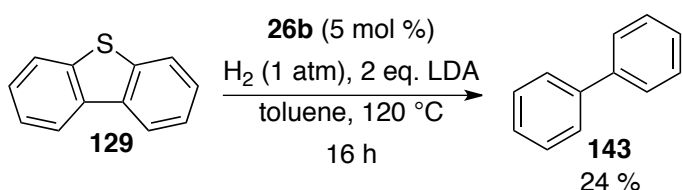
These results confirm the contribution of metal-free C–S bond hydrogenolysis to the silane-promoted desulfurization of DBT in the presence of stoichiometric KO^tBu. However, under otherwise identical reaction conditions, the desulfurization is significantly faster in experiments where catalyst **26b** is present than in the metal-free desulfurization (Entry 3 in Table 4.1 versus Equation 4.20). This suggests an active role of catalyst **26b** in the C–S bond activation catalysis under hydrosilylation conditions. Alternatively, the faster rate of C–S bond hydrogenolysis in the presence of catalytic quantities of **26b** could be due to the ability of base metals to initiate radical chain processes.²³⁹

4.3.1.2.2 Base-Promoted Catalytic Deep HDS

Concomitant with the discovery and optimization of the organosilane-promoted HDS, the use of strongly basic H₂S scavengers was also explored in hydrodesulfurization reactions using hydrogen as the reductant. Strong, bulky organic bases were initially used under the assumption that the steric bulk would inhibit or prevent competitive binding with the catalyst active site. The base-promoted catalytic HDS of **129** was

initially achieved using stoichiometric amounts of the soluble hindered base LDA (Equation 4.23). The reaction of DBT in the presence of 3 equivalents of LDA in toluene at 120 °C and under 1 atm H₂ resulted in the slow formation of biphenyl **143** (24% conversion). The yield of biphenyl corresponds to a turnover number of 8 C–S bonds cleaved per cluster (two C–S bonds per Ni center) over 16 hours.

Equation 4.23



The slow conversion in the presence of LDA suggests that diisopropylamine may not be bulky enough to inhibit competitive metal binding. In order to enhance the rates of the base-promoted HDS of **129**, we reasoned that strong but *non-coordinating* inorganic bases should be used. Groups 1 and 2 metal hydrides comprise an ideal set of H₂S scavengers, reacting irreversibly with H₂S or the putative thiol intermediate to produce H₂ and the corresponding sulfide salt. More importantly, alkali metal hydrides are insoluble in normal reaction media, avoiding high concentrations of soluble, competitively coordinating nucleophilic bases. A toluene-solution of DBT was thus treated with a catalytic amount of **26b** (1.7 mol%) and two equivalents of basic scavenger (Table 4.2, Equation 4.24) at 110 °C under 1 atm H₂. Though catalytic desulfurization was

observed in experiments using both NaH and KH as scavengers (Entries 1-2, Table 4.2), much faster desulfurization was observed in the presence of KH. The disparity in the rates of desulfurization is presumably due to the relative thermodynamic stability of NaH and the greater ionic character of the potassium hydride bond; stability of alkali metal hydrides decreases with increasing size of the metal cation; hence, a more facile reaction of hydride ions with acidic protons is expected using KH rather than NaH.²⁴⁰ The observed difference in rates of desulfurization parallels the observed “potassium ion effect” on supported CoMoS₂ catalysts.^{240b} The enhancement of desulfurization activity is being attributed to the ability of potassium to donate electrons to transition metal active sites thus, enhancing the latter’s π -backbonding abilities.^{240b}

Equation 4.24

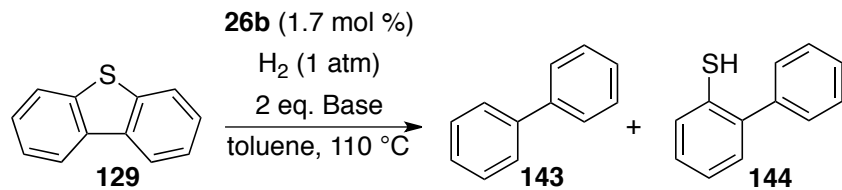
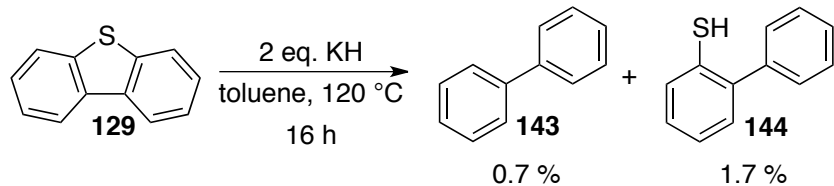


Table 4.2. Basic scavenger screening for Hydrogen-Promoted HDS of DBT.

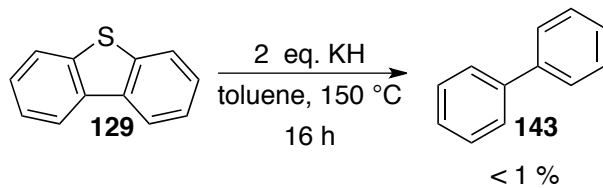
Entry	Base	% Conversion	
		143	144
1	NaH	13	0
2	KH	28	18
3	CaH ₂	stoichiometric	0

In the absence of H₂ and the nickel catalyst **26b**, KH induces only minimal conversion to hydrogenolysis products **143** (0.7 %) and **144** (1.7 %) under these reaction conditions (Equation 4.25). The formation of trace amounts of these reduction products is attributed to trace amounts of elemental potassium in KH. Potassium hydride purification was not necessary during the course of this investigation since the batch of KH used in the studies presented (*vide infra*) did not effect substantial dibenzothiophene desulfurization even under harsher reaction conditions: minimal biphenyl production (<1%) was observed at 150 °C (Equation 4.26). Nonetheless, others in the group have developed efficient KH purification strategies for KH batches with significant levels of elemental potassium. This procedure will be reported in due course.

Equation 4.25



Equation 4.26



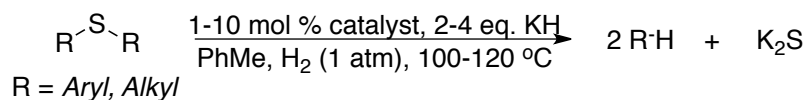
The significantly higher turnover number in the KH-promoted deep HDS encouraged us to explore the generality of the catalysis for a

representative range of sulfur functionality and substitution found in heavy petroleum. Furthermore, the specific role of KH in catalytic desulfurization was also further explored.

4.3.2 Substrate Scope of HDS Catalysis under Mild Conditions

The succeeding sections present the substrate scope for the nickel- and cobalt-catalyzed hydrodesulfurization of a range of sulfide ethers. The results were obtained from experiments generally represented by Equation 4.27. In these experiments, a toluene solution of each organosulfur substrate was treated with a catalytic quantity of **26a/26b** (0.8–10 mol%, depending on rate) and 2–4 equivalents of standard grade KH under one atmosphere of hydrogen at temperatures ranging from 100–120 °C.

Equation 4.27



4.3.2.1 Deep Hydrodesulfurization

Parallel experiments were conducted to compare the catalytic activity of the cobalt(I) and nickel(I) catalysts for the hydrodesulfurization of DBT at 120 °C and under 1 atm H₂ (Equation 4.28, Table 4.3). The rate of the cobalt-catalyzed C–S bond hydrogenolysis (**TON** = 28 DBT; **TOF** =

3/h, Entry 1) was almost two times faster than corresponding nickel-catalyzed desulfurization (**TON** = 16 DBT; **TOF** = 1.9/h, Entry 2). The product distribution observed in these experiments provides useful insights into the observed difference in hydrodesulfurization activity of the cobalt and nickel catalysts. Over the course of 8.5 hours, the nickel-catalyzed hydrodesulfurization resulted in a 37% conversion of DBT into a 3 : 1 mixture of biphenyl **143** and 2-phenylthiophenol **144**. On the other hand, cobalt-catalyzed reaction afforded a 74% conversion to a mixture of products in which the partially desulfurized thiol **144** dominates (**144** : **143** = 2 : 1). The higher ratio of biphenyl to thiol in the nickel-catalyzed desulfurization suggests that the slower nickel cluster **26b** nonetheless has a higher propensity to activate the second carbon–sulfur bond in DBT over cobalt catalyst **26a**. The observed rates do not reflect differences in the relative strengths of the metal-sulfide bonds: faster HDS rates are expected from the nickel catalyst since Co=S bonds are stronger than Ni=S bonds.^{202,205,241}

Equation 4.28

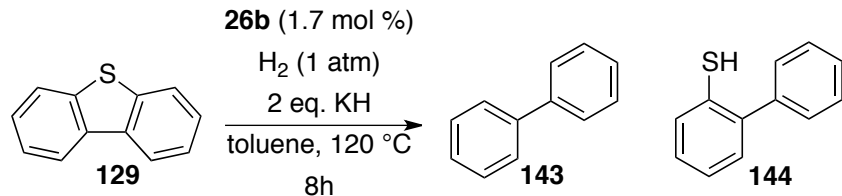
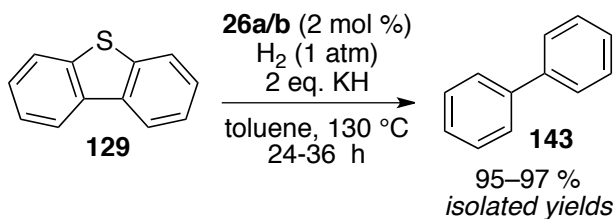


Table 4.3. HDS of DBT.

Catalyst	% Conversion		TON (DBT/cat)	TOF (DBT/cat/hr)
	143	144		
26a	21	52	28	3.3
26b	23	9	16	1.9

The HDS rates observed under these conditions are, however, sluggish relative to ideal catalyst rates for industrial hydrotreatment. The strongly basic scavenger inhibits the final desulfurization step due to the deprotonation of the thiol and formation of an insoluble potassium thiolate salt, inhibiting the hydrogenolysis of the remaining C–S bond. This assumption is confirmed by the observation of precipitate formation in concentrated reaction mixtures using liquid hydrocarbons as solvents. Two strategies were adopted to achieve faster hydrodesulfurization rates. In the first approach, experiments were conducted at high dilution and increased temperatures, as well as and prolonged reaction periods. Catalytic hydrodesulfurization of DBT conducted at higher temperatures (>130 °C) over a longer time (36–48 hours) results in quantitative hydrodesulfurization, giving *isolated* yields of biphenyl ranging from 95 to 97% (e.g., Equation 4.29). This highlights the efficiency of the desulfurization process.

Equation 4.29



The second approach to solving the rate inhibition adopts the use of polar solvents, in which the intermediate potassium thiolate salt is expected to be more soluble, particularly at elevated temperatures. HDS experiments conducted in THF rather than toluene result in quantitative conversion of DBT into mixtures of biphenyl **143** and 2-phenylthiophenol **144**, without visible precipitate formation during the course of the catalysis (Table 4.4). The switch to a polar solvent, THF, increases the rate of HDS by a factor of ten, despite the lower reaction temperature (110 °C) and lower catalyst loading (0.1 mol%, Equation 4.30). At this point, there is insufficient experimental data to determine the origin of this *solvent effect*. The profound increase in HDS rates in THF could also arise from factors other than enhanced solubility. Cluster dissociation into *lower nuclearity active species* could occur competitively in polar coordinating solvents, especially under *forcing reaction conditions*.²⁴² Dissociation would result in an increase in the effective concentration of the active catalyst; hence, faster turnover. Furthermore, polar solvents may favor contributions from a single-electron transfer mechanism for the activation of C–S bonds,²⁴³ unsurprising for both Co(I) and Ni(I) clusters since the catalysts exhibit metalloradical character in solution. Systematic kinetic investigation is thus

needed to understand the origin of the observed *solvent effects*. The investigation of substrate scope was conducted using toluene as solvent, providing conveniently slow rates for the comparison of catalyst turnover frequencies for reactions run to partial conversion.

Equation 4.30

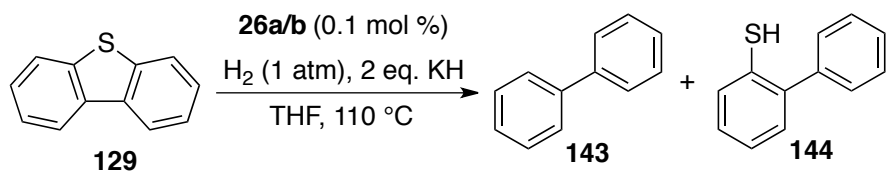


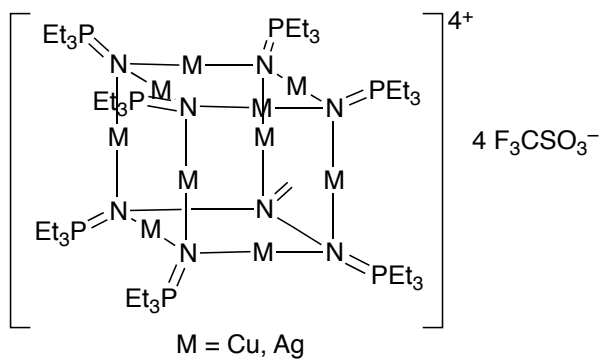
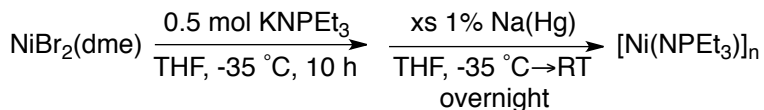
Table 4.4. HDS of DBT in THF.

Catalyst	Time (h)	% Conversion		TON	TOF
		143	144		
26a	17	39	61	703	41
26b	20	68	32	595	30

To validate that the catalyst design produces a family of high activity catalysts for reductive organic transformations, nickel(I) catalysts stabilized by smaller trialkylphosphoranimide ligands were synthesized (Equation 4.31). The soluble nickel(II) precursor (dme) NiBr_2 was treated with substoichiometric quantities of KNPEt₃ in THF at -35 °C and stirred for 10 hours. The crude reaction mixture was then treated with excess 1% (w/w) Na/Hg amalgam at room temperature. The reduction produced a brownish-green, pentane-soluble powder that does not form X-ray quality crystals under standard conditions. Such species, supported by sterically small triethylphosphoranimide ligands, are expected to adopt a three-dimensional cluster structure with higher cluster nuclearity. This

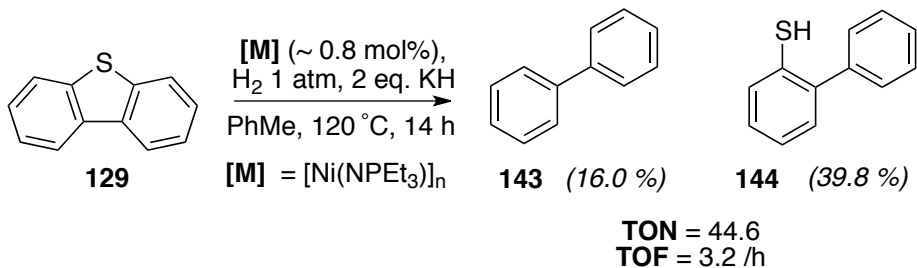
assumption is based on Dehnicke and coworkers' report of octametallic heterocubane clusters **175** supported by triethylphosphoranimide ligands.²⁴⁴ The purported triethylphosphoranimidonickel(I) complex did not pass elemental analysis; however, catalytic quantities of this presumably impure species hydrodesulfurizes dibenzothiophene to a mixture of **143** (16 %) and **144** (40%) in toluene over 14 hours at 120 °C under one atmosphere of hydrogen (Equation 4.32).

Equation 4.31



175

Equation 4.32



The use of sterically smaller phosphoranimide ligands clearly results in faster HDS turnover. The approximate C–S bond hydrogenolysis rate observed using the uncharacterized triethylphosphoranimidonickel catalyst (3.2/h) was almost two times faster than the rate observed using the tri-*tert*-butylphosphoranimidonickel(I) catalyst (1.9/h).

4.3.2.2 Ultra-deep Hydrodesulfurization

Under similarly mild conditions, both catalysts effect the desulfurization of 4,6-diethyldibenzothiophene **176** into 3,3'-diethylbiphenyl **177**, accompanied by the incompletely converted thiol **178**, albeit at significantly slower rate (Equation 4.33, Table 4.5). Cobalt catalyst **26a** hydrodesulfurizes **176** into a 3.5 : 1 mixture of **177** and **178**, respectively. The rate observed ($\text{TOF} = 0.3/\text{h}$) is comparable to the rate of the nickel-catalyzed hydrodesulfurization ($\text{TOF} = 0.4/\text{h}$), for which a higher catalyst loading was employed. This is the first direct demonstration of catalytic hydrodesulfurization of the sterically-encumbered thiophene core in *o,o*-dialkyldibenzothiophenes – *ultra-deep hydrodesulfurization*. The reaction gave small quantities of the thiol product. This could be suggestive of the possible concomitant activation of both C–S bonds in **176** by a polymetallic active site.

Equation 4.33

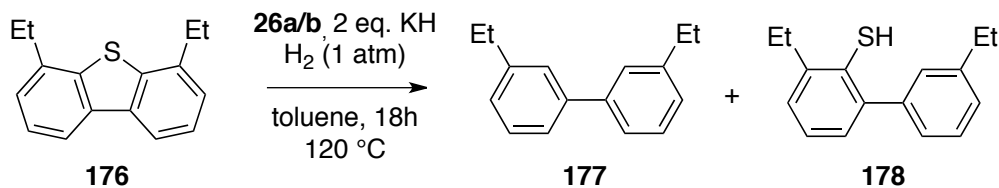


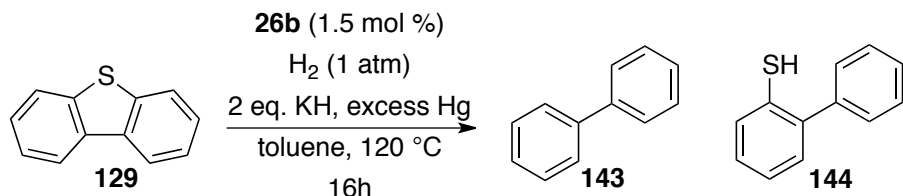
Table 4.5. HDS of 4,6-diethyldibenzothiophene **176**.

Catalyst	Loading (mol %)	% Conversion		TON	TOF
		177	178	(mol 144/mol cat)	(TON/time)
26a	4.9	21	6	6	0.3
26b	9.4	44	0.2	7	0.4

No aromatic hydrogenation products were detected in the product mixture obtained from catalytic hydrodesulfurization of dibenzothiophene and 4,6-diethyldibenzothiophene **176**, even under forcing reaction conditions (150 °C, 500 psi H₂). These observations strongly suggest that the active hydrodesulfurization catalyst is homogeneous, as both colloidal metals are known to hydrogenate aromatic rings.^{131-135,197} In addition, the homogeneous nature of the active catalyst is supported by the unattenuated rate of nickel-catalyzed hydrodesulfurization of **129** when conducted in the presence of excess metallic mercury; a TOF of 1.6 C–S bonds per hour was observed with or without elemental Hg (Equation 4.34). The possibility that bulk metal sulfides are the active catalysts under the given conditions was also explored: under otherwise identical conditions, commercial bulk Ni₃S₂ fails to catalyze the hydrodesulfurization

of dibenzothiophene, suggesting that classic metal sulfides cannot be responsible for the catalysis observed with **26a** and **26b**.

Equation 4.34



4.3.2.3 Aryl Sulfide HDS

Catalysts **26a** and **26b** also activate the C–S bonds in simple diaryl sulfides. Under identical conditions, cobalt catalyst **26b** effected the hydrogenolysis of diphenylsulfide **179** into a 1 : 1 mixture of benzene **180** and thiophenol **181** at a rate of 0.7/h (Entry 2, Table 4.5; Equation 4.35). By comparison, the corresponding cobalt-catalyzed desulfurization was conducted over a prolonged period (60 h, 120 °C), resulting in quantitative hydrogenolysis into a 6 : 4 mixture of **180** and **181** (Entry 1, Table 4.6). The faster rate (**TOF** = 2.1/h) and the product distribution observed in the cobalt-catalyzed reaction suggest that the potassium thiophenolate ion also undergoes desulfurization, albeit at a significantly slower rate.

Equation 4.35

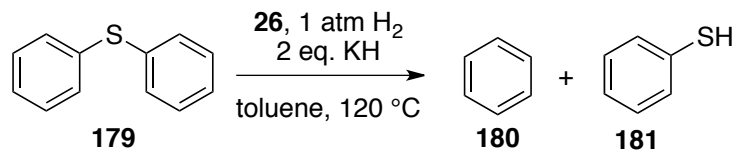
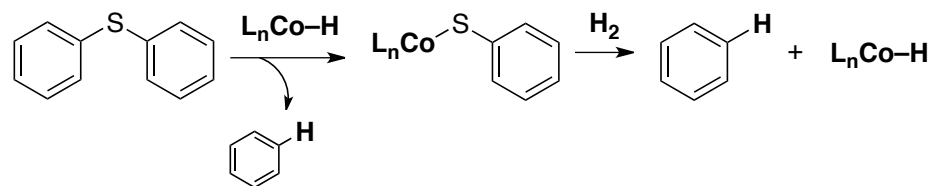


Table 4.6. HDS of Diphenylsulfide.

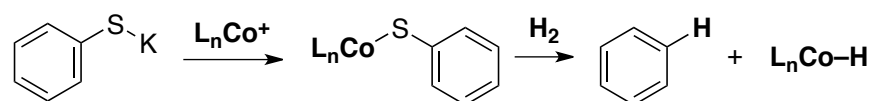
Catalyst	Loading (mol %)	Time (h)	% Conversion		TON	TOF
			180	181	(mol 179 / mol cat)	(TON/time)
26a	0.8	20	61	39	125	2.1
26b	1.9	60	24	23	13	0.7

The rates calculated in these experiments are obscured by concomitant pathways that produce benzene. The higher levels of benzene in the cobalt-catalyzed experiment could be a result of the desulfurization of a cobalt-bound thiophenolate ion (Equation 4.36) or the hydrogenolysis of a potassium thiophenolate salts (Equation 4.37).

Equation 4.36



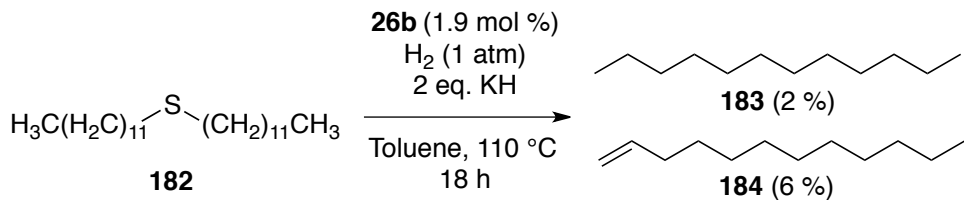
Equation 4.37



4.3.2.4 Alkyl Sulfide HDS

Interestingly, both catalysts exhibit higher selectivity for the stronger C-S bond in diaryl sulfides over the weaker C-S bond in dialkyl sulfides. Dodecylsulfide **182** undergoes only stoichiometric desulfurization, producing dodecane **183** and 1-dodecene **184** at 110 °C using 1.9 mol % of **26b** (Equation 4.38). Desulfurization reagents reportedly more selective toward diarylsulfide activation over dialkylsulfides are generally proposed to proceed via a single electron transfer mechanism.²⁴⁵ The low reactivity of dialkyl thioethers is attributed to a less favorable formation of an alkyl radical intermediate. It would not be surprising if the nickel-catalyzed desulfurization were to proceed via a radical mechanism since each metal center in **26b** is effectively a one-electron paramagnet. The conformational fluxionality of the thioether core in dodecyl sulfide, potentially lowering the probability of productive sulfur coordination to a metal center, is also suspected responsible for the observed low reactivity. Contrary to aryl sulfides, dialkyl sulfides are incapable of π-assisted substrate precoordination. Mechanistic investigations to rule out these possible mechanisms are thus required.

Equation 4.38

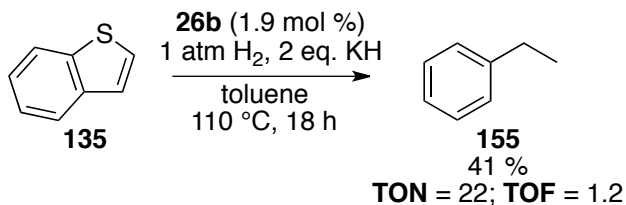


4.3.2.5 Benzothiophene and Thiophene Substrates

The catalytic hydrodesulfurization of simpler thiophenic substrates was also explored. Benzothiophene **135** and the trisubstituted thiophene **185** each undergo catalytic hydrodesulfurization under mild conditions (Equations **4.39-4.40**). Surprisingly, desulfurization of the more reactive substrates proceed at rates comparable to or more slowly than that of DBT itself.

Benzothiophene **135** undergoes nickel-catalyzed desulfurization and alkene hydrogenation to give ethylbenzene **155** at 110 °C under 1 atm H₂ for 18 hours (**TOF** = 1.2/h, Equation **4.39**). This rate is slower than the observed rate of the corresponding nickel-catalyzed DBT desulfurization (**TOF** = 1.9/h, Entry **2**, Table **4.3**).

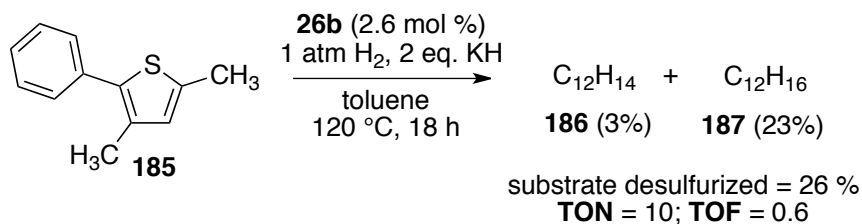
Equation 4.39



The reduction of 2-phenyl-3,5-dimethylthiophene **185** under the conditions described in Equation **4.32** also proceeds slowly, giving a mixture of two unsaturated hydrocarbons with molecular weights C₁₂H₁₄ **186** and C₁₂H₁₆ **187** (Equation **4.40**). The observed 26% substrate conversion translates to a desulfurization rate of 0.6/h at this temperature.

The surprising persistence of unsaturation in the product is indicative of catalyst selectivity for direct C–S bond scission. This selectivity for hydrodesulfurization of thiophene-type substrates is unprecedented since organometallic models generally hydrogenate thiophene carbon–carbon double bonds prior to C–S bond scission.

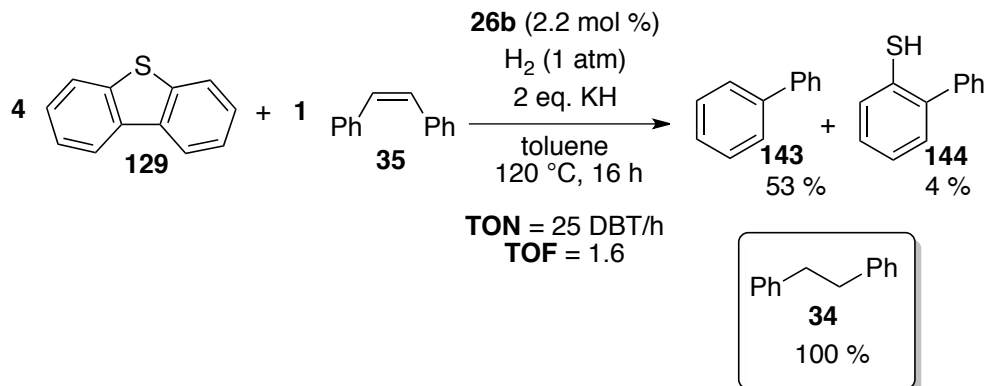
Equation 4.40



The slower rate of C–S bond hydrogenolysis observed for simpler thiophenes may be attributed to the competitive hydrogenation of the carbon–carbon double bonds in the thiophene core of each substrate. With some HDS catalysts, thiophenic substrates are known to undergo C=C double bond hydrogenation prior to C–S bond scission.^{15,203} *In lieu*, a control experiment was conducted to determine the effects of substrates that competitively hydrogenate during the hydrodesulfurization of dibenzothiophene **129**. The hydrodesulfurization proceeds more slowly in the presence of a substoichiometric quantity of *cis*-stilbene **35** (25 mol%), an alkene that is both hydrogenated and isomerized by these catalysts (**TOF** = 1.6/h, Equation 4.41). This rate is 16% slower than rate of the corresponding alkene-free hydrodesulfurization of **129** (1.9/h) under

otherwise identical conditions. During this reduction, alkene **35** is completely converted to 1,2-diphenylethane **34**.

Equation 4.41



The catalysts were further challenged by the presence of nitrogen-containing inhibitors. Dibenzothiophene hydrodesulfurization experiments were conducted in the presence of 20 mol% of the potential nitrogen inhibitors *N*-methylcarbazole **188** and bipyridine **189** (Equation 4.42, Table 4.7). In the presence of *N*-methylcarbazole **188**, a weakly basic nitrogen compound, a 5% inhibition in the catalytic HDS rate was observed. Surprisingly, although the presence of bipyridine **189** was expected to completely poison the catalyst, but effected only a 30% inhibition in the HDS rate, with no obvious sign of irreversible catalyst poisoning. In both cases, catalytic conversion is still observed, albeit over more prolonged reaction times. This demonstrates the robustness of the Ni(I) catalyst to deactivation by nitrogen-containing substrates. These observations also

encouraged us to explore mild catalytic hydrodenitrogenation (HDN). The activity of these clusters for catalytic C–N bond hydrogenolysis is presented in Chapter 6.

Equation 4.42

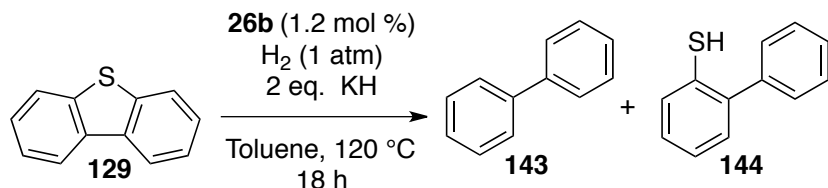


Table 4.7. HDS of DBT 129 in the presence of *N*-inhibitors.

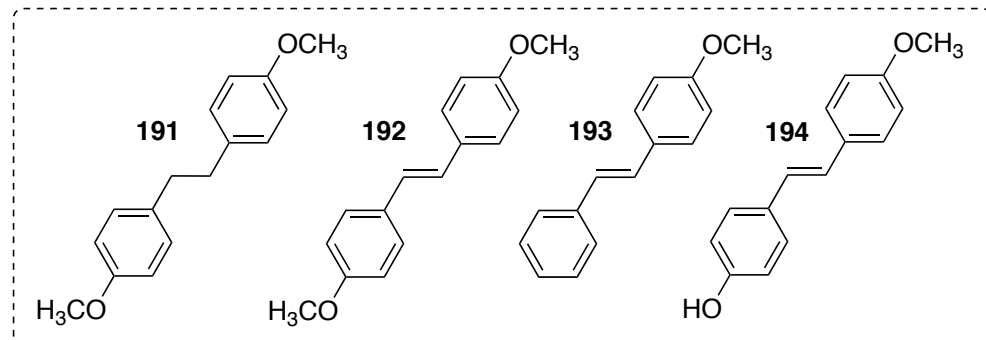
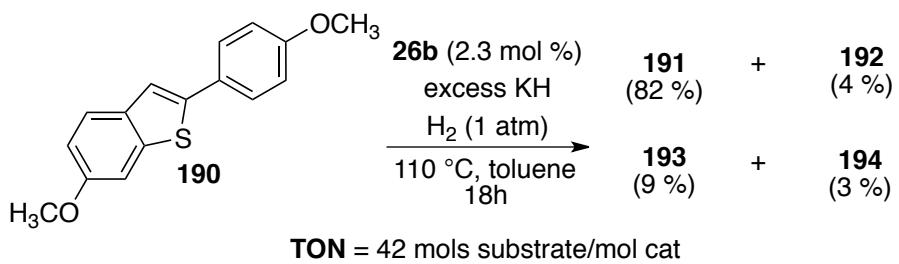
Entry	Additive	% Conversion		TON (mol 129 / mol cat)	TOF (TON/time)
		143	144		
1	No Additive	20	26	27	1.5
2	CH_3 188 (20 mol %)	17	22	23	1.3
3	 189 (20 mol %)	13	37	21	1.1

4.3.3. Catalyst Chemoselectivity: C–S versus C–O Bond Activation

The chemoselectivity for competitive hydrogenolysis of C–O and C–S bonds was evaluated using 6-methoxy-2-(4-methoxyphenyl)-1-benzothiophene 190 as the substrate (Equation 4.43). This ether-

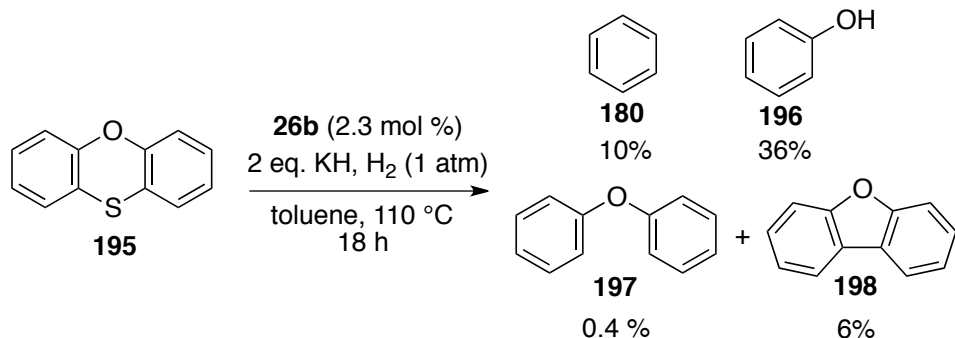
functionalized benzothiophene derivative undergoes quantitative hydrodesulfurization in the presence of 2.3 mol% **26b** in toluene at 110 °C under 1 atm H₂. The reaction affords a mixture of desulfurized products **191-194** comprised mainly of 1,2-bis(4-methoxyphenyl)ethane **191** (83%) and 1,2-bis(4-methoxyphenyl)ethane **192** (4%). Unexpectedly however, substantial minor products from C–O bond hydrogenolysis were also detected: 1-phenyl-2-(4-methoxyphenyl)ethane **193** (9%) from aryl C–O bond scission, and 1-(4-hydroxyphenyl)-2-(4-methoxyphenyl)ethane **194** (3%) from alkyl C–O cleavage. The product distribution clearly demonstrates the selectivity of the catalyst for extrusion of the weaker C–S bond over the C–O linkages.

Equation 4.43



Selectivity for C–S bonds was also observed in the hydrogenolysis of phenoxathiin **195** using catalyst **26b** (Equation 4.44). Relative to **190**, this diarylsulfide undergoes slow desulfurization (56% conversion), giving a mixture of C–S and C–O hydrogenolysis products: phenol **196** (36%), benzene **180** (10%), dibenzofuran **198** (6%), and diphenyl ether **197** (0.4%).

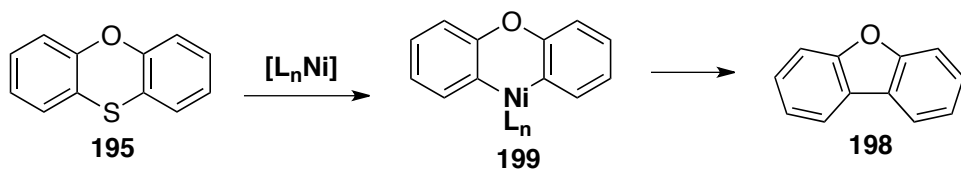
Equation 4.44



The unexpected formation of dibenzofuran **198** can proceed via at least two reasonable mechanisms. The first involves double oxidative C–S bond scission, affording a biaryl-substituted organometallic intermediate **199**. This then undergoes reductive elimination to give dibenzofuran **198** (Equation 4.45). This pathway, purportedly proceeding via single-electron activation of C–S bonds, was first demonstrated by Eisch and coworkers^{245,246} using low-valent, mononuclear nickel complexes capable of substoichiometric desulfurization of DBT and phenoxathiin **195**. In our case, the homolytic/non-hydrogenolytic activation of C–S bonds is supported by the tendency of the nickel catalyst **26b** to mediate radical-

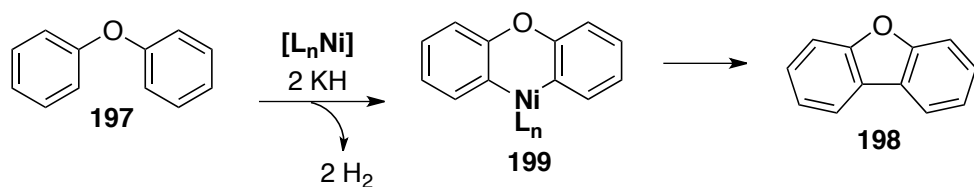
type transformations (Section 3.7, Chapter 3) and the results of control experiments showing that the tetrametallic Ni(I) cluster stoichiometrically activates C–S bonds in DBT in the absence of H₂ at temperatures as low as 60 °C.

Equation 4.45



The second, equally probable mechanism, involves the KH–induced directed metallation at the positions *ortho* to the sulfur, followed by transmetallation of the carbanionic aryl fragments to an active nickel center to form dialkyl complex **199** (Equation 4.46). The biaryl groups in **199** then reductively eliminate to liberate dibenzofuran **198**. This proposed mechanism is based on precedents demonstrating that at high temperatures, KH indeed mediates aryl deprotonation at positions *ortho* to heteroatom substituents.²⁴⁷ At this point, however, there is insufficient mechanistic information to discriminate between the two proposed mechanisms or determine the nuclearity of the active metal species **199**.

Equation 4.46



The catalytic reduction of the oxygenated substrates **190** and **195** demonstrates that the hydrogenolysis of diarylethers is surprisingly facile, a key reaction for the potential catalytic processing of lignin. The optimization of catalysts **26a** and **26b** for ether hydrogenolysis and hydrodeoxygenation under mild conditions will be discussed in Chapter **5**.²⁶

4.4 Mechanism of Catalytic HDS

The absence of aromatic hydrogenation products supports an HDS mechanism that involves direct scission of the strong $C_{\text{aryl}}-\text{S}$ bonds during the catalytic cycle. Various mechanistic pathways have been proposed for homogeneous catalytic hydrodesulfurization, depending on the class of substrates. Results of mechanistic investigations using heterogeneous HDS catalysts suggest that under high H_2 pressure, dibenzothiophene undergoes aromatic hydrogenation *prior to* C–S bond scission. On the other hand, Bianchini's homogeneous iridium catalyst effected sulfur-directed aryl C–H bond activation prior to the “directed” intramolecular C–S bond cleavage.²³¹ Interestingly, the desulfurization of 4,6-diethyl-DBT **176**

catalyzed by **26a** and **26b** is not consistent with the mechanism of the iridium-catalyzed HDS; no evidence for metal-mediated C-H bond activation has been obtained, although this role could in principle be filled by the KH used as scavenger. With these considerations, a highly tentative mechanism shown in Figure 4.2 is proposed.

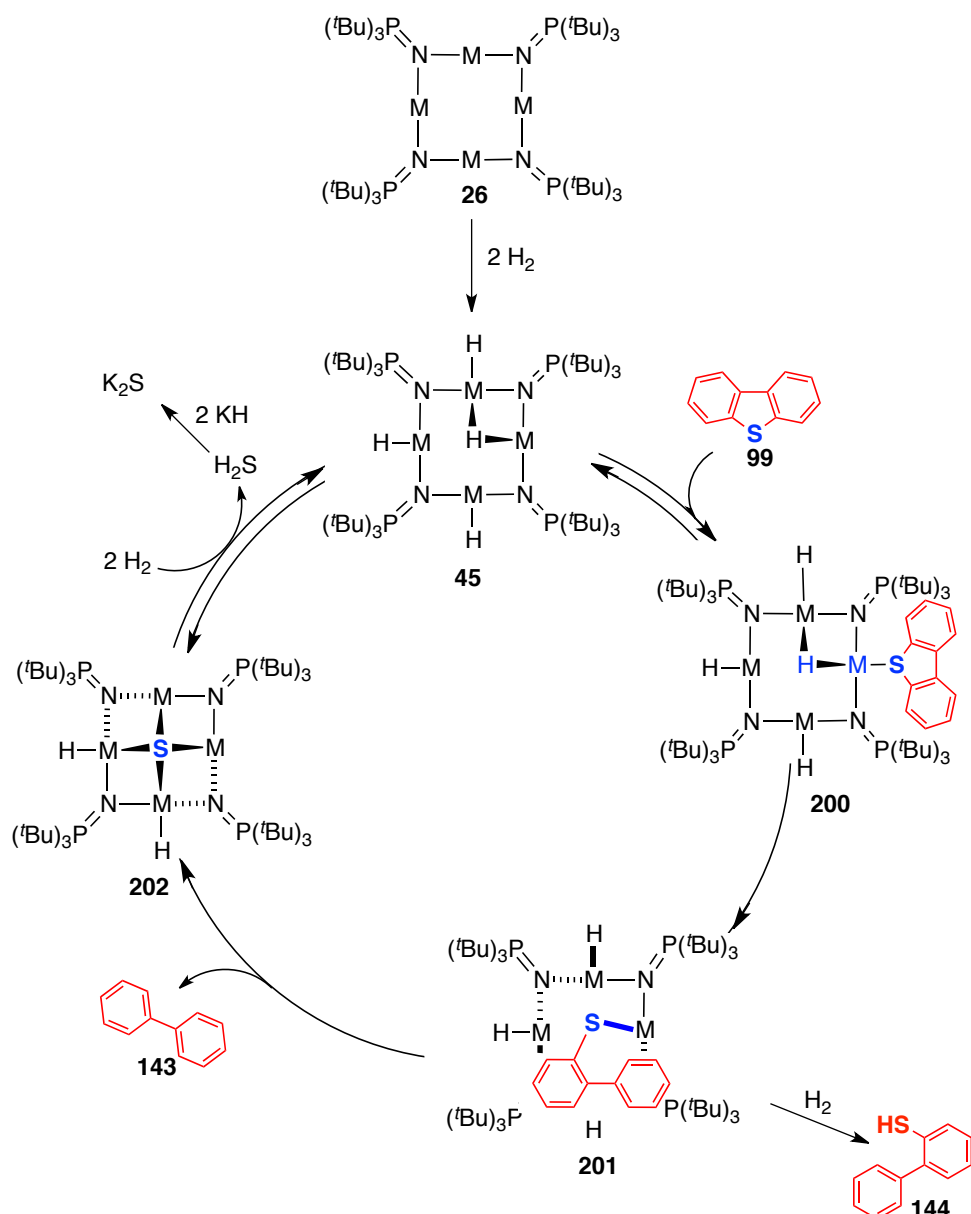


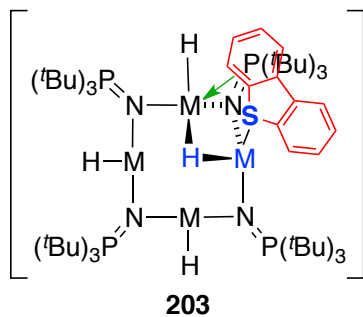
Figure 4.2. Mechanism of Desulfurization

We have established that the tetrametallic clusters **26a/b** react irreversibly with H₂ even at room temperature, presumably forming base metal hydrides (e.g. **45**, Figure 4.2). Results of IR monitoring of the reaction between catalyst **26b** and H₂ suggest the formation of both bridging and terminal metal hydrides (Chapter 2). These preliminary mechanistic features, however, do not provide definitive information on the nature of the active catalyst under HDS conditions (*i.e.*, reversibility of hydride formation, fluxionality of metal-hydride and metal-dihydrogen bonds, metal coordinative unsaturation, etc). These mechanistic details can be captured through *spectroscopic* characterization of the active catalysts during the course of hydrodesulfurization. *In operando* IR- and Raman spectroscopic analysis can be used to confirm the involvement of metal hydrides (terminal and/or bridging) and metal-dihydrogen complexes as the active catalytic species.²⁴⁸ Furthermore, *in operando* X-ray analysis could provide useful insights on the oxidation state(s) and nuclearity of the active catalyst(s) through the detection of M–M bonds and polynuclear phases during the course of desulfurization.^{248–250}

DFT simulations¹³⁶ suggest that the low-valent and terminally low coordinate precatalysts **26a** and **26b** form tetrahydrido-cluster **45** upon instantaneous reaction with two molecules of H₂ (Chapter 2). The simulations, however, further suggest that the subsequent addition of three more H₂ molecules leads to the formation of hydride-functionalized

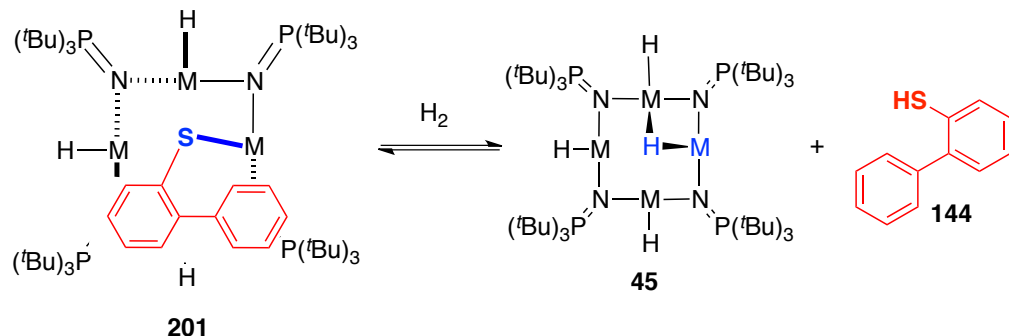
clusters where the metal centers are also involved in metal-dihydrogen coordination. The DFT modeling results, however, do not provide sufficient information as to the nature of the hydride– and dihydrogen–functionalized active species (i.e. group fluxionality, reversible hydride migration). Nonetheless, the tetranuclear hydridometal(II) cluster **45** was selected as a tentative representation of the active HDS catalyst, as it includes an open-shell metal center that can function as a *vacant site* for substrate precoordination, leading to intermediate **200**.

The metal-bound dibenzothiophene in intermediate **200** then undergoes C–S bond hydrogenolysis to produce the nickel thiolate intermediate **201**. The hydrogenolysis step presumably proceeds through π -coordination of the aromatic ring, as illustrated in structure **203**. The π -coordination decreases somewhat the aromaticity of the metal-bound ring, hence, activating the substrate toward the nucleophilic attack of hydride at the electrophilic carbon center of the C–S bond.

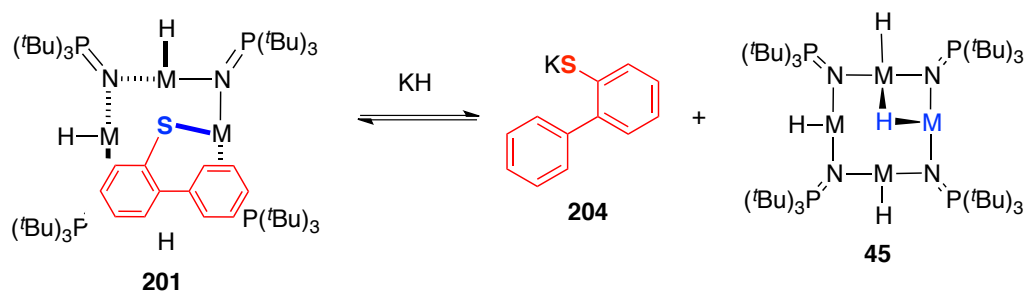


Nickel thiolate **201** is a precursor to the formation of both of the DBT-hydrogenolysis products observed in this reaction. The formation of 2-phenylthiophenol **144** can proceed by two reasonable mechanisms. Intermediate **201** could undergoes M–S bond hydrogenolysis, forming a metal hydride complex (**45**) and liberating thiol **144**, which rapidly reacts with the scavenger to form the potassium thiophenolate salt (Equation 4.47). Another reasonable mechanism involves the direct ionic exchange between **201** and KH, which would free the potassium thiophenolate salt **204** and replace it with a M–H bond (**45**, Equation 4.48).

Equation 4.47



Equation 4.48

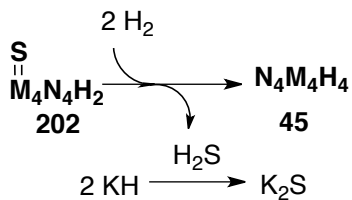


The formation of the terminal HDS product biphenyl presumably proceeds through similar mechanisms. The intramolecular hydrogenolysis of the C–S bond in **201**, proceeding through a metal- π arene complex, liberates biphenyl **143** and generates the sulfide catalyst **202** (Figure 4.2). Coordination of the thiophenolate ion **204** to the catalyst, forming an anionic thiophenolatometallate intermediate related to **201** potentially also contributes to the formation of biphenyl.

It is assumed that the rate-limiting step in the catalytic cycle involves the thermodynamically challenging desulfurization of the transition metal sulfide **202**, releasing H₂S and returning the active metal hydride **45**. However, the release of H₂S is unlikely to happen under the very mild reaction temperatures in the presence of a strongly basic scavenger. A proposed mechanism for the scavenger-driven catalyst regeneration is discussed in the succeeding section.

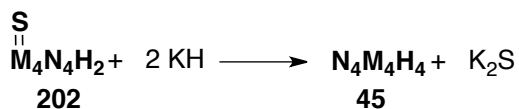
It is crucial to ascertain the actual role played by KH in the catalyst regeneration step. The reduction of sulfido intermediate **202** to **45** can proceed by at least two different mechanisms. Most directly, the sulfided organometallic intermediate could react heterolytically with two molecules of H₂ to produce the active metal hydride **45** and liberate H₂S, which then reacts with two moles of KH to form K₂S (Equation 4.49). In this proposal, the scavenger plays an essentially passive role.

Equation 4.49



The pronounced cation effects on the rate of desulfurization (Na^+ versus K^+), however, suggest the intervention of a salt metathesis mechanism for this reduction. The greater ionic character of KH makes hydride delivery to the metal center more facile. This leads to the exchange of the nickel/cobalt-bound sulfide ion for potassium, directly producing insoluble K_2S and regenerating the active catalyst **45** (Equation 4.50). The use of potassium deuteride (KD) will undoubtedly provide important details on the scavenger-driven catalyst turnover.

Equation 4.50



To determine whether it is hydrogen or KH than induces catalyst turnover, the nickel catalyst was primed with H_2 for a short period before evacuating the reaction vessel (Entry 1, Table 4.7; Equation 4.51). In this experiment, DBT, KH, and **26b** (0.5 mol %) in toluene were treated at room temperature under 1 atm of H_2 for 30 minutes followed by removal of H_2 *in vacuo*. Subsequent heating of the H_2 -primed reaction mixture at 120

^{°C} for 16 hours resulted in the observation of some C–S bond hydrogenolysis, giving a mixture of **143** and **144**. The observation of catalytic desulfurization in the absence of H₂ using the hydrogen-primed nickel catalyst strongly suggests that KH itself *can* act as an active hydride donor to liberate the HDS product and effect catalyst turnover – consistent with the mechanism shown in Eq. **4.50**. However, this observation is inconsistent with the fact that, at elevated temperatures, the strongly basic KH competitively deprotonates both benzylic and arene C–H bonds in toluene, producing a low concentration of H₂ *in solution*, which could also act as the active reductant. Potassium hydride-induced C–H activation is supported by the formation of a minor amount of toluene dehydrocoupling, giving 1,2-diphenylethane **30** (Equation **4.52**). In addition, since H₂ is produced at a slow rate in solution, a slow HDS rate is expected, and observed (TOF = 0.6/h). This is also supported by the faster rate of hydrodesulfurization of DBT **129** observed under a full atmosphere of H₂ (TOF = 2.5/h; Entry **2**, Table **4.8**).

Equation 4.51

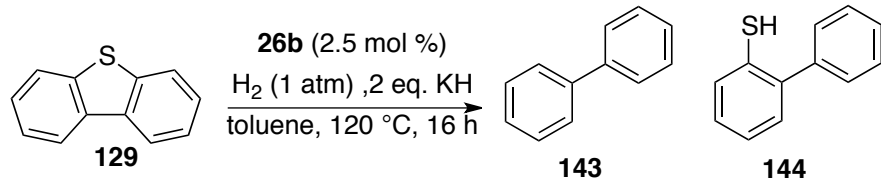
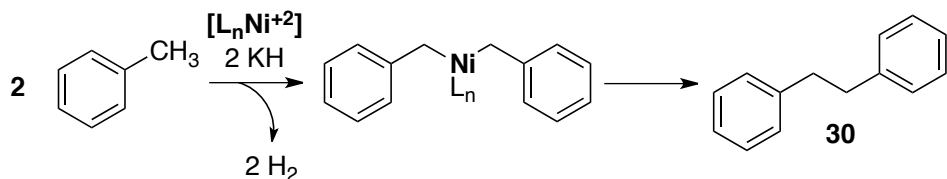


Table 4.8

Entry	H ₂ (atm)	% Conversion		TON (mol 129 / mol cat)	TOF (TON/time)
		143	144		
1	0 ^a	6	13	10	0.6
2	1	20	28	40	2.5

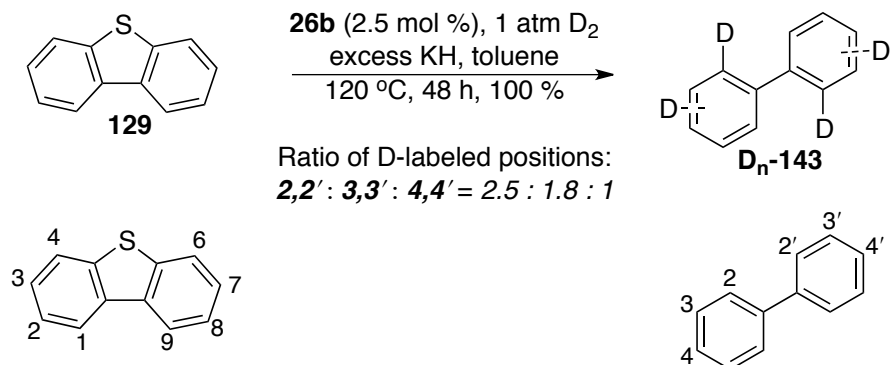
^aThe vessel was initially charged with 1 atm of H₂, stirred for 30 minutes and the headspace of the reactor was evacuated prior to heating.

Equation 4.52

To gain additional mechanistic insight and to further delineate the complicated role of the scavenger KH in our experimental design, a complete set of deuterium-labeling and control experiments were conducted. The nickel-catalyzed hydrodesulfurization of DBT and 4,6-diethyl-DBT was conducted in the presence of excess KH under an atmosphere of D₂ gas at 120 °C. The “deutero-desulfurization” of DBT showed a substantial primary kinetic isotope effect, giving k_H/k_D = 3.0 (Equation 4.53). This does not provide a definitive indication of the nature of the rate-determining step, since KH mediates a range of competitive C–H activation reactions that obscure the extent of deuterium incorporation into the desulfurization products. The strong basicity of KH results in a variable extent of deuterium incorporation at the C2, C3 and C4 positions of biphenyl. Integration of the chemical shifts in the ²D-NMR spectrum of

143 revealed a 2.5 : 1.8 : 1 ratio of deuterium labels in the C2, C3 and C4 positions, respectively. It is, however, important to note that the quantification deuterium incorporated in each position is extremely difficult due to the concomitant KH-induced deuterium-hydrogen exchange at the C3 and C4 positions. The molecular weights for each desulfurization product detected by mass spectrometry (e.g. $C_{12}H_8D_2$) could correspond to a number of isomeric deuterium-labeled species. This highlights the need to identify scavenger-free conditions that allow for the development of HDS mechanistic probes highly specific for key steps mediated by the active nickel and cobalt catalysts.

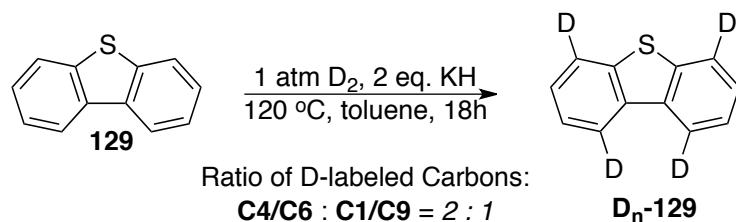
Equation 4.53



Control experiments conducted under a deuterium atmosphere but in the absence of the catalyst revealed the origin of the unexpected deuterium incorporation (Equation 4.54). Under these conditions, biphenyl production is completely suppressed, but significant deuterium

incorporation is observed at the C1/C9 and C4/C6 positions of DBT (ratio of integration = 2 : 1, respectively).

Equation 4.54



The KH-induced C–H activation at the C4 and C6 positions supports the possible contribution of directed C–S activation in DBT (Figure 4.4). KH-induced *ortho*-metallation of DBT would arise from substrate coordination through the anionic carbon center in **205**, forming the anionic intermediate **206** (Figure 4.4). Considering the strongly basic reaction environment, the active catalyst may function in an anionic reactivity manifold. The anionic cluster **206** can then undergo intramolecular C–S bond cleavage from rearrangement of the anionic DBT ligand to enyne intermediate **207**. The enyne moiety in cluster **207** then inserts into a M–H bond, to form a thiophenolate intermediate **208**.

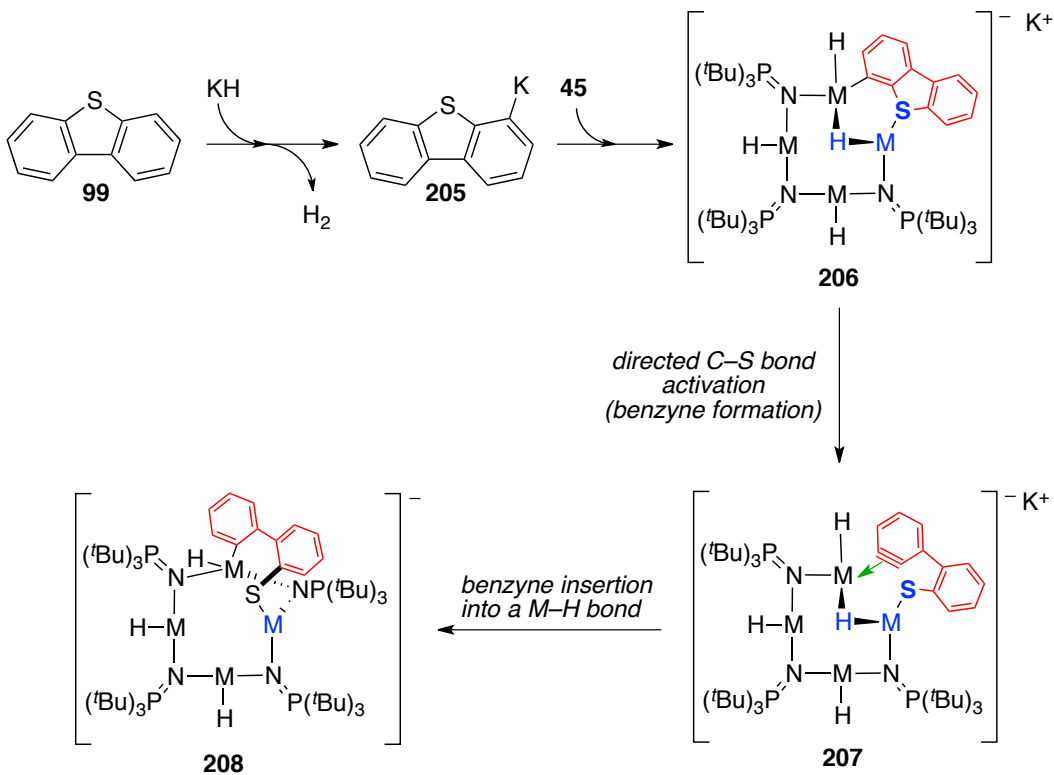
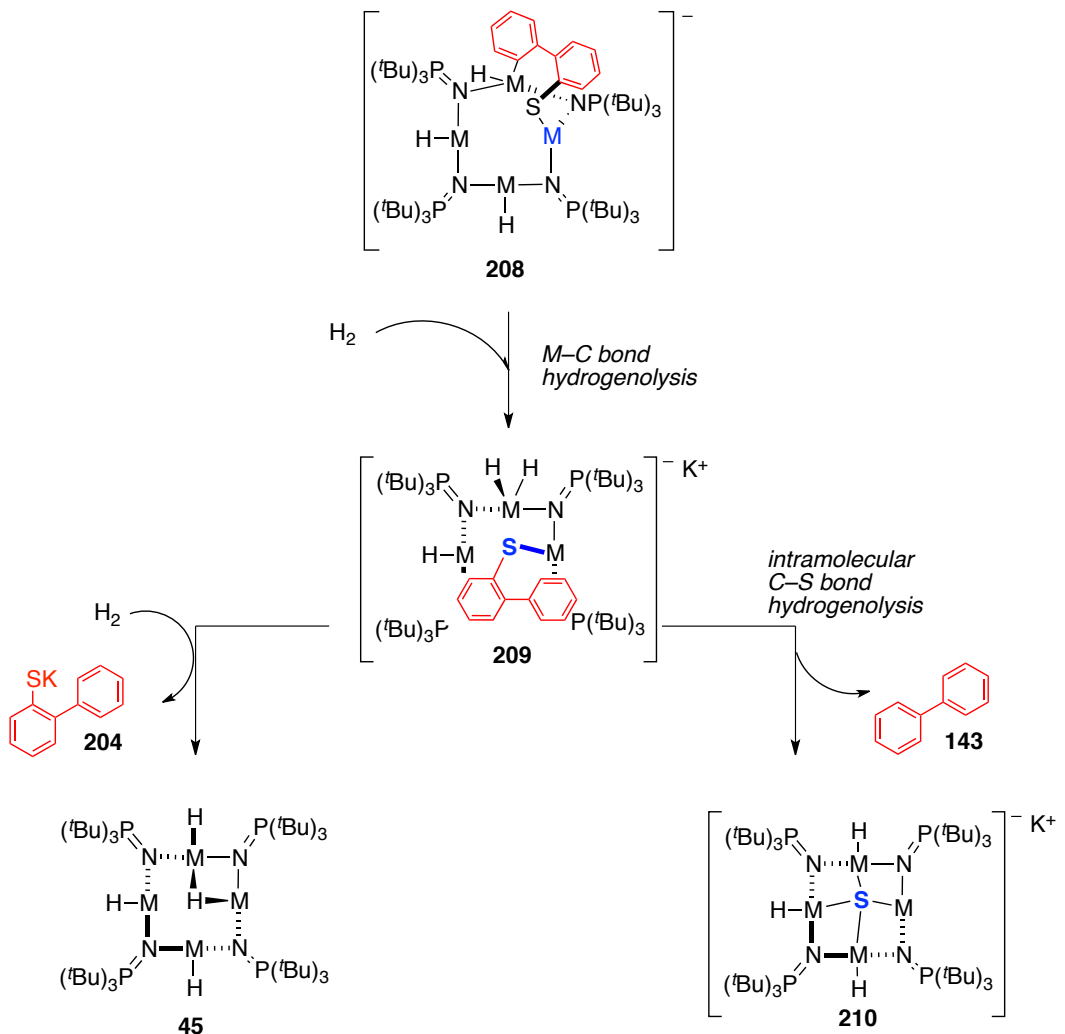


Figure 4.3

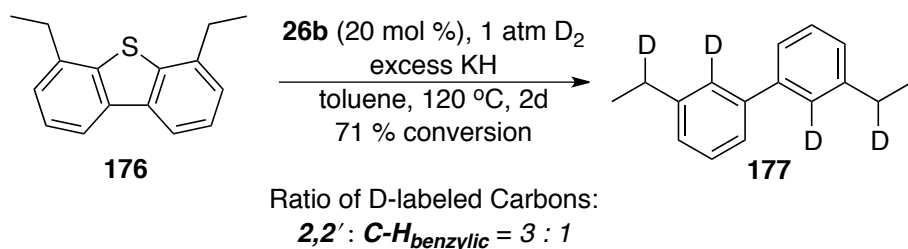
Anionic cluster **208** presumably undergoes hydrogenolysis to give the anionic, thiophenolate-substituted cluster **209** (Figure 4.4). This complex is potentially involved in the formation of both partially desulfurized product **144** and biphenyl **143**. Thiophenolate transfer from the tetrametallic cluster to the potassium counter ion regenerates the active hydrido cluster **45** and the potassium thiophenolate salt **204**. On the other hand, intramolecular C–S bond hydrogenolysis in **209** results in the formation of biphenyl and an anionic, sulfided cluster **210**, ready for hydrogenolytic turnover.



An *ortho*-metallation directed C–S bond hydrogenolysis mechanism is not supported by the hydrodesulfurization of 4,6-diethyl-DBT **176** under a D₂ atmosphere ($k_H/k_D = 2.3$ at 120 °C, Equation 4.55), which shows deuterium incorporation only at the sulfur-bearing carbons and the benzylic positions of the side chains. This reaffirms the earlier hypothesis of direct C–S bond activation in DBT-type substrates. A single aromatic C–

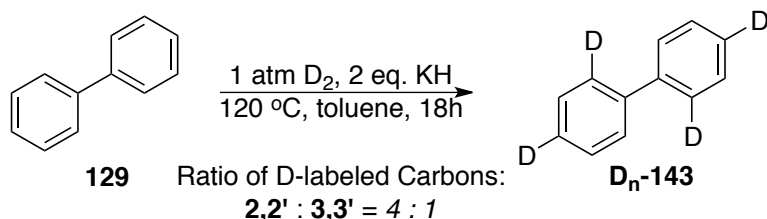
D chemical shift was observed; the KH apparently no longer deprotonates the arene, reacting exclusively at the side chains.

Equation 4.55



The exclusive labeling of the C2/C2' positions in 177 is strongly suggestive, though inconclusively so, that D₂ acts as the actual reductant in the catalytic hydrodesulfurization. However, deuterium incorporation at this position could potentially occur after the C–S bond hydrogenolysis is complete. Similar control experiments using unlabeled biphenyl as the substrate results in extensive hydrogen/deuterium exchange at the four *ortho*- and two *para*-positions, clearly incompatible with the previous labeling experiment (C2/C4 = 4 : 1; Equation 4.56). Concomitant KH-induced hydrogen-deuterium exchange at C2 and C4 positions once again makes quantification of deuterium incorporated difficult.

Equation 4.56



These results clearly establish the fact that dependence on KH as an internal scavenger renders mechanistic investigation extremely challenging and too complicated for routine investigation. This further emphasizes the need to identify conditions for scavenger-free desulfurization catalyzed by **26a** and **26b**.

4.4 Summary and Conclusions

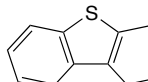
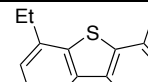
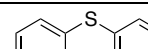
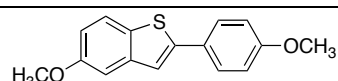
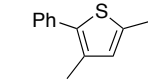
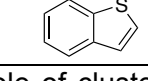
Mild reaction conditions optimized for catalytic hydrodesulfurization of thiophenic substrates have been unidentified using tetrametallic Co(I) and Ni(I) clusters **26a** and **26b** as catalysts. Catalytic carbon-sulfur bond hydrogenolysis can be achieved in the absence of strongly basic scavengers under hydrosilylation conditions. Metal-free carbon-sulfur bond hydrogenolysis by a hypervalent silicon hydride reagent was also discovered during the course of this investigation.

Significantly faster rates of hydrogenolysis and higher conversions are observed in the presence of stoichiometric amounts of basic

scavengers. These results feature the most efficient homogeneous base metal catalysts ever discovered for deep and ultra-deep hydrodesulfurization of dibenzothiophene and substituted dibenzothiophenes. Aryl sulfides, thiophenes and benzothiophene-type substrates efficiently undergo catalytic carbon-sulfur bond hydrogenolysis under similarly mild reaction conditions. The catalysts show high chemoselectivity for carbon-sulfur over carbon-oxygen bonds. Moreover, alkenes and nitrogen-containing organic substrates inhibit but do not completely deactivate the catalysts for hydrodesulfurization.

Control experiments establish the essentially passive role of KH in the desulfurization, but not in the overall catalytic reaction. Potassium hydride mediates competitive reversible C–H activation of both substrates and products, complicating the results of control experiments and mechanistic studies. Hence, the identification of optimum conditions for scavenger-free desulfurization is crucial to gaining concrete insights into the mechanism of hydrodesulfurization.

Table 4.9. Summary of catalytic hydrodesulfurization of aromatic sulfur heterocycles.

Entry	Substrate	Cat (mol%)	Time (h)	Temp (°C)	%Conv		TON ^a
					ArH	ArSH	
1		26b (1.7)	8	120	23	9	16
2		26a (1.7)	8	120	21	52	28
3		26b (9.4)	18	120	44	trace	7
4		26a (4.9)	18	120	21	6	6
5		26b (1.9)	20	120	24	23	20
6		26a (0.8)	60	120	61	39	144
7		26b (2.3)	18	110	>98	0 ^b	42
8		26b (2.6)	18	120	26	0 ^b	10
9		26b (1.9)	18	110	41	0 ^b	31

^a Moles of substrate converted per mole of cluster; in cases wherein a mixture of the partially and fully desulfurized products was obtained, one catalytic turnover was (conservatively) calculated as requiring that two moles of C-S bonds be activated per mole of cluster. Calculated turnover numbers were based on results of GC-MS analysis.

^b None detected by GC-MS analysis.

Chapter 5

Base Metal-Catalyzed Hydrogenolysis of C–O and C–N Bonds

5.1 Introduction and Background

Industrial hydrodeoxygenation (HDO) and hydrodenitrogenation (HDN) are critically important hydrotreatment processes for the valorization of highly complex chemical feedstocks with inherently high heteroatom contents (e.g. petroleum and biomass).^{17,224,251-256} In contrast to catalytic hydrodesulfurization (HDS), industrial research on catalytic hydrogenolysis of C–O and C–N bonds is less developed. The research emphasis currently given to catalytic hydrodesulfurization (HDS) is mainly driven by the inherently higher concentration of sulfur compounds in petroleum feedstocks and the potency of H₂S and sulfide ions in poisoning industrial hydrotreatment catalysts.^{15,203} This has resulted in the implementation of hydrotreatment conditions mainly optimized for HDS and rather ineffective for the hydrogenolysis of C–O and C–N bonds. Hydrodenitrogenation (HDN) and hydrodeoxygenation (HDO) are achieved under harsher and more costly conditions over longer processing periods, due to the greater thermodynamic stability of C–O and C–N bonds. In order to increase the economic profitability and sustainability of petroleum upgrading, industrial hydrotreatment researchers have aggressively strived to develop high activity catalyst technologies equally promiscuous for the activation of all three C–X bonds (X = S, O, N), ideally, under mild process conditions.²⁵⁴⁻²⁵⁷

In this chapter is briefly reviewed the literature pertinent to transition metal-mediated activation of C–O and C–N bonds. More importantly, we present our development of hydrodeoxygenation and hydrodenitrogenation catalyzed by low-coordinate, phosphoranimide-supported complexes of cobalt and nickel under exceptionally mild conditions.

5.1.1 Base Metal-Mediated C–O Bond Hydrogenolysis and Hydrodeoxygenation: A Prelude to Lignin Valorization

The ever-increasing demand for fossil-derived fuels and the relatively slow discovery of new petroleum sources are major driving forces for the utilization of alternative sources of fuel and as substitutes for petroleum-derived feedstock chemicals.^{17,258,259} Among current renewable sources of energy, the utilization of biomass, a collection of highly oxygenated biopolymers, is the most promising. The diverse molecular composition of biomass makes it, potentially, a cheap and abundant source of gaseous and liquid fuels, as well as value-added commodity and fine chemicals.^{259,260} However, practical and efficient catalyst technologies for industrial-scale biomass upgrading remain unavailable. Most contemporary biomass refining technologies involve pyrolytic gasification – an energy- and resource-intensive processes that belies the supposedly

“zero-carbon-footprint” claimed for the biomass-based fuel and chemical economy.²⁵⁷

5.1.2 Lignin Valorization

From a fuel production point of view, lignin processing deserves particular attention. The structural composition of lignin makes it, potentially, a good source of liquid fuels (etherified gasoline) and aromatic feedstock chemicals (Figure 5.1).^{17,251,258,261} Unfortunately, this biopolymer remains the most underutilized fraction of lignocellulosic biomass.²⁵⁸ Of the annual lignin generated, only about 2% is used as a source of low-quality chemical products including simple dispersants and binding agents. The remaining bulk is used principally as a poor quality fuel for on-site heating in the pulp and paper industry.²⁵⁸

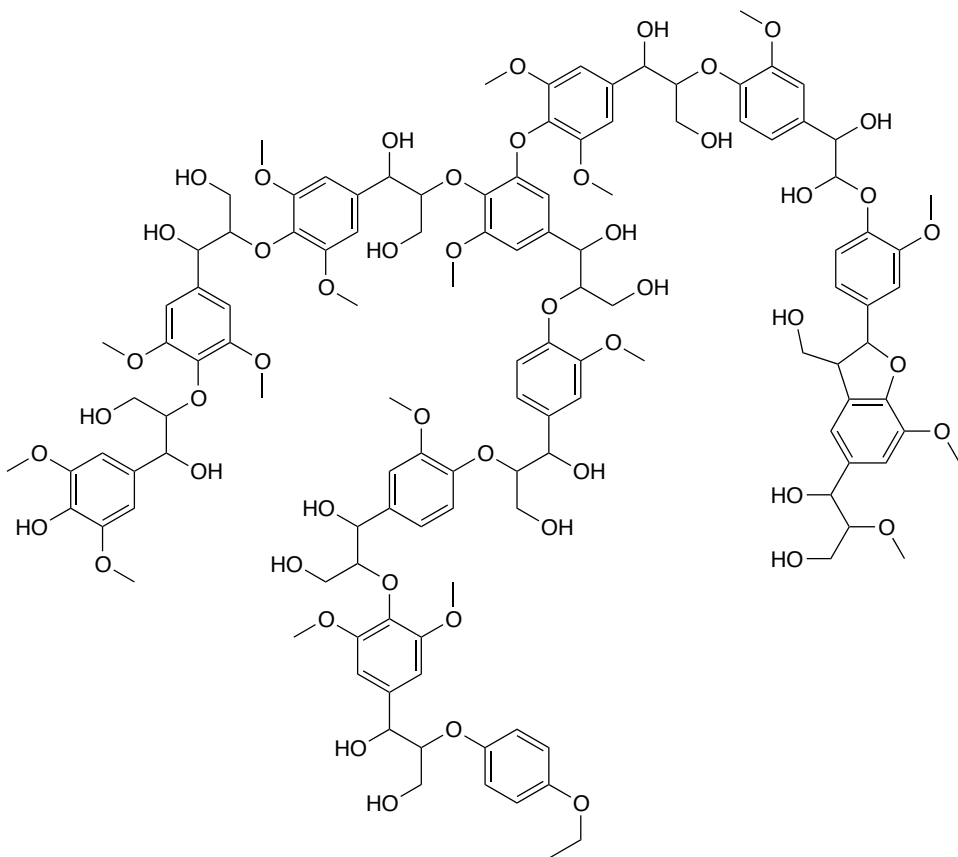


Figure 5.1. Representative structure of lignin.

Catalysis is an optimal strategy for the economical processing of lignocellulosic biomass.^{251,260,262} The few reported biomass hydrotreatment catalysts generally compromise precious- and semi-precious transition metal catalysts (CoMoS_2 and NiWS_2) and operate under high-temperature and high-pressure conditions at high catalyst loadings.²⁵⁸ The heterogeneous nature of the catalysts and harsh process conditions impact process selectivity; complex mixtures of reduction products are obtained from non-selective oxygen extrusion from these diversely functionalized biopolymers through various concomitant mechanistic pathways.^{17,263} In addition, the inherently high oxygen content of

lignocellulosic biomass, typically ranging from 40 to 45% (weight basis) induces facile coke formation under such harsh processing conditions, further reducing catalyst efficiency.²⁵⁸

Ideal lignin hydrotreatment strategies involve two crucial steps: (1) *hydrogenolytic depolymerization to produce bio-oils*, which consist of highly substituted phenols and ethers, and (2) *catalytic refining by deoxygenation*, affording a mixture of etherified liquid fuel. The selective deoxygenation of bio-oils under mild conditions is one of the ultimate goals of industrial biomass refining, as it provides economical routes to large-scale production of biomass-based, first-generation (unfunctionalized) bulk aromatics, including benzenes, toluenes, and xylenes (BTX), substituted by various alkyl residues.^{17,263} Optimal catalysts for biomass hydrodeoxygenation are systems that afford high conversion under modest reaction conditions. The hydrogenolysis of C–O bonds under relatively mild conditions is expected to minimize or eliminate coke formation and other competitive thermal processes that commonly impact process selectivity.

High selectivity for direct C–O bond hydrogenolysis is desired to suppress excessive hydrogen consumption, as most heterogeneous catalysts hydrogenate aromatic rings prior to C–O bond scission, which produces lower quality fuels and chemicals (e.g. cycloalkanes and cycloalkanols).²⁶⁴ Several processes have been shown to be effective for

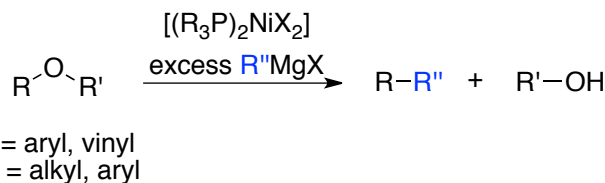
direct C–O bond scission without competitive aromatic ring hydrogenation. These strategies are, however, impractical for large-scale implementation since (1) *stoichiometric quantities* of hazardous alkali metals and/or organoalkali reagents are used^{265,266} and (2) *electrocatalytic techniques* are involved.²⁶⁷

5.1.3 Base Metal-Catalyzed C–O Bond Cleavage

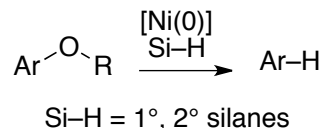
Although most literature examples of lignocellulose refining strategies are mediated by second- and third-row metals, it is important to note that *the most efficient known lignin upgrading catalyst is heterogeneous FeS*.^{17,258,263} Though extremely rare, a few base metal catalysts selectively cleave carbon-oxygen bonds under mild hydrogenolysis conditions, with efficient suppression of competitive aromatic ring hydrogenation. Wenkert and coworkers first reported the nickel-catalyzed cleavage of C–O bonds in aromatic and enol ethers using stoichiometric quantities of Grignard reagents as the reductant, producing hydrocarbon coupling products (Equation 5.1).^{268,269,270,271} The *in-situ prepared* catalyst was not structurally characterized, but the process does produce hydrocarbons. Further improvement of this methodology resulted in higher yields and tolerance of a wider scope of functionalized substrates.^{269,270} Unfortunately, the process remains industrially unattractive because stoichiometric quantities of expensive and hazardous

reductants are required. One selective C–O hydrogenolysis strategy has recently been reported using low-valent nickel precatalysts and utilizing milder organosilanes as the reductant, under considerably milder conditions (Equation 5.2).²⁷⁰⁻²⁷²

Equation 5.1



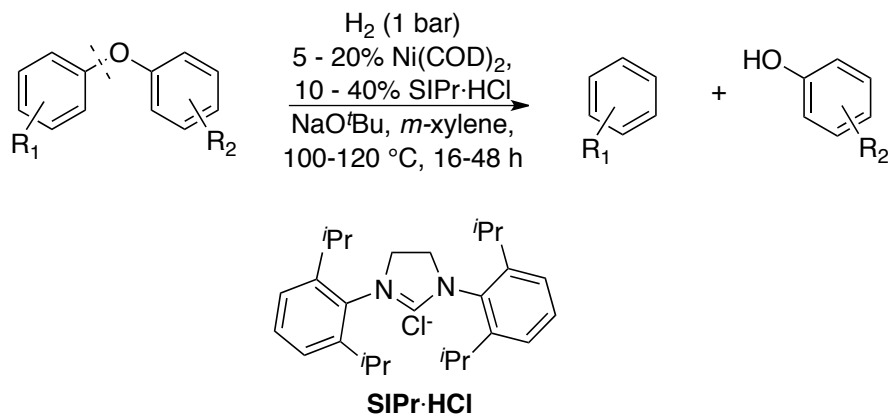
Equation 5.2



There remains a notable dearth of selective, high-activity C–O bond hydrogenolysis catalysts that utilize the mild and inexpensive reductant, hydrogen (H_2). Hartwig, *et al.*, recently disclosed the selective hydrogenolysis of aromatic C–O bonds catalyzed by an *in situ*-prepared, purportedly homogeneous nickel catalyst supported by an N-heterocyclic carbene ligand (Equation 5.3).²⁷³ The hydrogenolysis proceeds under mild conditions, but requires very high catalyst loading. Hartwig's catalyst selectively cleaves the $\text{C}_{\text{aryl}}\text{--O}$ bonds in unsymmetrical aryl ethers and lignin model compounds, affording mixtures of aromatic hydrocarbons and alcohols with complete suppression of aromatic ring hydrogenation.²⁷³ More recently, Hartwig revealed that nickel nanoparticles effect catalytic

aryl ether hydrogenolysis under similarly mild conditions. However, this heterogeneous nickel catalyst unsurprisingly also produces aromatic hydrogenation products.¹⁰⁶

Equation 5.3



5.2 Results and Discussion

We evaluated the activities of cobalt and nickel clusters **26a** and **26b** for hydrogenolytic C–O bond activation under conditions optimized for catalytic hydrodesulfurization. Exploration of the generality of the catalysis was focused particularly on nickel catalyst **26b** since preliminary reactivity comparisons showed faster C–O hydrogenolysis for nickel compared to cobalt. The lower activity of the cobalt catalyst for C–O bond hydrogenolysis is surprising, but presumably due to the greater stability of the cobalt alkoxide intermediates. Symmetrical and unsymmetrical ethers and a few model compounds representative of key linkages in lignin were used as substrates. The latter part of this section presents the successful

development of modified methodology effective for the complete, selective deoxygenation of dibenzofuran substrates – *deep hydrodeoxygenation* – under remarkably mild conditions.

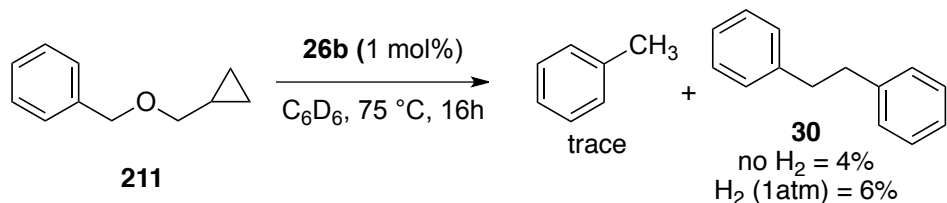
Catalytic cleavage of carbon-oxygen bonds generally necessitates processing conditions harsher than those employed in catalytic HDS (Chapter 4). In the succeeding sections, catalyst turnover number (**TON**) corresponds to moles of C–O bonds cleaved per mole of cluster, while the turnover frequency (**TOF**) is the ratio of TON to reaction period (in hours).

5.2.1 Preliminary Results: Stoichiometric C–O Bond Hydrogenolysis

Nickel cluster **26b** was initially challenged with additive/scavenger-free hydrogenation of C–O bonds in unsymmetrical aryl and benzyl ethers (Equation 5.4 – 5.5), which are anticipated to be among the easiest substrates for HDO. The following are preliminary studies of C–O bond activation mediated by the tetrametallic Ni(I) catalyst. Benzyl methylcyclopropyl ether **211** was chosen as substrate to simultaneously probe the potential activity of the nickel catalyst for (1) activation C–O bond and / or (2) directed C–C bond cleavage in cyclopropyl rings. Exhaustive identification and quantification of all hydrogenolysis products in these preliminary experiments were not pursued. Benzyl cyclopropylmethyl ether **211** returned 1,2-diphenylethane (**30**, 4%) and trace amounts of toluene and 1,2-diphenylethane upon treatment with 1

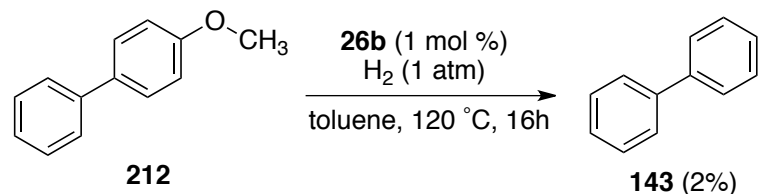
mol% **26b** in THF at 70 °C. A slight increase in the yield of the dimerization product **30** was observed when the reaction was conducted under one atmosphere of H₂ (Equation 5.4). The formation of toluene and diphenylethane demonstrates catalyst selectivity for cleavage of the weaker benzylic C–O bond. The formation of benzyl alcohol from cleavage of the cyclopropylmethyl C–O bond was not detected.

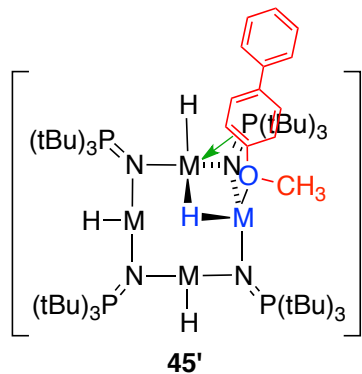
Equation 5.4



Under identical conditions, cluster **26b** showed selectivity for activation of the C_{aryl}–O bond in 4-methoxybiphenyl **211**, stoichiometrically and exclusively forming biphenyl **143** (Equation 5.5). The catalyst selectivity for activating the C_{aryl}–O bond could be kinetically driven by substrate precoordination, forming a metal–π aryl complex (**45'**). This mode of coordination potentially activates the aryl C(a) for metal-mediated hydride delivery.

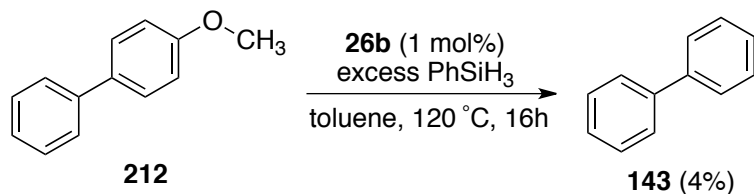
Equation 5.5





Similar catalyst selectivity is observed under hydrosilylation conditions. Biphenyl **143** was exclusively obtained in higher yield (4%) from the reaction of **212** with excess PhSiH₃ in the presence of catalytic amounts of **26b** (1 mol%) in toluene at 120 °C (Equation 5.6). Since the use of organosilyl hydrides as both reductant and alkoxide scavenger resulted in unimpressive conversion, we then proceeded to adopt the hydrogenolysis conditions and basic scavengers shown optimal for catalytic hydrodesulfurization of thiophenic substrates.

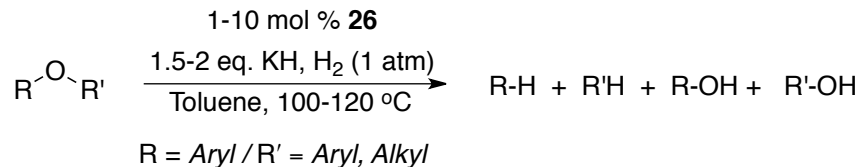
Equation 5.6



5.2.2 Catalytic C–O Bond Hydrogenolysis: $C_{\text{aryl}}-\text{O}$ Bond Scission

Catalytic hydrogenolysis of C–O bonds requires the use of stoichiometric KH to scavenge acidic species (i.e. water, alcohols) that can reversibly inhibit or irreversibly poison the active catalyst. The succeeding results were obtained from experiments conducted under the conditions summarized in Equation 5.7, where symmetrical and unsymmetrical aryl ethers were treated with catalytic amounts of **26b** (1-10 mol %) and 1 atm H₂ at 100-120 °C.²² To the best of our knowledge, these clusters constitute the *only fully-characterized pre-catalysts for C–O hydrogenolysis under conditions comparable to those reported by Hartwig.*²⁷³

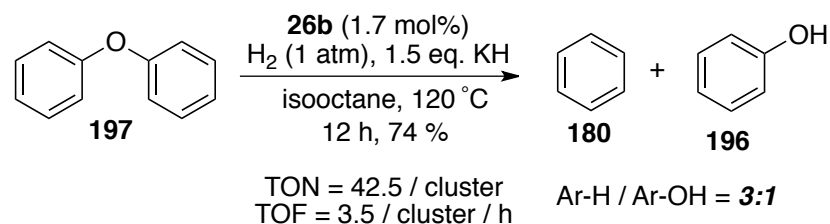
Equation 5.7



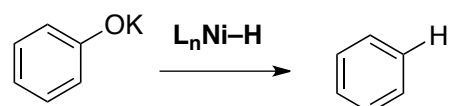
Diphenyl ether **197** was reductively cleaved to a mixture of benzene **180** and phenol **196** (3 : 1) *under one atmosphere of hydrogen*, in the presence of KH in toluene over 12 hours (TON = 43; Eq. 5.8).²⁰ The higher proportion of benzene compared to phenol establishes that the phenolic $C_{\text{aryl}}-\text{O}$ bond in the intermediate potassium phenolate (KOC_6H_5) is also cleaved catalytically, albeit at a much slower rate (Equation 5.9). This result is an important indication of the catalyst's activity for complete

deoxygenation of phenols. At this point, complete conversion of diphenyl ether to benzene has not been demonstrated. This is presumably due to the strong tendency of the phenoxide ion to competitively bind with active metal center(s) and, in turn, inhibit the catalysis. Interestingly, the hydrogenolysis of **197** does not mediate aromatic hydrogenation: neither cyclohexane, cyclohexanol, or cyclohexanone were observed (GC-MS). This result makes **26b** the second (presumably) homogeneous base metal catalyst that activates aryl C–O bonds under exceptionally mild hydrogenation conditions. Importantly, the conversion rates observed at much lower catalyst loading are comparable to the rates reported by Hartwig's (1.7 mol % vs 20 mol %).²⁷³

Equation 5.8



Equation 5.9



5.2.3 Hydrogenolysis of Alkyl Aryl Ethers

Selective aromatic C–O bond activation in unsymmetrical alkyl/aromatic ethers is desired not only for the production of high-value liquid fuels but also for applications in fine chemical synthesis. The nickel catalyst **26b** shows moderate selectivity for C_{aryl}–O bond cleavage in methyl ethers of 4-methoxybiphenyl and 2-methoxynaphthalene, affording mixtures of aromatic hydrocarbons, phenols, methanol, and (unquantified) methane under similarly mild conditions.

Treatment of anisole **212** with 1.5 equivalents of KH and catalyst **26b** in toluene at 110 °C under one atmosphere of H₂ thus afforded a 17 : 1 mixture of biphenyl **143** and 4-hydroxybiphenyl **213** after relatively short reaction time (Entry 1, Table 5.1; Equation 5.10). Interestingly, a 10-degree increase in reaction temperature and prolonged exposure to hydrogen resulted in loss of catalyst selectivity, giving a 50 : 50 mixture of **143** and **213** after 36 hours (Entry 2).

Equation 5.10

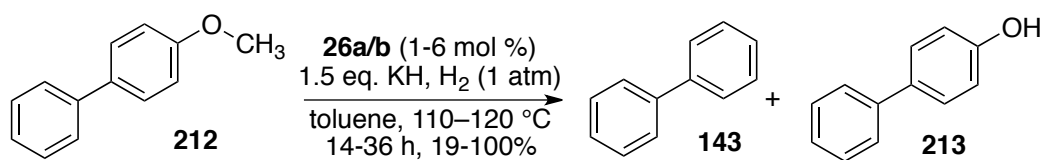
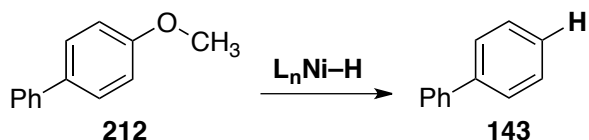


Table 5.1. Hydrogenolysis of **212** (110-120 °C)

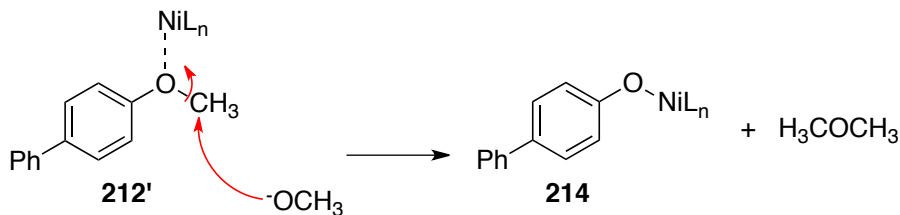
Entry	Cat / (mol%)	Time (h)	Temp (°C)	% Conversion		TON
				143	213	
1	5.6	15	110	17	1	4
2	5.6	36	120	50	50	18
3	1.6	15	120	12	31	27

The loss of catalyst selectivity at higher temperatures and over longer reaction periods can be rationalized by two reasonable arguments. The formation of biphenyl **143** is principally attributed to nickel-mediated direct C_{aryl}–O bond hydrogenolysis (Equation 5.11). This process produces strongly nucleophilic methoxide ions, the concentration of which increases over time. The increased methoxide concentration in solution may make methoxide attack on the methyl carbon of **212** fully competitive. Coordination of the oxygen-center to nickel presumably increases the electrophilicity of the methyl carbon sufficiently to favor S_N2-type attack by methoxide (e.g., **212'**) producing dimethyl ether and a nickel-bound phenoxide **214** (Equation 5.12). This hypothesis is supported by the reversal of catalyst selectivity at lower catalyst loading (Entry 3, Table 5.1). The lower concentration of the active nickel catalyst renders the S_N2-type cleavage of the C_{methyl}–O bond dominant.

Equation 5.11

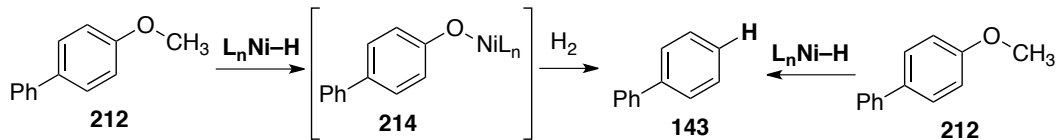


Equation 5.12



The rates of unsymmetrical ether hydrogenolysis are slower relative to the observed HDS rates (Chapter 4). However, as calculated from these experiments, the hydrogenolysis rates are somewhat obscured: the formation of biphenyl **143** can proceed via two contributing mechanistic pathways. Biphenyl can be formed (1) from direct $\text{C}_{\text{aryl}}-\text{O}$ hydrogenolysis of **212** and/or (2) from the combination of alternative $\text{C}-\text{O}$ hydrogenolysis events, involving initial cleavage of the $\text{C}_{\text{methoxy}}-\text{O}$ bond followed by the scission of the $\text{C}_{\text{aryl}}-\text{O}$ bond (Equation 5.13). At this point, there is insufficient mechanistic information to favor one mechanism over the other.

Equation 5.13



Similar hydrogenolysis selectivity is observed in the case of 2-methoxynaphthalene **215** (Equation 5.14). The nickel-catalyzed hydrogenolysis afforded a 2 : 1 naphthalene-to-naphthol ratio (Entries 1-2,

Table 5.2), slightly favoring C_{aryl}–O bond scission. Importantly, the presence of a small amount of potassium iodide in the reaction mixture reverses the regioselectivity of the C–O bond hydrogenolysis, affording a ~1 : 3 mixture of **216** to **217**.²⁰ This reversal of selectivity, once optimized, is expected to provide a versatile catalyst technology, one that can be tuned to process biomass for specific purposes. In this case, a simple catalytic additive (KI) induces the catalyst to preferentially produce naphthol and methane rather than naphthalene and methanol.

Equation 5.14

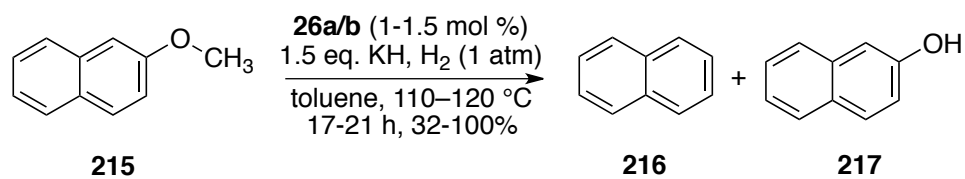


Table 5.2. Hydrogenolysis of **215** (110-120 °C)

Entry	Cat / (mol%)	Temp (°C)	Time (h)	% Conversion		TON
				216	217	
1	26b (1.4)	110	17	22	10	24
2	26b (1.7)	120	21	68	32	58
3 ^a	26a (1.2)	120	15	13	50	53

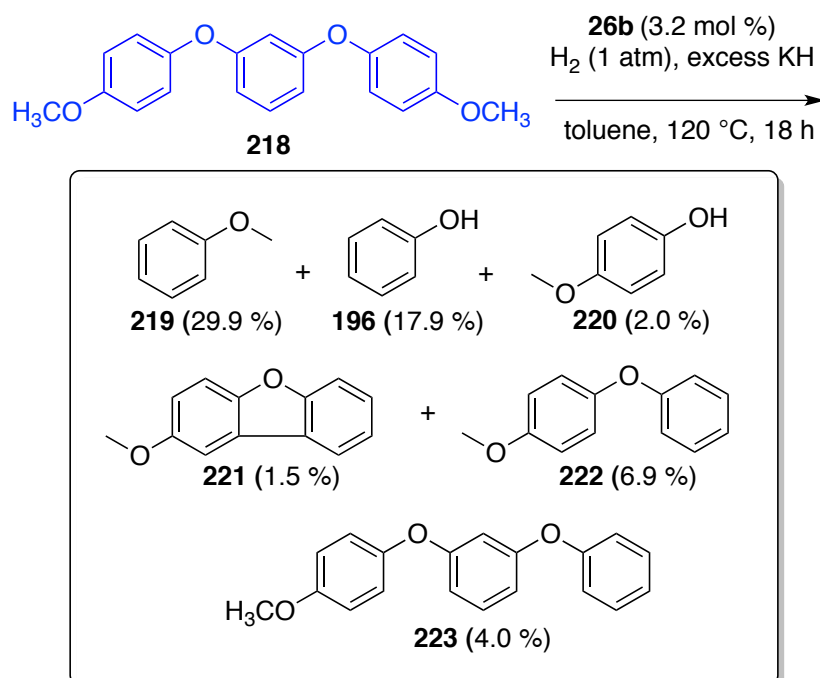
^a The batch of KH used contains KI as impurity.

5.2.4 Hydrogenolysis of Polyethers

The regioselectivity of C–O bond activation was also evaluated using a polyphenolic lignin surrogate, 1,3-bis(4-methoxyphenoxy)benzene

218. Treatment of **218** with nickel catalyst **26b** and excess KH in toluene (1 atm H₂, 120 °C) produced a complex mixture of hydrogenolysis products (Equation 5.15) in which liquid monoaromatic species (anisole **219** and phenol **196**) were dominant. The composition of the product mixture shows pronounced catalyst selectivity for the stronger C_{aryl}—O bond over the weaker and sterically more accessible C_{methyl}—O linkages. The product distribution is a convincing demonstration of the potential utility of this hydrodeoxygenation process for upgrading of solid polyether substrates under mild conditions to high value-added liquid aromatic products.

Equation 5.15

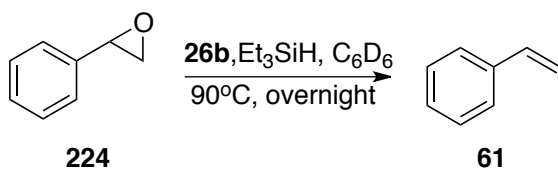


5.2.5 Base Metal-Mediated Deoxygenation

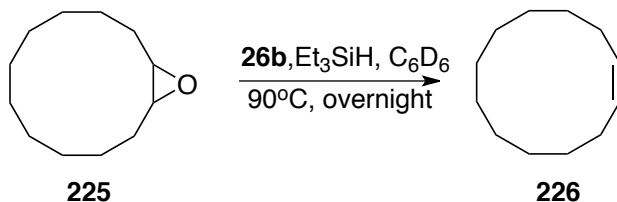
The succeeding sections present the stoichiometric and catalytic base metal-mediated deoxygenation of a range of ether substrates under mild conditions.

Styrene oxide **224** and cyclododecene oxide **225** were stoichiometrically converted to styrene **61** and cyclododecene **226** in the presence of nickel catalysts **26b** and triethylsilane (Equations 5.16 and 5.17). The yields of **61** and **226** were not quantified in these preliminary experiments. The surprising persistence of the C=C double bond in the products despite the presence of a reactive silane suggests a non-hydrogenolytic deoxygenation mechanism. The observed cleavage of epoxide C–O bonds presumably proceeds through homolytic activation by the tetrametallic nickel cluster. Radical-type cleavage of C–O bonds is not surprising since each Ni(I) center in the tetrametallic cluster **26b** behaves as a single-electron paramagnet in solution at room temperature. Although the reaction conditions are unoptimized, these results demonstrate one of the rare cases of base metal-mediated epoxide deoxygenation.²⁷⁶⁻²⁷⁸

Equation 5.16

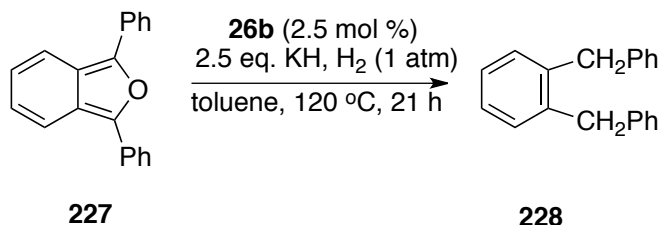


Equation 5.17



Catalytic hydrodeoxygenation was initially demonstrated by the reduction of 1,3-diphenylisobenzofuran **227**. Treatment of **227** with catalyst **26b** and excess KH under one atmosphere of H₂ resulted in quantitative deoxygenation, giving 1,2-bis(phenylmethyl)benzene **228** exclusively at 120 °C over 21 hours (Equation 5.18). The relatively facile deoxygenation of **227** is thermodynamically driven by the increased aromaticity of the resulting 1,2-disubstituted benzene derivative **228** over the nearly nonaromatic **227**.

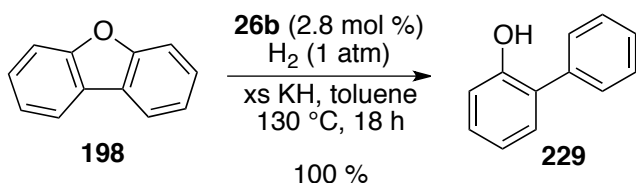
Equation 5.18



These initial results prompted us to investigate the hydrodeoxygenation of dibenzofuran, one of the most inert classes of oxygen-containing aromatic heterocycles. Under standard conditions,

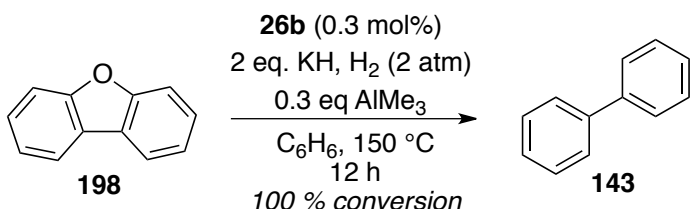
nickel cluster **26b** quantitatively cleaves the first C–O bond in DBF **198**, almost exclusively affording 2-hydroxybiphenyl **229** after 18 hours (Equation 5.19). Only a trace amount of biphenyl **143** was obtained in this experiment. The slow deoxygenation of **229** even at increased temperatures is presumably a consequence of scavenger inhibition. The conversion to **229** surprisingly proceeds without competitive aromatic ring hydrogenation, clearly demonstrating the selectivity of the catalyst for direct C–O bond hydrogenolysis.

Equation 5.19



Hypothetically, Lewis acid additives could promote complete deoxygenation of DBF **198** by coordinative activation of the phenolic C–O bond. The addition of a substoichiometric quantity of AlMe₃ (0.3 equivalents) to the hydrogenolysis of dibenzofuran at lower catalyst loading (0.3 mol% **26b**) and higher temperature resulted in the quantitative deoxygenation to biphenyl **143** (Equation 5.20). Toluene-insoluble solids, presumably oxides of aluminum and potassium, were observed after 12 hours. Complete hydrodeoxygenation of DBF **198** with lower loading of the Lewis acid promoter (<0.3 eq.) has not been conducted at this point.

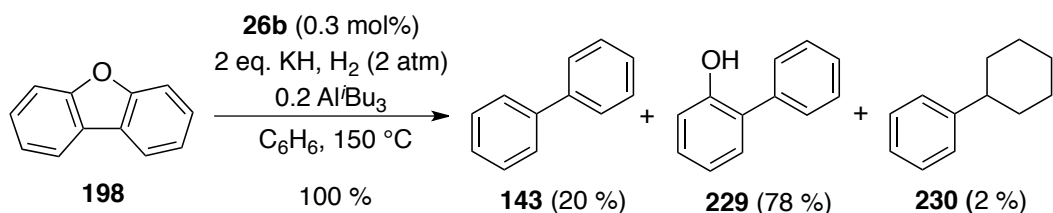
Equation 5.20



The complete hydrodeoxygenation of dibenzofuran **198** is surprising, and features an unprecedented *direct* metal-mediated C–O oxygen bond scission, completely bypassing ring hydrogenation pathways favoured by the use of heterogeneous catalysts.²⁶⁴ This hydrodeoxygenation process constitutes the first potentially practical process for the upgrading of polyarylated ethers into value-added *aromatic* fuels and feedstock chemicals under mild conditions – a long-sought solution to sourcing chemicals from renewable biomass.

The more hindered Lewis acid tri-isobutylaluminum (Al*i*Bu₃) unsurprisingly exhibited slower, but effective, deoxygenation rates even at higher temperatures. Surprisingly, treatment of dibenzofuran with catalyst **26b** and a substoichiometric amount of Al*i*Bu₃ under more forcing conditions (150 °C, 2 atm H₂) afforded a mixture of biphenyl **143**, 2-phenylphenol **229**, and for the first time, trace levels of cyclohexylbenzene **230**, the product of aromatic ring hydrogenation (Equation 5.21). This is perhaps an indication of slow catalyst decomposition under harsher process conditions.

Equation 5.21



Control experiments were conducted to verify the role of the Lewis acid additive, AlMe₃, and the basic scavenger (KH) in the deoxygenation process. Potassium hydride itself does not deoxygenate DBF under the given conditions. Treatment with two equivalents of KH and 0.5 equivalents of AlMe₃ in the absence of **26b** does not produce detectable levels of deoxygenation or C–O bond hydrogenolysis. This suggests that the nickel cluster **26b** is mainly responsible for the catalytic hydrodeoxygenation.

We have also evaluated the ability of trialkylaluminum reagents to act simultaneously as Lewis acid activators of C–O bonds and as stoichiometric scavengers of protic catalyst byproducts/poisons. Treatment of dibenzofuran with 0.5 equivalents of AlMe₃ and catalytic **26b** (0.5 mol%) in the absence of KH, however, does not produce detectable levels of C–O bond hydrogenolysis. This shows that, under the given reaction conditions, KH is an optimal proton scavenger, promoting catalytic turnover but not itself inducing C–O bond scission.

Moreover, treatment of **26b** with stoichiometric AlMe₃ in toluene results in an abrupt color change and precipitate formation, potentially indications of the formation of a minimally soluble **26b**–AlMe₃ adduct that is catalytically less active or inactive.

5.2.4 Mechanism of Hydrodeoxygenation

As discussed in Chapter 4, the complexity that KH causes in deuterium labeling experiments makes systematic studies of the reaction mechanism both complicated and challenging. At this point, there are insufficient experimental data to propose a detailed reaction mechanism for the nickel-catalyzed C–O bond hydrogenolysis. Since trace amounts of aromatic ring hydrogenation is detected at 150 °C under higher H₂ pressures in the presence of trimethylaluminum, definitive claims on the homogeneous nature of the active catalyst cannot be made at this point.

Nonetheless, the absence of aromatic hydrogenation products in the majority of the C–O hydrogenolysis and complete hydrodeoxygenation studies strongly suggests that the catalyst is highly selective for direct C–O bond activation. In this regard, we tentatively propose a pathway similar to the mechanism proposed for catalytic hydrodesulfurization of DBT **129** in Chapter 4. This catalytic cycle involves substrate precoordination to the active catalyst **50** through the Lewis basic oxygen

center, forming intermediate **231**. The catalyst selectivity for direct C–O bond hydrogenolysis presumably proceeds through a metal– π arene complex **232** (Figure 5.2). This binding motif increases the electrophilicity of the C(α) center, allowing for C–O bond scission through hydride delivery. The catalyst selectivity for direct C–O bond hydrogenolysis with complete suppression of ring hydrogenation potentially results from substrate-dependent strength(s) of metal– π coordination. The π -type binding of highly aromatic aryl substrates (e.g. dibenzofuran) to active metal centers presumably results in weak disruption of ring aromaticity, insufficient to activate the substrate for ring hydrogenation reactions. This mode of C_{aryl} –O bond activation is supported by mechanistic studies reported by the groups of Agapie²⁷⁴ and Martin²⁷⁵ on alkyl aryl ether hydrogenolysis mediated by mononuclear nickel complexes. Substrate reactivity resulting from p-type substrate precoordination is expected to vary with substrate class. For example, polycyclic substrates with lower aromaticity (e.g. benzofuran) are known to adopt various modes of metal coordination, undergoing ring hydrogenation prior to C–O bond scission (Figure 5.3).²²³

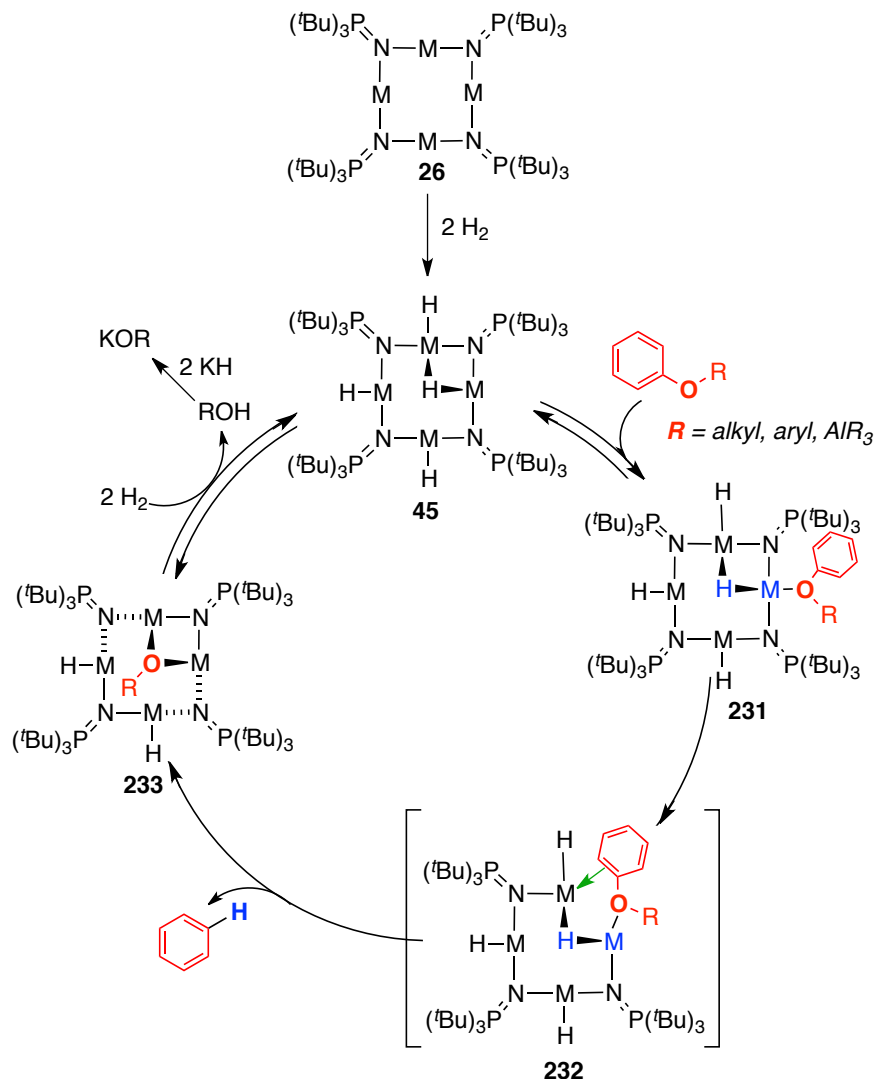


Figure 5.2. Proposed Hydrodeoxygenation Mechanism Catalyzed by **26b**.

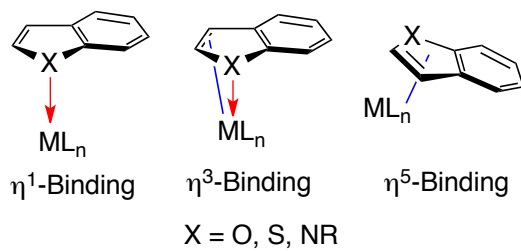
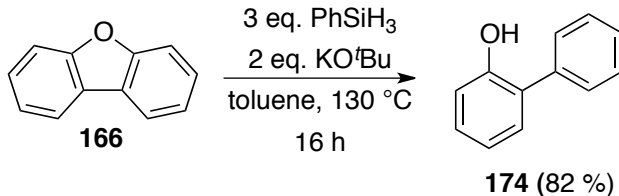


Figure 5.3. Binding Modes of Benzothiophene- and Benzofuran-type Substrates.

5.2.5 Metal-Free C–O Bond Hydrogenolysis

It was proposed in Chapter 4 that an activated organosilyl hydride is generated *in situ* from the reaction of silane with strong nucleophilic bases, and that such hydridic silylates are capable of metal-free hydrogenolysis of the C–S bonds in dibenzothiophene **129**. This metal-free methodology was also evaluated for the hydrogenolysis of C–O bonds in dibenzofuran **198**. Treatment of dibenzofuran with excess PhSiH₃ and KO*t*Bu at elevated temperature surprisingly resulted in highly selective cleavage of only the first C–O bond, exclusively forming of 2-phenylphenol **229** (Equation 5.22). The formation of biphenyl was not observed in this preliminary trial. This result demonstrates the potential generality of the metal-free C–X bond hydrogenolysis strategy that has been observed, albeit not optimized. In early 2013, Grubbs and coworkers just recently published the use of organosilyl hydride reagents activated by a range of potassium ion-containing organic and inorganic bases for aryl ether cleavage.²³⁷.

Equation 5.22



5.3 Catalytic C–N Bond Hydrogenolysis and Hydrodenitrogenation

Catalytic activation of carbon-nitrogen bonds is a critical process for the production of environmentally safe, petroleum-derived fuels and commodity chemicals. Relative to hydrodesulfurization, the reductive removal of nitrogen (HDN) is more difficult and more costly since traditional hydrotreatment catalysts (CoMoS_2 and NiWS_2) can only effect practical HDN rates under the harshest process conditions (200 bars H_2 , 350–500 °C).²⁵³⁻²⁵⁴

Petroleum feedstocks contain a myriad of nitrogen-containing components known to create a wide range of undesirable effects in the production and use of transportation fuels (Figure 5.4).²⁵⁶ Gaseous nitrogen oxides (NO_x), formed from combustion of nitrogen-containing compounds, contribute to the *acid rain* phenomenon and are considered greenhouse gases. In addition, N-containing compounds irreversibly poison most heterogeneous industrial hydrotreatment catalysts, reducing process efficiencies and catalyst lifespan. Residual nitrogen compounds present in petroleum-derived chemical products also cause consumer-related issues such as (1) odor and color, (2) thermal and oxidative fuel instability, and (3) fuel processing and fuel cell poisoning.

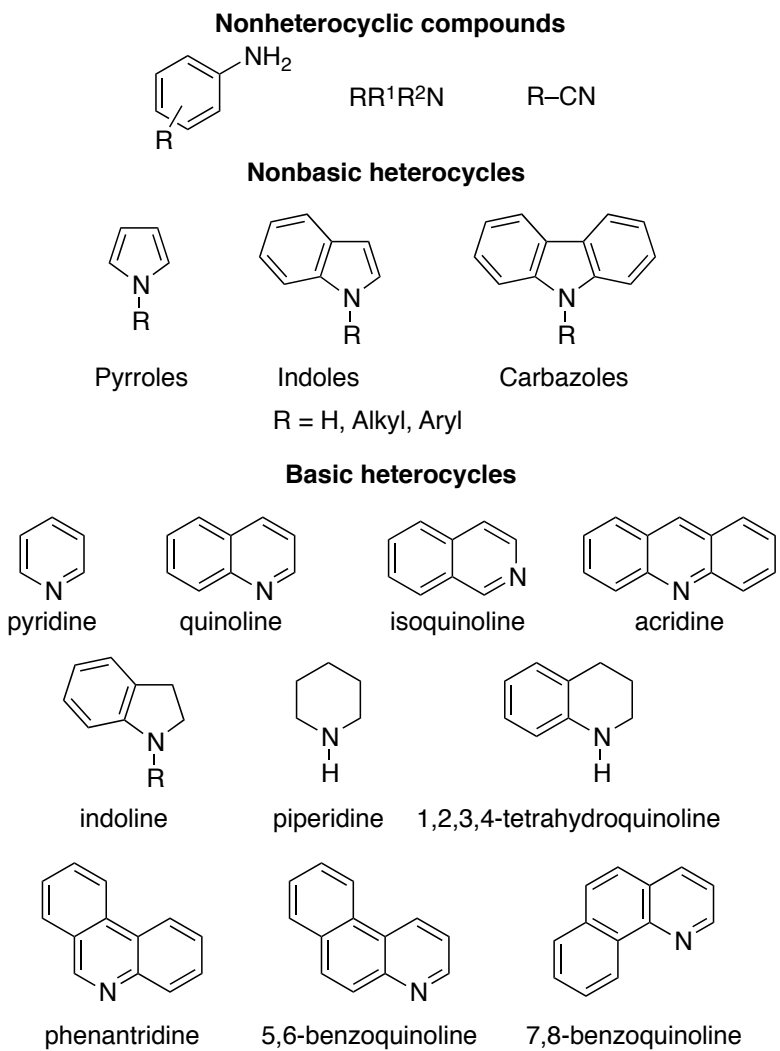


Figure 5.4. Classes of nitrogen-containing components of petroleum.

Figure 5.4 illustrates several classes of nitrogen-containing compounds present in petroleum. Among these components, aromatic N-heterocycles are the most resistant to C–N bond hydrogenolysis. Figure 5.5 illustrates purported denitrogenation pathways of quinolone 234 mediated by heterogenous transition metal catalysts.²⁵⁶ Similar to aromatic ethers, hydrogenolysis of aromatic heterocycles by heterogeneous catalysts generally produces mixtures of alkanes and olefins due to

prerequisite aromatic ring hydrogenation to weaken the strong C–N bonds. The removal of nitrogen thus proceeds through a series of ring hydrogenations. Industrial research revealed that acidic hydrotreatment poisons (BH, Fig. 5.5) such as H₂S and H₂O improve rates of hydrodenitrogenation. These acidic species are believed to protonate amino functionalities, hence, allowing for facile extrusion of ammonia or amino fragments through Hoffman-type elimination (Equation 5.23) or the direct nucleophilic substitution of the amino leaving group by nucleophiles (Equation 5.24).²⁷⁹ Lewis acidic sites on heterogeneous catalyst surfaces also promote this mode of C–N activation.

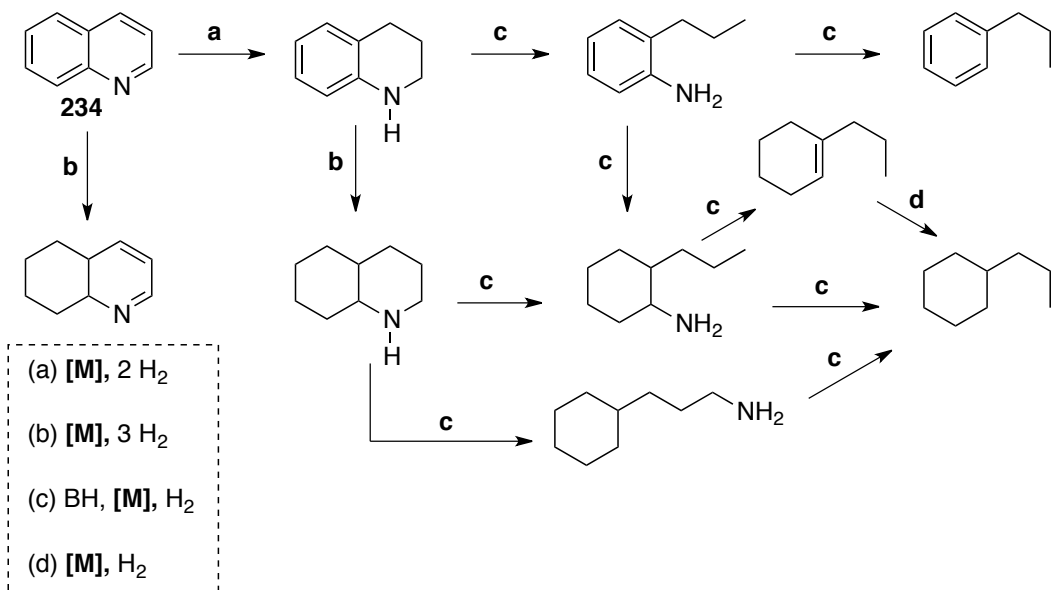
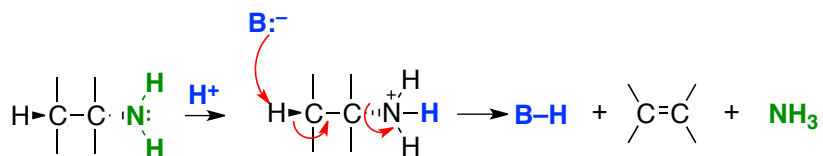
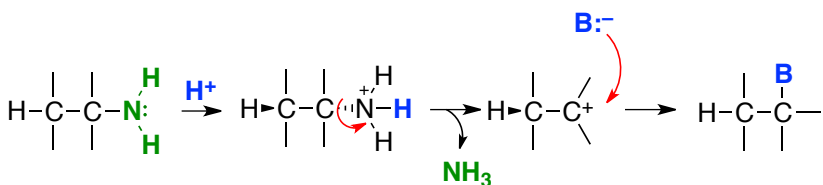


Figure 5.5. Hydrodenitrogenation of benzoquinoline substrates.²⁵⁰

Equation 5.23



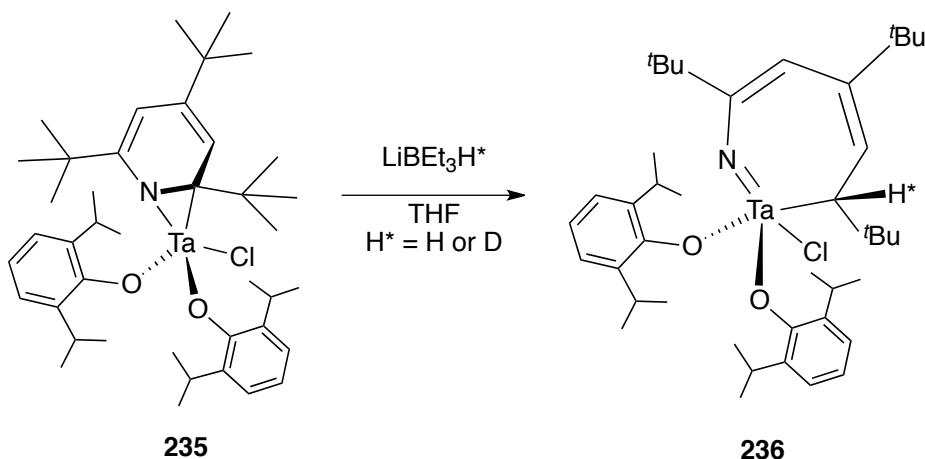
Equation 5.24



Organometallic modeling of HDN catalyst active sites is expected to provide fundamental information on productive and unproductive metal-substrate binding motifs that may lead, ultimately, to carbon-nitrogen bond scission. Unfortunately, the great diversity in the types of nitrogen-containing compounds contributes to the lack of a consensus strategy for the design of optimum homogeneous catalysts, since each distinct class of nitrogen compound can adopt various modes of binding and, in turn, reactivity. A few comprehensive reviews on mononuclear and polynuclear organometallic models for C–N bond scission have been published in the past two of decades.^{203,224,256,280,281} The current literature, however, clearly shows a dearth of molecular transition metal complexes capable of activating carbon-nitrogen bonds. Reported organometallic models are generally limited to catalytic aromatic ring hydrogenation and, even more rarely, stoichiometric C–N bond activation.²⁵⁶

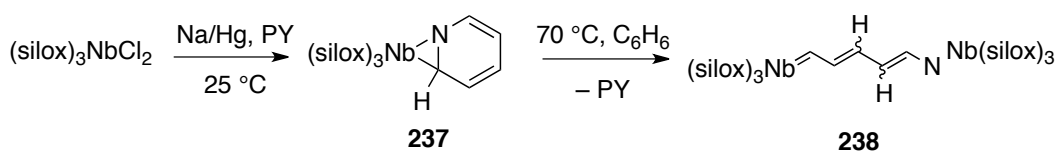
Pioneering reports by Wigley²⁸¹ and Wolczanski^{83,283} on transition metal insertion into C–N bonds in pyridine-type substrates revealed two crucial structural prerequisites for organometallic HDN models: (1) coordinative unsaturation and (2) low valency. Wigley and coworkers²⁸²⁻²⁸⁴ were the first to report stoichiometric metal insertion into a C–N bond in a tantalum metallaziridine complex **235** (Equation 5.26). Their findings revealed that pyridine and quinoline-type substrates prefer to adopt $\eta^2(\text{C},\text{N})$ -coordination with nominally d² tantalum complexes. This $\eta^2(\text{C},\text{N})$ -binding motif disrupts ring aromaticity, hence, decreasing the C–N bond order and, ultimately, activating the C(α) center for nucleophilic attack by an incoming hydride ion. Treatment of the metallaziridine complex **235** with stoichiometric LiBEt₃H results in selective hydride delivery at the C2 position, cleaving the C–N bond and forming the azametallacycloheptatriene complex **236**. This transformation, however, is strain-driven; pyridine (PY) and quinoline (Q) ligands in [(silox)₃Ta{ $\eta^2(\text{N},\text{C})$ -(PY)}] and [(DIPP)₂Ta{ $\{\eta^2(\text{N},\text{C})\}$ -Q}] do not undergo C–N bond cleavage upon treatment with inorganic hydrides. The tert-butyl substituents in **235** potentially torque the aromatic ring, which may reduce the aromaticity of the pyridine core.^{281,282}

Equation 5.25



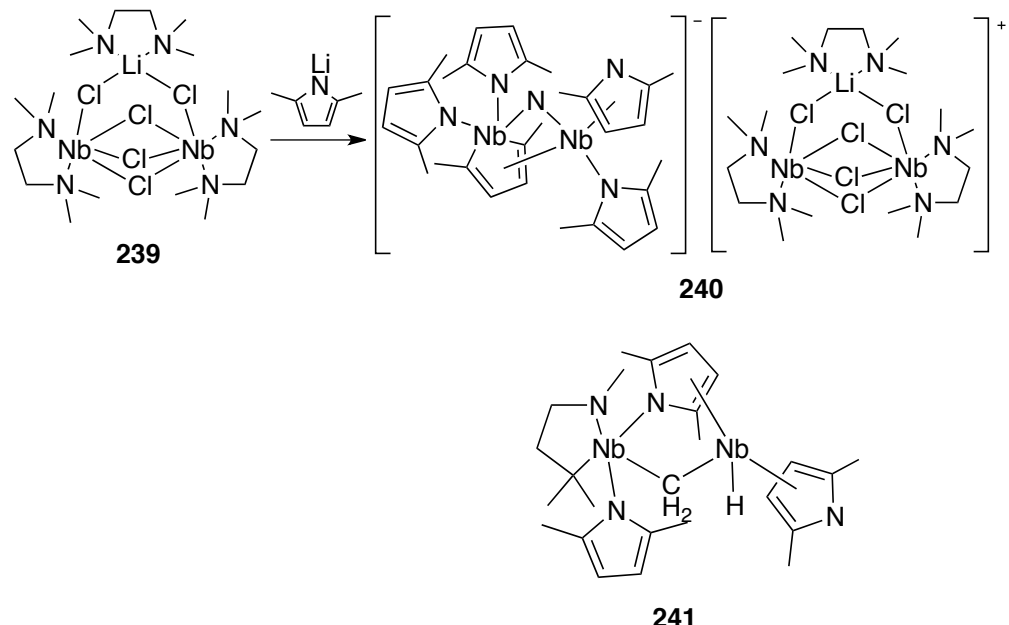
Contrary to Wigley's report on strain-driven C–N bond activation in pyridines, Wolczanski and coworkers reported the oxidative insertion of low-valent niobium fragments into one C–N bond in unsubstituted pyridine.²⁷⁴ Structural confirmation of the disruption of aromaticity was observed in the η^2 -coordinated pyridine molecule in complex **237** (Equation 5.26). Facile niobium insertion into the C–N bond was achieved under mild thermolysis conditions.²⁷⁴ To the best of our knowledge, direct C–N bond cleavage of pyridine-type substrates mediated by first row transition metal complexes has only been demonstrated using a titanium-pincer complex,²⁵⁵ pyridines and quinolines preferentially bind in a $\eta^1(N)$ -fashion with first row transition metal complexes, producing coordination complexes which are inactive for intramolecular C–N bond scission.^{256,281}

Equation 5.26



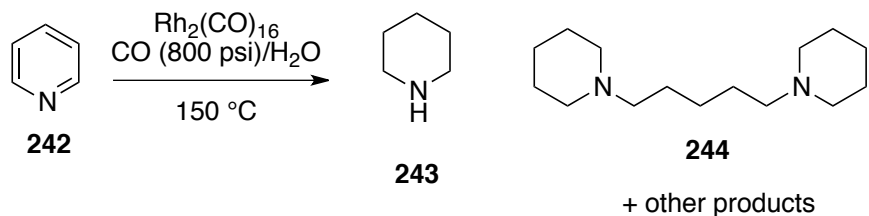
Ligand-supported transition metal clusters have been used as ideal models for polynuclear active sites for C–N bond activation.²⁵⁶ Bimetallic niobium complex **239** effected the substoichiometric denitrogenation of anionic 2,5-dimethylpyrrolide, affording the complex salt **240**, where the bimetallic anion bears a doubly bridging nitride moiety.²⁸⁵ The reaction also produces the neutral bimetallic product **241**, arising from metal-mediated C–C and C–H bond activation of the TMEDA ligand in **239** (Equation 5.26). This transformation clearly features the bimetallic activation of C–N bonds in pyrrolyl anions, although the hydrocarbon residue was not identified. The oxidative scission of the two C–N bonds is attributed to the oxidation of four formally Nb⁺² centers that form the complex salt – an isolated example of a polynuclear complex capable of multi-electron scission of C–N bonds.²⁸⁵

Equation 5.26



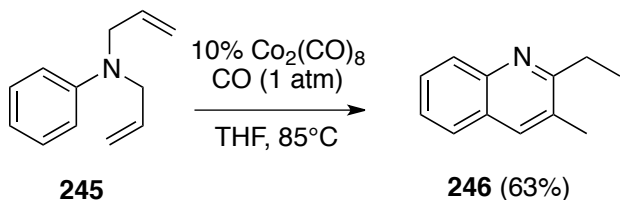
Catalytic C–N bond cleavage is extremely rare. Several reported examples are catalyzed by polynuclear transition metal complexes under non-hydrogenative conditions. The bimetallic rhodium carbonyl complex Rh₆(CO)₁₆ catalytically hydrogenates and hydrogenolyzes pyridine **242** under the conditions of the water-gas shift reaction, forming piperidine **243** and bis(piperidinyl) products (e.g., **244**).²⁸⁶ The formation of the latter is attributed to catalytic C–N bond hydrogenolysis (Equation 5.27).

Equation 5.27



William Jones and coworkers reported a pivotal contribution by demonstrating that base metal carbonyl clusters can catalyze C–N bond scission. The bimetallic cobalt carbonyl, $\text{Co}_2(\text{CO})_8$, catalytically converts arylamines **245** to quinolines **246** under carbon monoxide atmosphere (Equation 5.28). This transformation must involve a rare base metal-catalyzed activation of a C–N bond under mild conditions. The rearrangement of allylamines is proposed to proceed through bimetallic activation of a C–N bond, giving an allyl-cobalt complex **248** and amido-cobalt intermediate **247** (Figure 5.6).¹⁰⁸

Equation 5.29



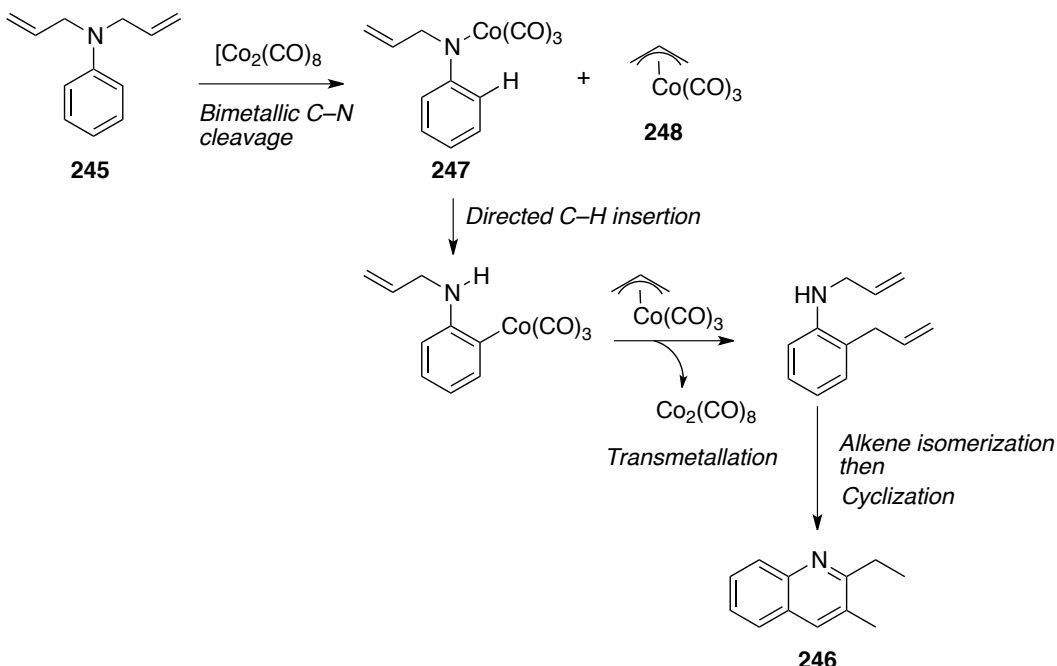


Figure 5.6. Bimetallic activation of C–N bond mediated by $\text{Co}_2(\text{CO})_8$.²⁸⁷

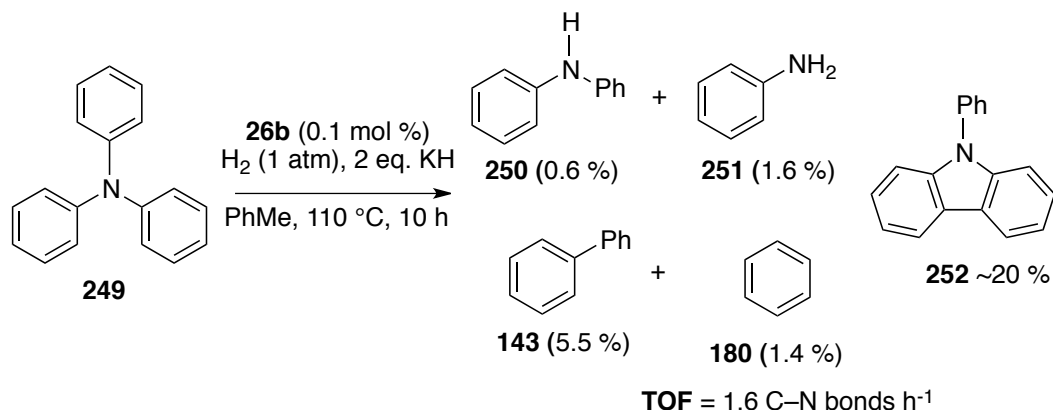
5.3.1 Results and Discussion: C–N bond Hydrogenolysis

The succeeding sections present our preliminary findings in the catalytic hydrogenolysis of C–N bonds in neutral and basic nitrogenous compounds. The optimization of conditions for reductive C–N bond activation was conducted concurrently with C–O bond hydrogenolysis and hydrodeoxygénéation studies, hence, the C–N bond experiments presented (*vide infra*) were obtained from experiments catalyzed by the low-coordinate nickel cluster **26b** employing the conditions shown optimal for catalytic HDO. Nickel-catalyzed hydrogenolysis of C–N bonds in several classes of nitrogenous substrates was achieved under mild reaction

conditions (1–2 atm H₂, 110–160 °C as opposed to 400 °C for industrial hydrodenitrogenation). The latter part of this section briefly presents the surprising, albeit preliminary, demonstration of the hydrodenitrogenation activity of the mononuclear Co(III) complex [Co(NP^tBu₃)₃] **22**; which gives an unprecedented *complete denitrogenation* of N-alkylcarbazole was achieved with complete suppression of aromatic ring hydrogenation.

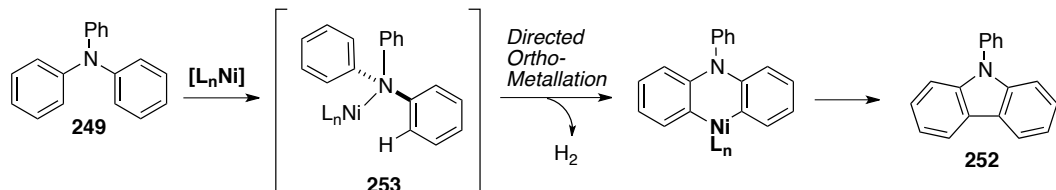
Under mild conditions, the tetrametallic Ni(I) cluster **26b** catalytically cleaves the strong C–N bonds in triphenylamine **249**, affording a complex mixture of arylamines and aromatic hydrocarbons (Equation 5.29), including some unanticipated reaction products. Benzene, the expected major product of C–N bond hydrogenolysis was obtained only in minor quantities. This is presumably due to the strong tendency of the resulting aniline **251** and diphenylamine **250** to bind competitively with the active metal centers.

Equation 5.29

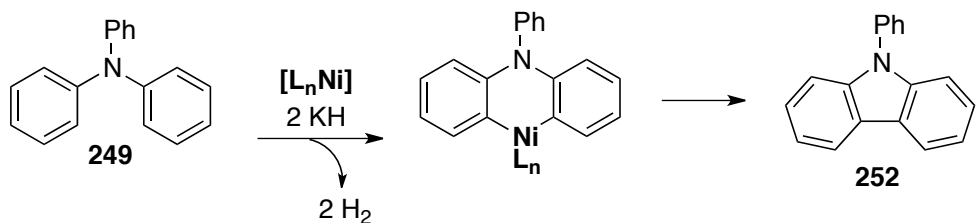


The reaction surprisingly returned *N*-phenylcarbazole **252** as the major product. This derivative presumably forms from directed *ortho*-metallation of triphenylamine **249**. Under the given process conditions, directed *ortho*-metallation can presumably proceed via two reasonable pathways. The first mechanism involves the directed insertion of a nitrogen-bound nickel fragment (**253**) into an *ortho*-C–H bond. Reductive coupling of two orthometallated aryl fragments produces *N*-phenylcarbazole (Equation 5.30). An equally probable mechanism involves KH-induced *ortho*-metallation followed by transmetalation to an organometallic nickel fragment for the reductive coupling (Equation 5.31). At this point, however, there is insufficient experimental observation to rule out either of the two possible mechanisms. Purposeful optimization of conditions and investigation of the mechanism of *N*-phenylcarbazole formation could provide a synthetically useful methodology for the synthesis of *N*-alkylcarbazoles from diarylamines.

Equation 5.31



Equation 5.32

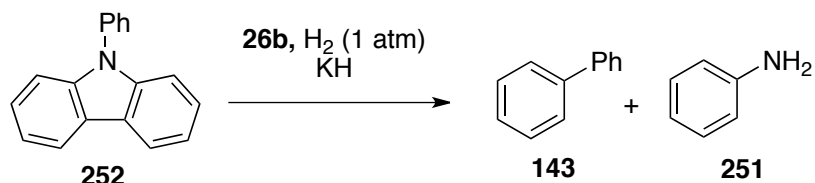


The second major product from carbon-carbon bond formation, biphenyl **143**, also dominated the denitrogenated fractions. Biphenyl can originate from nickel-mediated dehydrogenative coupling of benzene or KH-induced C–H activation in benzene, followed by transmetalation to nickel and reductive aryl coupling. If nickel-mediated C–H activation is the main contributing mechanism, the prevalence of aryl coupling pathways becomes indicative of the polynuclear nature of the active catalyst since the concomitant C–H bond activation of two benzene molecules is, ideally, more facile in the presence of more than one metal active site. At this point, however, we do not have sufficient mechanistic information to propose the nuclearity of the active catalyst.

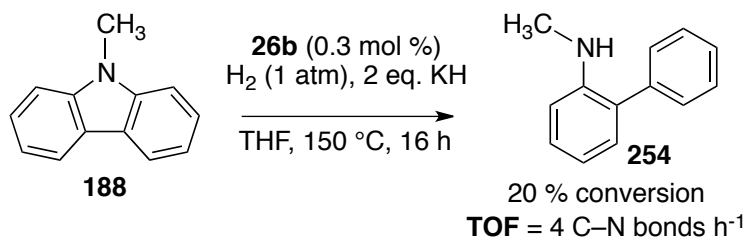
Considering the prevalence of *N*-phenylcarbazole **252** formation during the course of the reaction, it could also be reasoned that biphenyl originates from the complete hydrogenation of **252**, producing aniline **251** and **143** (Equation 5.32). To validate or refute this hypothesis, the hydrogenation of *N*-methylcarbazole **188** was conducted in THF under purposefully mild conditions. Treatment of **188** with catalytic

amounts of **26b** and KH in toluene at 150 °C resulted in a 20% conversion to *N*-methyl-2-phenylaniline **254** as the only product detected by GC-MS (**TON** = 4 C–N bonds/h, Equation 5.33). The catalyst does not yield biphenyl **143** even under harsher conditions (2 atm H₂, 150 °C, longer time). This suggests that the formation of biphenyl in the hydrogenolysis of *N*-triphenylamine does not proceed through the hydrogenation of *N*-phenylcarbazole.

Equation 5.32



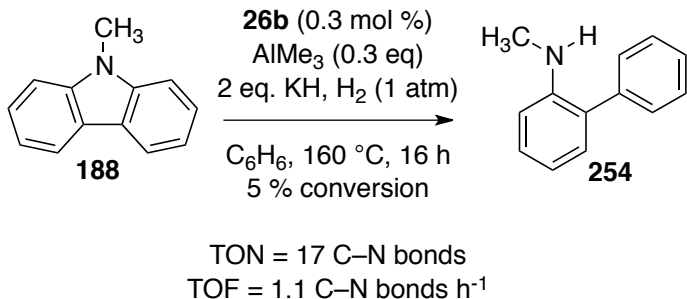
Equation 5.33



The addition of Lewis acid promoters to the Ni(I) catalyst in benzene surprisingly resulted in attenuated rates of C–N bond hydrogenolysis under otherwise identical process conditions (Equation 5.34). This can be tentatively attributed to a solvent effect, assuming cluster dissociation to be more favored in polar coordinating solvents such as THF. Cluster dissociation to lower nuclearity species could explain the

faster rates of C–N bond scission observed in THF. The slower conversion might also be due to the formation of a stabilized adduct between AlMe₃ and **26b**, which could be less active toward C–N bond activation.

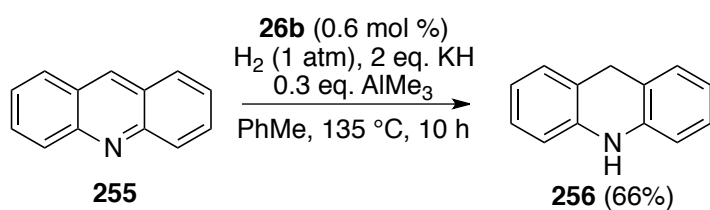
Equation 5.34



The catalytic hydrogenolysis of C–N bonds in *N*-methylcarbazole prompted us to explore the activity of catalyst **26b** for the reduction of nitrogenous aromatic substrates with basic nitrogen centers such as acridine **255**. Treatment of **255** with catalytic amount of **26b** under mild conditions (135 °C, 1 atm H₂, Equation 5.35) resulted mainly in ring hydrogenation to give 9,10-dihydroacridine **256** while products from C–N bond hydrogenolysis were not observed. Acridine undergoes slower hydrogenation of the middle ring (25%) under the given conditions in the absence of the tetrametallic Ni(I) catalyst **26b**. The formation of 9,10-dihydroacridine under the given conditions could be Lewis acid-assisted; quenching of the *N*-Al bond in an acridine-AlMe₃ adduct could essentially produce the observed hydrogenated species. The observed faster rate of acridine hydrogenation in the presence of the tetrametallic Ni(I) cluster

suggests an active role of the nickel catalyst in the selective ring reduction. The unsurprising prevalence of ring-hydrogenation products is mainly driven by the increased total aromatic stabilization energy of the terminal phenyl rings in the hydrogenation product. This transformation highlights a key step necessary for the catalytic reduction of basic nitrogen heteroaromatics. In addition, selective ring hydrogenation of such substrates has been an important methodology for fine chemical synthesis.²⁸⁸⁻²⁹⁰

Equation 5.35



Despite our lack of insight into the nature of the active catalyst, the product distributions observed in C–N bond hydrogenolyses provide important mechanistic clues. The activation of C–N bonds in triphenylamine **249** and *N*-methylcarbazole **188** proceeds without competitive aromatic hydrogenation. This is consistent with the catalyst selectivity earlier demonstrated for direct C–S and C–O bond hydrogenolysis in heteroaromatic substrates. This is more than a little surprising, especially in the case of carbazole-type substrates since it has been established that under harsh process conditions, heterogeneous

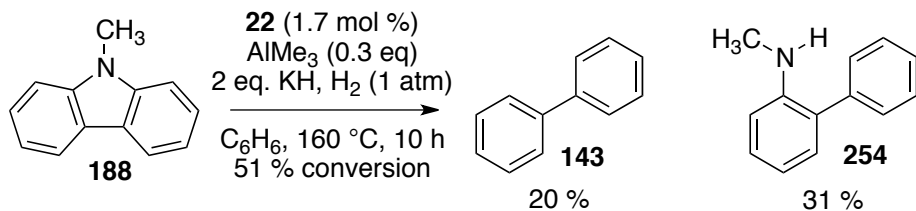
catalysts hydrogenate the aromatic rings, weakening the C–N bonds prior to scission.^{253,254,291}

5.3.2 Catalytic Hydrodenitrogenation with a Mononuclear Co(III) Precatalyst

The profound effect of Lewis acid promoters on the activity of the Ni(I) cluster **26b**, driving the reaction to the complete hydrodeoxygenation of dibenzofuran **198**, inspired us to evaluate the effect of Lewis acids on the catalytic activity of the mononuclear Co(III) complex [Co(NP^tBu₃)₃] **22**. In contrast to the Ni(I) precatalyst, the homoleptic three-coordinate complex **22** exhibited much higher activity for C–N bond hydrogenolysis in the presence of AlMe₃ than in its absence. Treatment of *N*-methylcarbazole **188** with catalytic amount of **22** under hydrogen but in the absence of AlMe₃ does not afford hydrodenitrogenation products. However, treatment of *N*-methylcarbazole **188** with catalytic amount of **22**, 2 equivalents of KH and substoichiometric AlMe₃ under hydrogen resulted in faster C–N bond hydrogenolysis and complete HDN, giving a 2 : 3 mixture of biphenyl **113** and the expected intermediate *N*-methyl-2-phenylaniline **254** (Equation 5.36). This experiment, albeit preliminary, is the *first demonstration of complete hydrodenitrogenation of the carbazole framework by a base metal catalyst* – a reaction that proceeds under exceptionally mild conditions. No competitive aromatic hydrogenation was

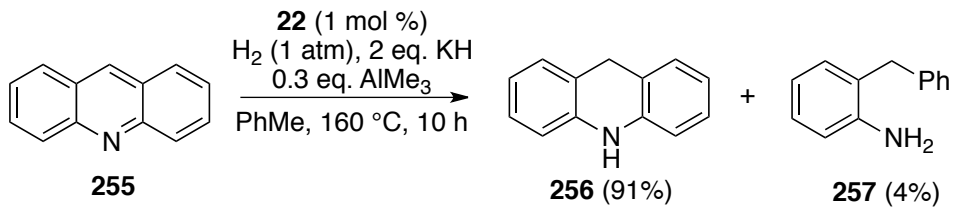
observed, again unprecedented among homogeneous catalysts.²⁵⁶ Thorough investigation is needed to understand the nature of the active hydrodenitrogenation species.

Equation 5.36



The enhanced activity of the Co(III) precatalyst in the presence of AlMe₃ was also observed in the C–N bond hydrogenolysis of acridine (Equation 5.37). Treatment of acridine with catalytic amount of **22** gave a mixture of 9,10-dihydroacridine **256** (91%) and, gratifyingly, 2-(phenylmethyl)aniline **257** (4%).

Equation 5.37



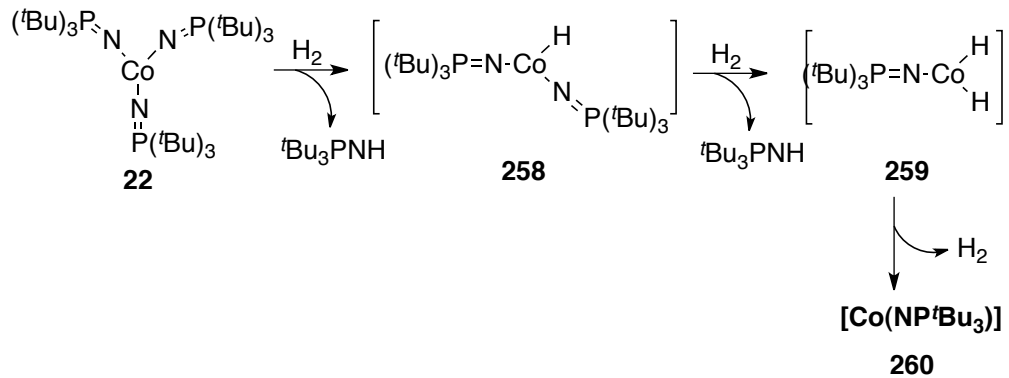
The higher activity of the Co(III) catalyst **22** is more than a little surprising, raising questions as to the nature of the poorly understood active species formed upon reaction with hydrogen. Considering the

process conditions, the cobalt(III) precatalyst can presumably form a range of potentially active organometallic derivatives with different oxidation states and cluster nuclearities.

The addition of AlMe₃ to a solution containing the Co(III) precatalyst **22** results in abrupt color change from cherry red to intensely dark red. This could be indicative of the formation of an adduct between AlMe₃, a basic lone pair of the terminal phosphoranimide ligand, and the coordinatively unsaturated Co(III) center. If a heteropolymetallic cobalt-aluminum derivative is responsible for the observed catalytic activity, this demonstration could parallel and potentially model the integral role of Lewis acidic sites on heterogeneous hydrotreatment catalysts. In addition to the purported proton-assisted cleavage of C–N that may occur during industrial hydrodenitrogenation,^{292,293} there is considerable speculation about the crucial role of Lewis acidic sites on alumina-supported catalysts in the cooperative activation of C–N bonds. In this respect, the nuclearity of the precatalyst in our system appears to be crucial for the formation of an active hydrodenitrogenation catalyst, given the attenuation of the C–N bond hydrogenolysis rates observed using the Ni(I) precatalyst cluster in the presence of AlMe₃. The purposeful synthesis, isolation and characterization of adducts of AlMe₃ with precatalysts **22** and **26a (26b)** will undoubtedly provide a more definitive explanation of the observed difference in catalyst activity.

Conversely, it can be reasoned that under the relatively harsh hydrogenation conditions, the monomeric Co(III) precatalyst mediates heterolytic activation of hydrogen to give the hydridobis(*tri-tert*-butylphosphoranimido)cobalt(III) complex **258** (Equation 5.38) with loss of the neutral phosphoranimine. The low-coordinate complex **258** can potentially act as a mononuclear active catalyst, binding with the nitrogen-containing substrate present in significantly higher concentration. Complex **258** can also form aggregates with other cobalt-phosphoranimide fragments in solution to form dinuclear or polynuclear cobalt-phosphoranimide clusters. In addition, complex **258** can potentially activate another dihydrogen molecule to form the dihydridocobalt(III) derivative **259**, which can undergo reductive release of hydrogen to produce a monophosphoranimidocobalt(I) fragment **260** – *the monomeric unit that comprises the tetrametallic precatalyst **26a***. This mechanistic proposal can be confirmed through systematic kinetic investigations, comparing the hydrogenolysis activity of the mononuclear Co(III) precatalyst **22** with the tetrametallic Co(I) cluster **26a** at a range of concentrations. These mechanistic proposals are highly speculative, hence, comparative studies of the HDN activities of **22** and **26a/b** undoubtedly comprise an important topic for future research.

Equation 5.38



5.4 Conclusions

Optimum conditions for catalytic activation of C–O bonds have been identified using low-coordinate phosphoranimide complexes of the base metals. Symmetrical aryl ethers are cleaved to give mixtures of aromatic hydrocarbons and phenols. The catalysts were shown to be moderately selective for $\text{C}_{\text{aryl}}-\text{O}$ bond cleavage in alkyl aryl ethers under mild reaction conditions. Deep hydrogenation (HDO) of dibenzofuran was achieved in the presence of substoichiometric (albeit non-optimized) amounts of the Lewis acid promoter AlMe_3 , exclusively affording biphenyl with complete suppression of aromatic ring hydrogenation.

Preliminary experiments clearly demonstrate the activity of tetrametallic nickel cluster **26b** and the mononuclear homoleptic Co(III) complex **22** toward catalytic C–N bond hydrogenolysis. The tetrametallic

cluster **26b** effects C–N bond hydrogenolysis in non-basic and basic nitrogenous substrates even in the absence of a Lewis acid promoter.

Intriguingly, the activity of the mononuclear precatalyst **22** is markedly enhanced in the presence of a Lewis acid additive, effecting an unprecedented denitrogenation of heteroaromatic nitrogen substrates.

With the preliminary HDN results at hand, the nature of the active catalysts obtained from both tetrametallic and mononuclear precatalysts requires systematic mechanistic and structural investigations to define the structure of the active catalyst(s). In addition, further optimization of the reaction conditions and thorough investigation of the scope of heteroaromatic substrates is clearly that next phase of this investigation.

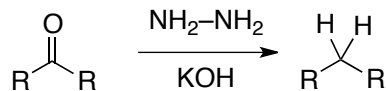
Chapter 6

**Exceptionally Active Base Metal Catalysts for Deoxygenation of
Carbonyl Compounds Under Mild Conditions**

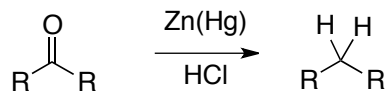
6.1 Introduction

Efficient and cost-effective deoxygenation of carbonyl functional groups remains one of the most sought-after industrial and laboratory processes for its wide range of applications in organic synthesis and biomass hydrotreatment.^{258,294-296} Traditional carbonyl deoxygenation strategies generally operate under strongly acidic/basic conditions, in some cases, requiring stoichiometric heavy metal reagents. Wolff-Kishner carbonyl reduction requires excess amounts of explosive hydrazines at elevated temperatures²⁹⁶⁻²⁹⁸ (Equation 6.1) while Clemmensen reduction uses mixtures of strong acids and toxic heavy metals (e.g. mercury; Equation 6.2).²⁹⁹⁻³⁰² Other laboratory approaches involve the conversion of carbonyl substrates to their dithiane derivatives, followed by stoichiometric reductive cleavage of relatively weaker C–S bonds using strong reducing agents (e.g. main group hydrides or Raney Nickel; Equation 6.3).²¹¹ This dependency on expensive and hazardous reagents limits the economic profitability of these strategies.

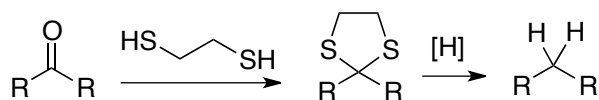
Equation 6.1



Equation 6.2



Equation 6.3



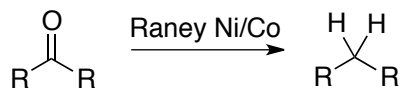
The field continues to develop cost-effective carbonyl deoxygenation strategies. Metal-free³⁰³ and transition metal-mediated³⁰⁴⁻³⁰⁷ methodologies have been reported in recent decades, but catalytic methodology remains elusive. Transition metal-catalyzed carbonyl reduction constitutes an ideal alternative strategy; however, high-activity transition metal reagents and catalysts remain scarce. Most transition metal catalysts are limited to reduction of C=O bonds to the corresponding alcohol(s).

Transition metal-catalyzed carbonyl deoxygenation is extremely rare. Most literature examples describe heterogeneous second- and third-row transition metal catalysts. Tungsten/molybdenum oxides,³⁰⁴ promoted by first row transition metals and heterogeneous palladium nanoparticles, have been reported for the deoxygenation of a range of carbonyl substrates under hydrosilylation conditions.^{306,307} Among transition metals, palladium is the most extensively studied for carbonyl deoxygenation. Palladium nanoparticles catalytically reduce aryl carbonyl substrates to mixtures of alcohols and hydrocarbons under hydrosilylation conditions. These processes, however, require harsh reaction conditions and the use

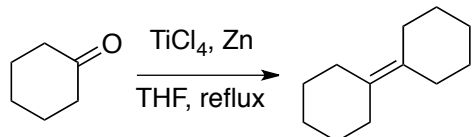
of excess quantities of activators and additives (e.g. F^- ions and Lewis acids).^{306,307}

Naturally abundant and less toxic first row transition metals are, potentially, ideal reagents and catalysts for carbonyl deoxygenation. Base metal-mediated carbonyl deoxygenation has previously been reported only using excess (and hazardous) Raney cobalt or Raney nickel for conversion of C=O to methylene,^{308,309} or a large excess of low-valent titanium for carbonyl reductive olefination – the *McMurry coupling* (Equations 6.4-6.5).^{294,305,310,311} Until this work, base metal-catalyzed carbonyl deoxygenation was unprecedented.

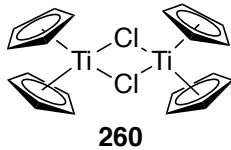
Equation 6.4



Equation 6.5



Organometallic titanium complexes such as bimetallic Nugent's reagent **260** are used to model heterogeneous titanium active sites for mechanistic investigation of carbonyl coupling olefination. Mechanistic studies reveal that low-valent titanium radicals are the active species for the *McMurry* reaction.^{305,312}

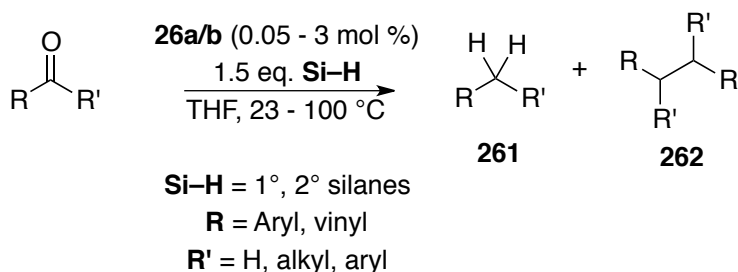


The high activity of catalysts **26a** and **26b** (Figure 6.1) for carbonyl hydrosilylation and the formation of trace carbonyl deoxygenation products at room temperature (Chapter 3) prompted us to identify optimum conditions for cobalt and nickel-catalyzed deoxygenation of carbonyl substrates.

6.2 Results and Discussion

In this chapter, we report unprecedented, additive/activator-free cobalt- and nickel-catalyzed deoxygenations of functionalized aryl and α,β -unsaturated carbonyl compounds. These reactions are mediated by both tetrametallic clusters **26a** and **26b** under exceptionally mild hydrosilylation conditions (25 – 100 °C). The catalytic deoxygenation is non-selective; mixtures of monomeric **261** and dimeric **262** deoxygenation products are formed with product distributions varying with substrate-type, catalyst, used and reductant concentration (Equation 6.6).

Equation 6.6



**6.2.1 Deoxygenation of α,β -unsaturated Carbonyl Substrates:
Prelude to Catalytic Terpene Upgrading**

Since the deoxygenation of α,β -unsaturated ketones was initially demonstrated using the nickel catalyst **26b**, most of the results presented in the succeeding subsections were obtained from nickel-catalyzed reactions. Both clusters **26a** and **26b** effect the deoxygenation of the α,β -unsaturated ketone, 2-cyclohexen-1-one **263**, with PhSiH₃ as the reducing agent under mild conditions. The nickel catalyst **26b** deoxygenates **263** at *room temperature*, affording a mixture of alkoxy silanes (**265-267**) and the dimeric hydrocarbon **264** – an over-reduced but otherwise *McMurry-type reductive dimerization* (Equation 6.7). At room temperature, the hydrosilylation resulted in a 15% substrate conversion to **264** (Entry 1, Table 6.1). Increasing the temperature to 60 °C increased substrate deoxygenation to 35%; the remaining 65% of the starting material was converted to the intermediate alkoxy silanes (Entry 2, Table 6.1). The product distribution suggests the strong propensity of the catalyst to reduce polar C=O bonds over nonpolar C=C bonds. The catalytic reaction

only proceeds efficiently with aryl- and α,β -unsaturated carbonyl substrates. Saturated aliphatic ketones (e.g. cycloheptanone) undergo quantitative reduction to the corresponding silyl ether, but only deoxygenate stoichiometrically.

Equation 6.7

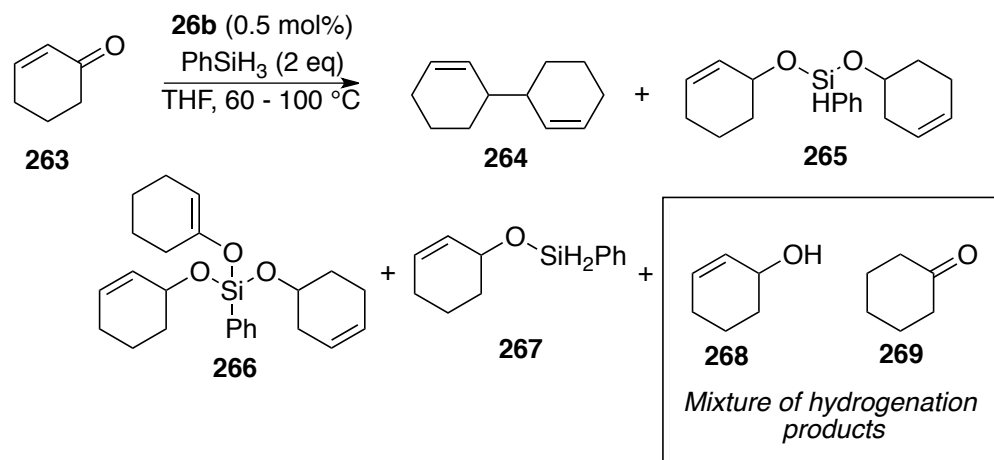


Table 6.1. Catalytic deoxygenation of 2-cyclohexen-1-one under various conditions.

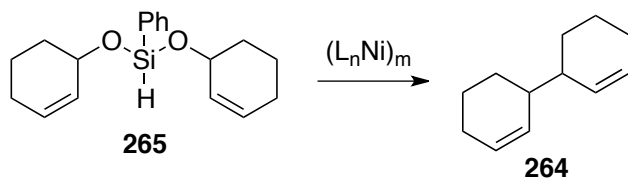
Product	% Conversion		
	T = 25 °C (91% conv) ^a	60 °C (100% conv)	80 °C (100% conv)
264	14	39	61
265	21	31	17
267	10	26	22
266	22	0	0
268 + 269	7	5	7

^aGC-MS analysis of sample revealed the formation of dimerized product C₁₂H₁₈O₂ (16%).

The selective formation of the dimeric deoxygenation product **264** can be explained by several reasonable mechanistic pathways. Since the

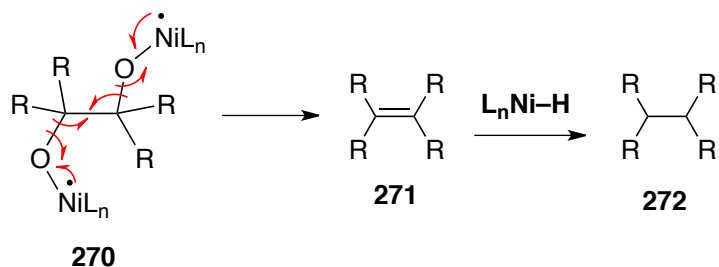
catalysis gives bis(2-cyclohexenyoxy)phenylsilane **265** as the second major carbonyl reduction product, it might be reasoned that the nickel-catalyzed deoxygenative coupling of the two hydrocarbon fragments of **265** produces the dimeric product (Equation 6.8).

Equation 6.8

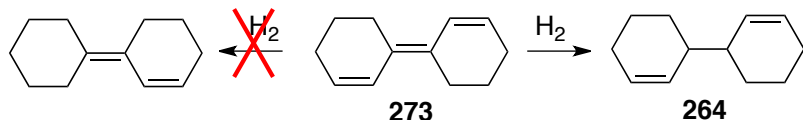


One reasonable mechanism echoes similar McMurry-type coupling pathways – a metal-induced carbonyl dimerization proceeding via single electron transfer to give a bimetallic pinacolato intermediate **270**, which then undergoes radical rearrangement to form oxonickel complexes and the olefin intermediate **271** (Equation 6.9). The nickel-catalyzed deoxygenative carbonyl dimerization leads unsurprisingly to the hydrogenated McMurry coupling product **272**, since **26b** has been shown to be active for catalytic hydrogenation of unactivated and hindered olefins, even under hydrosilylation conditions. *This pathway, however, does not explain the preferential hydrogenation of the more hindered exocyclic carbon-carbon double bond in the McMurry coupling product **273** over the more sterically accessible ring unsaturation (Eq. 6.10).*

Equation 6.9

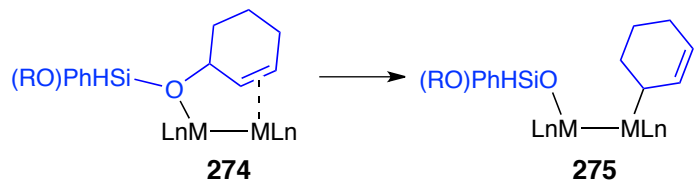


Equation 6.10



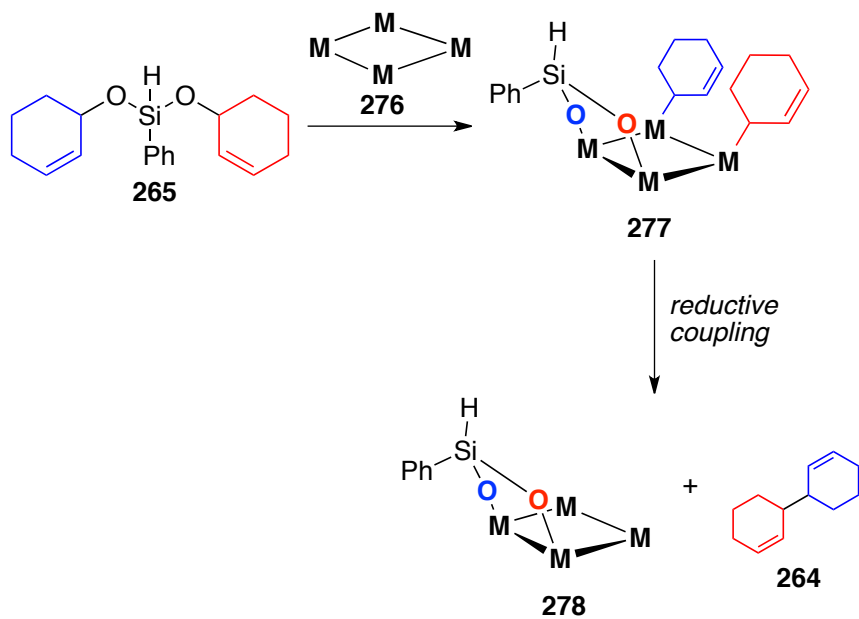
The preferential hydrogenation of the tetrasubstituted exocyclic carbon-carbon double bond in **273** encourages us to propose a highly tentative mechanistic pathway that involves the homolytic scission of C–O bonds induced by a bimetallic active catalyst. This mechanism presumably involves substrate precoordination across bimetallic active sites through the oxygen center and the endocyclic carbon-carbon double-bond (**274**, Equation 6.11). Bimetallic, single-electron cleavage of the ether C–O bond in **274** then results in the formation of an alkoxy- and cyclohexenyl-substituted bimetallic intermediate **275**. Coupling of two cyclohexenyl radical fragments will produce the dimer **264**.

Equation 6.11



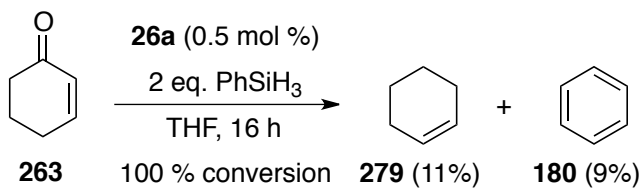
The selectivity of the nickel catalyst for the dimeric product could be suggestive of a high nuclearity active catalyst. Although kinetically and entropically less probable, the catalytic deoxygenation of the bis(alkoxy)silane precursors catalyzed by a tetrametallic active site **276** provides a reasonable mechanism accounting for the catalyst selectivity for the dimeric product (Equation 6.12). A series of bimetallic homolysis of the two C–O bonds in **265** would then result in the formation of intermediate **277** where two adjacent metal centers are functionalized by two cyclohexenyl fragments. This intermediate can then undergo bimetallic reductive elimination, generating the dimeric deoxygenation product **264** and the siloxane-functionalized tetrametallic complex **278**.

Equation 6.12

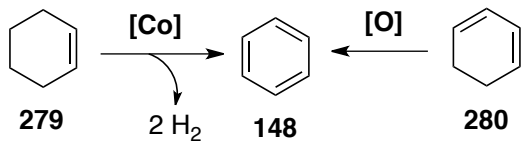


Under otherwise identical conditions, the cobalt catalyst selectively deoxygenates *but does not dimerize* cyclohexenone, giving only monomeric hydrocarbon products as a nearly 1 : 1 mixture of benzene **180** and cyclohexene **279** (Equation 6.13). The formation of benzene could be due to cobalt-catalyzed dehydrogenation of cyclohexene (Equation 6.14) but could also arise from aerobic oxidation of 1,3-cyclohexadiene **280**. The catalyst could potentially generate 1,3-cyclohexadiene from β -hydride of a cobalt-bound cyclohexenyl fragment (Equation 6.14).

Equation 6.13



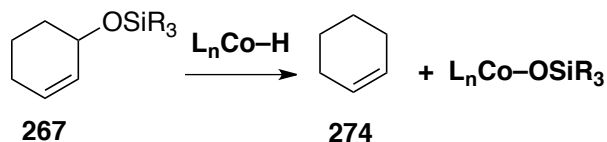
Equation 6.14



This difference in catalyst selectivity and reactivity is consistent with our preliminary mechanistic findings, as discussed in Chapter 3. The cobalt-catalyzed hydrosilylation, we propose, proceeds via a non-radical mechanism, while the results of the radical clock reduction suggests that the nickel-catalyzed reactions proceed with contributions from a radical mechanism. The selectivity of the cobalt catalyst for the monomeric

deoxygenation product then suggests that the catalyst is highly active for the heterolytic reductive scission of allylic C–O bonds in the silyl enol intermediate **267** (Equation 6.15).

Equation 6.15



Furthermore, the observed difference in deoxygenation selectivity of the Co(I) and Ni(I) catalysts provide pertinent clues on the nuclearity of the active catalyst(s). Since a tetrametallic catalyst is perceived ideal for the formation of dimeric deoxygenation product(s), the selectivity of the cobalt catalyst for monomeric hydrocarbons might then be interpreted to be due to lower nuclearity active catalyst(s). A bimetallic active catalyst could explain the observed product distribution in the cobalt-catalyzed deoxygenation of **263** (Figure 6.1). Homolytic cleavage of the C–O bond in the precoordinated bis(alkoxy)silane substrate in intermediate **281** forms the silyloxo- and cyclohexenyl-functionalized bimetallic intermediate **282**. Contrary to the tetrametallic intermediate **277** (Equation 6.12), the bimetallic intermediate **282** is less kinetically favored to undergo bimetallic reductive coupling of two cyclohexenyl radical fragments. Intermediate **282** can, however, readily undergo β -hydride elimination, producing 1,3-cyclohexadiene and a metal hydride intermediate **283**. Alternatively,

intermediate **282** can undergo reductive cleavage of the M–C bond under hydrosilylation conditions to give cyclohexene, and presumably, a silyl-functionalized organometallic intermediate **284**. At this point, clearly, the mechanistic pathways proposed are highly speculative; hence, systematic investigation of the mechanisms of deoxygenation mediated by the tetrametallic Co(I) and Ni(I) precatalysts is needed.

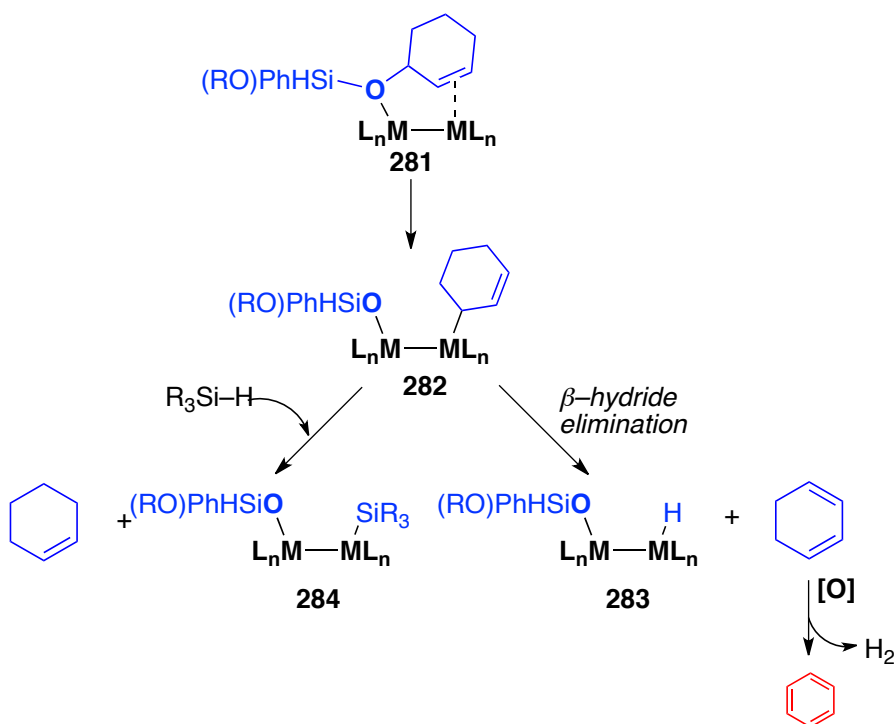


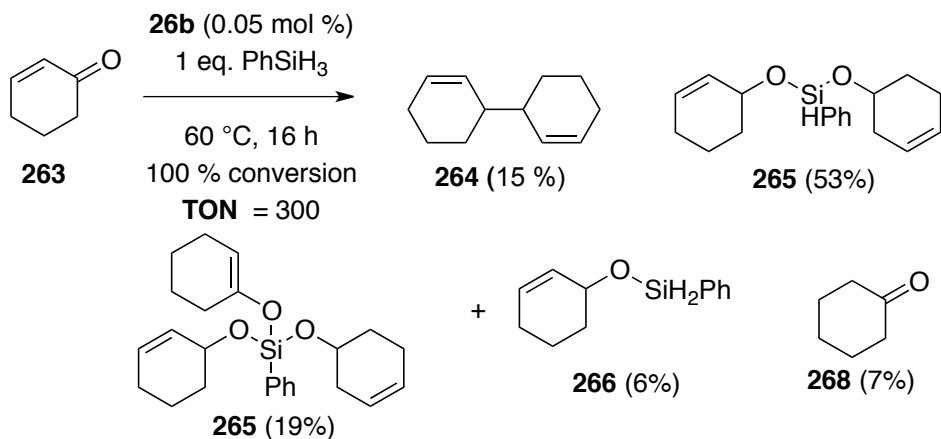
Figure 6.1. Bimetallic deoxygenation pathways for the formation of cyclohexene and benzene.

6.2.2 Solvent-Free Carbonyl Deoxygenation

The catalytic deoxygenation of **263** proceeds efficiently even in the absence of an added solvent. Treatment of **263** with catalytic **26b** (0.05

mol%) and stoichiometric amounts of PhSiH₃ resulted in a 15% substrate conversion to **264** at 60 °C over 16 hours (TON = 300, Equation 6.13). No visible signs of catalyst decomposition (i.e. decolorization, precipitate formation) were observed during the course of the solvent-free catalysis.

Equation 6.16



6.2.3 Enone Substrate Scope

A preliminary attempt to apply this methodology to the reductive upgrading of naturally-occurring carbonyl derivatives was conducted using (+)-carvone **285** – a monoterpenoid – at 60 °C with PhSiH₃ as a reducing agent (Equation 6.14). In the event, carvone was deoxygenated (60% conversion) into a 1 : 11 mixture of the highly branched monomeric and dimeric hydrocarbons **286** and **287**. The dimeric product **287** was obtained as an undetermined mixture of diastereoisomers. Interestingly, the observed product distribution (Table 6.2) indicates that, at identical

reaction temperatures, the catalyst selectivity for deoxygenative-dimerization indifferent to organosilyl hydride concentration.

Equation 6.17

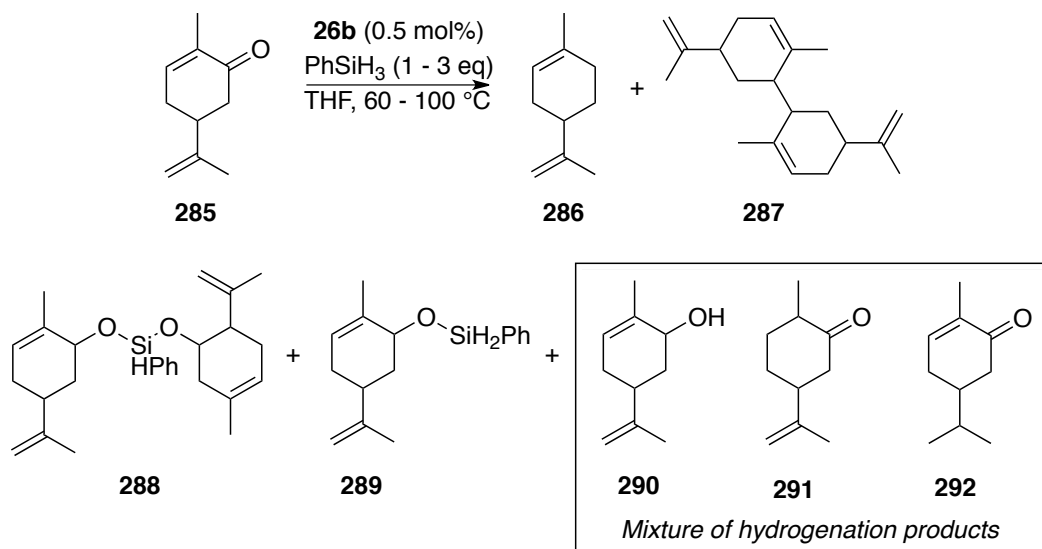


Table 6.2. Catalytic deoxygenation of (+)-Carvone under various conditions.

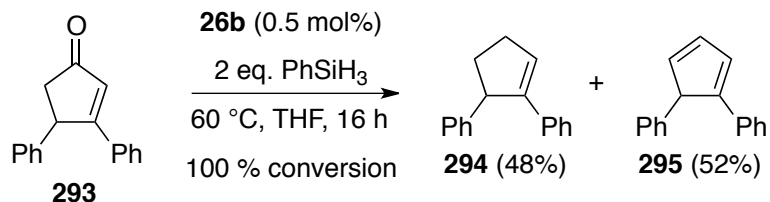
Product	% Conversion	
	T = 60 °C 275 : PhSiH ₃ = 1 : 1	60 °C 1 : 3
286	6	3
287	41	46
288	40	36
289	4	1
290 + 291 + 292	8	14

This demonstration, though preliminary, shows the potential of this catalyst family for the reductive upgrading of plant-extractable fractions under mild conditions. This biomass fraction, comprised mainly of terpenes, is a cheap and readily available bioresource for the production

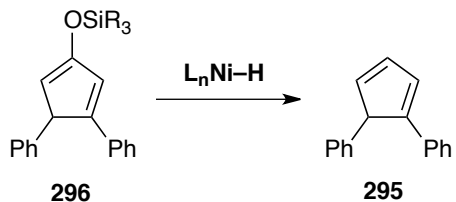
of highly branched, partially unsaturated liquid transportation fuels (C_{10} for biodiesel; C_{20} for aviation fuels^{313,314}). Strict environmental policies are being imposed on the levels of volatile plant extractables that can be released to the environment, as these compounds contribute to serious environmental problems such as air pollution and eutrophication. There is currently no catalytic upgrading process for terpene valorization; modern industrial strategies for the removal of plant extractables are costly and usually conducted during energy-intensive biomass pretreatment, involving sequential (1) vaporization and (2) solvent extraction.

Quantitative deoxygenation of enones was initially demonstrated in the reduction of 3,4-diphenyl-2-cyclopenten-1-one **293**. Treatment of **293** with nickel catalyst **26b** (0.5 mol%) and PhSiH_3 exclusively formed a mixture of **294** (42%) and **295** (52%) over 16 hours at 60 °C in THF (Equation 6.18). The quantitative conversion is a strong indication of the efficiency and longevity of the catalyst. Interestingly, the formation of styrene **295** potentially results from the metal-catalyzed hydrogenolysis of an intermediate silyl enol ether **296** (Equation 6.19). The formation of **295** could also result from β -hydride elimination of a metal-bound allyl fragment in **297** (Equation 6.20). Interestingly, in this reaction, dimeric deoxygenation products were not detected, suggesting that the selectivity of the nickel catalyst for the formation of dimeric hydrocarbons could also be highly substrate-dependent.

Equation 6.18



Equation 6.19



Equation 6.20



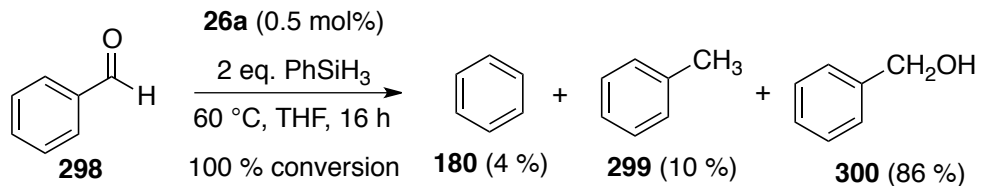
6.2.4 Deoxygenation of Aryl Ketones

The scope of catalytic deoxygenation was more extensively explored for the reduction of aryl aldehydes and ketones. The succeeding sections present experimental results comparing the catalytic activities and selectivities of catalysts **26a** and **26b**.

6.2.4.1 Preliminary Deoxygenation of Unactivated Aryl Carbonyl

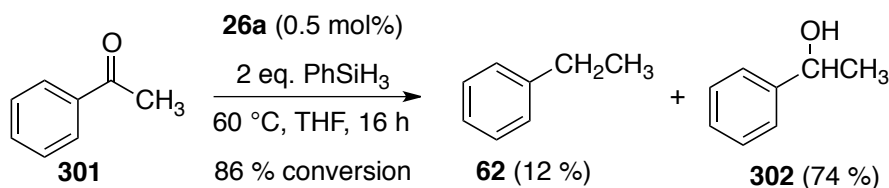
Preliminary deoxygenation experiments were conducted using unactivated aromatic carbonyl compounds. Aryl aldehydes expectedly undergo faster hydrosilylation compared to aryl ketones. The cobalt-catalyzed reduction of benzaldehyde **298** under the conditions employed for enone reduction (1 : 2 substrate-to- PhSiH_3 ratio; 60 °C, 16h; Equation 6.16) resulted in quantitative conversion into a mixture of benzene **180** (4%), toluene **299** (10%) and benzyl alcohol **300** (86%). The formation of benzene **180** is an indication of the ability of the cobalt cluster to catalytically decarbonylate aldehydes.

Equation 6.21



Cobalt-catalyzed deoxygenation of acetophenone **301** was achieved under similarly mild conditions (0.5 mol% catalyst, 2 equiv PhSiH_3 at 60 °C; Equation 6.17), giving nearly quantitative conversion (86%) into a 1 : 6 mixture of ethylbenzene **62** (12%) and 1-methyl-1-phenylmethanol **302** (74%).

Equation 6.22



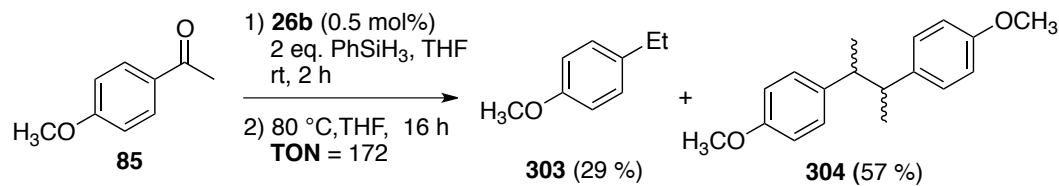
The dominance of alcohol rather than alkoxy silane products, even in the absence of an aqueous workup, suggests that at elevated temperatures, concomitant hydrogenolysis of aryl alkoxides is highly competitive and can be promoted by polyhydrosilanes (e.g. PhSiH₃). This was confirmed by experiments showing that the formation of benzylic alcohols is suppressed by the use of tertiary organosilanes (e.g. PhMe₂SiH); alkoxy silanes were formed as the major reduction products. However, the use of less reactive tertiary organosilyl hydrides also resulted in significant inhibition of the rates of carbonyl deoxygenation.

Since it was previously established that aryl ketones preferentially formed alkoxy silanes at room temperature (Chapter 3), we reasoned that pretreatment of carbonyl substrates with an organosilyl hydride at room temperature prior to heating, might also suppress the direct formation of benzylic alcohols. This hypothesis was tested using functionalized acetophenones and benzaldehydes.

6.2.4.2 Deoxygenation of Aryl Ketones Under Optimum Conditions

The nickel-catalyzed deoxygenation of the electron-rich ketone, 4-methoxyacetophenone **85**, was conducted by inserting an initial “incubation” at room temperature prior to stirring under reflux at 80 °C. This resulted in near quantitative carbonyl deoxygenation over 16 hours (Equation 6.23). The catalytic reduction gave a 1 : 2 mixture of the monomeric and dimeric deoxygenation products, 4-ethylanisole **303** (29%) and diastereomeric 3,4-bis(4-methoxyphenyl)butane **304** (57%). Interestingly, in this experiment, cleavage of the C_{aryl}-O ether to give methanol as a product was not observed. This suggests that under given hydrosilylation conditions, catalyst **26b** is highly selective for the benzylic C–O bond cleavage.

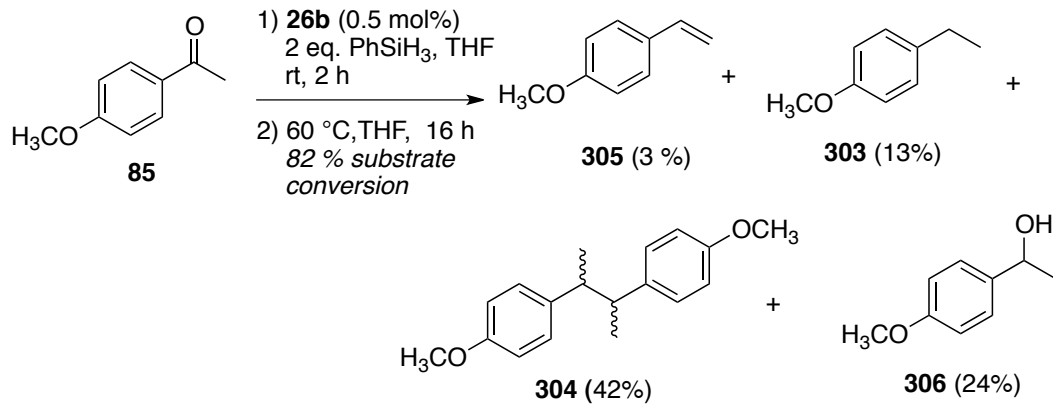
Equation 6.23



Cobalt-catalyzed deoxygenation of **85** afforded a more revealing mixture of deoxygenated products, providing some important mechanistic insight (Equation 6.24). Treatment of **85** with a catalytic amount of **26a** (1.5 mol%) and phenylsilane at 60 °C produced *p*-methoxystyrene **305** (3%), *p*-ethylanisole **303** (13%) and diastereomeric 3,4-bis(4-

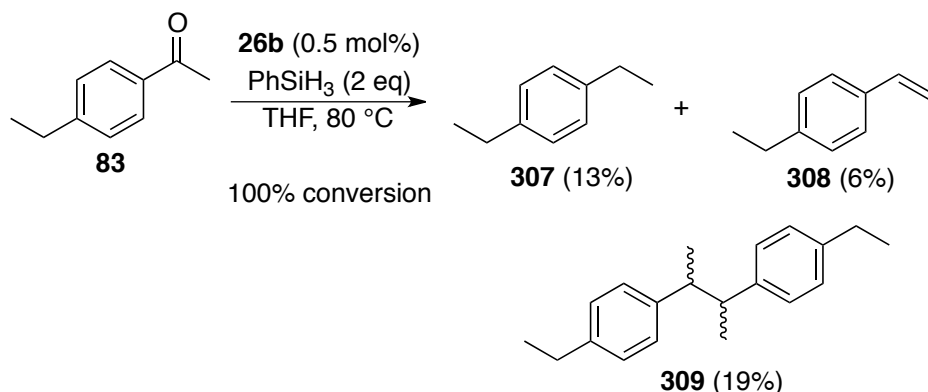
methoxyphenyl)butane **304** (42%). The observed conversion translates to a turnover number of 116 C=O bonds deoxygenated per mole of **26b** over 16 hours.

Equation 6.24



Counterintuitively, the catalytic reduction proceeds faster with more electron-rich substrates. The rate of the deoxygenation of 4-ethylacetophenone **83** (**TON** = 100) is slower than the rate observed in the reduction of the more electron-rich substrate 4-methoxyacetophenone **85** (**TON** = 172) under otherwise identical conditions. Treatment of **83** with catalyst **26b** (0.5 mol%) with PhSiH₃ as the reductant at 80 °C afforded a 2 : 1 : 3 mixture of 1,4-diethylbenzene **307**, 4-ethylstyrene **308** and 2,3-di(4-ethylphenyl)butane **309** (mixture of diastereomers), respectively (Equation **6.25**).

Equation 6.25



6.2.5 Deoxygenation of Aryl Aldehydes

Comparison of the activities of clusters **26a** and **26b** for catalytic deoxygenation of a wide range of functionalized aryl aldehydes has revealed profound differences in the chemoselectivity of the isostructural cobalt and nickel catalysts.

6.2.5.1 Deoxygenation of Amino-Functionalized Aryl Aldehydes

Catalytic deoxygenation of the deactivated aldehyde 4-N,N'-dimethylaminobenzaldehyde **89** manifests surprising reactivity differences between the Co(I) and Ni(I) catalysts (Equation 6.26). Treatment of **89** with catalytic amounts of **26a** or **26b** using PhSiH₃ as the reductant results in near-quantitative conversions, affording complex mixtures of monomeric, dimeric, and pseudo-dimeric products. Both cobalt- and nickel-catalyzed deoxygenations afford the monomeric deoxygenated 4-N,N'-dimethylaminotoluene **310** as the major product (Entry 1, Table 6.2).

Relative to the Ni(I) catalyst, the Co(I) cluster **26a** showed higher selectivity for the formation of the hydrogenated reductive dimerization product, 1,2-bis(4-N,N'-dimethylaminophenyl)ethane **312** (41 % against 9 %; Entry **2**, Table **6.2**). The reluctance of nickel catalyst **26b** to promote the formation of dimer arises from a greater tendency to mediate aldehyde decarbonylation, as evident from the formation of 1,1-bis(4-N,N'-dimethylaminophenyl)methane **313** as the principal secondary product (Entry **3**, Table **6.3**).

Equation 6.26

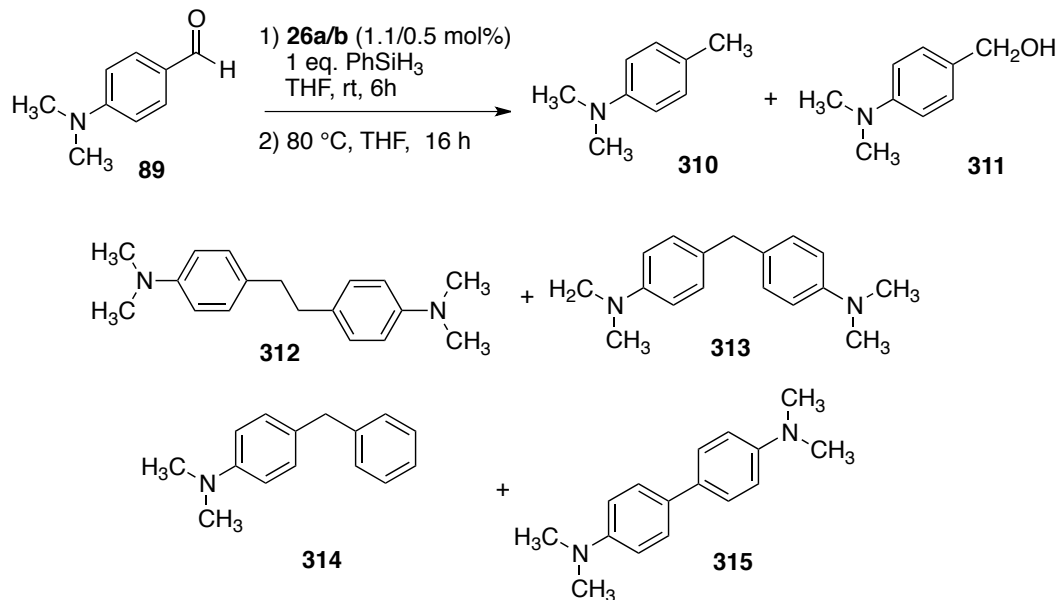


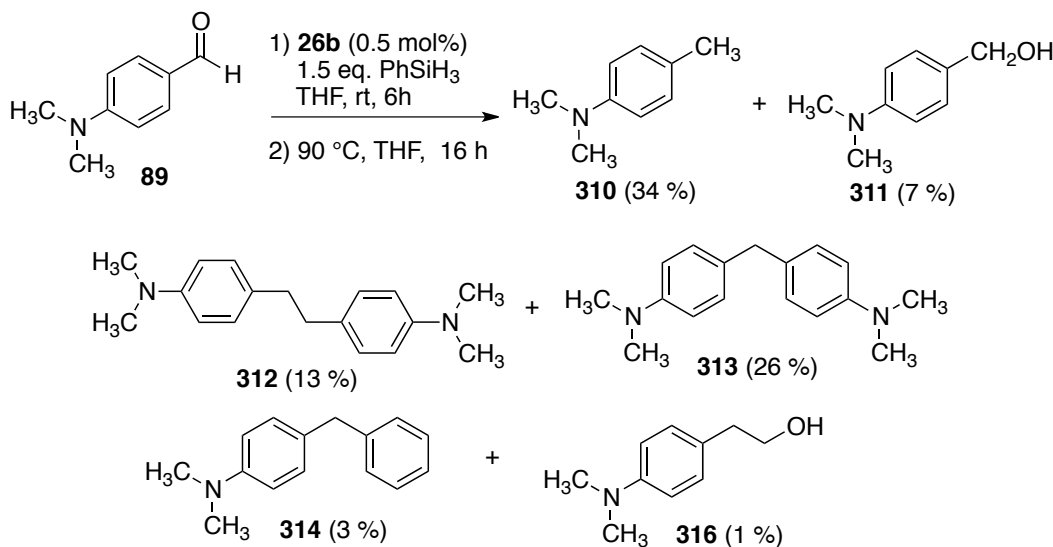
Table 6.3. Product distribution of catalytic deoxygenation of **89**.

Entry	Product	% 242 Converted	
		Cat: 26a (1.1 mol%)	Cat: 26b (0.5 mol%)
1	310	47	43
2	311	5	4
3	312	41	9
4	313	2	36
5	314	0	2
6	315	5	0

The nickel-catalyzed reaction unexpectedly produces a minor amount of 1-(4-*N,N*'-dimethylaminophenyl)-1-phenylmethane **314** (2%, Entry 5, Table 6.2), as tentatively identified by GC-MS. This species presumably forms from C_{aryl}-N bond hydrogenolysis either before or after the decarbonylative coupling that leads to 1,1-bis(4-*N,N*'-dimethylaminophenyl)methane **313**. In contrast, the cobalt-catalyzed reaction produces instead a species with molecular ion peak suggestive of biphenyl pseudodimer **315**. The proposed structure for this species, however, remains tentative.

A ten-degree increase in the temperature of the nickel-catalyzed reaction resulted in a higher conversion to the reductive coupling product **312** (13%) and correspondingly lower conversion to decarbonylated **313** (26%). In addition, a unique new product was observed in trace yield: substrate homologation to give 2-(4-*N,N*'-dimethylaminophenyl)ethanol **316**. This product reveals the ability of the nickel catalyst to capture and reduce the carbon monoxide fragment extruded during aldehyde decarbonylation (Equation 6.27).

Equation 6.27



6.2.5.2 Deoxygenation of Methoxy-Functionalized Aryl Aldehydes

Anisaldehyde **317** undergoes quantitative reduction under equally mild conditions. Cobalt catalyst **26a** is more selective for carbonyl deoxygenation (Equation 6.24, Table 6.3), affording a mixture of the monomeric and dimeric deoxygenated species **318** (36%) and **320** (42%). Interestingly, the nickel catalyst produced instead 4-methoxybenzyl alcohol **319** as the major reduction product (68%). The remaining 32 % of the starting material was converted into 4-methylanisole **318** (6 %) and a mixture of two dimeric deoxygenated species, 1,2-bis(4-methoxyphenyl)ethane **320** (17 %) and 1,2-di(4-methoxyphenyl)ethene **321** (7 %). The formation of **321** strongly suggests that the formation of **320** proceeds through the product of reductive olefination (*McMurry-type coupling*), followed by silane-mediated alkene hydrogenation.

Consistently, the nickel catalyst produces a greater proportion of aldehyde decarbonylation products; in this case, however, only a trace amount of 1,1-bis(4-methoxyphenyl)methane **322** (2%) was detected.

Equation 6.24

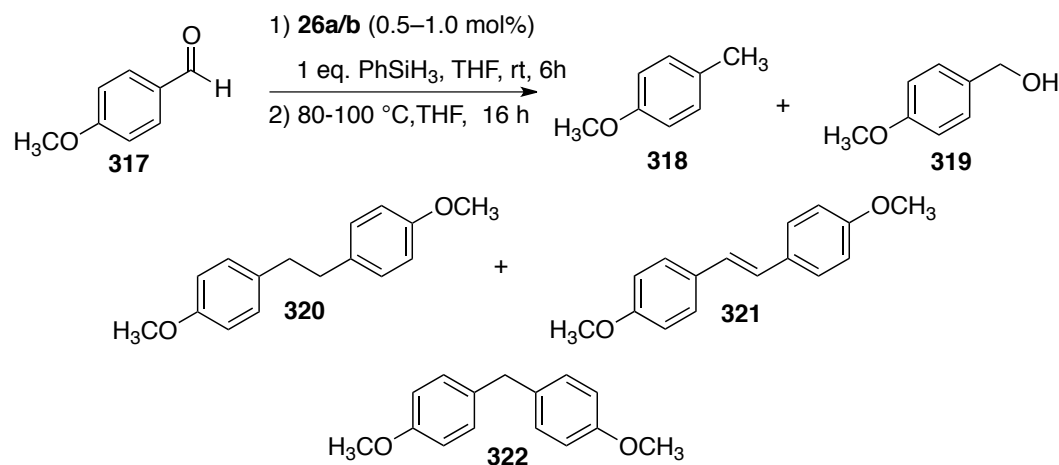


Table 6.4. Product distribution of catalytic deoxygenation of **312**.

Entry	Product	% 312 Converted	
		Cat: 26a (1.1 mol%) ^a	Cat: 26b (0.5 mol%) ^b
1	318	36	6
2	319	22	68
3	320	42	17
4	321	0	7
5	322	0	2

^a Conditions: 1.1 mol% **26a**; 1.5 PhSiH₃, 80 °C, 16h.

^b Conditions: 0.5 mol% **26b**; 2 PhSiH₃, 100 °C, 16h.

On the other hand, conjugation of electron-releasing group(s) to the aldehyde functionality proved crucial to efficient catalytic deoxygenation. Benzaldehyde substrates with non-conjugated electron-donors such as 3,5-dimethoxybenzaldehyde **99** only reluctantly undergo deoxygenation,

giving benzyl alcohol **324** as the major product regardless of catalyst (Equation 6.29; Table 6.4). As expected however, the cobalt-catalyzed reaction was more selective for the formation of the monomeric deoxygenation product, 3,5-dimethoxytoluene **323** (9%), while the nickel-catalyzed hydrosilylation shows a greater (albeit minor) tendency to produce dimeric product **325** (2%).

Equation 6.29

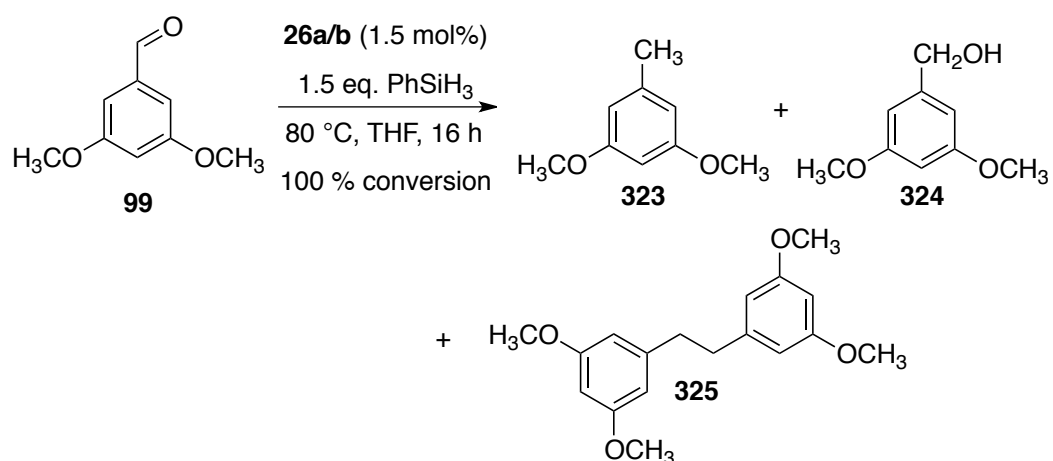


Table 6.5. Product distribution of catalytic deoxygenation of **99**.

Entry	Product	% 99 Converted	
		Cat: 26a	Cat: 26b
1	323	9	5
2	324	91	93
3	325	0	2

Interestingly, no products arising from $\text{C}_{\text{ary}}-\text{OCH}_3$ bond activation were detected in the hydrosilylative deoxygenation of either methoxybenzaldehyde **85** or **99**.

6.2.5.3 Deoxygenation of Thioether-Functionalized Aryl Aldehydes

The high selectivity of both cobalt and nickel catalysts for the reductive cleavage of C–X bonds (X = S, O) was further challenged using the thioether-functionalized benzaldehyde, 4-(methylthio)benzaldehyde **87**. Neither catalyst effects detectable levels of C–S bond hydrogenolysis products under hydrosilylation conditions. A very pronounced difference in carbonyl deoxygenation activity is, however, observed (Equation **6.26**, Table **6.5**). Catalyst **26a** is more selective for simple deoxygenation, giving mainly 4-(methylthio)toluene **321** (86%). Under these conditions, the formation of benzyl alcohol **322** (4%) was minimal. The selective formation of **321** clearly shows the potential utility of the cobalt-catalyzed deoxygenation in fine chemical synthesis. Curiously, such pronounced selectivity for the monomeric deoxygenation product is not mirrored in the deoxygenations of other electron-rich substrates (e.g., **85** and **99**). A thorough investigation of the electronic effects of donor/acceptor substituents on benzaldehyde deoxygenation selectivity is thus an important topic for future study.

Equation 6.26

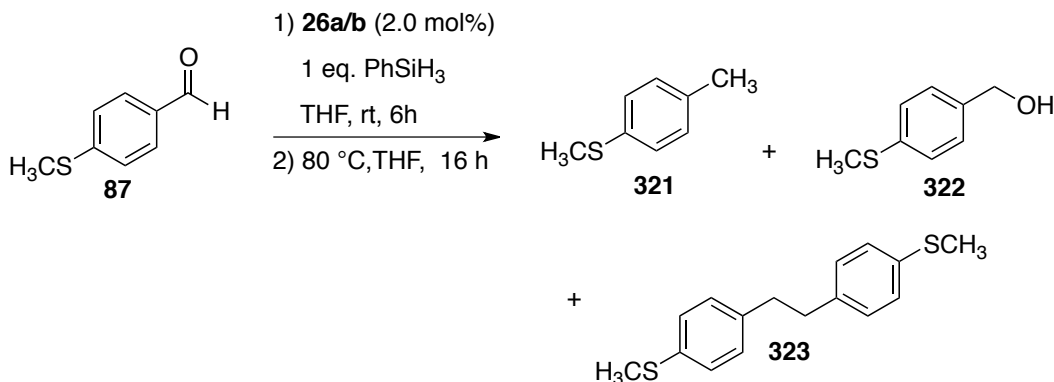


Table 6.6. Product distribution of catalytic deoxygenation of **87**.

Entry	Product	% 87 Converted	
		Cat: 26a	Cat: 26b
1	321	86	20
2	322	4	73
3	323	10	7

The nickel-catalyzed experiment, on the other hand, led to the selective formation of benzyl alcohol **322** (73%), establishing that the nickel catalyst is less effective for carbonyl deoxygenation than cobalt, at least in this series of aromatic aldehydes.

6.2.5.4 Deoxygenation of Ester-Functionalized Aryl Aldehydes

Chemoselectivity for reduction of carbonyl functionalities was tested using methyl 4-formylbenzoate **91** – an electron-deficient substrate bearing both aldehyde and ester groups. Under otherwise identical reaction conditions, the tetrametallic cobalt catalyst **26a** was more aggressive toward catalytic reduction of *both* C=O bonds in **91** (Equation

6.30, Table **6.6**), returning a mixture comprised of four monomeric derivatives showing varying extents of carbonyl reduction. The cobalt-catalyzed reaction principally gave aldehyde hydrogenation product **327** (63%). The remaining substrate fraction (37%) was converted into a mixture of methyl 4-methylbenzoate **326** (10 %), 4-(hydroxymethyl)toluene **328** (15 %) and 1,4-bis(hydroxymethyl)benzene **329** (12 %). The latter two products strongly suggest that the cobalt catalyst is capable of reducing carboxylic esters under hydrosilylation conditions. The remaining product arises from exclusive hydrogenation of the aldehyde C=O bond. Hydroxymethyltoluene **328** results from four reduction events, two each for deoxygenation of the aldehyde C=O bond and hydrogenolysis of the methyl ester functionality to give the benzyl alcohol. Bis(hydroxymethyl)benzene **329** demonstrates clearly that the rate of benzoic ester reduction is competitive with benzylic deoxygenation. The formation of these reduction products (**326**, **328**, and **329**) suggests the potential utility of our catalysts for upgrading various biomass streams, where diverse sets of carbonyl functional groups abound. Furthermore, the catalysis appear to be an important demonstration of base metal-catalyzed ester hydrogenolysis under mild conditions, which is rare if not unprecedented.³¹⁵

Equation 6.30

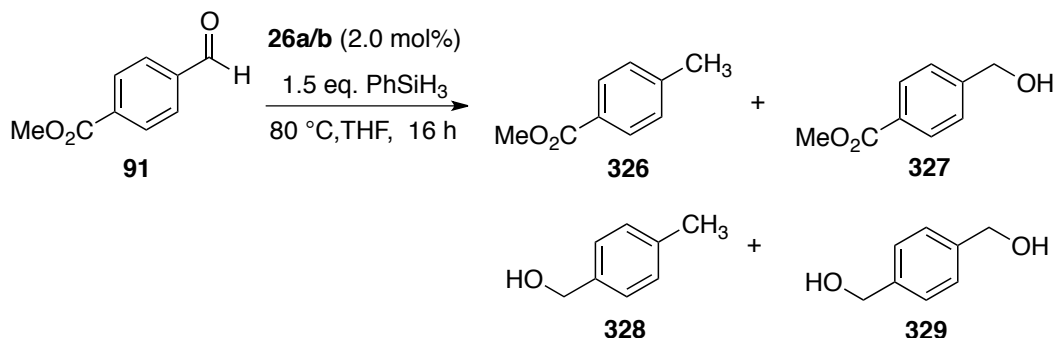


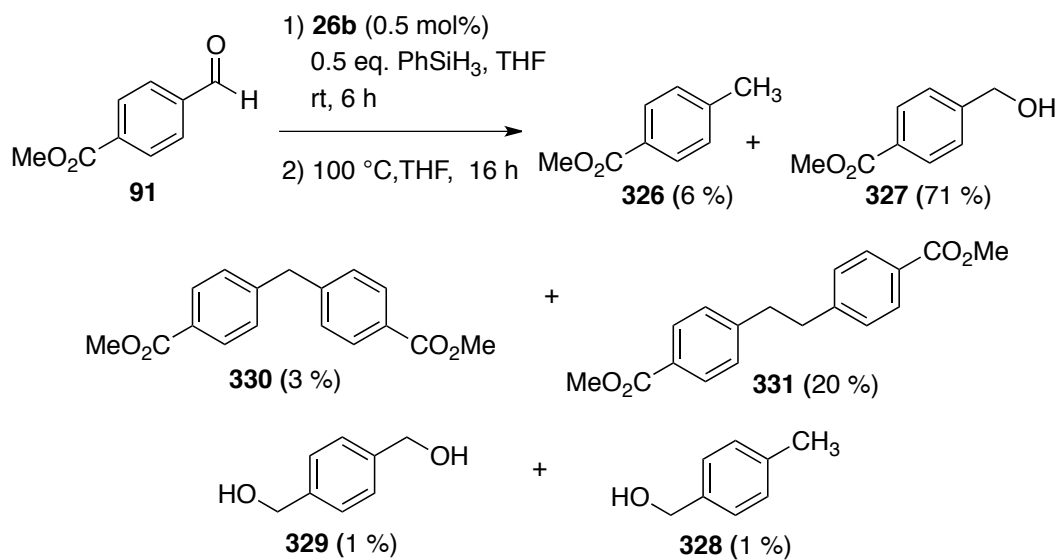
Table 6.7. Product distribution of catalytic deoxygenation of **91**.

Entry	Product	% 91 Converted	
		Cat: 26a (1.1 mol%)	Cat: 26b (0.5 mol%)
1	326	10	7
2	327	63	93
3	328	15	0
4	329	12	0

The corresponding nickel-catalyzed reduction of dicarbonyl substrate **91** gave benzyl alcohol derivative **327** (93%) as the only significant product; the monomeric deoxygenation product **326** was obtained in minor amount (7%). The lower activity of the nickel catalyst for aldehyde deoxygenation led us to suspect that excess polyhydrosilane (e.g. PhSiH₃) could be detrimental to the deoxygenation pathway. Treatment of **91** with limiting quantities of PhSiH₃ at room temperature for 6 hours prior to heating at 100 °C indeed resulted in a significant increase in the proportion of aldehyde deoxygenation (Equation 6.31). The yield of methyl 4-hydroxymethylbenzoate **327** was reduced from 93% to 71% and the

remaining 29% of the substrate was converted to three deoxygenated species, toluene derivative **326** (6%), decarbonylated dimer **330** (3%) and the dimeric deoxygenated product **331** (20 %). Surprisingly, only trace amounts of ester hydrogenolysis was observed under the conditions of limited silane.

Equation 6.28

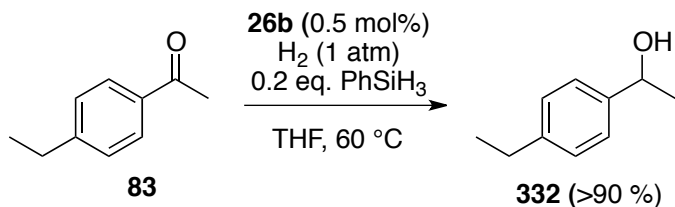


6.2.6 Hydrogen as a Carbonyl Reductant

The catalytic reduction/deoxygenation of carbonyl substrates was also briefly investigated using the mild and relatively inexpensive reductant, dihydrogen (H₂). The nickel-catalyzed reduction of 4-ethylacetophenone **83** under one atmosphere of H₂ at 60 °C resulted in low conversion to the benzyl alcohol **332** exclusively. Importantly, the hydrogenation of **83** *in the presence of stoichiometric quantities of*

*PhSiH*₃ resulted in clean and near-quantitative conversion to alcohol **330** (Equation 6.29). The catalytic activity of **26a** and **26b** for carbonyl hydrogenation was not further pursued, as this line of research has become the principal focus of another member of the Stryker group.

Equation 6.29



6.2.7 Mechanism of Carbonyl Deoxygenation

Both Co(I) and Ni(I) catalysts show an impressive range of reductive reactivity as evidenced by the formation of complex product mixtures from mono- and bifunctional substrates. At this point, there is insufficient information to propose a detailed mechanistic pathway for carbonyl deoxygenation, one that effectively explains the diversity of products and the fascinating selectivity differences observed between cobalt catalyst **26a** and its isostructural nickel congener **26b**. Hence, systematic kinetic and mechanistic investigations, as well as more rigorous structural characterization of the active species, are needed.

On the other hand, our observations have provided a few preliminary mechanistic details. The active role of the catalysts in these

reductions was confirmed by control experiments showing that the reduction of carbonyl substrates does not proceed in the absence of either **26a** or **26b**. Under operating conditions, the reaction mixtures remained visibly homogeneous, without observable precipitate formation or decolorization, which might signal catalyst decomposition. Furthermore, since the catalytic reactions proceed at practical rates under mild reaction temperatures (25–100 °C), catalyst decomposition to catalytically competent cobalt and nickel nanoparticles must be considered unlikely. This supposition is supported by the absence of aromatic hydrogenation products in any of the carbonyl reduction experiments we have conducted.

6.3 Summary and Conclusions

Optimum conditions for carbonyl deoxygenation catalyzed by clusters **26a** and **26b** have been identified. The catalysts effect the deoxygenation of a range of functionalized aryl and α,β -unsaturated aldehydes and ketones under exceptionally mild hydrosilylation conditions. Catalytic deoxygenation proceeds efficiently at temperatures ranging from 25–100 °C, unprecedented for such energy-demanding transformations. The catalysts effect deoxygenative reduction of carbonyl substrates bearing ether, amino, thioether and ester functionality. In most cases, the catalysis process is non-selective, delivering mixtures of alcohols, monomeric and dimeric deoxygenation products, and pseudo-dimeric products from aldehyde decarbonylation. The observed product

distributions suggest that the selectivity for deoxygenation is substrate-dependent and highly sensitive to temperature and organosilyl hydride (reductant) identity and concentration.

Cobalt catalyst **26a** shows significantly higher activity for the deoxygenation of carbonyl substrates and ester hydrogenolysis, making it the most promising catalyst for reductive upgrading of carbonyl-rich substrates derived from biomass. Tetrametallic nickel catalyst **26b**, on the other hand, is more sensitive to reductant concentration and shows a modest tendency to catalyze aldehyde decarbonylation under mild conditions.

Further exploration and optimization of precatalyst structure and reaction conditions is needed to gain full control of the deoxygenation selectivity. The complex composition of product mixtures renders the delineation of reasonable reaction mechanisms, even tentative ones, extremely challenging. Hence, systematic investigation of the mechanism is an important topic for future studies.

6.4. Summary of Deoxygenation Results.

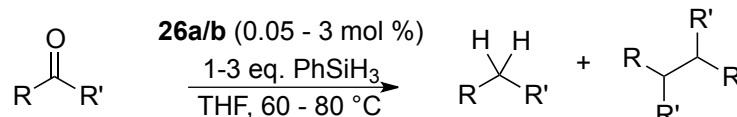


Table 6.8. Summary of catalytic deoxygenation of α,β -unsaturated ketones.^a

Entry	Substrate	Cat (mol%)	PhSiH ₃ (eq)	Time (h)	Temp (°C)	Deoxygenation Product(s)	%Substrate Conversion (GC-MS)
1		26b (0.5)	2	16	80		61
2		26b (0.05)	1	16	60		15
3		26a (0.5)	2	16	80		11, 9
4		26b (0.5)	3	18	60	(mixture of isomers)	3 46 ^b
5		26b (0.5)	2	18	60	(mixture of isomers)	52, 48 ^b

^aAll substrates underwent quantitative reduction affording mixtures of alcohols, alkoxysilanes and deoxygenation products.

^bProduct obtained as a mixture of diastereomers.

In most entries, only products of deoxygenation were shown in this table.

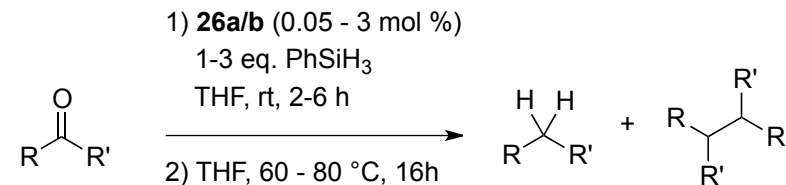
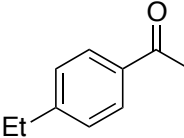
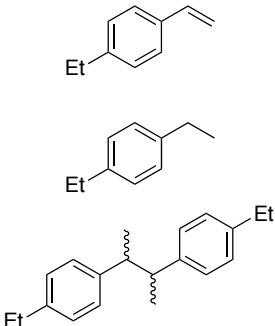


Table 6.9. Summary of catalytic deoxygenation of aryl ketones.^a

Entry	Substrate	Cat (mol%)	PhSiH ₃ (eq)	Temp (°C)	Deoxygenation Product(s)	%Conversion (GC-MS)
1		26b (0.5)	2	80		29
						57 ^b
2		26a (0.5)	2	60		3
						13
						42 ^b

3		26b (0.5)	2	80		6 13 19 ^b
---	---	---------------------	---	----	---	----------------------------

^aAll substrates underwent quantitative reduction affording mixtures of alcohols, alkoxysilanes and deoxygenation products.

^bProduct obtained as a mixture of diastereomers.

In most entries, only products of deoxygenation were shown in this table.

Table 6.10. Summary of catalytic deoxygenation of aryl aldehydes.^a

Entry	Substrate	Cat (mol%)	PhSiH ₃ (eq)	Temp (°C)	Deoxygenation Product(s)	%Substrate Conversion (GC-MS)
1		26a (1.1)	1	80		47 41 2
5		26b (0.5)	1	80		43 9 36 2

3	<chem>O=Cc1ccc(O)cc1</chem>	26a (1.1)	1.5	80	<chem>Cc1ccc(O)cc1</chem>	36
					<chem>CC(O)c1ccc(O)cc1</chem>	22
4	<chem>O=Cc1ccc(O)cc1</chem>	26b (0.5)	2	100	<chem>Cc1ccc(O)cc1</chem>	6
					<chem>CC(O)c1ccc(O)cc1</chem>	68
					<chem>CCc1ccc(O)cc(Cc2ccc(O)cc2)O</chem>	17
					<chem>CC=CCc1ccc(O)cc(Cc2ccc(O)cc2)O</chem>	7
					<chem>CCc1ccc(O)cc(Cc2ccc(O)cc2)O</chem>	2

5		26a (1.5)	1.5	80		9 91
6		26b (1.5)	1.5	80		5 93 2

7	<chem>H3CSc1ccc(C=O)cc1</chem>	26a (2.0)	1	80	
					<p>Chemical structures of three products from reaction 7:</p> <ul style="list-style-type: none"> 4-methylbenzenethione: <chem>Cc1ccc(S(=O)(=O)C)cc1</chem> 4-methylbenzyl alcohol: <chem>OCC(c1ccc(S(=O)(=O)C)cc1)c2ccccc2</chem> 4-(4-methylbenzyl)benzenethione: <chem>Cc1ccc(Cc2ccc(S(=O)(=O)C)cc2)cc1</chem>
8	<chem>H3CSc1ccc(C=O)cc1</chem>	26b (2.0)	1	80	
					<p>Chemical structures of three products from reaction 8:</p> <ul style="list-style-type: none"> 4-methylbenzenethione: <chem>Cc1ccc(S(=O)(=O)C)cc1</chem> 4-methylbenzyl alcohol: <chem>OCC(c1ccc(S(=O)(=O)C)cc1)c2ccccc2</chem> 4-(4-methylbenzyl)benzenethione: <chem>Cc1ccc(Cc2ccc(S(=O)(=O)C)cc2)cc1</chem>

Entry	Substrate	Cat (mol%)	PhSiH ₃ (eq)	Temp (°C)	Deoxygenation Product(s)	%Substrate Conversion (GC-MS)
9		26a (2.0)	1.5	80		63
						10
						15
						12
10		26b (2.0)	1.5	80		93
						7

^aAll substrates underwent quantitative reduction affording mixtures of alcohols, alkoxysilanes and deoxygenation products.

In most entries, only products of deoxygenation were shown in this table.

Chapter 7

Experimental Section

7.1 Synthesis of Phosphoranimide-Supported Complexes of Fe, Co and Ni

General Consideration

All manipulations were carried out using inert-atmosphere techniques. The preparation of each reaction mixture was carried out in a Labmaster SP MBRAUN drybox operating under a N₂ atmosphere. Experiments that required heating were conducted under a Schlenck manifold. Thoroughly dried and degassed solvents were used in all experiments. Anhydrous iron, cobalt and nickel precursors were used. Trialkylphosphoranimide ligands precursors Ph₃P=N-SiMe₃, LiNP^tBu₃ and LiNPCy₃ were synthesized using literature procedures.⁶⁶ NMR spectra were recorded on an Agilent/Varian Inova two-channel 400 MHz spectrometer at room temperature. ¹H-NMR spectra were referenced to residual protio solvent peaks (CDCl₃ and C₆D₆).

High-Temperature Synthesis of Metal-Phosphoranimide Clusters

Synthesis of [Co₃(OOCCH₃)₆(HNPPh₃)₂]**13**

A 100 mL Teflon-sealing glass reactor was charged with 51 mg (0.29 mmol) Co(CH₃COO)₂, 113 mg (0.32 mmol) Ph₃P=N-Si(CH₃)₃, 2.00 mL chlorobenzene and a magnetic stir bar. The reactor was sealed and heated to 120 °C while stirring at 1200 rpm. The initially faint blue suspension turned dark blue over the 16-h reaction period. The mixture

was then cooled to room temperature and the solvent was removed *in vacuo* at 50 °C. A dark blue, toluene-soluble fraction was obtained from washing of the product mixture, leaving a purple, THF-insoluble residue. The toluene-soluble solids formed X-ray quality crystals from a concentrated toluene solution after a month of cooling at -35 °C. The solid-state structure of this material revealed the molecular structure $[\text{Co}_3(\text{OOCCH}_3)_6(\text{HNPPPh}_3)_2]$ **13** (crude yield = 33 mg, 30 %). Analytical purity of the isolated fraction of **13** was not determined.

Reaction of **13** with LDA

A 10-mL Schlenk flask was charged with 40 mg (0.04 mmol) **13**, 2.00 mL THF and a magnetic stir bar under a N₂ atmosphere. The vessel was then connected to an Argon manifold and was cooled in a dry ice-acetone bath. A one mL THF solution containing 8 mg (0.08 mmol) LDA was canula transferred to the solution of **13** and the solution was stirred from -78 °C to room temperature overnight. The dark blue solution of **13** in THF turned green over the course of the reaction. The solvent was then removed under vacuum, giving a THF-soluble green residue. The product, unfortunately, did not form X-ray quality crystals.

Synthesis of Metal-Phosphoranimide Clusters Through Anionic Metathesis

Synthesis of $[\text{Co}(\text{NP}^t\text{Bu}_3)(\text{PPh}_3)]$ 16

A five-dram glass vial was charged with 150 mg (0.017 mmol) $[\text{CoCl}(\text{PPh}_3)_3]$, 3.00 mL THF and a magnetic stir bar under a N_2 atmosphere. A two-mL THF suspension containing 40 mg (0.17 mmol) LiNP^tBu_3 was added in small portions over two h, resulting in a change in the color of the solution from green to dark green. The reaction mixture was stirred at room temperature overnight. The solvent was then removed *in vacuo* and a brown-green residue was extracted with pentane. The pentane-soluble fraction was then purified through a series of ten fractional recrystallization steps to remove PPh_3 impurities. The result of elemental analysis of the final pentane-soluble fraction nearly passed for a compound with empirical formula $[\text{Co}(\text{NP}^t\text{Bu}_3)(\text{PPh}_3)]$ **16** (64 mg, 35 %). Elemental composition (calculated): %C, 67.03; %H, 7.88; %N, 2.61; (expected) %C, 71.24; %H, 7.24; %N, 2.63.

Synthesis of $[\text{Co}(\text{HNP}^t\text{Bu}_3)_2(\text{NC}_{12}\text{H}_8)_2]$ 17

A five-dram glass vial was charged with 150 mg (0.017 mmol) $[\text{CoCl}(\text{PPh}_3)_3]$, 3.00 mL THF and a magnetic stir bar under a N_2 atmosphere. A two-mL THF suspension containing 40 mg (0.17 mmol) LiNP^tBu_3 was added in small portions over two h, resulting in a change in the color of the solution from green to dark green. The reaction mixture was stirred at room temperature for three h. To the solution was added 71 mg

(0.43 mmol) carbazole, resulting in an immediate color change from dark green to dark blue. The solvent was then removed under vacuum, giving a benzene-soluble dark blue residue. X-ray quality crystals of the benzene-soluble solids were obtained from a concentrated THF solution at $^{\circ}35$ $^{\circ}\text{C}$. Crystallographic analysis revealed a solid-state structure consistent with the formula $[\text{Co}(\text{HNP}^t\text{Bu}_3)_2(\text{NC}_{12}\text{H}_8)_2]$ **17**. Crude yield = 56 mg, 75 %.

Reaction of **17** with LDA

A five-dram glass vial was charged with 40 mg (0.05 mmol) **17**, 2.00 mL THF and a magnetic stir bar under a N_2 atmosphere. The vessel was then connected to an Argon manifold and was cooled inside the glovebox freezer. To the solution was added 6 mg (0.06 mmol) LDA and the solution was allowed to stand inside the glovebox freezer at -35 $^{\circ}\text{C}$ overnight. The dark blue solution of **17** in THF turned dark green over the course of the reaction. The solvent was then removed under vacuum, giving a THF-soluble green residue. The product, unfortunately, did not form X-ray quality crystals.

Synthesis of $[\text{tBu}_3\text{PNH}_2]^+[\text{Co}(\text{SC}_6\text{H}_5)_3(\text{HNP}^t\text{Bu}_3)]^-$ **18**

A five-dram glass vial was charged with 150 mg (0.017 mmol) $[\text{CoCl}(\text{PPh}_3)_3]$, 3.00 mL THF and a magnetic stir bar under a N_2 atmosphere. A two-mL THF suspension containing 40 mg (0.17 mmol) LiNP^tBu_3 was added in small portions over two h, resulting a change in the

color of the solution from green to dark green. The reaction mixture was stirred at room temperature for three h. A two-mL THF solution containing 47 mg (0.43 mmol) thiophenol was then added, resulting in an immediate color change from dark green to bright green. The solvent was then removed under vacuum, giving a benzene-soluble dark blue residue. X-ray quality crystals of the benzene-soluble solids were obtained from a concentrated THF solution at 35 °C. Crystallographic analysis revealed a solid-state structure consistent with the formula $[^t\text{Bu}_3\text{PNH}_2]^+[\text{Co}(\text{SC}_6\text{H}_5)_3(\text{HNP}^t\text{Bu}_3)]^-$ **18** (20 mg, 28 %).

Reaction of **18** with LDA

A 10-mL Schlenk flask was charged with 20 mg (0.02 mmol) **18**, 2.00 mL THF and a magnetic stir bar under a N₂ atmosphere. The vessel was then connected to an Argon manifold and was cooled in a dry ice-acetone bath. A two mL THF solution containing 5.2 mg (0.05 mmol) LDA was added through canula transfer. The solution was stirred from -78 °C to room temperature overnight. The dark blue solution of **18** in THF turned dark green over the course of the reaction. The solvent was then removed under vacuum, giving a THF-soluble green residue. The product, unfortunately, does not form X-ray quality crystals.

Reaction of **16** with Ethylene: Formation of $[\text{Co}(\text{NP}^t\text{Bu}_3)_3]$ **22**

A five-dram glass vial was charged with 150 mg (0.017 mmol) $[\text{CoCl}(\text{PPh}_3)_3]$, 3.00 mL THF and a magnetic stir bar under a N_2 atmosphere. A two-mL THF suspension containing 40 mg (0.17 mmol) LiNP^tBu_3 was added in small portions over two h, resulting in a change in the color of the solution from green to dark green. The reaction mixture was stirred at room temperature for three h. The vessel was then connected to an Argon manifold and was cooled in a dry ice-acetone bath. The Argon atmosphere was then replaced with a stream of purified ethylene (1 atm). The dark brown THF solution of **16** immediately turned cherry red upon exposure to ethylene. The solvent was then removed under vacuum, giving a cherry red, pentane-soluble residue. The product formed X-ray quality crystals from a concentrated THF solution at -35 °C. The X-ray characterization revealed a mononuclear structure with the formula $[\text{Co}(\text{NP}^t\text{Bu}_3)_3]$ **22**. The yield of **22** in this experiment was not determined.

Synthesis of $[\text{Co}(\text{NP}^t\text{Bu}_3)\text{Cl}(\text{THF})]_2$ **24**

A five-dram glass vial was charged with 60 mg (0.46 mmol) CoCl_2 , 2.00 mL THF and a magnetic stir bar. A separate five-dram vial was charged with 2.00 mL THF and 45 mg (0.20 mmol) LiNP^tBu_3 . Both vials were cooled to -35 °C in a drybox freezer for 1 h. While stirring and maintaining a -35 °C temperature, small portions of the LiNP^tBu_3 suspension were added to the CoCl_2 -containing vial over four h. The

addition of LiNP^tBu₃ resulted in an immediate color change pale blue to dark blue. The reaction mixture was left standing in the dry box freezer at –35 °C overnight. The solvent was then removed under vacuum, giving a benzene-soluble dark blue residue. X-ray quality crystals of the benzene-soluble solids were obtained from a concentrated THF solution at 35 °C (133 mg, 87 %). Crystallographic analysis revealed a solid-state structure consistent with the formula [Co(NP^tBu₃)Cl(THF)]₂ **24**.

Synthesis of [Co(NP^tBu₃)(C₃H₅)] **25**

A five-dram glass vial was charged with 30 mg (0.04 mmol) **24**, 1.00 mL THF and a magnetic stir bar. A separate five-dram vial was charged with 1.00 mL THF and 15 mg (0.15 mmol) allyl magnesium chloride, Mg(C₃H₅)Cl. While stirring at room temperature, small portions of the Mg(C₃H₅)Cl solution was added to the THF solution of **24** over four h. The addition of LiNP^tBu₃ resulted in an immediate color change dark blue to dark green. The reaction mixture was left stirring at room temperature overnight. The solvent was then removed under vacuum, giving a pentane-soluble dark green residue (17 mg, 42 %). Unfortunately, the product forms microcrystalline materials from THF. Elemental analysis of **25** suggests an empirical formula of [Co(NP^tBu₃)(C₃H₅)]. Elemental composition (found): %C, 55.31; %H, 10.39; %N, 4.61; (calculated) %C, 56.95; %H, 10.20; %N, 4.43.

Two-Step Synthesis of $[M(NP^tBu_3)_4]$ from M(II) Halide Precursors

The metal precursor (1.62 mmol) and LiNP^tBu₃ (0.81 mmol) were separately suspended in 5 mL portions of THF in 15 mL screw-capped vials. Both suspensions were cooled to -35 °C in a drybox freezer for an h. The LiNP^tBu₃ suspension was added dropwise into the metal halide suspension with occasional stirring for four h period with the temperature maintained at -35 °C. After the addition of the ligand, the reaction mixture was left in the freezer overnight. The solvent was removed *in vacuo* and the residue was washed with 4 mL portions of hexane thrice. The residue was dissolved in 7 mL THF, charged with 7.5 g of 1% Na/Hg and stirred overnight. The solvent was evaporated and the product was extracted with pentane and filtered through a plug of Celite. The solvent was removed and a concentrated THF solution of the product was prepared for recrystallization. The product precipitates as prismatic crystals upon cooling to -35 °C. Both compounds were characterized by X-ray crystallography, magnetic susceptibility measurement by the Evan's method,³¹⁶ and elemental analysis (*vide infra*).

26a: $[Co(NP^tBu_3)_4]$

The Co(I) tetramer was synthesized from CoCl₂ at 65 % yield. The reddish-brown, pentane soluble solid crystallizes out as prisms from a concentrated THF solution. Elemental composition (calculated): C, 52.36 %; H, 9.89 %; N, 5.09 %; (found): C, 52.68 %; H, 10.09 %; N, 4.86 %. The

solution magnetic susceptibility experiments revealed that **2** is an 8-electron paramagnet ($\mu_{\text{eff}} = 8.98 \mu_{\text{Bo}}$) at 27 °C.

26b [Ni(NP^tBu₃)₄]

The Ni(I) tetramer was synthesized from NiBr₂(dme) at 80 % yield. The dark green, pentane soluble solid crystallizes out as prisms from a concentrated THF solution. Elemental composition (calculated): C, 52.41 %; H, 9.90 %; N, 5.09 %; (found): C, 52.38 %; H, 9.89 %; N, 4.96 %. The solution magnetic susceptibility experiments revealed that **1** is a 3.50-electron paramagnet ($\mu_{\text{eff}} = 4.40 \mu_{\text{Bo}}$) at 27 °C.

Synthesis of **22** from **24**

A five-dram glass vial was charged with 40 mg (0.05 mmol) **24**, 1.50 mL THF and a magnetic stir bar. To the solution was added 50 mg (0.22 mmol) LiNP^tBu₃ at room temperature. The addition of LiNP^tBu₃ resulted in an immediate color change dark blue to intensely dark green. The solution was stirred for three h. White stirring, 28 mg (0.10 mmol) Ph₃CCl was added to the solution, resulting in an immediate color change (dark green to cherry red). The reaction mixture was left stirring at room temperature overnight. The solvent was then removed under vacuum, giving a pentane-soluble cherry red residue (crude yield = 31 mg, 44 %). X-ray quality crystals were obtained from a cold, concentrated THF solution. The

crystals obtained shows unit cell parameters identical to **22**. The sample did not pass elemental analysis presumably due to Ph₃CCl impurities.

One-Pot Synthesis of **28** from M(II) Halide Precursors

A five-dram glass vial was charged with 40 mg (0.31 mmol) CoCl₂, two mL THF and a magnetic stir bar. A separate five-dram vial was charged with two mL THF and 207 mg (0.93 mmol) LiNP^tBu₃. While stirring at room temperature, small portions of the LiNP^tBu₃ suspension were added to the THF solution of **24**. The addition of LiNP^tBu₃ resulted in an immediate color change dark blue to intensely dark green. White stirring, 87 mg (0.31 mmol) Ph₃CCl was added to the solution, resulting in an immediate color change (dark green to cherry red). The reaction mixture was left stirring at room temperature overnight. The solvent was then removed under vacuum. A pentane-soluble red residue was extracted and purified by recrystallization in THF at -35 °C. The crystals obtained shows unit cell parameters identical to **22**. The sample did not pass elemental analysis presumably due to Ph₃CCl impurities (crude yield = 175 mg, 80 %). ¹H-NMR (C₆D₆, 399.79 MHz) 1.49 ppm (s); ³¹P-NMR (C₆D₆, 399.79 MHz) 50.33 ppm (s).

One-Pot Synthesis of [Fe(NPCy₃)Cl₂]**28** from M(II) Halide Precursors

A five-dram glass vial was charged with 9 mg (0.07 mmol) FeCl₂, 1.00 mL THF and a magnetic stir bar. A separate five-dram vial was

charged with 1.00 mL THF and 72 mg (0.24 mmol) LiNPCy₃. While stirring at room temperature, small portions of the LiNPCy₃ suspension were added. The addition of LiNPCy₃ resulted in an immediate color change dark blue to intensely dark brown. White stirring, 20 mg (0.07 mmol) Ph₃CCl was added to the solution, resulting in an immediate color change (dark green to red-orange). The reaction mixture was left stirring at room temperature overnight. The solvent was then removed under vacuum, giving to product fractions: a pentane-soluble red residue and a THF-soluble red-orange material. X-ray quality crystals of the THF-soluble residue were obtained from a cold, concentrated THF solution. The crystals obtained shows unit cell parameters identical to [Fe(NPCy₃)Cl₂]₂**28** which was first reported by Dehnicke and coworkers. Dimer **28** was obtained in trace quantities; hence, the yield was not determined.

7.2 Base Metal–Catalyzed Hydrogenation of Alkenes and Alkynes

General Consideration

All manipulations were carried out using Schlenk techniques. The preparation of each reaction mixture was carried out under a purified N₂ atmosphere in an drybox. Experiments that required heating were conducted under a Schlenck manifold. Thoroughly dried and degassed solvents were used in all experiments. Liquid alkenes and alkynes were degassed and passed through anhydrous silica prior to use. High-purity grade H₂, purchased from Praxair Canada, was used in all hydrogenation experiments. NMR spectra were recorded on an Agilent/Varian Inova two-channel 400 MHz spectrometer at room temperature. ¹H NMR spectra were referenced to residual protio solvent peaks (CDCl₃ and C₆D₆).

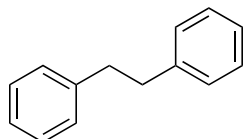
GC-MS Analysis

GC-MS analysis was conducted using an Agilent 5890 GC equipped with a 7673 Automatic Liquid Sampler (ALS). The column used for the analysis is an Agilent DB-5 MS (25m x 0.25mm x 0.25 micron film thickness). The following GC conditions were applied in all analyses: (1) injector port temperature: 300 °C; (2) initial temperature: 50 °C (hold for 2 min); (3) temperature ramp: 10 °C/min; (4) final temperature: 280 °C (5 minutes hold time); (5) detector temperature: 300 °C. Total run time: 35 minutes.

The detectors used are HP 5971 MSD or HP 5870 MSD calibrated using perfluorotributylamine (PFTBA). The data were acquired using Agilent Chemstation software and identification of known compounds produced from the succeeding reactions was conducted by spectral matching with the NIST/EPA/NIH 2011 Mass Spectral Library and Software package (NIST11) and by comparison of experimental data with literature structure characterization reports.

Quantitative Hydrogenation of Diphenylacetylene **39**

A 100 mL Teflon-sealing glass reactor equipped with a Teflon-covered magnetic stirring bar was charged with 10 mg (0.009 mmol) of **26a/26b**, 50 mg (0.28 mmol) diphenylacetylene **39** and 3 mL tetrahydrofuran (THF). The reactor was sealed and taken out of the dry box. The reactor was attached to a hydrogen manifold and the reactor was charged with a stream of hydrogen (1 atm). The reaction mixture was stirred at room temperature, at a speed of 1200 rpm overnight. Excess hydrogen gas was then vented out and 3 mL of water was added. The organic product was extracted with 2 mL portions of diethyl ether thrice and the organic fractions were pooled and dried over anhydrous Na₂SO₄. The solvent was removed *in vacuo* and the solid residue was dissolved in CDCl₃ for ¹H-NMR. Quantitative conversion to 1,2-diphenylethane **30** was observed in both cobalt- and nickel-catalyzed hydrogenation based on ¹H-NMR analysis of the product.



1,2-Diphenylethane **30**. $^1\text{H-NMR}$ (CDCl_3 , 399.79 MHz) δ 7.40 (m, 4H), 7.29 (m, 6H), 3.02 (s, 4H). GC-MS m/z 182 (M^+), 165, 104, 91, 77, 65, 51.

Quantitative Hydrogenation of *Trans*-Stilbene **29**

A 100 mL Teflon-sealing glass reactor equipped with a Teflon-covered magnetic stirring bar was charged with 10 mg (0.009 mmol) of **26a/26b**, 50 mg (0.28 mmol) *trans*-stilbene **29** and 2 mL tetrahydrofuran (THF). The reactor was sealed and taken out of the dry box. The reactor was attached to a hydrogen manifold and the reactor was charged with a stream of hydrogen (1 atm). The reaction mixture was stirred at room temperature, at a speed of 1200 rpm overnight. Excess hydrogen gas was then vented out and 3 mL of water was added. The organic product was extracted with 2 mL portions of diethyl ether thrice and the organic fractions were pooled and dried over anhydrous Na_2SO_4 . The solvent was removed *in vacuo* and the solid residue was dissolved in CDCl_3 for $^1\text{H-NMR}$. Quantitative conversion to 1,2-diphenylethane **30** was observed in both cobalt- and nickel-catalyzed hydrogenation based on $^1\text{H-NMR}$ analysis of the product.

Partial Hydrogenation of *Trans*-Stilbene **29**

A 250 mL Teflon-sealing glass reactor equipped with a Teflon-covered magnetic stirring bar was charged with 6 mg (0.005 mmol) of **26a/26b**, 200 mg (1.11 mmol) *trans*-stilbene **29** and 2 mL tetrahydrofuran (THF). The reactor was sealed and taken out of the dry box. The reactor was attached to a hydrogen manifold and the reactor was charged with a stream of hydrogen (1 atm). The reaction mixture was stirred at a speed of 1200 rpm for 40 min at room temperature. Excess hydrogen gas was then vented out and 3 mL of water was added. The organic product was extracted with 2 mL portions of diethyl ether thrice and the organic fractions were pooled and dried over anhydrous Na₂SO₄. The solvent was removed *in vacuo* and the solid residue was dissolved in CDCl₃ for ¹H-NMR and GC-MS analysis. The hydrogenation rate was calculated based on the GC-MS analysis results and ratios of characteristic ¹H-NMR chemical shifts of *trans*-stilbene **29** (7.23 ppm, singlet, 2H, vinyl C-H) and 1,2-diphenylethane **30** (3.02 ppm, singlet, 4H, -CH₂CH₂-) in CDCl₃.

Table 7.1.1. Partial hydrogenation of *Trans*-Stilbene **29**.

Catalyst	% Conversion to 30 (GC-MS)
26a	39
26b	35

Partial Hydrogenation of *Cis*-Stilbene **31**

A 250 mL Teflon-sealing glass reactor equipped with a Teflon-covered magnetic stirring bar was charged with 6 mg (0.005 mmol) of

26a/26b, 200 mg (1.11 mmol) *cis*-stilbene **31** and 4 mL tetrahydrofuran (THF). The reactor was sealed and taken out of the dry box. The reactor was attached to a hydrogen manifold and the reactor was charged with a stream of hydrogen (1 atm). The reaction mixture was stirred at a speed of 1200 rpm for 40 min at room temperature. Excess gas was then vented out and 3 mL of water was added. The organic product was extracted with 2 mL portions of diethyl ether thrice and the organic fractions were pooled and dried with anhydrous Na₂SO₄. The solvent was removed *in vacuo* and the solid residue was dissolved in CDCl₃ for ¹H-NMR and GC–MS analysis. A ¹H-NMR chemical shift at 3.0 ppm in CDCl₃ corresponds to 1,2-diphenylethane **30**, the hydrogenation product. The hydrogenation rate was calculated based on the GC-MS analysis results and ratios of ¹H-NMR chemical shifts of *trans*-stilbene (6.70 ppm, singlet, 2H, *vinyl C-H*) and 1,2-diphenylethane (3.0 ppm, singlet, 4H, -CH₂CH₂-) ppm in CDCl₃.

Table 7.1.2. Partial hydrogenation of *Cis*-Stilbene **31**.

Catalyst	% Conversion to 30 (GC-MS)
26a	23
26b	18

Partial Hydrogenation of Allylbenzene **34**

A 250 mL Teflon-sealing glass reactor equipped with a Teflon-covered magnetic stir bar was charged with **26a/26b**, allylbenzene **34** and 0.5 mL tetrahydrofuran (Table 7.3). The reactor was sealed and taken out

of the dry box. The reactor was attached to a hydrogen manifold and the reactor was charged with a stream of hydrogen (1 atm). The reaction mixture was stirred at a speed of 1200 rpm for 40 min at room temperature. Excess hydrogen gas was then vented out and the reaction mixture was filtered through a plug of Florisil. The THF-fraction was subjected to GC-MS and ¹H-NMR analysis. The formation of *n*-propylbenzene was confirmed by comparison of GC-MS and ¹H-NMR analysis results with reported spectral data.³¹⁷

Table 7.1.3. Partial hydrogenation of Allylbenzene **34**.

Mass 34 (mg)	Catalyst mass in mg (mol%)	% Conversion			TOF^c
		35	36a	36b	
182	26a 6 (0.5)	54	9	3	230
120	26b 10 (0.9)	49	25	trace	71

Isomerization of β-Pinene **37**

A 100 mL Teflon-sealing glass reactor equipped with a Teflon-covered magnetic stir bar was charged with 7 mg (0.006 mmol) of **26b**, 128 mg (0.94 mmol) β-pinene **37**, 6 mg (0.05 mmol) Et₃SiH and 1 mL C₆D₆. The reactor was sealed and taken out of the dry box. The reaction mixture was heated to 80 °C and stirred at 1200 rpm for 16 h. The mixture was then cooled to room temperature, exposed to air and filtered through a plug of Florisil. The solution was then subjected to ¹H-NMR analysis. Quantitative isomerization of b-pinene **37** to a-pinene **38** was observed by the complete disappearance of the terminal alkene (C=CH₂)

chemical shift (4.61 ppm) and formation of a single vinyl C–H signal at 5.36 ppm (s) in the product. The identity of the product was also confirmed through spiking experiments with authentic α -pinene **38** and comparison with literature spectra.^{318,319}

Partial Hydrogenation of Diphenylacetylene **39**

A 250 mL Teflon-sealing glass reactor equipped with a Teflon-covered magnetic stirring bar was charged with **26a/26b**, diphenylacetylene **39** and 2 mL tetrahydrofuran (Table 7.4). The reactor was sealed and taken out of the dry box. The reactor was attached to a hydrogen manifold and the reactor was charged with a stream of hydrogen (1 atm). The reaction mixture was stirred at a speed of 1200 rpm for 40 min at room temperature. Excess gas was then vented out and 3 mL of water was added. The organic product was extracted with 2 mL portions of diethyl ether thrice and the organic fractions were pooled and dried with anhydrous Na_2SO_4 . The solvent was removed *in vacuo* and the solid residue was dissolved in CDCl_3 for $^1\text{H-NMR}$ and GC–MS analysis. The identification of hydrogenation-isomerization products was conducted through comparison with literature data.

Table 7.1.4. Partial hydrogenation of diphenylacetylene **39**.

Mass 39 (mg)	Catalyst / mass in mg (mol%)	% Conversion			TOF^c
		29	31	30	
200	26a / 6 (0.5)	2	11	ND	40
120	26b / 10 (0.9)	3	8	ND	59

Hydrogenation of 1,1,2,2-tetraphenylethene **40**

A 100 mL Teflon-sealing glass reactor equipped with a Teflon-covered magnetic stir bar was charged with 3 mg (0.002 mmol) of **26b**, 200 mg (0.60 mmol) 1,1,2,2-tetraphenylethene **40** and 3 mL toluene. The reactor was sealed and taken out of the dry box. The reactor was attached to a hydrogen manifold and the reactor was charged with a stream of hydrogen (1 atm). The reaction mixture was stirred at a speed of 1200 rpm for 24 h at 120 °C. The reactor was then cooled to room temperature and excess hydrogen gas was then vented out. The reaction mixture was filtered through a plug of Florisil. The solvent was removed under vacuum and the residue was dissolved in CDCl₃ for ¹H-NMR analysis. The formation of 1,1,2,2-tetraphenylethane **41** (8.1 %; TOF = 0.7/h) was confirmed by the expected formation of a singlet chemical shift at 4.83 ppm.³¹⁷

Hydrogenation of Anthracene **42**

A 100 mL Teflon-sealing glass reactor equipped with a Teflon-covered magnetic stir bar was charged with 5 mg (0.004 mmol) of **26b**, 169 mg (0.95 mmol) anthracene **42** and 3 mL toluene. The reactor was sealed and taken out of the dry box. The reactor was attached to a hydrogen manifold and the reactor was charged with a stream of hydrogen (1 atm). The reaction mixture was stirred at a speed of 1200 rpm for 12 h at 120 °C. The reactor was then cooled to room temperature and excess

hydrogen gas was then vented out. The reaction mixture was filtered through a plug of Florisil. The solvent was removed under vacuum and the residue was dissolved in CDCl₃ for ¹H-NMR analysis. The yield of 9,10-dihydroanthracene **43** (13.4 %; TOF = 2.3/h) was determined based on the ratio of integrations of characteristic chemical shifts of the starting material and the product.³²¹

Reaction Between **26b** and H₂

Carefully weighed amount of the catalyst **26b** (0.006 mmol) was dissolved in 3.0 mL C₆D₆. The solution was divided into three equal portions. The first fraction was subjected to solution FT-IR and ¹H-NMR analysis. The remaining two 1-mL portions were transferred into Teflon-stopcock-sealed glass reactors. The reaction vessel was then charged with a constant stream of hydrogen (1 atm), employing strict inert-atmosphere laboratory techniques, and stirred at 1200 rpm. After first 10 min of exposure, excess hydrogen was vented off from one of the two reactors and the solution was subjected to solution FT-IR and ¹H-NMR experiments. The FT-IR and ¹H-NMR of the second solution were obtained after 20 min of stirring under a H₂ atmosphere. The IR band at 2280 cm⁻¹ arises from the solvent C₆D₆. Time = 10 min: 1621, 1967 cm⁻¹. Time = 20 min: 1715, 2118 cm⁻¹.

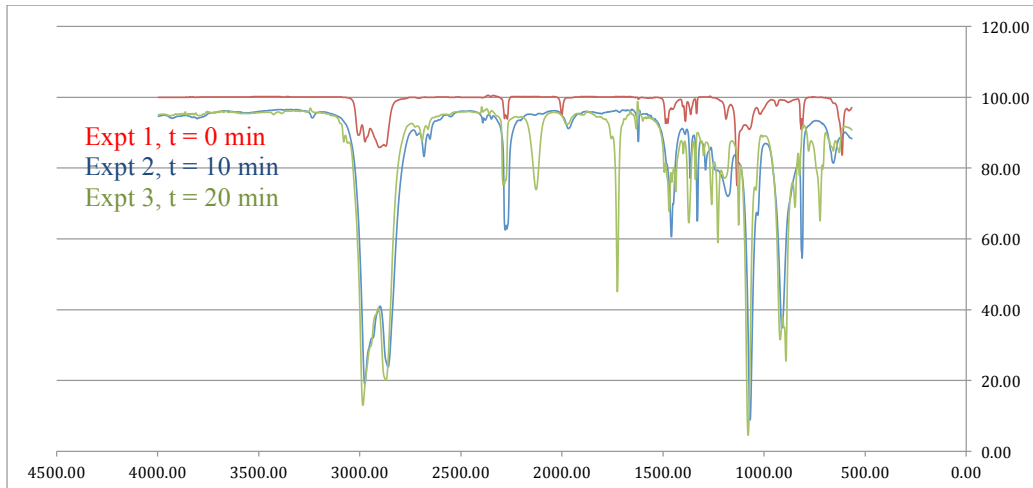


Figure 7.1. FT-IR spectra of **26b** in C_6D_6 upon exposure to H_2 .

Paramagnetic ^1H -NMR spectra obtained from these experiments are not reproduced here, as there were no obvious changes observed in the solution spectra over the course of the experiment.

Test of Catalyst Homogeneity: Hydrogenation of *Trans*-Stilbene **29**

A 100 mL Teflon-sealing glass reactor equipped with a Teflon-covered magnetic stirring bar was charged with 9 mg (0.008 mmol) of **26a**, 93 mg (0.52 mmol) *trans*-stilbene **29**, 600 mg $\text{Hg}(0)$ and 3 mL tetrahydrofuran (THF). The reactor was sealed and taken out of the dry box. The reactor was attached to a hydrogen manifold and the reactor was charged with a stream of hydrogen (1 atm). The reaction mixture was stirred at a speed of 1200 rpm for 40 min at room temperature. Excess hydrogen gas was then vented out and 3 mL of water was added. The

organic product was extracted with 2 mL portions of diethyl ether thrice and the organic fractions were pooled and dried over anhydrous Na₂SO₄. The solvent was removed *in vacuo* and the solid residue was dissolved in CDCl₃ for ¹H-NMR. The hydrogenation rate was calculated based on the GC-MS analysis results and ratios of characteristic ¹H-NMR chemical shifts of *trans*-stilbene and 1,2-diphenylethane. No significant difference in the rates of hydrogenation was observed even in the presence of excess Hg(0). The nickel-catalyzed hydrogenation afforded 1,2-diphenylethane in 29% yield (TOF_{Hg(0)} = 0.49/min) while the corresponding reduction in the absence of Hg(0) resulted in 33% conversion (TOF = 0.53/min).

Hydrogenation of Diphenylacetylene with a Nickel-tricyclohexylphosphoranimide Catalyst

Synthesis of [Ni(NPCy₃)_n] from NiBr₂(dme): A 10-dram vial was charged with 31 mg (0.10 mmol) NiBr₂(dme) and 5 mL THF, cooled to -35 °C, stirred, and then treated with 30 mg (0.05 mmol) LiNPCy₃ over an hour. The mixture was then treated with 275 mg 1% Na(Hg) (0.24 mmol Na) reagent at room temperature and stirred for 2 h. The THF fraction of the mixture was separated from any remaining solid components by filtration through a plug of Celite. The THF fraction was used directly as dissolved catalyst and solvent for the hydrogenation of diphenylacetylene **39**. A 100 mL Teflon-sealing glass reactor equipped with 250 mg (1.40 mmol) **39** and the THF fraction. The reactor was sealed and taken out of the dry box. The

reactor was hooked up to a hydrogen manifold and the reactor was charged with a stream of hydrogen (1 atm). The reaction mixture was stirred for 45 min at room temperature. Excess gas was then vented out and 3 mL of water was added. The organic product was extracted with 2 mL portions of diethyl ether thrice and the organic fractions were pooled and dried with anhydrous Na₂SO₄. The solvent was removed *in vacuo* and the solid residue was dissolved in CDCl₃ for ¹H-NMR and GC-MS analysis. A 21% substrate conversion was observed: *trans*-stilbene **29**, 5%; *cis*-stilbene **31**, 15%; 1,2-diphenylethane **30**, 1%.

Hydrogenation of Diphenylacetylene with an Iron-*tri-tert*-butylphosphoranimide Catalyst

Synthesis of [Fe(NP^tBu₃)₄] from [Br₂Fe₂(μ-NP^tBu₃)₂]: 0.05 mmol of [Br₂Fe₂(μ₂-NP^tBu₃)₂] was dissolved in 5 mL THF, stirred, and then treated with 0.05 mmol of Na using a 1 % Na(Hg) reagent at room temperature 2 h. The THF fraction of the mixture was separated from any remaining solid components by filtration through a plug of Celite. The THF fraction was used directly as dissolved catalyst and solvent for the hydrogenation of diphenylacetylene **39**. A 250 mL Teflon-sealing glass reactor equipped with a Teflon-covered magnetic stirring bar was charged with the THF solution from the previous step and 200 mg (1.11 mmol) **39**. The reactor was sealed and taken out of the dry box. The reactor was connected to a hydrogen manifold and the reactor was charged with a stream of hydrogen

(1 atm). The reaction mixture was stirred for 30 min at room temperature. Excess gas was then vented out and 3 mL of water was added. The organic product was extracted with 2 mL portions of diethyl ether thrice and the organic fractions were pooled and dried with anhydrous Na₂SO₄. The solvent was removed *in vacuo* and the solid residue was dissolved in CDCl₃ for ¹H-NMR and GC–MS analysis. A conversion of 11% was obtained. The products of this reaction are: *trans*–stilbene **29** (4 %) and *cis*–stilbene **31** (7 %).

[2+2+2] Cycloaddition of Diphenylacetylene **39**

A 100 mL Schlenk flask equipped with a Teflon-covered magnetic stir bar was charged with 1 mg (0.001 mmol) of **26b**, 52 mg (0.29 mmol) **39** and 2 mL THF. The reactor was sealed and taken out of the dry box and stirred at 50 °C for 10 h. The reactor was cooled to room temperature and the mixture was filtered through a plug of Florisil. The solvent was removed under vacuum and the residue was dissolved in CDCl₃ for ¹H-NMR analysis. The formation of 1,2,3,4,5,6-hexaphenylbenzene **55** was confirmed by the appearance of a singlet chemical shift at 6.86 ppm, consistent with literature ¹H-NMR chemical shift,³²² and by spiking experiments using authentic material. A 13% substrate conversion to **55** was observed over 10 h (TOF = 0.5 C₆Ph₆/h).

[2+2+2] Cycloaddition of 2-butyne **56**

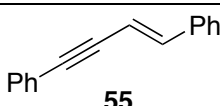
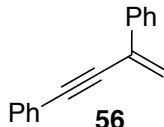
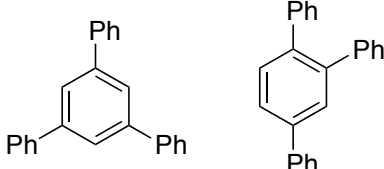
A 100 mL Schlenk flask equipped with a Teflon-covered magnetic stir bar was charged with 2.5 mg (0.002 mmol) of **26b**, 25 mg (0.46 mmol) **56** and 2 mL THF. The reactor was sealed and taken out of the dry box and stirred at 50 °C for 2 h. The reactor was cooled to room temperature and the mixture was filtered through a plug of Florisil. The solvent was removed under vacuum and the residue was dissolved in CDCl₃ for ¹H-NMR analysis. The formation of 1,2,3,4,5,6-hexamethylbenzene was confirmed by a singlet chemical shift at 2.24 ppm, consistent with reported ¹H-NMR spectral data and by spiking experiments using authentic material.³²² A 40% substrate conversion to 1,2,3,4,5,6-hexaphenylbenzene (10 mg) was observed over two h (TOF = 17 C₆Me₆/h).

Hydrogenation of Phenylacetylene **54**

A 100 mL Teflon-sealing glass reactor equipped with a Teflon-covered magnetic stir bar was charged with 135 mg (1.30 mmol) phenylacetylene **58** and 7 mg (0.006 mmol) of **26b** dissolved in a few drops of THF. The reactor was sealed and taken out of the dry box. The reactor was attached to a hydrogen manifold and the reactor was charged with a stream of hydrogen (1 atm). The reaction mixture was stirred at a speed of 1200 rpm for 16 h at room temperature. Excess hydrogen gas was then vented out and the reaction mixture was filtered through a plug of Florisil. The solvent (THF) was then removed *in vacuo* and the residue

was dissolved in CDCl_3 for $^1\text{H-NMR}$ analysis. Since the products are known compounds, the identity of the product(s) was confirmed by GC-MS library matching and based on characteristic $^1\text{H-NMR}$ chemical shifts.^{323,324} A 92% substrate conversion was observed over 16 h.

Table 7.1.5. Hydrogenation of phenylacetylene **58**.

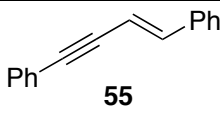
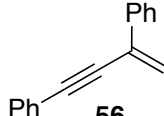
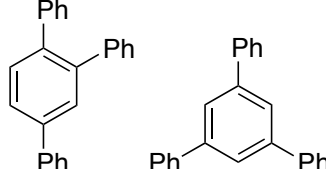
Product	% Yield (GC-MS)
	50
	5
	10
	27

Linear Dimerization of Phenylacetylene **54**

A 100 mL Teflon-sealing glass reactor equipped with a Teflon-covered magnetic stir bar was charged with 135 mg (1.30 mmol) phenylacetylene **54** and 7 mg (0.006 mmol) of **26b** dissolved in 2 mL THF. The reaction mixture was stirred for 16 h at room temperature. The reaction mixture was exposed to air and then filtered through a plug of Florisil. The solvent was removed under vacuum and the residue was dissolved in CDCl_3 and subjected to $^1\text{H-NMR}$ and GC-MS analyses. Since the products are known compounds, the identity of the product(s) was

confirmed by GC–MS library matching and comparison with literature ^1H -NMR chemical information.

Table 7.1.6. Linear dimerization of phenylacetylene.

Product	% Yield (GC-MS)
 55	51
 56	12
 37	37

7.3 Base Metal-Catalyzed Hydrosilylation of Carbonyl Substrates

General considerations.

All manipulations were carried out using Schlenk techniques. The preparation of each reaction mixture was carried out under a purified N₂ atmosphere in an drybox. Experiments that required heating were conducted under a Schlenck manifold. Thoroughly dried and degassed solvents were used in all experiments. Liquid silanes, aldehydes and ketones were degassed and passed through anhydrous silica prior to use. NMR spectra were recorded on an Agilent/Varian Inova two-channel 400 MHz spectrometer at room temperature. ¹H NMR spectra were referenced to residual protio solvent peaks (CDCl₃ and C₆D₆).

GC-MS Analysis

GC-MS analysis was conducted using an Agilent 5890 GC equipped with a 7673 Automatic Liquid Sampler (ALS). The column used for the analysis is an Agilent DB-5 MS (25m x 0.25mm x 0.25 micron film thickness). The following GC conditions were applied in all analyses: (1) injector port temperature: 300 °C; (2) initial temperature: 50 °C (hold for 2 min); (3) temperature ramp: 10 °C/min; (4) final temperature: 280 °C (5 minutes hold time); (5) detector temperature: 300 °C. Total run time: 35 minutes.

The detectors used are HP 5971 MSD or HP 5870 MSD calibrated using perfluorotributylamine (PFTBA). The data were acquired using Agilent Chemstation software and identification of known compounds produced from the succeeding reactions was conducted by spectral matching with the NIST/EPA/NIH 2011 Mass Spectral Library and Software package (NIST11) and by comparison of experimental data with literature structure characterization reports.

Hydrosilylation of Cyclohexanone **72** with PhSiH₃

The following procedure was employed for the hydrosilylation of cyclohexanone using both cobalt and nickel catalysts, [M(NP^tBu₃)₄] (M = Co, Ni).

A 5-dram vial was charged with 4.08×10^{-3} mmol **26a** (or **26b**), 165 mg (1.53 mmol) PhSiH₃, 1.5 mL THF and a magnetic stir bar. A vigorous reaction occurs upon mixing PhSiH₃ with the catalyst. The mixture was stirred for five min and 100 mg (1.02 mmol) cyclohexanone was added. The mixture was then stirred at a rate of 1200 rpm over 16 h. The reaction mixture was then exposed to air and filtered through a plug of alumina. The solvent and excess silanes were evaporated under vacuum at 40 °C. Mixtures of *PhSiH₂OCy* **73** and *PhSiH(OCy)₂* **74** were obtained from the cobalt- and nickel-catalyzed experiments. These *product mixtures* were subjected to ¹H-NMR and GC-MS analyses. The products of cyclohexanone hydrosilylation with PhSiH₃ are known compounds, hence,

identification of the hydrosilylation products was conducted through GC-MS library matching and comparison of mass spectra with literature reports.³²⁵ Carbonyl hydrosilylation was confirmed by the appearance of the expected carbinol C–H bond resulting from the C=O double bond reduction was confirmed by the appearance of a multiplet at 3.89 ppm (products *PhSiH₂O Cy* **73** and *PhSiH(O Cy)₂* **74** have overlapping chemical shifts). The reported ratio of **73** and **74** for each experiment was based on the GC-MS results.

The cobalt-catalyzed reaction resulted in 51 % substrate conversion into a 2:1 mixture of **73** (34 %) and **74** (17 %). The nickel-catalyzed reaction resulted in 95 % substrate conversion affording **73** and **74** in 22 % and 73 % yield, respectively.

Hydrosilylation of Cyclohexanone **72** with Limiting Amount of PhSiH₃

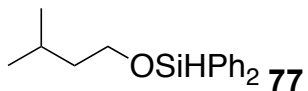
A 5-dram vial was charged with 4.5 mg (4.1×10^{-3} mmol) 26b, 55 mg (0.51 mmol) PhSiH₃, 1.5 mL THF and a magnetic stir bar. The vial was sealed and stirred for five min and 100 mg (1.02 mmol) cyclohexanone was added. The mixture was then stirred at 1200 rpm over 16 h. The reaction mixture was then exposed to air and filtered through a plug of alumina. The solvent and excess silanes were evaporated *in vacuo* at 40 °C. The residue was then subjected to ¹H-NMR (in CDCl₃) and GC-MS analyses. A 90% substrate conversion to *PhSiH(O Cy)₂* **73** was detected based on GC-MS results.

General Methodology for Hydrosilylation of Aldehydes and Ketones with 0.4 mol% 26b

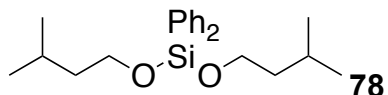
This methodology was employed in the hydrosilylation of isovaleraldehyde **76**, cyclohexanone **72** and 3-cyclohexene-1-carboxaldehyde **81**. A 5-dram vial, equipped with a magnetic stir bar, was charged with a solution of 1.53 mmol Ph₂SiH₂ and 0.0041 mmol 26b in 1.00 mL THF. A vigorous reaction occurs upon mixing Ph₂SiH₂ with 26b. The solution was stirred for five min and charged with 1.02 mmol substrate and an additional 0.5 mL portion of THF. The vial was sealed and stirred at 1200 rpm over 16 h. The reaction mixture was then exposed to air and filtered through a plug of alumina. The solvent and excess silanes were evaporated *in vacuo* at 40 °C. The residue was then subjected to ¹H-NMR and GC-MS analyses.

Isovaleraldehyde 76

The hydrosilylation of isovaleraldehyde afforded a mixture of the monoalkoxy- and dialkoxyphenylsilane products PhSiH₂(OC₅H₁₁) **77** and PhSiH(OC₅H₁₁)₂ **78**. Hydrosilylation of the carbonyl functional group was confirmed by the appearance of a triplet carbinol C–H chemical shift at 3.89 ppm (products **77** and **78** have overlapping chemical shifts). The reported ratio of **77** and **78** for each experiment was based on the GC-MS results.



GC-MS *m/z* 270 (M^+), 213, 192, 183, 137, 123, 114, 105, 91, 77, 51. Yield (GC-MS): 59 %.



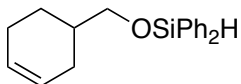
GC-MS *m/z* 356 (M^+), 299, 270, 235, 213, 200, 192, 183, 167, 153, 139, 123, 91, 77, 69, 55. Yield (GC-MS): 41 %.

Cyclohexanone 72

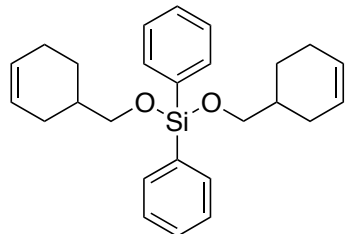
The product mixture was submitted for GC-MS and $^1\text{H-NMR}$ analyses as a mixture. Thorough characterization of the products of this experiment was reported by Tilley and coworker, hence, the yields of cyclohexyloxydiphenylsilane **79** (55%) and bis(cyclohexyloxy)diphenylsilane **80** (5%) was determined by spectral matching with literature data.¹⁹³

Hydrosilylation of 3-cyclohexene-1-carboxaldehyde 81

The *mixture of products* was submitted for $^1\text{H-NMR}$ and GC-MS analyses. The identity of each hydrosilylation product was determined based on the M^+ peaks detected by the GC-MS analysis and the appearance of a doublet carbinol C-H chemical shift at 4.23 ppm (CDCl_3 , 399.79 MHz). The vinyl C-H chemical shift at 5.65 ppm remained after the course of the catalysis.

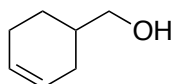


GC-MS m/z 294 (M^+), 233, 199, 183, 139, 94, 79, 66, 51. Yield (GC-MS): 91%



GC-MS m/z 404 (M^+), 326, 292, 199, 183, 139, 94, 77, 51. Yield (GC-MS): 9 %.

The product mixture was then hydrolyzed by treatment with a 1M HCl solution. Retention of the carbon-carbon double bond in the six-membered ring was further confirmed through comparison of experimental GC-MS and $^1\text{H-NMR}$ data for the acid-hydrolyzed product 3-cyclohexene-1-methanol with literature information.³²⁵

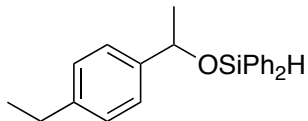


Methodology for Hydrosilylation of Aldehydes and Ketones with 0.4 mol% 26b

A 5-dram vial, equipped with a magnetic stir bar, was charged with 1.53 mmol Ph_2SiH_2 , 0.0051 mmol **26b** and 1.00 mL THF. A vigorous reaction occurs upon mixing Ph_2SiH_2 with **26b**. The solution was stirred for five min and charged with 1.02 mmol substrate and an 0.5 mL THF. The

vial was sealed and stirred at 1200 rpm over 16 h. The reaction mixture was then exposed to air and filtered through a plug of alumina. The solvent and excess silanes were evaporated *in vacuo* at 40 °C. The residue was then subjected to ^1H -NMR and GC-MS analyses.

Hydrosilylation of 4-Ethylacetophenone **83**

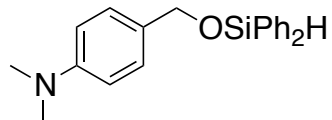


84: ^1H -NMR (CDCl_3 , 399.79 MHz) δ

9-7.60 (m), 7.48-7.37 (m), 7.35-7.18 (m), 5.47 (s, 1H, SiH), 5.04 (q, $J_{HH} = 6.4$ Hz, 1H, CH-O), 2.69 (q, $J_{HH} = 8$ Hz, 2H, CH₂), 1.57 (d, $J_{HH} = 6.4$ Hz, 3H, CH₃), 1.29 (t, $J_{HH} = 8$ Hz, 3H, CH₃). M⁺ (expected): 332. GC-MS *m/z* 332 (M⁺), 317, 287, 225, 199, 183, 133, 105, 77, 51. Yield (GC-MS): 48 %.

The formation of the 1,4-diethylbenzene³²⁶ and 4-ethylstyrene was detected by GC-MS analysis.

Hydrosilylation of 4-*N,N'*-Dimethylaminobenzaldehyde **89**

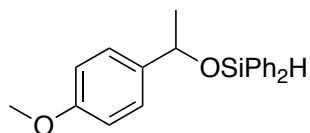


90: ^1H -NMR (CDCl_3 , 399.79 MHz) δ 7.65 (m), 7.40 (m), 7.35-7.19 (m), 6.72 (d, $J_{HH} = 8.6$ Hz, 2H), 5.47 (s, 1H, SiH), 4.78 (s, 2H, CH₂), 2.96 (s,

6H, CH₃). GC-MS *m/z* 333 (M⁺), 151, 134, 120, 107, 91, 77, 51. Yield (GC-MS): 85 %.

4-*N,N*'-Dimethylanimotoluene, product of carbonyl deoxygenation, was detected as a minor product.³²⁷

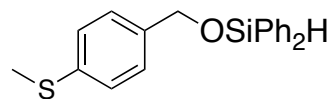
Hydrosilylation of 4-Methoxyacetophenone 85



86: ¹H-NMR (CDCl₃, 399.79 MHz) δ 7.64-7.57 (m), 7.49-7.32 (m), 7.29-7.26 (m), 6.86 (d, *J*_{HH} = 8.4 Hz, 2H), 5.41 (s, 1H, SiH), 4.98 (q, *J*_{HH} = 6.4 Hz, 1H, CH-O), 3.82 (s, 3H, O-CH₃), 1.52 (d, *J*_{HH} = 6.4 Hz, 3H, CH₃). GC-MS *m/z* 334 (M⁺), 319, 289, 256, 225, 199, 183, 135, 121, 105, 91, 77, 51. Yield (GC-MS): 45 %.

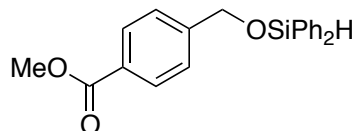
Products of deoxygenation 4-ethylanisole³²⁸ and 4-methoxystyrene³²⁹ were detected in trace amounts (GC-MS). The quantitative hydrosilylation of 4-methoxyacetophenone (> 98 %) was achieved at a higher catalyst loading (3 mol%).

Hydrosilylation of 4-(Methylthio)benzaldehyde 87



88: $^1\text{H-NMR}$ (CDCl_3 , 399.79 MHz) δ 7.67-7.47 (m, 4H, aromatic C-H), 7.46-7.24 (m, 10H, aromatic C-H), 5.62 (s, 1H, SiH), 4.83 (s, 1H, CH), 2.49 (s, 3H, CH_3). GC-MS m/z 336 (M^+), 289, 257, 243, 199, 183, 167, 152, 137, 122, 105, 91, 77, 51. Yield (GC-MS): 97%.

Hydrosilylation of Methyl 4-formylbenzoate **91**

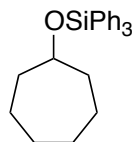


92: $^1\text{H-NMR}$ (CDCl_3 , 399.79 MHz) δ 7.98 (d, $J_{HH} = 8$ Hz, 2H), 7.73-7.52 (m), 7.49-7.26 (m), 5.61 (s, 1H, SiH), 4.88 (s, 2H, CH_2O), 3.92 (s, 3H, OCH_3). GC-MS m/z 348 (M^+), 317, 269, 257, 211, 199, 183, 149, 118, 105, 91, 77, 51. Yield (GC-MS): 90%.

Hydrosilylation of Cycloheptanone **102** with Ph_3SiH and 0.5 mol% **26b**

A 25-mL Teflon-sealed glass reactor, equipped with a magnetic stir bar, was charged with 116 mg (1.07 mmol) Ph_3SiH , 4 mg (0.0036 mmol) **26b** and 2.00 mL THF. The solution was stirred for five min and charged with 80 mg (0.71 mmol) substrate and 1.00 mL THF. The reactor was sealed, taken out of the drybox and then heated to 60 °C in a mineral oil bath. The reaction mixture was stirred at 1200 rpm over a period of 16 h. The reaction mixture was cooled to room temperature, exposed to air and filtered through a plug of alumina. The solvent was evaporated *in vacuo* at 40 °C. The *product mixture* was subjected to GC-MS analysis. The

formation of the desired product *cycloheptyloxytriphenylsilane* **103** was confirmed by the GC-MS data.



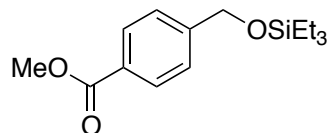
103: GC-MS *m/z* 372 (M^+), 315, 294, 259, 199, 181, 155, 105, 77, 55.

Yield (GC-MS): 15%.

Hydrosilylation of Methyl 4-formylbenzoate **91** with Et_3SiH and 0.7 mol%

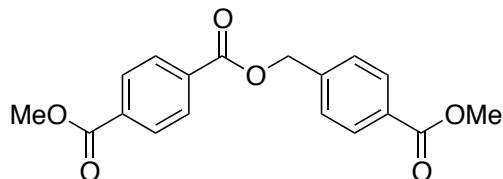
26b

A 5-dram vial, equipped with a magnetic stir bar, was charged with 124 mg (1.07 mmol) Et_3SiH , 4 mg (0.0036 mmol) 26b and 1.00 mL THF. The solution was stirred for five min and charged with 116 mg (0.71 mmol) substrate and 0.5 mL THF. The vial was sealed and stirred at 1200 rpm over 16 h. The reaction mixture was then exposed to air and filtered through a plug of alumina. The solvent and excess silanes were evaporated *in vacuo* at 40 °C. The residue was then subjected to 1H -NMR and GC-MS analyses.



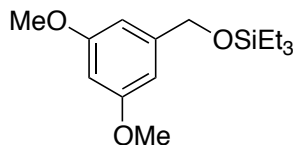
101: 1H -NMR ($CDCl_3$, 399.79 MHz) δ 8.00 (d, $J_{HH} = 8$ Hz, 2H), 7.41 (d, $J_{HH} = 8$ Hz, 2H) 4.79 (s, 2H, CH_2 -O), 3.96 (s, 3H, O- CH_3), 0.98 (t, $J_{HH} = 8$ Hz, 9H, CH_3), 0.66 (q, $J_{HH} = 8$ Hz, 6H, CH_2). GC-MS *m/z* 280 (M^+), 251, 221, 193, 149, 133, 121, 91, 77, 65, 59. Yield (GC-MS): 48 %.

An aldehyde dimerization product was detected by GC-MS analysis as a minor product of the catalysis. This product is reportedly formed from the *Tishchenko* dimerization of the aldehyde starting material.³³⁰



Hydrosilylation of Methyl 3,5-dimethoxybenzaldehyde **99** with Et₃SiH and 0.8 mol% 26b

A 5-dram vial, equipped with a magnetic stir bar, was charged with 178 mg (1.53 mmol) Et₃SiH, 9 mg (0.0082 mmol) 26b and 1.00 mL THF. The solution was stirred for five min and charged with 169 mg (1.02 mmol) substrate and 0.5 mL THF. The vial was sealed and stirred at 1200 rpm over 16 h. The reaction mixture was then exposed to air and filtered through a plug of alumina. The solvent and excess silanes were evaporated *in vacuo* at 40 °C. The residue was then subjected to ¹H-NMR and GC-MS analyses.



100: ¹H-NMR (CDCl₃, 399.79 MHz) δ 6.71 (t, J_{HH} = 2.3 Hz, 2H), 6.35 (t, J_{HH} = 2.3 Hz, 1H) 4.69 (s, 2H, CH₂-O), 3.79 (s, 6H, O-CH₃), 0.99 (t, J_{HH} = 8 Hz, 9H, CH₃), 0.66 (q, J_{HH} = 8 Hz, 6H, CH₂). GC-MS m/z 282 (M⁺), 253, 223, 195, 166, 151, 137, 121, 108, 91, 77, 65, 59. Yield (GC-MS): 62%.

Hydrosilylation of Methyl 4-N,N'-dimethylaminobenzaldehyde **89** with Et₃SiH and 0.9 mol% **26b**

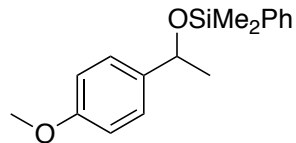
A 5-dram vial, equipped with a magnetic stir bar, was charged with 178 mg (1.53 mmol) Et₃SiH, 10 mg (0.0092 mmol) **26b** and 1.00 mL THF. The solution was stirred for five min and charged with 152 mg (1.02 mmol) substrate and 0.50 mL THF. The vial was sealed and stirred at 1200 rpm over 16 h. The reaction mixture was then exposed to air and filtered through a plug of alumina. The solvent and excess silanes were evaporated *in vacuo* at 40 °C. The residue was then subjected to ¹H-NMR and GC-MS analyses. The formation of the desired product was confirmed by comparison with the characterization data reported by Mindiola and coworkers.¹⁹²

A similar experiment with higher catalyst loading (3 mol%) resulted in a 55 % conversion of the substrate to the desired silyl derivative.

Hydrosilylation of *p*-methoxyacetophenone with 1.0 mol % [Co(NP^tBu₃)₄]

A 5-dram vial, equipped with a magnetic stir bar, was charged with 76 mg (0.56 mmol) PhSiMe₂H, 4 mg (0.0037 mmol) **26a** and 0.50 milliliter THF. The solution was stirred for five minutes and charged with 150 mg (0.37 mmol) substrate and 0.50 milliliter THF. The vial was sealed and stirred at 1200 rpm over 16 hours. The reaction mixture was then exposed to air and filtered through a plug of alumina. The solvent and excess

silanes were evaporated *in vacuo* at 40 °C. The residue was then subjected to ¹H-NMR and GC-MS analyses.

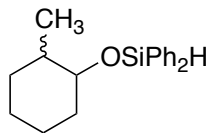


¹H-NMR (CDCl₃, 399.79 MHz) δ 7.59-7.56 (m, 2H), 7.41-7.37 (m, 3H), 7.24 (d, *J_{HH}* = 8.8 Hz, 2H), 6.86 (d, *J_{HH}* = 8.8 Hz, 2H), 4.84 (q, *J_{HH}* = 6.4 Hz, 1H), 3.82 (s, 3H), 1.43 (s, *J_{HH}* = 6.4 Hz, 3H), 0.35 (s, 3H, SiCH₃), 0.31 (s, 3H, SiCH₃). GC-MS *m/z* 286 (M⁺), 207, 197, 177, 135, 119, 105, 91, 77, 65, 51. Yield (GC-MS): 87 %.

Hydrosilylation of 2-Methylcyclohexanone **111** with 0.4 mol% **26b**

The following procedure was employed to study the stereoselectivity of the hydrosilylation catalysis. A 5-dram vial, equipped with a magnetic stir bar, was charged with 280 mg (1.52 mmol) Ph₂SiH₂, 10 mg (0.0092 mmol) 26b and 1.00 mL THF. The solution was stirred for five min and charged with 114 mg (1.02 mmol) substrate and 0.5 mL THF. The vial was sealed and stirred at 1200 rpm over a period of 16 h. The reaction mixture was then exposed to air and filtered through a plug of alumina. The solvent and excess silanes were evaporated *in vacuo* at 40 °C. The product mixture was then subjected to ¹H-NMR (in CDCl₃) and GC-MS analyses. The following carbinol C-H chemical shifts

corresponding to the *cis* and *trans* products were observed: δ 3.94 (m 1H) and 3.35 (m, 1H), respectively.

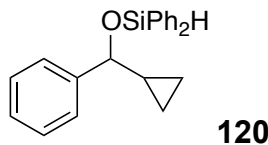


GC-MS 296 (M_+), 253, 239, 218, 199, 183, 161, 140, 123, 105, 94, 77, 55.

Yield (GC-MS): 37% (*trans*) and 24% (*cis*).

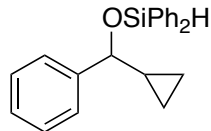
Hydrosilylation of Cyclopropyl Phenyl Ketone **120** with 0.4 mol% **26a**

A 5-dram vial, equipped with a magnetic stir bar, was charged with 282 mg (1.53 mmol) Ph_2SiH_2 , 4.51 mg (0.0041 mmol) **26a** and 1.00 mL THF. The solution was stirred for five min and charged with 150 mg (1.02 mmol) substrate and 0.50 mL THF. The vial was sealed and stirred at 1200 rpm over a period of 16 h. The reaction mixture was then exposed to air and filtered through a plug of alumina. The solvent and excess silanes were evaporated *in vacuo* at 40 °C. The residue was then subjected to ^1H -NMR and GC-MS analyses. The formation of the carbonyl group hydrosilylation product (28%) was confirmed by comparison of ^1H -NMR and GC-MS analyses results with data reported by Tilley and coworkers.¹⁹⁶



Hydrosilylation of Cyclopropyl Phenyl Ketone **120** with 0.4 mol% **26b**

A 5-dram vial, equipped with a magnetic stir bar, was charged with 282 mg (1.53 mmol) Ph₂SiH₂, 4.51 mg (0.0041 mmol) **26b** and 1.00 mL THF. The solution was stirred for five min and charged with 150 mg (1.02 mmol) substrate and 0.50 mL THF. The vial was sealed and stirred at 1200 rpm over 16 h. The reaction mixture was then exposed to air and filtered through a plug of alumina. The solvent and excess silanes were evaporated *in vacuo* at 40 °C. The residue was then subjected to ¹H-NMR and GC-MS analyses. The formation of the carbonyl group hydrosilylation product (31%) was confirmed by comparison with characterization data provided by Tilley and coworkers.¹⁹⁶

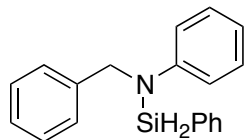


Phenyl propyl ketone **122**,³³¹ product of cyclopropyl ring opening, was also detected.

Hydrosilylation of *N*-benzylideneaniline **107** with 1.0 mol % [Co(NP^tBu₃)₄]

A 5-dram vial, equipped with a magnetic stir bar, was charged with 110 mg (1.02 mmol) PhSiH₃, 3 mg (0.002 mmol) **26a** and 0.50 milliliter THF. The solution was stirred for five minutes and charged with 87 mg (0.68 mmol) substrate and 0.50 milliliter THF. The vial was sealed and stirred at 1200 rpm over 16 hours. The reaction mixture was then exposed to air and filtered through a plug of alumina. The solvent and excess

silanes were evaporated *in vacuo* at 40 °C. The residue was then subjected to ^1H -NMR and GC-MS analyses. The experimental ^1H -NMR and mass spectra for the hydrosilylation product **108** product (42%) match the structure characterization data reported by Nolan and coworkers.³³²

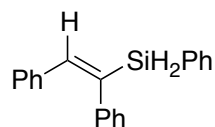


108

Acid hydrolysis of the product afforded the expected benzyl phenyl amine **109**.

Hydrogenation/Hydrosilylation of Diphenylacetylene **39**

A 250 mL Teflon-sealing glass reactor equipped with a Teflon-covered magnetic stirring bar was charged with 10 mg (0.009 mmol) of $[\text{NiNP}^t\text{Bu}_3]_4$, 200 mg (1.11 mmol) *trans*-stilbene, 200 mg (1.85 mmol) PhSiH_3 and 4 mL tetrahydrofuran (THF). The reaction mixture was stirred at a speed of 1200 rpm for 5 h at 60 °C temperature. The reaction mixture was then filtered through a plug of Florisil. The solvent was removed under vacuum and the residue was subjected to ^1H -NMR and GC-MS analysis. The products under this set of reaction conditions are: *cis*-stilbene **31** (4 %), *trans*-stilbene **29** (6.2 %) and a hydrosilylation product **106** (15 %) of the formula shown below:



The GC-MS and ^1H -NMR data for the product are similar to reported spectral data.³³³

Hydrogenation/Hydrosilylation of Allylbenzene **34**

A 250 mL Teflon-sealing glass reactor equipped with a Teflon-covered magnetic stirring bar was charged with 10 mg (0.009 mmol) of $[\text{MNP}^t\text{Bu}_3]_4$, 150 mg (1.27 mmol) allylbenzene, 200 mg (1.85 mmol) PhSiH_3 and 4 mL tetrahydrofuran (THF). The reaction mixture stirred in an oil bath at 60 °C was stirred at a speed of 1200 rpm for 5 h. The reactor was allowed to cool to room temperature. The reaction mixture was then filtered through a plug of Florisil and the THF-fraction was subjected to GC-MS analysis. The products of this reaction are: *n*-propylbenzene **35**, *trans*-1-phenylpropene **36a** and 3-phenylpropylphenylsilane **105**. The products of alkene isomerization and hydrogenation were identified through GC-MS library matching.³²⁰ The formation of trace amounts of 3-phenyl-1-(phenylsilyl)propane was confirmed based on reported characterization data.³³⁴

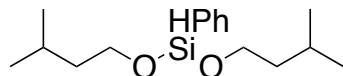
General Methodology for Solvent-Free Hydrosilylation

This methodology was employed for the solvent-free hydrosilylation of isovaleraldehyde and cyclohexanone. A 10-mL Teflon-sealed glass reactor, equipped with a magnetic stir bar, was charged with a solution of 393 mg (3.64 mmol) PhSiH_3 and 0.0036 mmol 26b. While stirring, the

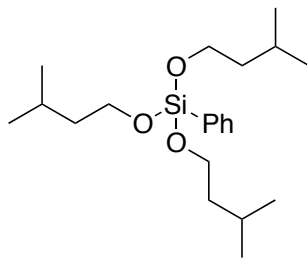
solution was charged with 0.71 mmol substrate. The reactor was sealed, taken out of the drybox and then heated to 60 °C in a mineral oil bath. The reaction mixture was stirred at 1200 rpm over 16 h. The reaction mixture was cooled to room temperature, exposed to air and filtered through a plug of alumina. The mixture was then subjected to GC-MS analyses. The identification and quantification of products was conducted through GC-MS analysis.

Hydrosilylation of Isovaleraldehyde **76** without a Solvent

The hydrosilylation of isovaleraldehyde afforded a mixture of the monoalkoxy- and dialkoxyphenylsilane products $\text{PhSiH}(\text{OC}_5\text{H}_{11})_2$ and $\text{PhSi}(\text{OC}_5\text{H}_{11})_3$. Hydrosilylation of the carbonyl functional group was confirmed by the appearance of a triplet carbinol C–H chemical shift at 3.76 ppm (the two alkoxy silane derivatives have overlapping chemical shifts). The reported ratio of $\text{PhSiH}(\text{OC}_5\text{H}_{11})_2$ and $\text{PhSi}(\text{OC}_5\text{H}_{11})_3$ for each experiment is based on the GC-MS results.



GC-MS m/z 280 (M^+), 223, 202, 187, 153, 137, 123, 117, 105, 91, 77, 69, 55. Yield (GC-MS): 61 %.



GC-MS m/z 366 (M^+), 349, 307, 293, 279, 209, 191, 167, 153, 139, 123, 91, 77, 69, 55. Yield (GC-MS): 39 %.

Hydrosilylation of Cyclohexanone **72** without a Solvent

The products of cyclohexanone hydrosilylation $PhSiH_2(OCy)$ **73** (88%) and $PhSiH(OCy)_2$ **74** (12%) are known compounds. Identification of the hydrosilylation products was conducted by GC-MS library matching and comparison with reported MS spectra.

Test of Homogeneity: Isovaleraldehyde **76** Hydrosilylation in the presence of $Hg(0)$

A 5-dram vial, equipped with a magnetic stir bar, was charged with 129 mg (0.70 mmol) Ph_2SiH_2 , 3.0 mg (0.0027 mmol) 26b and 275 mg (500 equivalents) liquid Hg in 1.100 mg C_6D_6 . While stirring, the solution was charged with 40 mg (0.46 mmol) isovaleraldehyde. The vial was sealed and stirred at 1200 rpm over 16 h. The reaction mixture was then exposed to air and filtered through a plug of alumina. The solution was subjected to 1H -NMR analysis. The rates of hydrosilylation were determined based on

the integration values of the chemical shifts corresponding to the aldehyde C-H bond (δ 9.30, singlet, 1H) and the resulting carbinol C-H bond (δ 3.76, triplet, 2H) in the product. A 36% substrate conversion (TOF = 82 hr⁻¹) was observed even in the presence of copious amounts of Hg(0). The expected 36% substrate conversion (TOF = 82 hr⁻¹) was also observed in the corresponding mercury-free experiment.

7.4 Base Metal–Catalyzed Hydrodesulfurization

General Considerations

All manipulations were carried out using Schlenk techniques. The preparation of each reaction mixture was carried out under a purified N₂ atmosphere in an drybox. Experiments that required heating were conducted under a Schlenck manifold. Thoroughly dried and degassed solvents were used in all experiments. Liquid substrates were degassed and passed through anhydrous silica prior to use. Solid substrates were used as received from suppliers. High-purity grade H₂, purchased from Praxair Canada, was used in all hydrogenation experiments. Hydrodesulfurization experiments requiring 1 atm H₂ were conducted in Teflon-sealed glass reactors. Experiments under H₂ pressures higher than 2 atm were conducted in glass-lined Parr metal reactors. NMR spectra were recorded on an Agilent/Varian Inova two-channel 400 MHz spectrometer at room temperature. ¹H NMR spectra were referenced to residual protio solvent peaks (CDCl₃ and C₆D₆).

GC-MS Analysis

GC-MS analysis was conducted using an Agilent 5890 GC equipped with a 7673 Automatic Liquid Sampler (ALS). The column used for the analysis is an Agilent DB-5 MS (25m x 0.25mm x 0.25 micron film thickness). The following GC conditions were applied in all analyses: (1)

injector port temperature: 300 °C; (2) initial temperature: 50 °C (hold for 2 min); (3) temperature ramp: 10 °C/min; (4) final temperature: 280 °C (5 minutes hold time); (5) detector temperature: 300 °C. Total run time: 35 minutes.

The detectors used are HP 5971 MSD or HP 5870 MSD calibrated using perfluorotributylamine (PFTBA). The data were acquired using Agilent Chemstation software and identification of known compounds produced from the succeeding reactions was conducted by spectral matching with the NIST/EPA/NIH 2011 Mass Spectral Library and Software package (NIST11) and by comparison of experimental data with literature structure characterization reports.

In most examples, the identification of desulfurization products was based on GC-MS library matching and comparison of experimental mass spectra with literature reports. In cases where known compounds were produced, confirmation of product identity was supported based on characteristic ¹H-NMR chemical shifts. In experiments where the products are unprecedented compounds, the structures were tentatively proposed based on the observed M⁺ values; thorough structural characterization of these compounds will be pursued as future work.

Stoichiometric HDS of DBT with **26a** and **26b**

A 100-mL Teflon-sealed glass reactor equipped with a magnetic stir bar was charged with 50 mg (0.27 mmol) DBT, 20 mg (0.018 mmol) of the

catalyst (**26a** or **26b**) and 6 mL toluene (Table 7.4.1). The reactor was taken out of the dry box and connected to a hydrogen manifold. The reaction vessel was then charged with H₂ (1 atm), employing rigorous inert-atmosphere laboratory techniques. The reaction mixture was then stirred at 1200 rpm for 12 h in an oil bath at 120 °C. The reactor was cooled to room and quenched with a 10% HCl solution. The organic products were extracted through diethyl ether–water extractions using three 4 mL portions of diethyl ether. The diethyl ether fractions were pooled, dried with anhydrous Na₂SO₄ and filtered through a small column of Florisil. The diethyl ether was removed *in vacuo* and the residue was dissolved in CDCl₃ for ¹H-NMR and GC-MS analyses.

Dibenzothiophene 129. ¹H-NMR (CDCl₃, 399.79 MHz) δ 8.21 (m, 2H), 7.88 (m, 2H), 7.50 (m, 4H). GC-MS *m/z* 184 (M⁺).

Biphenyl 143. ¹H-NMR (CDCl₃, 399.79 MHz) δ 7.63 (m, 4H), 7.47 (m, 4H), 7.38 (m, 2H). GC-MS *m/z* 154 (M⁺).

The formation of 2-phenylthiophenol **144** was confirmed by GC-MS library matching (M⁺ = 186).

Table 7.4.1. Comparison of the HDS activity of **26a** and **26b**.

Entr y	Cat	Conversion (%)		C–S bonds cleaved per M center
		143	144	
1	26b	12	0	0.5
2	26a	10	0	0.4

Silane-Promoted HDS of DBT **129**

A Teflon–sealed glass reactor was charged with 58 mg (0.32 mmol) DBT, 20 mg (0.018 mmol) **26b**, 90 mg (0.83 mmol) PhSiH₃, 6 mL toluene and a Teflon–sealed magnetic stir bar. The reaction mixture was stirred vigorously at 1200 rpm and the reactor, was heated to 120 °C in an oil bath for 36 h. The reactor was then cooled to room temperature, exposed to air and was treated with 3 mL 1M HCl solution. The organic products were then extracted by a series of diethyl ether extractions. The product mixture was then filtered through a column of Florisil. The solvent was removed *in vacuo*, dissolved in CDCl₃ and submitted for ¹H-NMR analysis. This example resulted in a 17 % conversion to biphenyl (1.5 C–S bonds / Ni center; 6 C–S bonds / cluster).

Silane-Promoted HDS of DBT: Screening of Basic Scavengers

A Teflon–sealed glass reactor was charged with 100 mg (0.54 mmol) DBT, 10 mg (0.009 mmol) **26b**, 174 mg (1.08 mmol) PhSiH₃, 6 mL toluene and a Teflon–sealed magnetic stir bar. The reaction mixture was stirred vigorously at 1200 rpm and the reactor, was heated to 120 °C in an oil bath for 16 h. The reactor was then cooled to room temperature, exposed to air and was treated with 3 mL 1M HCl solution. The organic products were then extracted by a series of diethyl ether extractions. The product mixture was then filtered through a column of Florisil. The solvent

was removed *in vacuo*, dissolved in CDCl₃ and submitted for ¹H-NMR and GC–MS analysis.

Table 7.4.2. Desulfurization of DBT in the presence of various scavengers.

Entry	Base	Mass of Base mg (mmol)	% Conversion	
			143	144
1	NaO ^t Bu	104 (1.08)	stoic	0
2	KO ^t Bu	121 (1.08)	28	18

Silane-Promoted HDS of DBT: KO^tBu as Scavenger

A 100 mL Teflon–sealed glass reactor was charged with 100 mg (0.54 mmol) DBT, 6 mg (0.005 mmol) **26b**, 160 mg (1.38 mmol) Et₃SiH, 160 mg (1.42 mmol) KO^tBu, 6 mL toluene and a Teflon–sealed magnetic stir bar. The reaction mixture was stirred vigorously at 1200 rpm and the reactor, was heated to 120 °C in an oil bath for 16 h. The reactor was then cooled to room temperature, exposed to air and was treated with 3 mL 1M HCl solution. The organic products were then extracted by a series of diethyl ether extractions. The product mixture was then filtered through a column of Florisil. The solvent was removed *in vacuo*, dissolved in CDCl₃ and submitted for ¹H-NMR and GC–MS analysis. The reaction gave biphenyl **143** (6 %) and 2-phenylthiophenol **144** (42 %, GC-MS).

Control Experiment: Metal-Free HDS of DBT at (110 °C)

A Teflon-sealed glass reactor was charged with 100 mg (0.54 mmol) DBT, 121 mg (1.08 mmol) KO^tBu, 117 mg (1.08 mmol) PhSiH₃, 6 mL toluene. The reaction mixture was heated to 120 °C in an oil bath for 16 h. The reactor was then cooled to room temperature, exposed to air and was treated with 3 mL 1M HCl solution. The organic products were then extracted by a series of diethyl ether extractions. The product mixture was then filtered through a column of Florisil. The solvent was removed *in vacuo*, dissolved in CDCl₃ and submitted for ¹H-NMR and GC-MS analysis. The reaction gave 2-phenylthiophenol **144** in 15 % yield (GC-MS).

Metal-Free HDS of DBT **129** at 140 °C

A Teflon-sealed glass reactor was charged with 100 mg (0.54 mmol) DBT, 121 mg (1.08 mmol) KO^tBu, 117 mg (1.08 mmol) PhSiH₃ and 6 mL toluene. The reaction mixture was stirred vigorously at 1200 rpm and the reactor, was heated to 140 °C in an oil bath for 16 h. The reactor was then cooled to room temperature, exposed to air and was treated with 3 mL 1M HCl solution. The organic products were then extracted by a series of diethyl ether extractions. The product mixture was then filtered through a column of Florisil. The solvent was removed *in vacuo*, dissolved in CDCl₃ and submitted for ¹H-NMR and GC-MS analysis. The reaction gave biphenyl **143** (23 %) and 2-phenylthiophenol **144** (58 %).

Catalytic HDS of DBT **129**: LDA as H₂S Scavengers

A 100-mL glass-lined Parr metal reactor was charged with 58 mg (0.32 mmol) DBT, 20 mg (0.018 mmol) **26b**, 69 mg (0.64 mmol) LDA, 4 mL toluene and a Teflon–sealed magnetic stir bar. The reactor was taken out of the dry box and connected to a hydrogen manifold. The reaction vessel was then charged with H₂ (60 psi), employing rigorous inert-atmosphere laboratory techniques. The reaction mixture was then stirred at 1200 rpm for 16 h in an oil bath at 120 °C. The reactor was cooled to room temperature and excess H₂ gas was released. The reaction mixture quenched with a 10% HCl solution. The organic products were extracted through diethyl ether–water extractions using three 4 mL portions of diethyl ether. The diethyl ether fractions were pooled, dried with anhydrous Na₂SO₄ and filtered through a small column of Florisil. The diethyl ether was removed *in vacuo* and the residue was weighed and dissolved in CDCl₃ for ¹H-NMR and GC-MS analyses. The reaction afforded biphenyl in 24.5 % yield (8.5 C–S bonds per cluster; 2.1 C–S bonds cleaver per Ni center).

Catalytic HDS of DBT **129**: Inorganic Bases as H₂S Scavengers

A Teflon–sealed reactor, equipped with a Teflon magnetic stir bar, was charged with 60 mg (0.33 mmol) DBT, 5 mg (0.004 mmol) **26b**, 1.12 mmol Group 1 hydride and 6 mL toluene. The reactor was taken out of the dry box and connected to a hydrogen manifold. The reaction vessel was

then charged with H₂ (1 atm), employing rigorous inert-atmosphere laboratory techniques. The reaction mixture was stirred vigorously at 1200 rpm and the reactor, was heated to 120 °C in an oil bath for 8 h. The reactor was cooled to room and the reaction mixture quenched with a 10% HCl solution. The organic products were extracted through diethyl ether–water extractions using three 4 mL portions of diethyl ether. The diethyl ether fractions were pooled, dried with anhydrous Na₂SO₄ and filtered through a small column of Florisil. The solvent was removed *in vacuo* and the residue dissolved in CDCl₃ for ¹H-NMR and GC-MS analyses.

Table 7.4.3. Desulfurization of DBT in the presence of Group 1 hydrides.

Entry	Base	Mass of Base mg (mmol)	Mass 26b mg (mmol)	% Conversion	
				143	144
1	NaH	27 (1.12)	10 (0.009)	13	0
2	KH	46 (1.12)	10 (0.009)	28	18

Control Experiment: KH-Mediated HDS of DBT **129** at 120 °C

A 100 mL Teflon–sealed reactor was charged with 100 mg (0.54 mmol) DBT, 54 mg (1.35 mmol) KH, 6 mL toluene and Teflon–sealed magnetic stir bar. The reactor was taken out of the dry box and connected to a hydrogen manifold. The reaction vessel was then charged with H₂ (1 atm), employing rigorous inert-atmosphere laboratory techniques. The reaction mixture was then stirred at 1200 rpm for 16 h in an oil bath at 120 °C. The reactor was cooled to room temperature and the reaction mixture

quenched with a 10% HCl solution. The organic products were extracted through diethyl ether–water extractions using three 4 mL portions of diethyl ether. The diethyl ether fractions were pooled, dried with anhydrous Na₂SO₄ and filtered through a small column of Florisil. The diethyl ether was removed *in vacuo* and the residue dissolved in CDCl₃ for ¹H-NMR and GC-MS analyses. The reaction gave trace amounts of biphenyl **143** (0.7 %) and 2-phenylthiophenol **144** (1.7 %).

Control Experiment: KH-Mediated HDS of DBT at 150 °C, 500 psi H₂

A glass-lined Parr metal reactor was charged with 100 mg (0.54 mmol) DBT, 54 mg (1.35 mmol) KH, 6 mL toluene and a Teflon–sealed magnetic stir bar. The reactor was taken out of the dry box and connected to a hydrogen manifold. The reaction vessel was then charged with H₂ (500 psi-g), employing rigorous inert-atmosphere laboratory techniques. The reaction mixture was then stirred at 1200 rpm for 18 h in an oil bath at 150 °C. The reactor was cooled to room temperature and the reaction mixture quenched with a 10% HCl solution. The organic products were extracted through diethyl ether–water extractions using three 4 mL portions of diethyl ether. The diethyl ether fractions were pooled, dried with anhydrous Na₂SO₄ and filtered through a small column of Florisil. The diethyl ether was removed *in vacuo* and the residue weighed and dissolved in CDCl₃ for ¹H-NMR and GC-MS analyses. Despite the harsher conditions, the reaction gave trace amounts of biphenyl **143** (< 1 %).

Catalytic HDS of DBT under varying temperature and pressure conditions

The following was the general procedure employed in the examples for the HDS of dibenzothiophene under varying catalyst load, pressure and temperature conditions, as shown in Table 7.4.4. The pressure-appropriate reactor was charged with the desired amount of substrate, catalyst, basic scavenger and toluene (5 to 10 mL). The mixture was transferred into the appropriate pressure reactor equipped with a Teflon magnetic stir bar. After the desired reaction time, the reaction mixture was cooled to room temperature and then quenched with a 10% HCl solution. The organic products were extracted through a series of diethyl ether-water extractions and the organic fractions were pooled, dried with anhydrous Na₂SO₄ and filtered through a small column of Florisil. The solvent was removed under vacuum and the weighed residue dissolved in CDCl₃ for ¹H-NMR and GC-MS analyses.

Table 7.4.4. Summary of HDS experiments of DBT catalyzed by **26b** in toluene.

Entry	DBT mg (mmol)	Cat mg (mmol)	KH mg (mmol)	H ₂ (atm)	Temp (°C)	Time (h)	% Conversion	
							143	144
1	60 (0.33)	9 (0.008)	55 (1.37)	24	140	18	100 ^a	0
2	74 (0.40)	10 (0.009)	60 (1.50)	17	135	24	100 ^b	0
3	90 (0.49)	10 (0.009)	60 (1.50)	2	135	18	82	8
4	90 (0.49)	9 (0.009)	60 (1.50)	1	120	8.5	23	9
5	80 (0.43)	9 (0.009)	60 (1.50)	1	110	20	58	4

^a Mass of **143** recovered = 48 mg (96 % isolated yield).

^b Mass of **143** recovered = 60 mg (97 % isolated yield).

Partial HDS of DBT 129

A 100 mL Teflon–sealed reactor was charged with 100 mg (0.54 mmol) DBT, 10 mg(0.009 mmol) catalyst, 54 mg (1.35 mmol) KH, 6 mL toluene and a Teflon–sealed magnetic stir bar. The reactor was taken out of the dry box and connected to a hydrogen manifold. The reaction vessel was then charged with H₂ (1 atm), employing rigorous inert-atmosphere laboratory techniques. The reaction mixture was then stirred at 1200 rpm for 8-15 h in an oil bath at 120 °C (Table 7.4.5). After the desired reaction time, the reaction mixture was cooled to room temperature and then quenched with a 10% HCl solution. The organic products were extracted through a series of diethyl ether–water extractions and the organic fractions were pooled, dried with anhydrous Na₂SO₄ and filtered through a small column of Florisil. The solvent was removed under vacuum and the residue was dissolved in CDCl₃ for ¹H-NMR and GC-MS analyses.

Table 7.4.5. Comparison of the HDS activity of **26a** and **26b** conditions.

Entry	Cat	Time (h)	Conversion (%)	
			143	144
1	26b	8	23.1	8.5
2	26a	8	21.0	52.2
3	26a	15	39.8	52.9

Test of Homogeneity: HDS of DBT **129** in the Presence of Hg(0)

A glass-lined Parr metal reactor was charged with 65 mg (0.35 mmol) DBT, 9 mg (0.008 mmol) **26b**, 31 mg (0.77 mmol) KH, 1.50 g liquid Hg, 5 mL toluene and a Teflon–sealed magnetic stir bar. The reactor was taken out of the dry box and connected to a hydrogen manifold. The reaction vessel was then charged with H₂ (500 psi-g), employing rigorous inert-atmosphere laboratory techniques. The reaction mixture was then stirred at 1200 rpm for 18 h in an oil bath at 140 °C. The reactor was cooled to room temperature and the reaction mixture quenched with a 10% HCl solution. The organic products were extracted through diethyl ether–water extractions using three 4 mL portions of diethyl ether. The diethyl ether fractions were pooled, dried with anhydrous Na₂SO₄ and filtered through a small column of Florisil. The diethyl ether was removed *in vacuo* and the residue weighed and dissolved in CDCl₃ for ¹H-NMR and GC-MS analysis. The reaction exclusively gave biphenyl **143** (57 %) as product (TOF = 1.6 DBT/h). HDS rates ranging from 1.67 to 1.9 DBT/h were observed in the absence of Hg(0) under similarly mild conditions.

Test of Homogeneity: HDS of DBT **129** in the Presence of Ni₃S₂

A glass-lined Parr metal reactor was charged with 60 mg (0.33 mmol) DBT, 6.5 mg (0.072 mmol) NiS, 29 mg (0.72 mmol) KH, 5 mL toluene and a Teflon–sealed magnetic stir bar. The reactor was taken out of the dry box and connected to a hydrogen manifold. The reaction vessel

was then charged with H₂ (500 psi-g), employing rigorous inert-atmosphere laboratory techniques. The reaction mixture was stirred at 1200 rpm for 18 h in an oil bath at 150 °C. The reactor was cooled to room temperature and the reaction mixture quenched with a 10% HCl solution. The organic products were extracted through diethyl ether–water extractions using three 4 mL portions of diethyl ether. The diethyl ether fractions were pooled, dried with anhydrous Na₂SO₄ and filtered through a small column of Florisil. The diethyl ether was removed *in vacuo* and the residue weighed and dissolved in CDCl₃ for ¹H-NMR and GC-MS analysis. The reaction formed only trace amounts of biphenyl (< 1%).

HDS of DBT catalyzed by [NiNP^tEt₃]_n

Synthesis of [Ni(NP^tEt₃)]_n from [BrNi(NP^tEt₃)]₄: 0.05 mmol of [BrNi(NP^tBu₃)]₄ was dissolved in 5 mL toluene, stirred, and then treated with 0.06 mmol of Na using a 1 % Na(Hg) reagent at -35 °C to room temperature 2 h. The THF fraction of the mixture was separated from any remaining solid components.

The toluene fraction from the synthesis above was used directly was used as solvent for the catalytic hydrodesulfurization of dibenzothiophene. A Teflon–sealed reactor was charged with 100 mg (0.54 mmol) DBT, 45 mg (1.12 mmol) KH and 4 mL of the toluene fraction containing the [Ni(NP^tEt₃)]_n catalyst. The reactor was taken out of the dry

box and connected to a hydrogen manifold. The reaction vessel was then charged with H₂ (1 atm), employing strict inert-atmosphere laboratory techniques. The reaction mixture was then stirred at 1200 rpm for 16 h in an oil bath at 120 °C. The reactor was cooled to room and the reaction mixture quenched with a 10% HCl solution. The organic products were extracted through diethyl ether–water extractions using three 4 mL portions of diethyl ether. The diethyl ether fractions were pooled, dried with anhydrous Na₂SO₄ and filtered through a small column of Florisil. The diethyl ether was removed *in vacuo* and the weighed residue dissolved in CDCl₃ for ¹H-NMR and GC-MS analyses. The process as described gives 36% conversion and produces biphenyl **143** (16%) and 2-phenylthiophenol **144** (20 %), exclusively, as products.

HDS of DBT catalyzed by [FeNP^tBu₃]_n

Synthesis of [Fe(NP^tBu₃)₄] from [Br₂Fe₂(μ-NP^tBu₃)₂]: 0.05 mmol of [Br₂Fe₂(μ-NP^t-Bu₃)₂] was dissolved in 5 mL THF, stirred, and then treated with 0.06 mmol of Na using a 1 % Na(Hg) reagent at -35 °C to room temperature 2 h. The THF fraction of the mixture was separated from any remaining solid components.

The THF fraction was used directly as dissolved catalyst and solvent for the HDS of dibenzothiophene. A Teflon–sealed reactor was charged with 100 mg (0.54 mmol) DBT, 45 mg (1.12 mmol) KH and 4 mL

of the THF fraction containing the $[\text{Fe}(\text{NP}^t\text{Bu}_3)]_n$ catalyst. The reactor was taken out of the dry box and connected to a hydrogen manifold. The reaction vessel was then charged with H_2 (1 atm), employing strict inert-atmosphere laboratory techniques. The reaction mixture was then stirred at 1200 rpm for 17 h in an oil bath at 120 °C. The reactor was cooled to room temperature and the reaction mixture quenched with a 10% HCl solution. The organic products were extracted through diethyl ether–water extractions using three 4 mL portions of diethyl ether. The diethyl ether fractions were pooled, dried with anhydrous Na_2SO_4 and filtered through a small column of Florisil. The diethyl ether was removed *in vacuo* and the residue dissolved in CDCl_3 for $^1\text{H-NMR}$ and GC-MS analyses. The process gave 50% conversion, to biphenyl **143** (40%) and 2-phenylthiophenyl **144** (10 %) as the only observed products.

HDS of 4,6-diethylDBT **176**

This is the general procedure employed in the catalytic desulfurization of 4,6-diethylbenzothiophene using catalysts **26a** and **26b**. The pressure-appropriate reactor was charged with the desired amount of substrate, catalyst, basic scavenger and 5-10 mL toluene (Table 7.4.6). The mixture was transferred into the appropriate pressure reactor equipped with a Teflon magnetic stir bar. The reaction vessels were charged with H_2 , employing strict inert-atmosphere laboratory techniques, and heated to the desired temperature in an oil bath on a

heating magnetic stir plate, stirring at 1200 rpm. After the desired reaction time, the reactor was cooled to room temperature and then quenched with a 10% HCl solution. The organic products were extracted through a series of diethyl ether–water extractions and the organic fractions were pooled, dried with anhydrous Na₂SO₄ and filtered through a small column of Florisil. The solvent was removed *in vacuo* and the weighed residue dissolved in CDCl₃ for ¹H-NMR and GC-MS analyses. The yields were calculated based on GC-MS results and ratio of integrations of benzylic methylene ¹H-NMR chemical shifts of the starting material **144** (δ 2.98 ppm; M⁺ = 240) and the desulfurized product **145** (δ 2.75 ppm; M⁺ = 210). The formation of trace amounts of the thiol intermediate **145** was detected by GC-MS analysis (M⁺ = 242).

Table 7.4.6. Summary of Hydrodesulfurization of 4,6-diethylDBT

	144 mg (mmol)	Cat 26b	Cat mg (mmol)	KH mg (mmol)	H ₂ (atm)	Temp (°C)	Time (h)	% Conversion	
								145	146
1	60 (0.25)	26b	10 (0.009)	30 (0.75)	34	140	18	39	0
3	35 (0.15)	26b	14 (0.014)	18 (0.45)	1	120	18	44	0.2
5	25 (0.10)	26b	13 (0.012)	13 (0.32)	1	120	36	78	1
2	74 (0.31)	26b	9 (0.008)	37 (0.92)	1	110	16	17	1
4	45 (0.19)	26b	10 (0.009)	23 (0.57)	1	120	18	21	6

HDS of Diphenyl Sulfide **179**

A Teflon-sealed reactor was charged with 60 mg (0.32 mmol) diphenyl sulfide **179**, 10 mg (0.0009 mmol) catalyst, 30 mg (0.75 mmol) KH, 8 mL toluene and a Teflon-magnetic stir bar. The reactor was taken out of the dry box and connected to a hydrogen manifold. The reaction vessel was charged with H₂ (1 atm), employing inert-atmosphere laboratory techniques. The reaction mixture was then stirred at 1200 rpm in an oil bath at 110 °C. The reactor was cooled to room and the reaction mixture quenched with a 10% HCl solution. The organic products were extracted through diethyl ether–water extractions using three 4 mL portions of diethyl ether. The diethyl ether fractions were pooled, dried with anhydrous Na₂SO₄ and filtered through a small column of Florisil. The diethyl ether was removed *in vacuo* and the residue was dissolved in CDCl₃ for ¹H-NMR and GC-MS analyses. The identity of the products, benzene and thiophenol, was determined by GC-MS library matching.

Table 7.4.7. Comparison of the HDS activity of **26a** and **26b** catalysts for the HDS of diphenylsulfide.

Entry	Catalyst	Time (h)	Conversion (%)	
			148	149
1	26b	20	24	23
2	26a	60	39	61

HDS of Dodecyl Sulfide **182**

A Teflon–sealed reactor was charged with 120 mg (0.32 mmol) dodecyl sulfide, 10 mg (0.009 mmol) **26b**, 40 mg (1.00 mmol) KH, a magnetic stir bar, and 8 mL toluene. The reactor was taken out of the dry box and connected to a hydrogen manifold. The reaction vessel was then charged with H₂ (1 atm), employing strict inert-atmosphere laboratory techniques. The reaction mixture was then stirred at 1200 rpm for 18 h in an oil bath at 110 °C. The reactor was cooled to room and the reaction mixture quenched with a 10% HCl solution. The organic products were extracted through diethyl ether–water extractions using three 4 mL portions of diethyl ether. The diethyl ether fractions were pooled, dried with anhydrous Na₂SO₄ and filtered through a small column of Florisil. The resulting diethyl ether solution was submitted for GC-MS analyses. Since the reaction is anticipated to produce known compounds, identification of the products was based on GC-MS results. The products obtained from this HDS are dodecane (C₁₂H₂₆; M⁺ = 170) and dodecene (C₁₂H₂₄; M⁺ = 168) in 2% and 6 % yield, respectively.

HDS of Benzothiophene **135**

A 100 mL Teflon–sealed reactor was charged with 100 mg (0.75 mmol) benzothiophene, 16 mg (0.015 mmol) **26b**, 60 mg (1.50 mmol) KH, 8 mL toluene, and a stir bar. The reactor was taken out of the dry box and connected to a hydrogen manifold. The reaction vessel was then charged

with H₂ (1 atm), employing strict inert-atmosphere laboratory techniques. The reaction mixture was then stirred at a 1200 rpm for 18 h in an oil bath at 110 °C. Since the reaction was expected to produce volatile products, the reactor was cooled to -60 °C and the reaction mixture quenched with a 10% HCl solution. The temperature of the reaction mixture was maintained at -60 °C and the organic layer was extracted with cold portions of diethyl ether. Since the reaction is expected to produce volatile hydrogenolysis products (i.e. ethylbenzene), a cooled portion of the diethyl ether was submitted for GC-MS analysis. Results of the GC-MS analysis revealed ethylbenzene (41%) as the exclusive product component.

HDS of 2-phenyl-3,5-dimethylthiophene 185

A Teflon-sealed reactor was charged with a stir bar, 120 mg (0.64 mmol) 2-phenyl-3,5-dimethylthiophene, 12 mg (0.011 mmol) 26b, 55 mg (1.37 mmol) KH and 8 mL toluene. The reactor was then taken out of the dry box and connected to a hydrogen manifold. The reaction vessel was then charged with H₂ (1 atm), employing strict inert-atmosphere laboratory techniques. The reaction mixture was stirred vigorously at 1200 rpm for 18 h in an oil bath at 120 °C. The reactor was cooled to room and the reaction mixture quenched with a 10% HCl solution. The organic products were extracted through diethyl ether–water extractions using three 4 mL portions of diethyl ether. The diethyl ether fractions were pooled, dried with anhydrous Na₂SO₄ and filtered through a small column of Florisil. The

solvent was removed *in vacuo* and the residue was dissolved in CDCl₃ for ¹H-NMR and GC-MS analyses. Results of ¹H-NMR analysis gave inconclusive structural information due to overlapping chemical shifts of the components of the product mixture. The GC-MS analysis, however, reveals the presence, exclusively, of product components with GC retention times and EIMS M⁺ values corresponding to HDS products of chemical formula: C₁₂H₁₄ (M⁺ = 158) and C₁₂H₁₆ (M⁺ = 160) in 3% and 23 % yields, respectively. The presence of unsaturated functional groups in the hydrocarbon products was confirmed by the appearance of ¹H-NMR chemical shifts in the range of 4.00 to 5.50 ppm, indicative of vinyl C-H bonds.

HDS of DBT in the Presence of *Cis*-Stilbene **31**

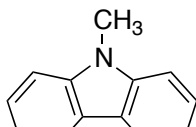
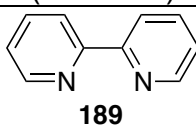
A 100 mL Teflon-sealed reactor was charged with 100 mg (0.54 mmol) DBT, 25 mg (0.14 mmol) *cis*-stilbene, 13 mg (0.012 mmol) **26b**, 43 mg (1.08 mmol) KH, 6 mL toluene and a Teflon-sealed magnetic stir bar. The reactor was taken out of the dry box and connected to a hydrogen manifold. The reaction vessel was then charged with H₂(1 atm), employing rigorous inert-atmosphere laboratory techniques. The reaction mixture was then stirred at 1200 rpm for 16 h in an oil bath at 120 °C. After the desired reaction time, the reaction mixture was cooled to room temperature and then quenched with a 10% HCl solution. The organic products were extracted through a series of diethyl ether–water extractions and the

organic fractions were pooled, dried with anhydrous Na₂SO₄ and filtered through a small column of Florisil. The solvent was removed under vacuum and the weighed residue dissolved in CDCl₃ for ¹H-NMR and GC-MS analyses. *Cis*-stilbene **31** underwent quantitative hydrogenation to 1,2-diphenylethane **30**. The reaction gave biphenyl **143** (53 %) and 2-phenylthiophenyl **144** (2 %).

HDS of DBT in the Presence of Nitrogenous Inhibitors

A 100 mL Teflon-sealed reactor was charged with 62 mg (0.34 mmol) DBT, 0.07 mmol inhibitor, 6 mg (0.005 mmol) **26b**, 30 mg (0.75 mmol) KH, 4 mL toluene and a Teflon-sealed magnetic stir bar. The reactor was taken out of the dry box and connected to a hydrogen manifold. The reaction vessel was then charged with H₂(1 atm), employing rigorous inert-atmosphere laboratory techniques. The reaction mixture was then stirred at 1200 rpm for 18 h in an oil bath at 120 °C. After the desired reaction time, the reaction mixture was cooled to room temperature and then quenched with a 10% HCl solution. The organic products were extracted through a series of diethyl ether–water extractions and the organic fractions were pooled, dried with anhydrous Na₂SO₄ and filtered through a small column of Florisil. The solvent was removed under vacuum and the weighed residue dissolved in CDCl₃ for ¹H-NMR and GC-MS analyses. The nitrogenous inhibitors remained unreacted under the given conditions.

Table 7.4.8. HDS of DBT in the presence of N-inhibitors.

Entry	Additive	% Conversion	
		143	144
1	No Additive	20	26
2	 188 (20 mol%)	17	22
3	 189 (20 mol%)	13	37

HDS of 6-methoxy-2-(4-methoxyphenyl)-1-benzothiophene **190**

A 100 mL Teflon–sealed reactor was charged with 106 mg (0.40 mmol) 6-methoxy-2-(4-methoxyphenyl)-1-benzothiophene, a magnetic stir bar, 20 mg 26b (0.019 mmol), 50 mg (1.25 mmol) KH and 8 mL toluene. The reactor was taken out of the dry box and connected to a hydrogen manifold. The reaction vessel was then charged with H₂ (1 atm), employing strict inert-atmosphere laboratory techniques. The reaction mixture was then stirred at 1200 rpm for 16 h in an oil bath at 120 °C. The reactor was cooled to room temperature and quenched with a 10% HCl solution. The organic products were extracted through diethyl ether–water extractions using three 4 mL portions of diethyl ether. The diethyl ether fractions were pooled, dried with anhydrous Na₂SO₄ and filtered through a small column of Florisil. The diethyl ether was removed *in vacuo* and the residue

dissolved in CDCl_3 for $^1\text{H-NMR}$ and GC-MS analyses. A mixture of sulfur-free products was obtained after 98.4 % overall substrate conversion, consisting of 1,2-bis(4-methoxyphenyl)ethane **191** ($M^+ = 242$; 83%)³³⁵ and 1,2-bis(4-methoxyphenyl)ethene **192** ($M^+ = 240$; 4%),³³⁵ 1-phenyl-2-(4-methoxyphenyl)ethene **193** ($M^+ = 212$; 9%)³³⁶ and 1-(4-hydroxyphenyl)-2-(4-methoxyphenyl)ethene **194** ($M^+ = 228$; 3%),³³⁷ as revealed by GC-MS analysis. The formation of the major hydrogenolysis product **240** was confirmed by the appearance of a single chemical shift at 2.82 ppm (- CH_2CH_2-).

HDS of Phenoxathiin **195**

A Teflon-sealed reactor was charged with 60 mg (0.30 mmol) phenoxathiin, 10 mg (0.009 mmol) 26b, 50 mg (1.25 mmol) KH, a Teflon magnetic stir bar, and 8 mL toluene. The reactor was then taken out of the dry box and connected to a hydrogen manifold. The reaction vessel was then charged with H_2 (1 atm), employing rigorous inert-atmosphere laboratory techniques. The reaction mixture was then stirred at 1200 rpm for 16 h in an oil bath at 110 °C. The reactor was cooled to -60 °C and the reaction mixture quenched with a 10% HCl solution. The organic products were extracted through diethyl ether–water extractions using three 4 mL portions of cold diethyl ether. The diethyl ether fractions were pooled, dried with anhydrous Na_2SO_4 and filtered through a small column of Florisil. Since the reaction was anticipated to produce known, volatile products,

analysis of the product mixture was conducted by GC-MS analysis. The identity of the hydrogenolysis products was determined by GC-MS library matching. The products obtained from this reaction (after 56% total conversion) are, in descending order of yield, phenol (36%), benzene (10%), dibenzofuran (6%), biphenyl (1%), and trace diphenyl ether (0.4%).

HDS of DBT: Nickel Catalyst Initially Primed with H₂

A 100 mL Teflon–sealed reactor was charged with 125 mg (0.68 mmol) DBT, 5 mg (0.004 mmol) **26b**, 60 mg (1.50 mmol) KH, 4 mL toluene and a Teflon–sealed magnetic stir bar. The reactor was taken out of the dry box and connected to a hydrogen manifold. The reaction vessel was then charged with H₂ (1 atm) and stirred for 30 min. The headspace of the reaction mixture was evacuated and resealed prior to stirring at 1200 rpm for 18 h in an oil bath at 120 °C. After the desired reaction time, the reaction mixture was cooled to room temperature and then quenched with a 10% HCl solution. The organic products were extracted through a series of diethyl ether–water extractions and the organic fractions were pooled, dried with anhydrous Na₂SO₄ and filtered through a small column of Florisil. The solvent was removed under vacuum and the weighed residue dissolved in CDCl₃ for ¹H-NMR and GC-MS analyses. Entry 1 of Table 7.4.8 shows the yield of biphenyl **143** and 2-phenylthiophenol **144** from this reaction. Under identical conditions but with a hydrogen atmosphere

maintained during the course of the reaction, higher yields of **143** and **144** were obtained (Entry 2).

Table 7.4.8 HDS of DBT with a hydrogen-activated catalyst.

Entry	H ₂ (atm)	% Conversion	
		143	144
1	0 ^a	6	13
2	1	20	28

^aThe vessel was initially charged with 1 atm of H₂, stirred for 30 min and the headspace of the reactor was evacuated prior to heating.

HDS of DBT under D₂

A 100 mL Teflon–sealed reactor was charged with 100 mg (0.54 mmol) DBT, 15 mg(0.014 mmol) catalyst, 54 mg (1.35 mmol) KH, 6 mL toluene and a Teflon–sealed magnetic stir bar. The reactor was taken out of the dry box and connected to a hydrogen manifold. The reaction vessel was then charged with D₂ (1 atm), employing rigorous inert-atmosphere laboratory techniques. The reaction mixture was then stirred at 1200 rpm for 48 h in an oil bath at 120 °C. After the desired reaction time, the reaction mixture was cooled to room temperature and then quenched with a 10% HCl solution. The organic products were extracted through a series of diethyl ether–water extractions and the organic fractions were pooled, dried with anhydrous Na₂SO₄ and filtered through a small column of Florisil. The solvent was removed under vacuum and the weighed residue dissolved in CD₂Cl₂ for ²H-NMR analysis. Quantitative conversion to deuterated biphenyl was observed. Deuterium incorporation at **C2/C2'** (δ

7.52 ppm), **C3/C3'** (δ 7.35 ppm) and **C4/C4'** (δ 7.26 ppm) were observed. The ratio of integrations of the ^2H -NMR chemical shifts was 3 : 2 : 1.

Reaction Between KH and DBT under D₂

A 100 mL Teflon–sealed reactor was charged with 100 mg (0.54 mmol) DBT, 54 mg (1.35 mmol) KH, 6 mL toluene and a Teflon–sealed magnetic stir bar. The reactor was taken out of the dry box and connected to a hydrogen manifold. The reaction vessel was then charged with D₂ (1 atm), employing rigorous inert-atmosphere laboratory techniques. The reaction mixture was then stirred at 1200 rpm for 48 h in an oil bath at 120 °C. After the desired reaction time, the reaction mixture was cooled to room temperature and then quenched with a 10% HCl solution. The organic products were extracted through a series of diethyl ether–water extractions and the organic fractions were pooled, dried with anhydrous Na₂SO₄ and filtered through a small column of Florisil. The solvent was removed under vacuum and the weighed residue dissolved in CD₂Cl₂ for ^2H -NMR analysis. Deuterium incorporation at the C1/C9 and C4/C6 positions were observed: **C1/C9** (δ 8.20 ppm) and **C4/C6** (δ 7.89 ppm). The ratio of integration of these ^2H -NMR signals was found to be (**C1/C9** : **C4/C6**) 2 : 1.

HDS of 4,6-diethylDBT under D₂

A 100 mL Teflon–sealed reactor was charged with 50 mg (0.21 mmol) 4,6-diethylDBT, 45 mg (0.044 mmol) **26b**, 21 mg (0.53 mmol) KH, 6 mL toluene and a Teflon–sealed magnetic stir bar. The reactor was taken out of the dry box and connected to a hydrogen manifold. The reaction vessel was then charged with D₂ (1 atm), employing rigorous inert-atmosphere laboratory techniques. The reaction mixture was then stirred at 1200 rpm for 48 h in an oil bath at 120 °C. After the desired reaction time, the reaction mixture was cooled to room temperature and then quenched with a 10% HCl solution. The organic products were extracted through a series of diethyl ether–water extractions and the organic fractions were pooled, dried with anhydrous Na₂SO₄ and filtered through a small column of Florisil. The solvent was removed under vacuum and the weighed residue dissolved in CD₂Cl₂ for ²H-NMR analysis. The reaction gave the desulfurized product **145** in 71 % yield. Deuterium incorporation at **C2/C2'** (δ 7.38 ppm) and at the benzylic carbon center (δ 2.65 ppm) was observed. The ratio of integrations of the ²H-NMR chemical shifts was 3 : 1.

Reaction Between KH and Biphenyl under D₂

A 100 mL Teflon–sealed reactor was charged with 50 mg (0.32 mmol) biphenyl **143**, 30 mg (0.71 mmol) KH, 3 mL toluene and a Teflon–sealed magnetic stir bar. The reactor was taken out of the dry box and

connected to a hydrogen manifold. The reaction vessel was then charged with D₂ (1 atm), employing rigorous inert-atmosphere laboratory techniques. The reaction mixture was then stirred at 1200 rpm for 18 h in an oil bath at 120 °C. After the desired reaction time, the reaction mixture was cooled to room temperature and then quenched with a 10% HCl solution. The organic products were extracted through a series of diethyl ether–water extractions and the organic fractions were pooled, dried with anhydrous Na₂SO₄ and filtered through a small column of Florisil. The solvent was removed under vacuum and the weighed residue dissolved in CD₂Cl₂ for ²H-NMR analysis. Deuterium incorporation at **C2/C2'** (δ 7.52 ppm) and **C4/C4'** (δ 7.26 ppm) was observed. The ratio of integrations of the ²H-NMR chemical shifts was 4 : 1.

7.5 Base Metal–Catalyzed C–O and C–N Bond Hydrogenolysis

General Considerations

All manipulations were carried out using Schlenk techniques. The preparation of each reaction mixture was carried out under a purified N₂ atmosphere in an drybox. Experiments that required heating were conducted under a Schlenck manifold. Thoroughly dried and degassed solvents were used in all experiments. Liquid substrates were degassed and passed through anhydrous silica prior to use. Solid substrates were used as received from suppliers. High-purity grade H₂, purchased from Praxair Canada, was used in all hydrogenation experiments. Hydrodesulfurization experiments requiring 1 atm H₂ were conducted in Teflon-sealed glass reactors. Experiments under H₂ pressures higher than 2 atm were conducted in glass-lined Parr metal reactors. NMR spectra were recorded on an Agilent/Varian Inova two-channel 400 MHz spectrometer at room temperature. ¹H NMR spectra were referenced to residual protio solvent peaks (CDCl₃ and C₆D₆).

GC-MS Analysis

GC-MS analysis was conducted using an Agilent 5890 GC equipped with a 7673 Automatic Liquid Sampler (ALS). The column used for the analysis is an Agilent DB-5 MS (25m x 0.25mm x 0.25 micron film thickness). The following GC conditions were applied in all analyses: (1)

injector port temperature: 300 °C; (2) initial temperature: 50 °C (hold for 2 min); (3) temperature ramp: 10 °C/min; (4) final temperature: 280 °C (5 minutes hold time); (5) detector temperature: 300 °C. Total run time: 35 minutes.

The detectors used are HP 5971 MSD or HP 5870 MSD calibrated using perfluorotributylamine (PFTBA). The data were acquired using Agilent Chemstation software and identification of known compounds produced from the succeeding reactions was conducted by spectral matching with the NIST/EPA/NIH 2011 Mass Spectral Library and Software package (NIST11) and by comparison of experimental data with literature structure characterization reports.

In most examples, the identification of hydrogenolysis products was based on GC-MS library matching and comparison of experimental mass spectra with literature reports. In cases where known compounds were produced, confirmation of product identity was supported based on characteristic $^1\text{H-NMR}$ chemical shifts. In experiments where the products are unprecedented compounds, the structures were tentatively proposed based on the observed M^+ values; thorough structural characterization of these compounds will be pursued as future work.

Base Metal-Mediated Ether Cleavage

Stoichiometric Cleavage of Benzyl Methylcyclopropyl Ether **211** with **26b**

The following are one of the preliminary studies of C–O bond activation mediated by the tetrametallic Ni(I) catalyst. Benzyl methylcyclopropyl ether was chosen as substrate to simultaneously probe the potential activity of the nickel catalyst for (1) activation C–O bond and / or (2) directed C–C bond cleavage in cyclopropyl rings. Exhaustive identification and quantification of all hydrogenolysis products in these preliminary experiments was not pursued.

A Teflon–sealed reactor was charged with 35 mg (0.22 mmol) benzyl methylcyclopropyl ether **211**, 3 mg (0.002 mmol) **26b**, 2 mL THF and a Teflon–sealed magnetic stir bar. The reactor was taken out of the dry box and stirred at 1200 rpm for 16 h in an oil bath at 75 °C. The reactor was cooled to room and the reaction mixture quenched with a 10% HCl solution. The organic products were extracted through diethyl ether–water extractions using three 2 mL portions of diethyl ether. The diethyl ether fractions were pooled and the solvent was evaporated. The residue was dissolved in CDCl₃ for ¹H-NMR analysis. Results of the ¹H-NMR analysis revealed the cleavage of the benzylic C–O bond based on the detection of 1,2-diphenylethane (4 %) and trace amounts of toluene. Detectable levels of benzyl alcohol were not observed. The conversion

was calculated based on the ratio of integration of characteristic NMR chemical shifts of the starting material **211** (δ 4.57 ppm, 2H) and 1,2-diphenylethane **30** (δ 2.95 ppm, 2H).

Cleavage of Benzyl Methylcyclopropyl Ether **211** with **26b** under H₂

A Teflon-sealed reactor was charged with 35 mg (0.22 mmol) benzyl methylcyclopropyl ether, 3 mg (0.002 mmol) **26b**, 2 mL THF and a Teflon-sealed magnetic stir bar. The reactor was taken out of the dry box and connected to a hydrogen manifold. The reaction vessel was then charged with H₂ (1 atm), employing rigorous inert-atmosphere laboratory techniques. The reaction mixture was then stirred at 1200 rpm for 16 h in an oil bath at 75 °C. The reactor was cooled to room and quenched with a 10% HCl solution. The organic products were extracted through diethyl ether–water extractions using three 4 mL portions of diethyl ether. The diethyl ether fractions were pooled and the solvent was evaporated. The residue was dissolved in CDCl₃ for ¹H-NMR analysis. Results of the ¹H-NMR analysis revealed the cleavage of the benzylic C–O bond based on the detection of 1,2-diphenylethane (6 %) and trace amounts of toluene. Detectable levels of benzyl alcohol were not observed. The conversion was calculated based on the ratio of integration of characteristic NMR chemical shifts of the starting material (δ 4.57 ppm, 2H) and 1,2-diphenylethane **30** (δ 2.95 ppm, 2H).

Stoichiometric Hydrogenolysis of 4-Methoxybiphenyl **212** with **26b**

A Teflon–sealed reactor was charged with 50 mg (0.27 mmol) 4-methoxybiphenyl **212**, 3 mg (0.002 mmol) **26b**, 2 mL toluene and a Teflon–sealed magnetic stir bar. The reactor was taken out of the dry box and connected to a hydrogen manifold. The reaction vessel was then charged with H₂ (1 atm), employing rigorous inert-atmosphere laboratory techniques. The reaction mixture was then stirred at 1200 rpm for 16 h in an oil bath at 120 °C. The reactor was cooled to room and quenched with a 10% HCl solution. The organic products were extracted through diethyl ether–water extractions using three 4 mL portions of diethyl ether. The diethyl ether fractions were pooled and the solvent was evaporated. The residue was dissolved in CDCl₃ for ¹H-NMR analysis. Results of the ¹H-NMR analysis revealed the formation of biphenyl **143** (2%).

Silane-Promoted Hydrogenolysis of 4-Methoxybiphenyl **212** with **26b**

A Teflon–sealed reactor was charged with 50 mg (0.27 mmol) 4-methoxybiphenyl, 3 mg (0.002 mmol) **26b**, 58 mg (0.54 mmol), 2 mL toluene and a Teflon–sealed magnetic stir bar. The reaction mixture was stirred vigorously at 1200 rpm and the reactor, was heated to 120 °C in an oil bath for 16 h. The reactor was then cooled to room temperature, exposed to air and was treated with 3 mL 1M HCl solution. The organic products were then extracted by a series of diethyl ether extractions. The product mixture was then filtered through a column of Florisil. The solvent

was removed *in vacuo*, dissolved in CDCl₃ and submitted for ¹H-NMR and GC–MS analysis. This reaction gave biphenyl **143** (4%).

Catalytic Hydrogenolysis of Diphenyl Ether **197**

A Teflon–sealed reactor was charged with 80 mg (0.47 mmol) diphenyl ether **197**, 9 mg (0.008 mmol) **26b**, 50 mg (1.25 mmol) KH, 3 mL isoctane and a Teflon–sealed magnetic stir bar. The reactor was taken out of the dry box and connected to a hydrogen manifold. The reaction vessel was then charged with H₂ (1 atm), employing rigorous inert-atmosphere laboratory techniques. The reaction mixture was then stirred at 1200 rpm for 12 h in an oil bath at 120 °C. Since the reaction produces volatile products, the reaction mixture was cooled to -60 °C and quenched with a 10% HCl solution. The organic products were extracted through diethyl ether–water extractions using three 2 mL portions of cold diethyl ether. The diethyl ether fractions were pooled and subjected to GC-MS analyses. The identity of each hydrogenolysis product was determined by GC-MS library matching. Complete conversion of the substrate to a 3 : 1 mixture of benzene **180** and phenol **196** was observed.

Catalytic Hydrogenolysis of 4-Methoxybiphenyl **212**

This is the general procedure employed in the hydrogenolysis of 4-methoxybiphenyl under varying pressure and temperature conditions. The desired amount of substrate, catalyst and basic scavenger, as indicated in

Table 7.5.1, were mixed in toluene (5 to 10 mL). The mixture was transferred into the appropriate pressure reactor equipped with a Teflon magnetic stir bar. The reaction vessels were charged with H₂, employing strict inert-atmosphere laboratory techniques, and heated to the desired temperature in an oil bath on a heating magnetic stir plate, stirring at 1200 rpm. After the desired reaction time, the reaction mixture was cooled to room temperature and then quenched with a 10% HCl solution. The organic products were extracted through a series of diethyl ether–water extractions and the organic fractions were pooled, dried with anhydrous Na₂SO₄ and filtered through a small column of Florisil. The solvent was removed *in vacuo* and the weighed residue was dissolved in CDCl₃ for ¹H-NMR and GC-MS analyses. The products of the reaction are known compounds. Quantification of methane and methanol produced was not pursued. The identification and quantification of non-volatile products was based on GC-MS library matching and integration of characteristic ¹H-NMR chemical shifts. ¹H-NMR and mass spectroscopic characterization 4-phenylphenol **174** was earlier reported by Wang and coworkers.³³⁸

Table 7.5.1. Hydrogenolysis of 4-methoxybiphenyl **173**.

Entry	173 mg (mmol)	Cat mg (mmol)	KH mg (mmol)	Temp (°C)	Time (h)	% Conversion	
						143	174
1	45 (0.24)	26b 15 (0.013)	29 (0.73)	110	15	18	1
2	45 (0.24)	26b 15 (0.013)	29 (0.73)	120	36	50	50
3	95	26b	62	120	15	12	31

	(0.52)	9 (0.008)	(1.55)				
4	100 (0.54)	26a 9 (0.008)	65 (1.63)	120	14	6	7

Catalytic Hydrogenolysis of 2-Methoxynaphthalene 215

This was a general procedure employed in the nickel-catalyzed hydrogenolysis of 2-methoxynaphthalene under varying pressure and temperature conditions. The preparation of reaction mixtures was conducted under an inert atmosphere, for example, in an Argon or nitrogen drybox. The desired amount of substrate, catalyst and basic scavenger, as indicated in Table 7.5.2, were mixed in toluene (5 to 10 mL). The mixture was transferred into the appropriate pressure reactor equipped with a Teflon magnetic stir bar. The reaction vessels were charged with H₂, employing strict inert-atmosphere laboratory techniques, and heated to the desired temperature in an oil bath on a heating magnetic stir plate, stirring at 1200 rpm. After the desired reaction time, the reaction mixture was cooled to room temperature and then quenched with a 10% HCl solution. The organic products were extracted through a series of diethyl ether–water extractions and the organic fractions were pooled, dried with anhydrous Na₂SO₄ and filtered through a small column of Florisil. The solvent was removed *in vacuo* and the residue was dissolved in CDCl₃ for ¹H-NMR and GC-MS analyses. The products of the reaction are known compounds. Quantification of methane and methanol produced

was not pursued. The identification of non-volatile hydrogenolysis products was conducted by GC-MS library matching and comparison of ¹H-NMR data with reported values.^{339,340}

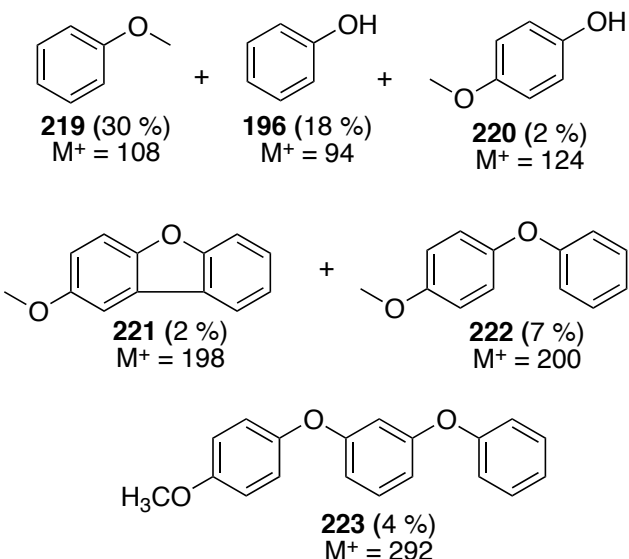
Table 7.5.2. Hydrogenolysis of 2-methoxynaphthalene **215**.

Entry	176 mg (mmol)	Cat mg (mmol)	KH mg (mmol)	Temp (°C)	Time (h)	% Conversion	
						216	217
1	85 (0.54)	8 (0.007)	64 (1.61)	110	17	22	10
2	85 (0.54)	10 (0.009)	64 (1.61)	120	21	68	32

Hydrogenolysis of 1,3-bis(4-methoxyphenoxy)benzene **218**

A Teflon–sealed reactor was charged with 120 mg (0.37 mmol) 1,3-bis(4-methoxyphenoxy)benzene, 13 mg (0.012 mmol) **26b**, 97 mg (2.42 mmol) KH, 6 mL toluene and a Teflon–sealed magnetic stir bar. The reactor was taken out of the dry box and connected to a hydrogen manifold. The reaction vessel was then charged with H₂ (1 atm), employing rigorous inert-atmosphere laboratory techniques. The reaction mixture was then stirred at 1200 rpm for 18 h in an oil bath at 120 °C. The reactor was cooled to room and the reaction mixture quenched with a 10% HCl solution. The organic products were extracted through diethyl ether–water extractions using three 2 mL portions of diethyl ether. The diethyl ether fractions were pooled and subjected to GC-MS analyses. The identities of compounds **220**,³⁴¹ **221**,³⁴² **222**³⁴³ and **223**³⁴⁴ were determined by

comparison of individual mass spectra with literature data. A mixture of the following composition was obtained:



The remaining 38 % of the mixture obtained was recovered starting material.

Stoichiometric Deoxygenation of Epoxides

The following are preliminary experiments to demonstrate the activity of the tetrametallic Ni(I) cluster for cleaving C-O bonds in epoxide.

Styrene Oxide 224

A Teflon–sealed glass reactor was charged with 67 mg (0.56 mmol) styrene oxide, 5 mg (0.004 mmol) **26b**, 150 mg (1.29 mmol) Et₃SiH, 1.5 mL C₆D₆ and a Teflon–sealed magnetic stir bar. The reaction mixture was stirred vigorously at 1200 rpm and the reactor, was heated to 90 °C in an

oil bath for 16 h. The reactor was then cooled to room temperature and the reaction mixture filtered through a column of Florisil. The formation of styrene was confirmed by the appearance of characteristic vinyl C–H chemical shifts of styrene. Styrene was formed in a stoichiometric fashion (~2%; 1 C–O bond / Ni center) based on integration of observed $^1\text{H-NMR}$ chemical shifts.

Cyclododecene Oxide **225**

A Teflon–sealed glass reactor was charged with 100 mg (0.56 mmol) cyclododecene oxide, 6 mg (0.005 mmol) **26b**, 1.5 mL C_6D_6 and a Teflon–sealed magnetic stir bar. The reaction mixture was stirred vigorously at 1200 rpm and the reactor, was heated to 90 °C in an oil bath for 16 h. The reactor was then cooled to room temperature and the reaction mixture filtered through a column of Florisil. Epoxide deoxygenation was confirmed by the appearance of vinyl C-H $^1\text{H-NMR}$ chemical shifts corresponding to cyclododecene.³⁴⁵ Cyclododecene was formed in a stoichiometric fashion (~2% 1 C–O bond / Ni center) based on integration of observed $^1\text{H-NMR}$ chemical shifts.

Catalytic Hydrodeoxygenation of 1,3-diphenylisobenzofuran **227**

A Teflon–sealed reactor was charged with 100 mg (0.37 mmol) diphenylisobenzofuran, 10 mg (0.009 mmol) **26b**, 44 mg (1.10 mmol) KH, 6 mL toluene and a Teflon–sealed magnetic stir bar. The reactor was

taken out of the dry box and connected to a hydrogen manifold. The reaction vessel was then charged with H₂ (1 atm), employing rigorous inert-atmosphere laboratory techniques. The reaction mixture was then stirred at 1200 rpm for 16 h in an oil bath at 120 °C. The reactor was cooled to room and the reaction mixture quenched with a 10% HCl solution. The organic products were extracted through diethyl ether–water extractions using three 2 mL portions of diethyl ether. The diethyl ether fractions were pooled and the solvent was removed under vacuum. The residue was then dissolved in CDCl₃ and subjected to ¹H-NMR and GC-MS analyses. The formation of 1,2-dibenzylbenzene (95%; EIMS M⁺ = 258) was confirmed by GC-MS library matching.

Catalytic Hydrogenolysis of Dibenzofuran 198

The following is the general procedure employed in the KH-promoted hydrogenolysis of dibenzofuran under varying pressure and temperature conditions. The desired amount of substrate, catalyst and basic scavenger, as indicated in Table 7.5.3, were mixed in toluene (5 to 10 mL). The mixture was transferred into the appropriate pressure reactor equipped with a Teflon magnetic stir bar. The reaction vessels were charged with H₂, employing strict inert-atmosphere laboratory techniques, and heated to the desired temperature in an oil bath on a heating magnetic stir plate, stirring at 1200 rpm. After the desired reaction time, the reaction mixture was cooled to room temperature and then quenched with a 10%

HCl solution. The organic products were extracted through a series of diethyl ether–water extractions and the organic fractions were pooled, dried with anhydrous Na₂SO₄ and filtered through a small column of Florisil. The formation of 2-phenylphenol was confirmed by GC-MS library matching and comparison of ¹H-NMR spectra with literature reports.³⁴⁶ The solvent was removed *in vacuo* and the weighed residue was dissolved in CDCl₃ for ¹H-NMR and GC-MS analyses. The catalysis gives 2-phenylphenol **229** as the major product.

Table 7.5.3. HDO of DBF catalyzed by **26b**.

Entry	166 mg (mmol)	Cat mg (mmol)	KH mg (mmol)	Temp (°C)	Time (h)	% Conversion	
						229	143
1	62 (0.37)	10 (0.009)	30 (0.74)	120	18	100	0
2	43 (0.26)	8 (0.007)	20 (0.50)	130	18	100	0
3	76 (0.45)	8 (0.007)	36 (0.90)	135	18	100	0
4	200 (1.18)	7 (0.006)	95 (2.38)	150	18	96	4
5	200 (1.18)	7 (0.006)	95 (2.38)	180	0.8	20	1

Lewis Acid-Promoted Complete Hydrodeoxygenation of Dibenzofuran **198**

AlMe₃ as Promoter

A glass-lined Parr metal reactor was charged with 480 mg (2.86 mmol) DBF, 9 mg (0.008 mmol) catalyst, 70 mg (0.97 mmol) AlMe₃, 240 mg KH (6.0 mmol), 6 mL benzene and a magnetic stir bar. The reaction

vessel was charged with H₂ (2 atm), employing strict inert-atmosphere laboratory techniques, and heated to 150 °C in an oil bath on a heating magnetic stir plate, stirring at 1200 rpm for 12 h. After the desired reaction time, the reaction mixture was cooled to room temperature and then quenched with a 10% HCl solution. The organic products were extracted through a series of diethyl ether–water extractions and the organic fractions were pooled, dried with anhydrous Na₂SO₄ and filtered through a small column of Florisil. The solvent was removed *in vacuo* and the residue was dissolved in CDCl₃ for ¹H-NMR and GC-MS analyses. The reaction resulted in 100% conversion to biphenyl **143**.

Al*i*Bu₃ as Promoter

A glass-lined Parr metal reactor was charged with 240 mg (1.43 mmol) DBF, 5 mg (0.004 mmol) **26b**, 70 mg (0.35 mmol) Al*i*Bu₃, 100 mg KH (2.5 mmol), 6 mL benzene and a magnetic stir bar. The reaction vessel was charged with H₂ (2 atm), employing strict inert-atmosphere laboratory techniques, and heated to 150 °C in an oil bath on a heating magnetic stir plate, stirring at 1200 rpm for 12 h. After the desired reaction time, the reaction mixture was cooled to room temperature and then quenched with a 10% HCl solution. The organic products were extracted through a series of diethyl ether–water extractions and the organic fractions were pooled, dried with anhydrous Na₂SO₄ and filtered through a small column of Florisil. The solvent was removed *in vacuo* and the residue was dissolved

in CDCl_3 for $^1\text{H-NMR}$ and GC-MS analyses. The reaction afforded a mixture of products: biphenyl **143** (20%), 2-phenylphenol **229** (78%) and cyclohexylbenzene **230** (2%; $M^+ = 160$). The formation of cyclohexylbenzene³⁴⁷ was confirmed by comparison of mass spectrum with literature reports.

Control Experiment: Catalyst-Free Hydrogenolysis of Ethers

Catalyst-Free HDO of DBF **198**

A glass-lined Parr metal reactor with 500 mg (3.0 mmol) DBF, 240 mg (6.0 mmol) KH, 80 mg (1.1 mmol) AlMe_3 , 6 mL benzene and a Teflon-sealed magnetic stir bar. The reaction vessel was charged with H_2 (2 atm), employing strict inert-atmosphere laboratory techniques, and heated to 160 °C in an oil bath on a heating magnetic stir plate, stirring at 1200 rpm for 16 h. The reaction mixture was cooled to room temperature and then quenched with a 10% HCl solution. The organic products were extracted through a series of diethyl ether–water extractions and the organic fractions were pooled, dried with anhydrous Na_2SO_4 and filtered through a small column of Florisil. The solvent was removed *in vacuo* and the weighed residue was dissolved in CDCl_3 for $^1\text{H-NMR}$ and GC-MS analyses. The starting material was unreacted after the 16 h.

KH-Free HDO of DBF **198** in the presence of **26b**

A glass-lined Parr metal reactor with 285 mg (1.70 mmol) DBF, 9 mg (0.008 mmol) **26b**, 40 mg (0.57) mmol AlMe₃, 6 mL benzene and a Teflon–sealed magnetic stir bar. The reaction vessel was charged with H₂ (2 atm), employing strict inert-atmosphere laboratory techniques, and heated to 150 °C in an oil bath on a heating magnetic stir plate, stirring at 1200 rpm for 16 h. The reaction mixture was cooled to room temperature and then quenched with a 10% HCl solution. The organic products were extracted through a series of diethyl ether–water extractions and the organic fractions were pooled, dried with anhydrous Na₂SO₄ and filtered through a small column of Florisil. The solvent was removed *in vacuo* and the weighed residue was dissolved in CDCl₃ for ¹H-NMR and GC-MS analyses. The starting material was unreacted after the 16 h.

KH-Free HDO of DBF in the presence of **22**

A glass-lined Parr metal reactor with 200 mg (1.20 mmol) DBF, 7 mg (0.009 mmol) **22**, 30 mg (0.42) mmol AlMe₃, 6 mL benzene and a Teflon–sealed magnetic stir bar. The reaction vessel was charged with H₂ (2 atm), employing strict inert-atmosphere laboratory techniques, and heated to 150 °C in an oil bath on a heating magnetic stir plate, stirring at 1200 rpm for 16 h. The reaction mixture was then cooled to room temperature and then quenched with a 10% HCl solution. The organic products were extracted through a series of diethyl ether–water extractions

and the organic fractions were pooled, dried with anhydrous Na₂SO₄ and filtered through a small column of Florisil. The solvent was removed *in vacuo* and the weighed residue was dissolved in CDCl₃ for ¹H-NMR and GC-MS analyses. The starting material was unreacted after the 16 h.

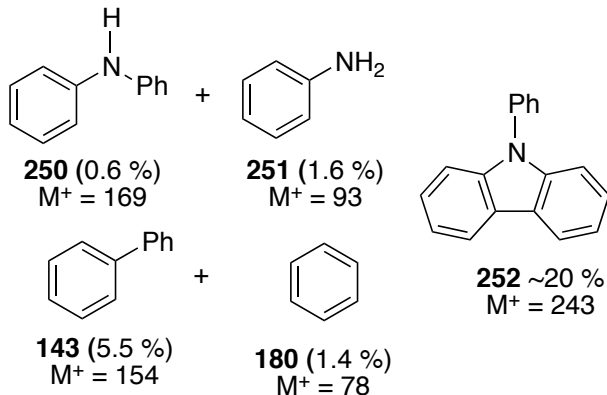
Metal-Free Hydrogenolysis of DBF 198

A Teflon-sealed reactor was charged with 100 mg (0.60 mmol) DBF, 128 mg (1.20 mmol) PhSiH₃, 135 mg (1.20 mmol) KO^tBu, 3 mL THF and a Teflon-sealed magnetic stir bar. The reactor was taken out of the dry box and stirred at 1200 rpm for 16 h in an oil bath at 120 °C. The reactor was cooled to room and the reaction mixture quenched with a 10% HCl solution. The organic products were extracted through diethyl ether-water extractions using three 2 mL portions of diethyl ether. The diethyl ether fractions were pooled and subjected to GC-MS analyses. An 82 % conversion of the substrate to 2-phenylphenol was observed.³⁸

C–N Bond Hydrogenolysis of Triphenylamine 249

A Teflon-sealed reactor was charged with 400 mg (1.63 mmol) triphenylamine **249**, 18 mg (0.017 mmol) **26b**, 130 mg (3.26 mmol) KH, 6 mL THF and a Teflon-sealed magnetic stir bar. The reactor was taken out of the dry box and connected to a hydrogen manifold. The reaction vessel was then charged with H₂ (1 atm), employing rigorous inert-atmosphere laboratory techniques. The reaction mixture was then stirred at 1200 rpm

for 10 h in an oil bath at 110 °C. Since the reaction is anticipated to produce volatile products, the reactor was cooled to -60 °C and the reaction mixture quenched with a 10% KOH solution. The organic products were extracted through CHCl₃-water extractions using three 2 mL portions of cold CHCl₃. The CHCl₃ fractions were pooled and subjected to GC-MS analyses. Since the expected products of triphenylamine hydrogenolysis are known compounds, the identity of each product was confirmed through GC-MS library matching and comparison of mass spectra with reported examples.³⁴⁸ A product mixture of the following composition was observed:



The remaining product fraction was composed of unreacted starting material.

C–N Bond Hydrogenolysis in *N*-methylcarbazole **188** by **26b**

A glass-lined Parr metal reactor was charged with 150 mg (0.83 mmol) *N*-methylcarbazole **188**, 9 mg (0.008 mmol) **26b**, 150 mg (3.75

mmol) KH, 4 mL THF and a Teflon–sealed magnetic stir bar. The reactor was taken out of the dry box and connected to a hydrogen manifold. The reaction vessel was then charged with H₂ (1 atm), employing rigorous inert-atmosphere laboratory techniques. The reaction mixture was then stirred at 1200 rpm for 16 h in an oil bath at 160 °C. The reactor was cooled to room and the reaction mixture quenched with a 10% KOH solution. The organic products were extracted through CHCl₃–water extractions using three 2 mL portions of CHCl₃. The CHCl₃ fractions were pooled and the solvent was removed under vacuum. The residue was dissolved in CDCl₃ and subjected to ¹H-NMR and GC-MS analyses. The reaction gave *N*-methyl-2-phenylaniline **254** (20 %). The formation of **254** was confirmed by GC-MS (M⁺ = 183) and the appearance of reported ¹H-NMR chemical shifts.³⁴⁹

AlMe₃-Promoted C–N Bond Hydrogenolysis in *N*-methylcarbazole by **26b**

A glass-lined Parr metal reactor was charged with 150 mg (0.83 mmol) *N*-methylcarbazole **188**, 3 mg (0.002 mmol) **26b**, 150 mg (3.75 mmol) KH, 18 mg (0.25 mmol) AlMe₃, 4 mL benzene and a Teflon–sealed magnetic stir bar. The reactor was taken out of the dry box and connected to a hydrogen manifold. The reaction vessel was then charged with H₂ (1 atm), employing rigorous inert-atmosphere laboratory techniques. The reaction mixture was then stirred at 1200 rpm for 16 h in an oil bath at 160 °C. The reactor was cooled to room and the reaction mixture quenched

with a 10% KOH solution. The organic products were extracted through CHCl₃–water extractions using three 2 mL portions of CHCl₃. The CHCl₃ fractions were pooled and the solvent was removed under vacuum. The residue was dissolved in CDCl₃ and subjected to ¹H-NMR and GC-MS analyses. The reaction gave *N*-methyl-2-phenylaniline **254** (5 %).

AlMe₃-Promoted Hydrodenitrogenation of *N*-methylcarbazole **188** by **22**

A glass-lined Parr metal reactor was charged with 500 mg (2.76 mmol) *N*-methylcarbazole **188**, 35 mg (0.05 mmol) **22**, 240 mg (6.0 mmol) KH, 70 mg (0.97 mmol) AlMe₃, 6 mL benzene and a Teflon–sealed magnetic stir bar. The reactor was taken out of the dry box and connected to a hydrogen manifold. The reaction vessel was then charged with H₂(1 atm), employing rigorous inert-atmosphere laboratory techniques. The reaction mixture was then stirred at 1200 rpm for 16 h in an oil bath at 160 °C. The reactor was cooled to room and the reaction mixture quenched with a 10% KOH solution. The organic products were extracted through CHCl₃–water extractions using three 2 mL portions of CHCl₃. The CHCl₃ fractions were pooled and the solvent was removed under vacuum. The residue was dissolved in CDCl₃ and subjected to ¹H-NMR and GC-MS analyses. The reaction gave biphenyl **143** (20 %) and *N*-methyl-2-phenylaniline **154** (5 %).

Hydrogenation of Acridine **255** in the Presence of **26b**

A glass-lined Parr metal reactor was charged with 260 mg (1.45 mmol) acridine **255**, 10 mg (0.009 mmol) **26b**, 30 mg (0.42) mmol AlMe₃, 110 mg (2.75 mmol) KH, 6 mL toluene and a Teflon–sealed magnetic stir bar. The reaction vessel was charged with H₂ (2 atm), employing strict inert-atmosphere laboratory techniques, and heated to 135 °C in an oil bath on a heating magnetic stir plate, stirring at 1200 rpm for 18 h. After the desired reaction time, the reaction mixture was cooled to room temperature and then quenched with a 10% KOH solution until strongly basic. The organic products were extracted through a series of CHCl₃–water extractions and the organic fractions were pooled, dried with anhydrous Na₂SO₄ and filtered through a small column of Florisil. The solvent was removed *in vacuo* and the weighed residue was dissolved in CDCl₃ for ¹H-NMR and GC-MS analyses. The substrate underwent 96 % conversion into a mixture composed mainly of 9,10-dihydroacridine **256** (66 %) and unidentified products with molecular ion peak of 235. The identity of **256** was confirmed by GC-MS library matching and the appearance of characteristic 1H-NMR chemical shift at 4.08 ppm (s, 2H, CH₂).

Control Experiment: A similar experiment was conducted in the absence of the Ni(I) cluster **26b**. 9,10-dihydroacridine **256** was produced in 25% yield under similar reaction conditions.

Hydrogenation of Acridine **255** Catalyzed by **22**

A glass-lined Parr metal reactor was charged with 260 mg (1.45 mmol) acridine **255**, 10 mg (0.014 mmol) **22**, 30 mg (0.42) mmol AlMe₃, 115 mg (2.88 mmol) KH, 6 mL toluene and a Teflon–sealed magnetic stir bar. The reaction vessel was charged with H₂ (2 atm), employing strict inert-atmosphere laboratory techniques, and heated to 135 °C in an oil bath on a heating magnetic stir plate, stirring at 1200 rpm for 18 h. After the desired reaction time, the reaction mixture was cooled to room temperature and then quenched with a 10% KOH solution until strongly basic. The organic products were extracted through a series of CHCl₃–water extractions and the organic fractions were pooled, dried with anhydrous Na₂SO₄ and filtered through a small column of Florisil. The solvent was removed *in vacuo* and the weighed residue was dissolved in CDCl₃ for ¹H-NMR and GC-MS analyses. The substrate underwent 95 % conversion into a mixture composed mainly of 9,10-dihydroacridine **256** (91%) and 2-(phenylmethyl)aniline **257** (4%; M⁺ = 183). The identity of **257** was confirmed by GC-MS (M⁺ = 181) and the characteristic 1H-NMR chemical shift at 4.08 ppm (s, 2H, CH₂).³⁵⁰

7.6 Base Metal–Catalyzed Deoxygenation of Carbonyl Compounds

General Considerations

All manipulations were carried out using Schlenk techniques. The preparation of each reaction mixture was carried out under a purified N₂ atmosphere in a drybox. Experiments that required heating were conducted under a Schlenck manifold. Thoroughly dried and degassed solvents were used in all experiments. Liquid substrates were degassed and passed through anhydrous silica prior to use. NMR spectra were recorded on an Agilent/Varian Inova two-channel 400 MHz spectrometer at room temperature. ¹H NMR spectra were referenced to residual protio solvent peaks (CDCl₃ and C₆D₆).

GC-MS Analysis

GC-MS analysis was conducted using an Agilent 5890 GC equipped with a 7673 Automatic Liquid Sampler (ALS). The column used for the analysis is an Agilent DB-5 MS (25m x 0.25mm x 0.25 micron film thickness). The following GC conditions were applied in all analyses: (1) injector port temperature: 300 °C; (2) initial temperature: 50 °C (hold for 2 min); (3) temperature ramp: 10 °C/min; (4) final temperature: 280 °C (5 minutes hold time); (5) detector temperature: 300 °C. Total run time: 35 minutes.

The detectors used are HP 5971 MSD or HP 5870 MSD calibrated using perfluorotributylamine (PFTBA). The data were acquired using Agilent Chemstation software and identification of known compounds produced from the succeeding reactions was conducted by spectral matching with the NIST/EPA/NIH 2011 Mass Spectral Library and Software package (NIST11) and by comparison of experimental data with literature structure characterization reports.

In most examples, the identification of deoxygenation products was based on GC-MS library matching and comparison of experimental mass spectra with literature reports. In cases where known compounds were produced, confirmation of product identity was supported based on characteristic $^1\text{H-NMR}$ chemical shifts. In experiments where the dimerization products are unprecedented compounds and diastereomeric mixtures, the structures were tentatively proposed based on the observed M^+ values; thorough structural characterization of these compounds will be pursued as future work.

Catalytic Deoxygenation of 2-cyclohex-1-enone **263** by **26b**

A 100 mL Teflon-sealing glass reactor equipped with a Teflon-covered magnetic stir bar was charged with 87 mg (0.91 mmol) 2-cyclohex-1-enone, 5 mg (0.004 mmol) **26b**, 196 mg (1.81 mmol) PhSiH_3 , and 1.5 mL tetrahydrofuran (THF). The reaction mixture was stirred at a

speed of 1200 rpm for 16 h at the desired temperature (Table 7.6.1). The reaction mixture was cooled to -60 °C, exposed to air and then filtered through a plug of Florisil, and the THF-fraction was subjected to GC–MS analysis. The identity of each reduction product was determined by GC–MS library matching. The identity of the main deoxygenation product 3,3'-biscyclohexyl was confirmed based on literature characterization data.³⁵¹

Table 7.6.1. Deoxygenation of 2-cyclohex-1-enone **263** by **26b**

Product	M^+ (GC-MS)	%Conversion		
		25 °C	60 °C	80 °C
	98	5	5	0
	98	2	0	0
	162	14	39	61
$\text{PhSiH}_2(\text{OR})^a$	204	10	26	22
$\text{PhSiH}(\text{OR})_2^a$	300	21	31	17
$\text{PhSi}(\text{OR})_3^a$	396	22	0	0
	194 ^a	16	0	0

^a The structure is tentatively assigned according to observed M^+ values. Literature structure characterization data are unavailable for the reduction product.

Solvent-Free Deoxygenation of 2-cyclohex-1-enone **263** by **26b**

A 100 mL Teflon-sealing glass reactor equipped with a Teflon-covered magnetic stir bar was charged with 150 mg (1.56 mmol) 2-

cyclohex-1-enone, 9 mg (0.008 mmol) **26b**, 169 mg (1.56 mmol) PhSiH₃, and 1.5 mL tetrahydrofuran (THF). The reaction mixture was stirred at a speed of 1200 rpm for 16 h at 60 °C. The reaction mixture was cooled to -60 °C, exposed to air and then filtered through a plug of Florisil, and the THF-fraction was subjected to GC–MS analysis. The identity of each reduction product was determined by GC-MS library matching (results in Table 7.6.2).

Table 7.6.2. Solvent-free deoxygenation of 2-cyclohex-1-enone by **26b**

Product	M ⁺ (GC-MS)	%Conversion
	98	7
	162	15
PhSiH ₂ (OR)	204	6
PhSiH(OR) ₂	300	53
PhSi(OR) ₃	396	19

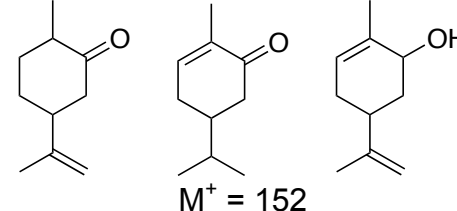
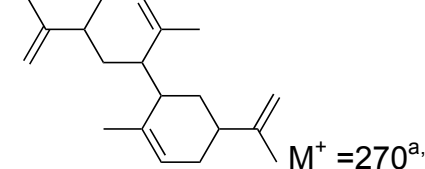
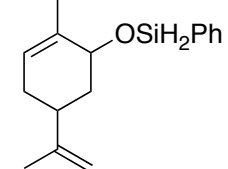
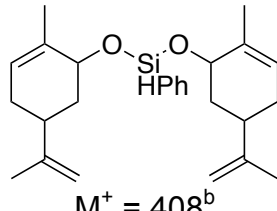
Catalytic Deoxygenation of 2-cyclohex-1-enone **263** by **26a**

A 100 mL Teflon-sealing glass reactor equipped with a Teflon-covered magnetic stir bar was charged with 87 mg (0.91 mmol) 2-cyclohex-1-enone, 5 mg (0.004 mmol) **26a**, 196 mg (1.81 mmol) PhSiH₃, and 1.5 mL tetrahydrofuran (THF). The reaction mixture was stirred at a speed of 1200 rpm for 16 h at 60 °C. The reaction mixture was stirred at a speed of 1200 rpm for 16 h at 60 °C. The reaction mixture was cooled to

-60 °C, exposed to air and then filtered through a plug of Florisil, and the THF-fraction was subjected to GC-MS analysis. The identity of each reduction product was determined by GC-MS library matching. The substrate was completely converted into a mixture of products identified to be the following: benzene **148** (9%), cyclohexene **217**(11%), cyclohexanone (27%), 2-cyclohexen-1-ol (42%) and an unidentified product with $M^+ = 178$ at 11%.

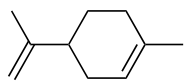
Catalytic Deoxygenation of *R*-Carvone **285** by **26b**

A 100 mL Teflon-sealing glass reactor equipped with a Teflon-covered magnetic stir bar was charged with 4 mg (0.003 mmol) **26b**, 100 mg (0.67 mmol) *R*-carvone, 0.67-1.28 mmol PhSiH₃ and 1.5 mL THF. The reaction mixture was stirred at a speed of 1200 rpm for 16 h at 60 °C. The reaction mixture was cooled to room temperature, exposed to air and then filtered through a plug of Florisil, and the THF-fraction was subjected to GC-MS analysis. The identity of each reduction product was determined by GC-MS library matching and spectral comparison with literature characterization data.

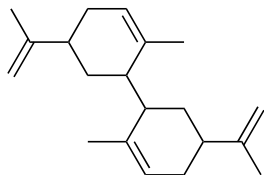
Product	%Conversion		
	1 : 1 (223 : PhSiH ₃) 60 °C	1 : 3 (223 : PhSiH ₃) 60 °C	1 : 3 (223 : PhSiH ₃) 100 °C
 $M^+ = 136^{352}$	6	3	6
 $M^+ = 152$	8	14	7
 $M^+ = 270^{a,b}$	41	46	40
 $M^+ = 258^b$	4	1	21
 $M^+ = 408^b$	40	36	26

^a The product was obtained as a mixture of isomers.

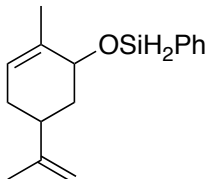
^b The structure is tentatively assigned according to observed M^+ values.
Literature structure characterization data are unavailable for the reduction product.



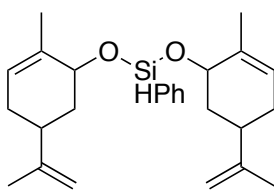
GC-MS *m/z* 136 (M^+), 121, 79, 67, 53.



GC-MS *m/z* 270 (M^+), 134, 119, 93, 77, 67, 55.



GC-MS *m/z* 258 (M^+), 243, 215, 202, 175, 137, 123, 107, 93, 77, 67, 55.



GC-MS *m/z* 408 (M^+), 273, 257, 229, 213, 153, 139, 123, 107, 91, 77, 67, 55.

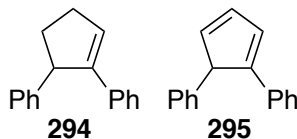
General Procedure for Catalytic Deoxygenation of 2,3-diphenylcyclopentene, Benzaldehyde and Acetophenone

A 100 mL Teflon-sealing glass reactor equipped with a Teflon-covered magnetic stir bar was charged with **26b**, carbonyl substrate, PhSiH₃ and 1.5 mL THF. The reaction mixture was stirred at a speed of 1200 rpm for 16 h at 60 °C. Since the deoxygenation of benzaldehyde and acetophenone generates volatile products, analysis of the product mixtures was conducted via GC-MS analysis.

Deoxygenation of 2,3-Diphenylcyclopentene **293**

A 100 mL Teflon-sealing glass reactor equipped with a Teflon-covered magnetic stir bar was charged with 4 mg (0.003 mmol) **26b**, 160 mg (0.73 mmol) substrate ($C_{17}H_{14}O$), 160 mg (1.48 mmol) $PhSiH_3$ and 1.5 mL THF. The reaction mixture was stirred at a speed of 1200 rpm for 16 h at 60 °C.

The reaction mixture was cooled to room temperature, exposed to air and then filtered through a plug of Florisil. The solvent was removed *in vacuo* and the residue was dissolved in $CDCl_3$ for 1H -NMR and GC–MS analysis. Structures of the deoxygenation products were confirmed by comparison of mass spectra with literature reports.³⁵³ The reaction produced **294** (48%) and **295** (mixture of isomers; 52%).



Benzaldehyde **298**

Reagents used: 4 mg (0.003 mmol) **26b**, 77 mg (0.73 mmol) benzaldehyde, 160 mg (1.48 mmol) $PhSiH_3$ and 1.5 mL THF. This reaction was anticipated to generate volatile products. The reaction mixture was cooled to -60 °C, exposed to air and then filtered through a plug of Florisil, and the cooled THF-fraction was subjected to GC–MS analysis. The reaction afforded benzene **148** (4%), toluene **229** (10%) and benzyl

alcohol **230** (86%). The identities of the products were confirmed by comparison of mass spectra with literature spectra.³⁵⁴

Acetophenone **301**

Reagents used: 4 mg (0.003 mmol) **26b**, 87 mg (0.73 mmol) acetophenone, 160 mg (1.48 mmol) PhSiH₃ and 1.5 mL THF. Since the reaction generates volatile products, the reaction mixture was cooled to -60 °C, exposed to air and then filtered through a plug of Florisil, and the cooled THF-fraction was subjected to GC-MS analysis. The reaction afforded ethylbenzene **62** (12%) and 1-phenylethanol **232** (74%). The identities of the products were confirmed by comparison of mass spectra with literature spectra.^{355,356}

General Procedure for Catalytic Deoxygenation of 4-methoxyacetophenone, 4-ethylacetophenone

A 100 mL Teflon-sealing glass reactor equipped with a Teflon-covered magnetic stir bar was charged with the catalyst **26a/28b**, carbonyl substrate, PhSiH₃ and 1.5 mL THF. The reaction mixture was stirred at a speed of 1200 rpm at room temperature for two h and then heated to 60 °C for an additional 16 h. The reaction mixture was cooled to room temperature, exposed to air and then filtered through a plug of Florisil. The solvent was removed *in vacuo* and the residue was dissolved in CDCl₃ for ¹H-NMR and GC-MS analysis. Structural confirmation of products was

conducted through GC-MS library matching and comparison with *cited* literature information.

4-methoxyacetophenone 85 with 26b

Reagents used: 4 mg (0.003 mmol) **26b**, 109 mg (0.73 mmol) 4-methoxyacetophenone, 160 mg (1.48 mmol) PhSiH₃ and 1.5 mL THF. The reaction afforded 4-ethylanisole **303** (29%),³²⁸ 1,2-bis(methoxyphenyl)butane **304** (57%; M⁺ = 270) and 4-(hydroxymethyl)anisole (14%).³⁵⁶ The dimerized deoxygenation product **304** was obtained as a mixture of isomers. The structure of **304** is tentatively assigned according to the experimental mass spectra and will have to be confirmed by further spectral characterization.

235: GC-MS m/z 270 (M⁺), 135, 105, 91, 77, 65.

4-methoxyacetophenone 85 with 26a

Reagents used: 4 mg (0.003 mmol) **26a**, 109 mg (0.73 mmol) 4-methoxyacetophenone, 160 mg (1.48 mmol) PhSiH₃ and 1.5 mL THF. The reaction afforded 4-ethylanisole **303** (13%), 4-methoxystyrene **305** (3%),³²⁹ 1,2-bis(methoxyphenyl)butane **304** (42%; M⁺ = 270) and 4-(hydroxymethyl)anisole **306** (24%). Unreacted substrate was also recovered (18%).

4-ethylacetophenone **83** with **26b**

Reagents used: 4 mg (0.003 mmol) **26a**, 108 mg (0.73 mmol) 4-ethylacetophenone, 160 mg (1.48 mmol) PhSiH₃ and 1.5 mL THF. The reaction afforded 1,4-diethylbenzene **307** (13%),³²⁶ 4-ethylstyrene **308** (6%), 1,2-bis(ethylphenyl)butane **309** (19%; M⁺ = 270)³⁵⁷ and mixtures of alkoxysilanes (50%). The dimerized deoxygenation product **309** was obtained as a mixture of isomers. The structure of **309** is tentatively assigned according to the experimental mass spectra and will have to be confirmed by further spectral characterization.

309: GC-MS *m/z* 266 (M⁺), 133, 105, 91, 77.

General Procedure for Catalytic Deoxygenation of 4-*N,N'*-dimethylaminobenzaldehyde, *p*-Anisaldehyde, 4-(methylthio)benzaldehyde and Methyl 4-formylbenzoate

A 100 mL Teflon-sealing glass reactor equipped with a Teflon-covered magnetic stir bar was charged with catalyst **26a/28b**, substrate, PhSiH₃ and THF. The reaction mixture was stirred at a speed of 1200 rpm at room temperature for six h and then heated to the desired temperature for an additional 16 h. The reaction mixture was cooled to room temperature, exposed to air and then filtered through a plug of Florisil, and the THF-fraction was subjected to GC-MS analysis.

4-N,N'-dimethylaminobenzaldehyde **89** with **26a** at 80 °C

Reagents used: 6 mg (0.005 mmol) **26a**, 74 mg (0.50 mmol) substrate, 54 mg (0.50 mmol) PhSiH₃ and 1.0 mL THF. The reaction afforded 4-N,N'-dimethylaminotoluene **310** (47%),³²⁷ 4-N,N'-dimethylaminobenzyl alcohol **311** (5%),³⁵⁸ 1,2-bis(4-N,N'-dimethylaminophenyl)ethane **312** (41%),³⁵⁹ 1,1-bis(4-N,N'-dimethylaminophenyl)methane **313** (2%)³⁶⁰ and an unidentified species with M⁺ = 240 (5%). The formation of the major products was also confirmed by their characteristic ¹H-NMR chemical shifts in CDCl₃. ¹H-NMR **310** (CDCl₃, 399.79 MHz) δ 2.63 (s, 3H, CH₃); **312** (CDCl₃, 399.79 MHz) δ 2.80 (s, 4H, –CH₂CH₂–).

Deoxygenation of 4-N,N'-dimethylaminobenzaldehyde **26b** at 80 °C

Reagents used: 5 mg (0.005 mmol) **26b**, 150 mg (0.92 mmol) substrate, 360 mg (1.84 mmol) PhSiH₃ and 1.0 mL THF. The reaction afforded **310** (43%), **311** (4%), **312** (9%), **313** (36%) and **314** (2%).³⁶¹ The formation of the major products were also confirmed by their characteristic ¹H-NMR chemical shifts in CDCl₃. ¹H-NMR **310** (CDCl₃, 399.79 MHz) δ 2.30 (s, 3H, CH₃).

4-N,N'-dimethylaminobenzaldehyde **89** with **26b** at 90 °C

Reagents used: 5 mg (0.005 mmol) **26b**, 150 mg (0.92 mmol) substrate, 190 mg (0.92 mmol) PhSiH₃ and 1.0 mL THF. The reaction afforded **310**

(34%), **311** (7%), **312** (13%), **313** (26%), **314** (3%) and 2-(4-N,N-dimethylaminophenyl)ethanol **316** (1%).³⁶²

4-N,N'-dimethylaminobenzaldehyde **242** with **26b** at 120 °C

Reagents used: 5 mg (0.005 mmol) **26b**, 150 mg (0.92 mmol) substrate, 190 mg (0.92 mmol) PhSiH₃ and 1.0 mL THF. The reaction afforded **310** (61%), **312** (17%), **313** (19%) and **316** (2%).

Anisaldehyde **317** with **26a** at 80 °C

Reagents used: 5 mg (0.005 mmol) **26a**, 124 mg (0.91 mmol) substrate, 98 mg (0.91 mmol) PhSiH₃ and 1.0 mL THF. The reaction afforded 4-methylanisole **318** (36%),³⁶³ 4-methoxybenzyl alcohol **319** (22%)³⁵⁴ and 1,2-bis(4-methoxyphenyl)ethane **320** (42%).³³⁵ The formation of the major products was also confirmed by their characteristic ¹H-NMR chemical shifts in CDCl₃. ¹H-NMR **318** (CDCl₃, 399.79 MHz) δ 2.30 (s, 3H, CH₃); **320** δ 2.84 (s, 4H, –CH₂CH₂–).

Anisaldehyde **317** with **26b** at 80 °C

Reagents used: 5 mg (0.005 mmol) **26a**, 62 mg (0.45 mmol) substrate, 50 mg (0.46 mmol) PhSiH₃ and 1.0 mL THF. The reaction afforded **318** (6%), **319** (68%), **320** (17%), **321** (7%)³⁶⁴ and **322** (2%).³⁶⁵ The formation of the major products was also confirmed by their characteristic ¹H-NMR

chemical shifts in CDCl_3 . $^1\text{H-NMR}$ **251** (CDCl_3 , 399.79 MHz) δ 2.30 (s, 3H, CH_3); **253** δ 2.84 (s, 4H, $-\text{CH}_2\text{CH}_2-$).

3,5-Dimethoxybenzaldehyde **99** by **26a** at 80 °C

Reagents used: 5 mg (0.005 mmol) **26a**, 50 mg (0.30 mmol) substrate, 32 mg (0.30 mmol) PhSiH_3 and 1.0 mL THF. The reaction afforded 3,5-dimethoxytoluene **323** (9%)³⁶⁶ and 3,5-dimethoxybenzyl alcohol **324** (91%).³⁶⁷ The formation of the major products was also confirmed by their characteristic $^1\text{H-NMR}$ chemical shifts in CDCl_3 . $^1\text{H-NMR}$ **323** (CDCl_3 , 399.79 MHz) δ 2.32 (s, 3H, CH_3); **324** δ 4.80 (s, 2H, $-\text{CH}_2-\text{O}$).

3,5-dimethoxybenzaldehyde **99** by **26b** at 80 °C

Reagents used: 5 mg (0.005 mmol) **26b**, 50 mg (0.30 mmol) substrate, 32 mg (0.30 mmol) PhSiH_3 and 1.0 mL THF. The reaction afforded **323** (5%), **324** (93%) and **325** (2%).³⁶⁸

4-(methylthio)benzaldehyde **87** with **26a**

Reagents used: 5 mg (0.005 mmol) **26a**, 35 mg (0.23 mmol) substrate, 25 mg (0.23 mmol) PhSiH_3 and 1.0 mL THF. The reaction afforded 4-(methylthio)toluene **321** (86%),³⁶⁹ 4-(methylthio)benzyl alcohol **322** (4%)³⁵⁸ and 1,2-bis(4-methylthiophenyl)ethane **323** (10%; $M^+ = 274$). The formation of the major products was also confirmed by their characteristic

¹H-NMR chemical shifts in CDCl₃. ¹H-NMR **321** (CDCl₃, 399.79 MHz) δ 2.33 (s, 3H, CH₃); **323** δ 2.84 (s, 4H, CH₂CH₂).

4-(methylthio)benzaldehyde **87** with **26b**

Reagents used: 5 mg (0.005 mmol) **26a**, 35 mg (0.23 mmol) substrate, 25 mg (0.23 mmol) PhSiH₃ and 1.0 mL THF. The reaction afforded **321** (20%), **322** (73%) and **323** (7%). The formation of the major products was also confirmed by their characteristic ¹H-NMR chemical shifts in CDCl₃. ¹H-NMR **262** (CDCl₃, 399.79 MHz) δ 4.77 (s, 2H, CH₂O).

Methyl 4-formylbenzoate **91** with **26a**

Reagents used: 5 mg (0.005 mmol) **26a**, 37 mg (0.23 mmol) substrate, 25 mg (0.23 mmol) PhSiH₃ and 1.0 mL THF. The reaction afforded methyl 4-methylbenzoate **326** (10%),³¹² methyl 4-(hydroxymethyl)benzoate **327** (63%),³⁷⁰ 4-methylbenzyl alcohol **328** (15%)³⁷¹ and 1,4-bis(hydroxymethyl)benzene **329** (12%).³⁷²

Methyl 4-formylbenzoate with **26b**

Reagents used: 5 mg (0.005 mmol) **26b**, 37 mg (0.23 mmol) substrate, 25 mg (0.23 mmol) PhSiH₃ and 1.0 mL THF. The reaction afforded **326** (7%) and **327** (93%).

Methyl 4-formylbenzoate with lower loading of PhSiH₃

Reagents used: 5 mg (0.005 mmol) **26b**, 37 mg (0.23 mmol) substrate, 13 mg (0.12 mmol) PhSiH₃ and 1.0 mL THF. The reaction afforded **326** (6%), **327** (71%), **328** (1%), **329** (1%), **330** (3%) and **331** (20%; M⁺ = 298).³⁷³

References

- (1) Vicic, D. A.; Jones, W. D. *J. Am. Chem. Soc.* **1999**, *121*, 7606–7617.
- (2) Startsev, A. N. *Catal. Rev.* **1995**, *37*, 353–423.
- (3) Fürstner, A. *Angew. Chem. Int. Ed. Engl.* **2009**, *48*, 1364–1367.
- (4) Bolm, C.; Legros, J.; Le Pailh, J.; Zani, L. *Chem. Rev.* **2004**, *104*, 6217–6254.
- (5) Ross, J. R. H. *Heterogeneous catalysis*; Elsevier Science Limited, 2011.
- (6) Catlow, C. R. A.; French, S. A.; Sokol, A. A.; Thomas, J. M. *Philosophical Transactions of the Royal Society A: Mathematical, Physical and Engineering Sciences* **2005**, *363*, 913–936.
- (7) Hansen, T. W. *Science* **2001**, *294*, 1508–1510.
- (8) Thomas, J. M.; Raja, R.; Lewis, D. W. *Angew. Chem. Int. Ed. Engl.* **2005**, *44*, 6456–6482.
- (9) Vicic, D. A.; Jones, W. D. *J. Am. Chem. Soc.* **1999**, *121*, 7606–7617.
- (10) Satterfield, C. N. *Heterogeneous Catalysis in Industrial Practice*; Krieger Publishing Company, 1991.
- (11) Rauchfuss, T. B. *Inorg. Chem.* **2004**, *43*, 14–26.
- (12) a) Puddephatt, R. J. In *Metal Clusters in Chemistry*; Wiley-VCH Verlag GmbH: Weinheim, Germany, 1999; pp. 604–615; b) Cotton, F. A. *Inorg. Chem.* **1964**, *3*, 1217.
- (13) Peri, J. B. *Catalyst Characterization Science: Surface and Solid State Chemistry* **1985**, *288*, 422.
- (14) Fout, A. R.; Basuli, F.; Fan, H.; Tomaszewski, J.; Huffman, J. C.; Baik, M.-H.; Mindiola, D. J. *Angew. Chem.* **2006**, *118*, 3369–3373.
- (15) Sánchez-Delgado, R. A. *J. Mol. Catal.* **1994**, *86*, 287–307.
- (16) Gates, B. C. *Chem. Rev.* **1995**, *95*, 511–522.
- (17) Bu, Q.; Lei, H.; Zacher, A. H.; Wang, L.; Ren, S.; Liang, J.; Wei, Y.; Liu, Y.; Tang, J.; Zhang, Q.; Ruan, R. *Bioresour. Technol.* **2012**, *124*, 470–477.
- (18) Hill, C. L.; Prosser-McCartha, C. M. *Coord. Chem. Rev.* **1995**, *143*, 407–455.
- (19) Holland, P. L. *Can. J. Chem.* **2005**, *83*, 296–301.
- (20) Fout, A. R.; Xiao, D. J.; Zhao, Q.; Harris, T. D.; King, E. R.; Eames, E. V.; Zheng, S.-L.; Betley, T. A. *Inorg. Chem.* **2012**, *51*, 10290–10299.
- (21) Pittman, C. U., Jr.; Ryan, R. C.; McGee, J.; O'Connor, J. P. *J. Organomet. Chem.* **1979**, *178*, C43–C49.
- (22) Muettterties, E. L. *Science* **1977**, *196*, 839–848.
- (23) Muettterties, E. L.; Krause, M. J. *Angew. Chem. Int. Ed. Engl.* **1983**, *22*, 135–148.

- (24) Lauher, J. W. *J. Am. Chem. Soc.* **1978**, *100*, 5305–5315.
- (25) Adams, R. D.; Horvth, I. T. In *Progress in Inorganic Chemistry*; Progress in Inorganic Chemistry; John Wiley & Sons, Inc.: Hoboken, NJ, USA, 1985; Vol. 33, pp. 127–181.
- (26) Macchi, P. *Coord. Chem. Rev.* **2003**, *238*-*239*, 383–412.
- (27) Dyson, P. J. *Coord. Chem. Rev.* **2004**, *248*, 2443–2458.
- (28) Femoni, C.; Iapalucci, M. C.; Kaswalder, F.; Longoni, G.; Zucchini, S. *Coord. Chem. Rev.* **2006**, *250*, 1580–1604.
- (29) Zhu, G.; Pang, K.; Parkin, G. *Inorg. Chim. Acta* **2008**, *361*, 3221–3229.
- (30) Riaz, U.; Curnow, O.; Curtis, M. D. *J. Am. Chem. Soc.* **1991**, *113*, 1416–1417.
- (31) Dyson, P. J.; McIndoe, J. S. *Transition Metal Carbonyl Cluster Chemistry*; Taylor & Francis, 2000.
- (32) Jackson, S. D.; Wells, P. B. *Platinum Met. Rev.* **1986**.
- (33) Beck, R.; Shoshani, M.; Johnson, S. A. *Angew. Chem.* **2012**, *124*, 11923-11926.
- (34) Matsubara, K.; Okamura, R.; Tanaka, M. *J. Am. Chem. Soc.* **1998**, *120*, 1108-1109.
- (35) Doi, Y.; Koshizuka, K.; Keii, T. *Inorg. Chem.* **1982**.
- (36) Ichikawa, M. *J. Catal.* **1979**, *59*, 67–78.
- (37) Alper, H.; Amaratunga, S. *Tetrahedron Lett.* **1980**, *21*, 2603–2604.
- (38) Laine, R. M.; Rinker, R. G.; Ford, P. C. *J. Am. Chem. Soc.* **1977**, *99*, 252-253.
- (39) van den Beuken, E. K.; Feringa, B. L. *Tetrahedron* **1998**, *54*, 12985–13011.
- (40) *Organometal Cluster Complexes*; Green, M., Ed. Royal Society of Chemistry: Cambridge, 2007; Vol. 33, pp. 179–229.
- (41) Thimmappa, B. H. S. *Coord. Chem. Rev.* **1995**, *143*, 1–34.
- (42) Vabrekamp, H. *Pure & Appl. Chem.* **1991**, *63*, 643-649.
- (43) Sivak, A. J.; Muettterties, E. L. *J. Am. Chem. Soc.* **1979**, *101*, 4878–4887.
- (44) Burch, R. R.; Muettterties, E. L.; Teller, R. G.; Williams, J. M. *J. Am. Chem. Soc.* **1982**, *104*, 4257–4258.
- (45) Thimmappa, B. H. S. *J. Clust. Sci.* **1996**, *7*, 1–36.
- (46) Muettterties, E. L.; Krause, M. J. *Angew. Chem.* **2006**, *95*, 135–148.
- (47) Zhao, Q.; Betley, T. A. *Angew. Chem. Int. Ed.* **2011**, *50*, 709–712.
- (48) Fout, A. R.; Zhao, Q.; Xiao, D. J.; Betley, T. A. *J. Am. Chem. Soc.* **2011**, *133*, 16750–16753.
- (49) Tsui, E. Y.; Day, M. W.; Agapie, T. *Angew. Chem.* **2011**, *123*, 1706–1710.
- (50) Powers, T. M.; Fout, A. R.; Zheng, S.-L.; Betley, T. A. *J. Am.*

- Chem. Soc.* **2011**, *133*, 3336–3338.
- (51) Cook, T. R.; Zheng, Y.-R.; Stang, P. J. *Chem. Rev.* **2013**, *113*, 734–777.
- (52) (1) Stephan, D. W. *Organometallics* **2005**, *24*, 2548–2560; (b) Steohan, D. W.; Stewart, J. C.; Guerin, F.; Courtenay, S.; Kickham, J.; Hollink, E.; Beddie, C.; Hoskin, A.; Graham, T.; Wei, P.; Spence, R. E. v. H.; Xu, W.; Koch, L.; Gao, X.; Harrison, D. G. *Organometallics*, **2003**, *22*, 1937–1947.
- (53) Gibson, V. C.; Spitzmesser, S. K. *Chem. Rev.* **2003**.
- (54) Brunelli, N. A.; Didas, S. A.; Venkatasubbaiah, K.; Jones, C. W. *J. Am. Chem. Soc.* **2012**, *134*, 13950–13953.
- (55) Müller, U.; Bock, O.; Sippel, H.; Gröb, T.; Dehnicke, K.; Greiner, A. Z. *Anorg. Allg. Chem.* **2002**, *628*, 1703.
- (56) Dehnicke, K.; Weller, F. *Coord. Chem. Rev.* **1997**, *158*, 103–169.
- (57) (a) Mai, H.-J.; zu Köcker, R. M.; Wocadlo, S.; Massa, W.; Dehnicke, K. *Angew. Chem. Int. Ed. Engl.* **1995**, *34*, 1235–1236; (b) Ackermann, H.; Leo, R.; Massa, W.; Neumüller, B.; Dehnicke, K. Z. *Anorg. Allg. Chem.* **2000**, *626*, 284–289; (c) Krieger, M.; Gould, R. O.; Neumüller, B.; Harms, K.; Dehnicke, K. Z. *Anorg. Allg. Chem.* **1998**, *624*, 1434–1442.
- (58) Sundermann, A.; Schoeller, W. W. *J. Am. Chem. Soc.* **2000**, *122*, 4729–4734.
- (59) Guérin, F.; Stewart, J. C.; Beddie, C.; Stephan, D. W. *Organometallics* **2000**, *19*, 2994–3000.
- (60) Schulz, S.; Raab, M.; Nieger, M.; Niecke, E. *Organometallics* **2000**, *19*, 2616–2620.
- (61) Dehnicke, K.; Krieger, M.; Massa, W. *Coord. Chem. Rev.* **1999**, *182*, 19–65.
- (62) Stephan, D.; Stewart, J.; Guérin, F.; Spence, R.; Wei Xu, A.; Harrison, D. G. *Organometallics* **1999**, *18*, 1116–1118.
- (63) Yue, N. L. S.; Stephan, D. W. *Organometallics* **2001**, *20*, 2303–2308.
- (64) Riese, U.; Faza, N.; Harms, K.; Massa, W.; Neumüller, B.; Dehnicke, K. *Phosphorus, Sulfur, and Silicon and the Related Elements* **1997**, *124*, 315–321.
- (65) Carraz, C.-A.; Stephan, D. W. *Organometallics* **2000**, *19*, 3791–3796.
- (66) LePichon, L.; Stephan, D. W.; Gao, X.; Wang, Q. *Organometallics* **2002**, *21*, 1362–1366.
- (67) Ong, C. M.; McKarns, P.; Stephan, D. W. *Organometallics* **1999**, *18*, 4197–4204.
- (68) Boese, R.; Harvey, D. F.; Malaska, M. J.; Volhardt, K. P. C. J. *Am. Chem. Soc.* **1994**, *116*, 11153–11154.
- (69) Stephan, D. W. In *Advances in Organometallic Chemistry*; Advances in Organometallic Chemistry; Elsevier, 2006; Vol. 54, pp. 267–291.

- (70) (a) Hebert, D. (Stryker Group) **2013**, Manuscript in preparation;
(b) Brown, H. (Stryker Group) **2013**, Manuscript in preparation;
Zhao, T. (Stryker Group) **2013**, Manuscript in preparation..
- (71) Laskowski, C. A.; Hillhouse, G. L. *J. Am. Chem. Soc.* **2008**, *130*, 13846–13847.
- (72) Laskowski, C. A.; Miller, A. J. M.; Hillhouse, G. L.; Cundari, T. R. *J. Am. Chem. Soc.* **2011**, *133*, 771–773.
- (73) Power, P. P. *J. Organomet. Chem.* **2004**, *689*, 3904–3919.
- (74) Ni, C.; Fettinger, J. C.; Long, G. J.; Power, P. P. *Inorg. Chem.* **2009**, *48*, 2443–2448.
- (75) Power, P. P. *Comments Inorg. Chem.* **1989**, *8*, 177–202.
- (76) Power, P. P. *Chem. Rev.* **2012**, *112*, 3482–3507.
- (77) Camacho-Bunquin, J.; Ferguson, M. J.; Stryker, J. M. *J. Am. Chem. Soc.* **2013**, *135*, 5537–5540.
- (78) Holland, P. L.; Cundari, T. R.; Perez, L. L.; Eckert, N. A.; Lachicotte, R. J. *J. Am. Chem. Soc.* **2002**, *124*, 14416–14424.
- (79) Chiang, K. P.; Barrett, P. M.; Ding, F.; Smith, J. M.; Kingsley, S.; Brennessel, W. W.; Clark, M. M.; Lachicotte, R. J.; Holland, P. L. *Inorg. Chem.* **2009**, *48*, 5106–5116.
- (80) Smith, J. M.; Lachicotte, R. J.; Holland, P. L. *Organometallics* **2002**, *21*, 4808–4814.
- (81) Ding, K.; Brennessel, W. W.; Holland, P. L. *J. Am. Chem. Soc.* **2009**, *131*, 10804–10805.
- (82) Poli, R. *Chem. Rev.* **1996**, *96*, 2135–2204.
- (83) Eppley, D. F.; Wolczanski, P. T.; Van Duyne, G. D. *Angew. Chem. Int. Ed. Engl.* **1991**, *30*, 584–585.
- (84) Laplaza, C. E.; Cummins, C. C. *Science* **1995**, *268*, 861–863.
- (85) Chen, B.; Dingerdissen, U.; Krauter, J. G. E.; Lansink Rotgerink, H. G. J.; Möbus, K.; Ostgard, D. J.; Panster, P.; Riermeier, T. H.; Seebald, S.; Tacke, T.; Trauthwein, H. *Appl. Catal., A, General* **2005**, *280*, 17–46.
- (86) Stanislaus, A.; Cooper, B. H. *Catal. Rev.* **1994**, *36*, 75–123.
- (87) Morris, R. H. *Chem. Soc. Rev.* **2009**, *38*, 2282.
- (88) Szymczak, N. K.; Tyler, D. R. *Coord. Chem. Rev.* **2008**, *252*, 212–230.
- (89) Vineyard, B. D.; Knowles, W. S.; Sabacky, M. J.; Bachman, G. L.; Weinkauff, D. J. *J. Am. Chem. Soc.* **1977**, *99*, 5946–5952.
- (90) van den Berg, M.; Minnaard, A. J.; Schudde, E. P.; van Eisch, J.; de Vries, H. M.; de Vries, J. G.; Feringa, B. L. *J. Am. Chem. Soc.* **2000**, *122*, 11539–11540.
- (91) Widegren, J. A.; Finke, R. G. *J. Mol. Catal. A: Chem.* **2003**, *191*, 187–207.
- (92) Gnanamgari, D.; Sauer, E. L. O.; Schley, N. D.; Butler, C.; Incarvito, C. D.; Crabtree, R. H. *Organometallics* **2009**, *28*, 321–325.
- (93) Church, T. L.; Andersson, P. G. *Coord. Chem. Rev.* **2008**, *252*,

- 513–531.
- (94) Roseblade, S. J.; Pfaltz, A. *Acc. Chem. Res.* **2007**, *40*, 1402–1411.
- (95) Dobereiner, G. E.; Nova, A.; Schley, N. D.; Hazari, N.; Miller, S. J.; Eisenstein, O.; Crabtree, R. H. *J. Am. Chem. Soc.* **2011**, *133*, 7547–7562.
- (96) Kluson, P.; Cerveny, L. *Appl. Catal., A, General* **1995**, *128*, 13–31.
- (97) Clapham, S. E.; Hadzovic, A.; Morris, R. H. *Coord. Chem. Rev.* **2004**, *248*, 2201–2237.
- (98) Shams, K. *Appl. Catal. A: General* **2004**, *258*, 227–234.
- (99) Lee, J. Y.; Raju, B.; Kumar, B. N.; Kumar, J. R.; Park, H. K.; Reddy, B. R. *Sep. Purif. Technol.* **2010**, *73*, 213–218.
- (100) Bernardis, F. L.; Grant, R. A.; Sherrington, D. C. *React. Funct. Polym.* **2005**, *65*, 205–217.
- (101) Stephan, D. W.; Erker, G. *Angew. Chem. Int. Ed. Engl.* **2009**, *49*, 46–76.
- (102) Stephan, D. W.; Greenberg, S.; Graham, T. W.; Chase, P.; Hastie, J. J.; Geier, S. J.; Farrell, J. M.; Brown, C. C.; Heiden, Z. M.; Welch, G. C.; Ullrich, M. *Inorg. Chem.* **2011**, *50*, 12338–12348.
- (103) Erős, G.; Mehdi, H.; Pápai, I.; Rokob, T. A.; Király, P.; Tárkányi, G.; Soós, T. *Angew. Chem.* **2010**, *122*, 6709–6713.
- (104) Enthaler, S.; Junge, K.; Beller, M. *Angew. Chem. Int. Ed.* **2008**, *47*, 3317–3321.
- (105) Sloan, M. F.; Matlack, A. S.; Breslow, D. S. *J. Am. Chem. Soc.* **1963**, *85*, 4014–4018.
- (106) Sergeev, A. G.; Webb, J. D.; Hartwig, J. F. *J. Am. Chem. Soc.* **2012**, *134*, 20226–20229.
- (107) Gray, J. I.; Russell, L. F. *J Am Oil Chem Soc* **1979**, *56*, 36–44.
- (108) Bullock, R. M. *Catalysis without Precious Metals*; Wiley-VCH, 2010.
- (109) Marko, L.; Bakos, J. J. *Organomet. Chem.* **1974**, *81*, 411–414.
- (110) Feder, H. M.; Halpern, J. *J. Am. Chem. Soc.* **1975**.
- (111) Harmon, R. E.; Gupta, S. K.; Brown, D. J. *Chem. Rev.* **1973**.
- (112) Rothwell, I. P. *Chem. Commun.* **1997**, *0*, 1331–1338.
- (113) SIEGEL, S. J. *Catal.* **1973**, *30*, 139–145.
- (114) Harman, W. H.; Peters, J. C. *J. Am. Chem. Soc.* **2012**, *134*, 5080–5082.
- (115) Vasudevan, K. V.; Scott, B. L.; Hanson, S. K. *Eur. J. Inorg. Chem.* **2012**, *2012*, 4898–4906.
- (116) Fouilloux, P. *Applied Catalysis*, **1983**, *8*, 1–42
- (117) De Thomas, W. R.; Hort, E. V. Catalyst comprising Raney nickel with adsorbed molybdenum compound. 4,153,578, 1979.
- (118) Adkins, H.; Billica, H. R. *J. Am. Chem. Soc.* **1948**, *70*, 695–698.
- (119) Brown, C. A. *J. Org. Chem.* **1970**, *35*, 1900–1904.

- (120) Brown, C. A.; Brown, H. C. *J. Am. Chem. Soc.* **1963**, *85*, 1003–1005.
- (121) Aller, B. V. *J. Appl. Chem.* **2007**, *7*, 130–134.
- (122) Alley, W. M.; Hamdemir, I. K.; Johnson, K. A.; Finke, R. G. *J. Mol. Catal. A: Chem.* **2010**, *315*, 1–27.
- (123) KROLL, W. J. *Catal.* **1969**, *15*, 281–288.
- (124) Waymouth, R.; Pino, P. *J. Am. Chem. Soc.* **1990**, *112*, 4911–4914.
- (125) Angulo, I. M.; Kluwer, A. M.; Bouwman, E. *Chem. Commun.* **1998**, *0*, 2689–2690.
- (126) Angulo, I. M.; Bouwman, E.; van Gorkum, R.; Lok, S. M.; Lutz, M.; Spek, A. L. *J. Mol. Catal. A: Chem.* **2003**, *202*, 97–106.
- (127) Hibino, T.; Makino, K.; Sugiyama, T.; Hamada, Y. *ChemCatChem* **2009**, *1*, 237–240.
- (128) Thomas, M. G.; Muettterties, E. L.; Day, R. O.; Day, V. W. *J. Am. Chem. Soc.* **1976**, *98*, 4645–4646.
- (129) Lochow, C. F.; Miller, R. G. *J. Org. Chem.* **1976**, *41*, 3020–3022.
- (130) Birdwhistell, K. R.; Lanza, J. *J. Chem. Ed.* **1997**, *74*, 579.
- (131) Lin, Y.; Finke, R. G. *Inorg. Chem.* **1994**, *33*, 4891–4910.
- (132) Crabtree, R. H. *Chem. Rev.* **2012**, *112*, 1536–1554.
- (133) Bayram, E.; Finke, R. G. *ACS Catal.* **2012**, *2*, 1967–1975.
- (134) Sonnenberg, J. F.; Coombs, N.; Dube, P. A.; Morris, R. H. *J. Am. Chem. Soc.* **2012**, *134*, 5893–5899.
- (135) Bayram, E.; Linehan, J. C.; Fulton, J. L.; Roberts, J. A. S.; Szymczak, N. K.; Smurthwaite, T. D.; Ozkar, S.; Balasubramian, M.; Finke, R. G. *J. Am. Chem. Soc.* **2011**, *133*, 18889–18902.
- (136) DFT Computational Method used: Generalized Gradient Approximation with the Perdew Burke–Ernzerhof exchange–correlation functional (GGA-PBE). The DFT calculations were conducted by a team of scientists at the National Institute of Nanotechnology. The study will be disclosed in due course.
- (137) Elias, X.; Pleixats, R.; Wong Chi Man, M. *Tetrahedron* **2008**, *64*, 6770–6781.
- (138) Kaafarani, B. R.; Wex, B.; Wang, F.; Catanescu, O.; Chien, L. C.; Neckers, D. C. *J. Org. Chem.* **2003**, *68*, 5377–5380.
- (139) Diver, S. T.; Giessert, A. *J. Chem. Rev.* **2004**, *104*, 1317–1382.
- (140) Ohmura, T.; Yorozuya, S.-I.; Yamamoto, Y.; Miyaura, N. *Organometallics* **2000**, *19*, 365–367.
- (141) Slugovc, C.; Mereiter, K.; Zobetz, E.; Schmid, R.; Kirchner, K. *Organometallics* **1996**, *15*, 5275–5277.
- (142) Chen, X.; Xue, P.; Sung, H. H. Y.; Williams, I. D.; Peruzzini, M.; Bianchini, C.; Jia, G. *Organometallics* **2005**, *24*, 4330–4332.
- (143) Murakami, M.; Ubukata, M.; Ito, Y. *Tetrahedron Lett.* **1998**, *39*, 7361–7364.
- (144) Walker, E. *Chem. Soc. Rev.* **1976**, *5*, 23–50.
- (145) Patai, S. *The Chemistry of Double-Bonded Functional Groups*;

- John Wiley & Sons, 1997.
- (146) Brieger, G.; Fu, T.-H. *J. Chem. Soc., Chem. Commun.* **1976**, 757a.
- (147) Andersson, P. G.; Munslow, I. *J. Modern Reduction Methods*; Wiley-VCH, 2008.
- (148) Marciniec, B. *Hydrosilylation*; Springer, 2009.
- (149) Roy, A. K. In *Adv. Organomet. Chem.* **2007**, 55, 1–59.
- (150) Clarson, S. J. *Silicon* **2009**, 1, 57–58.
- (151) Troegel, D.; Stohrer, J. *Coord. Chem. Rev.* **2011**, 255, 20–20.
- (152) Díez-González, S.; Nolan, S. P. *Org. Prep. Proced. Int.* **2007**, 39, 523–559.
- (153) Sabourault, N.; Mignani, G.; Wagner, A.; Mioskowski, C. *Org. Lett.* **2002**, 4, 2117–2119.
- (154) Clarke, M. L. *Polyhedron* **2001**, 20, 151–164.
- (155) Marciniec, B. *Hydrosilylation*; Springer, 2009.
- (156) Troegel; Stohrer *Coord. Chem. Rev.* **2011**, 255, 20–20.
- (157) Zuckerman, J. J. *Inorganic Reactions and Methods, Reactions Catalyzed by Inorganic Compounds*; Wiley-VCH, 2009.
- (158) Murahashi, S.-I. *Ruthenium in Organic Synthesis*; John Wiley & Sons, 2006.
- (159) Rudd, M. T.; Stanford University. Dept. of Chemistry *Ruthenium catalysis for atom economy*; 2004.
- (160) Mortreux, A.; Petit, F. *Industrial Applications of Homogeneous Catalysis*; Springer, 1988.
- (161) Riener, K.; Högerl, M. P.; Gigler, P.; Kühn, F. E. *ACS Catal.* **2012**, 2, 613–621.
- (162) Rivera; Elizalde; Roa; Montiel; Bernes *J. Organomet. Chem.* **2012**, 699, 5–5.
- (163) Krüger, A. A.; Albrecht, M. M. *Chem. Eur. J.* **2012**, 18, 652–658.
- (164) Egbert, J. D. J.; Nolan, S. P. S. *Chem. Commun.* **2012**, 48, 2794–2796.
- (165) Field, L. D.; Ward, A. J. *J. Organomet. Chem.* **2003**, 681, 91–97.
- (166) Malacea; Poli; Manoury *Coord. Chem. Rev.* **2010**, 254, 24–24.
- (167) Oro, L. A.; Claver, C. *Iridium Complexes in Organic Synthesis*; John Wiley & Sons, 2008.
- (168) Lambert, J. B.; Zhao, Y.; Wu, H. *Organometallics*, **1999**, 64, 2729–2736.
- (169) Yun, J.; Buchwald, S. L. *J. Am. Chem. Soc.* **1999**, 121, 5640–5644.
- (170) Štěpnička, P.; Gyepes, R.; Císařová, I.; Horáček, M.; Kubišta, J.; Mach, K. *Organometallics* **1999**, 18, 4869–4880.
- (171) Inagaki, T.; Phong, L. T.; Furuta, A.; Ito, J.-I.; Nishiyama, H. *Chem. Eur. J.* **2010**, 16, 3090–3096.
- (172) Tondreau, A. M.; Atienza, C. C. H.; Weller, K. J.; Nye, S. A.; Lewis, K. M.; Delis, J. G. P.; Chirik, P. J. *Science* **2012**, 335, 567–570.

- (173) Buitrago, E.; Tinnis, F.; Adolfsson, H. *Adv. Synth. Catal.* **2012**, *354*, 217–222.
- (174) Muraoka, T.; Shimizu, Y.; Kobayashi, H.; Ueno, K.; Ogino, H. *Organometallics* **2010**, *29*, 5423–5426.
- (175) Albright, A.; Gawley, R. E. *J. Am. Chem. Soc.* **2011**, *133*, 19680–19683.
- (176) Lipshutz, B. H.; Servesko, J. M.; Petersen, T. B.; Papa, P. P.; Lover, A. A. *Org. Lett.* **2004**, *6*, 1273–1275.
- (177) Lipshutz, B. H.; Noson, K.; Chrisman, W.; Lower, A. *J. Am. Chem. Soc.* **2003**, *125*, 8779–8789.
- (178) Lipshutz, B. H. B.; Lower, A. A.; Noson, K. K. *Org. Lett.* **2002**, *4*, 4045–4048.
- (179) Lipshutz, B. H.; Noson, K.; Chrisman, W. *J. Am. Chem. Soc.* **2001**, *123*, 12917–12918.
- (180) Sattler, W. W.; Parkin, G. G. *J. Am. Chem. Soc.* **2012**, *134*, 17462–17465.
- (181) Das, S. S.; Addis, D. D.; Junge, K. K.; Beller, M. M. *Chem. Eur. J.* **2011**, *17*, 12186–12192.
- (182) Junge, K. K.; Möller, K. K.; Wendt, B. B.; Das, S. S.; Gördes, D. D.; Thurow, K. K.; Beller, M. M. *Chem. Asian. J.* **2012**, *7*, 314–320.
- (183) Enthalter, S. S.; Eckhardt, B. B.; Inoue, S. S.; Irran, E. E.; Driess, M. M. *Chem. Asian. J.* **2010**, *5*, 2027–2035.
- (184) Sauer, D. C.; Wadeohl, H.; Gade, L. H. *Inorg. Chem.* **2012**, *51*, 12948–12958.
- (185) Yu, F.; Zhang, X.-C.; Wu, F.-F.; Zhou, J.-N.; Fang, W.; Wu, J.; Chan, A. S. C. *Org. Biomol. Chem.* **2011**, *9*, 5652.
- (186) Ojima, I.; Clos, N.; Donovan, R. J.; Ingallina, P. *Organometallics* **1990**, *9*, 3127–3133.
- (187) Inagaki, T.; Phong, L. T.; Furuta, A.; Ito, J.-I.; Nishiyama, H. *Chem. Eur. J.* **2010**, *16*, 3090–3096.
- (188) Kira, K.; Tanda, H.; Hamajima, A.; Baba, T.; Takai, S.; Isobe, M. *Tetrahedron* **2002**, *58*, 6485–6492.
- (189) Field, L. D.; Ward, A. J. *J. Organomet. Chem.* **2003**, *681*, 91–97.
- (190) Wu, F.-F. F.; Zhou, J.-N. J.; Fang, Q. Q.; Hu, Y.-H. Y.; Li, S. S.; Zhang, X.-C. X.; Chan, A. S. C. A.; Wu, J. *J. Chem. Asian. J.* **2012**, *7*, 2527–2530.
- (191) Kong; Kim; Choi; Choi *Tetrahedron Lett.* **2007**, *48*, 4–4.
- (192) Tran, B. L.; Pink, M.; Mindiola, D. J. *Organometallics* **2009**, *28*, 2234–2243.
- (193) Irrgang; Schareina; Kempe *J. Mol. Catal. A: Chem.* **2006**, *257*, 5–5.
- (194) Marciniec *Coord. Chem. Rev.* **2005**, *249*, 17–17.
- (195) Abbina, S.; Bian, S.; Oian, C.; Du, G. *ACS Catal.* **2013**, *3*, 678–684.
- (196) Yang, J.; Tilley, T. D. *Angew. Chem. Int. Ed.* **2010**.

- (197) Aiken, J. D., III; Finke, R. G. *J. Mol. Catal. A: Chem.* **1999**, *145*, 1–44.
- (198) Radu, N. S.; Hollander, F. J.; Tilley, T. D.; Rheingold, A. L. *Chem. Commun.* **1996**, 2459.
- (199) Khalimon, A. Y.; Simionescu, R.; Nikonov, G. I. *J. Am. Chem. Soc.* **2011**, *133*, 7033–7053.
- (200) Rosenberg, L.; Davis, C. W.; Yao, J. *J. Am. Chem. Soc.* **2001**, *123*, 5120–5121.
- (201) Abbina, S.; Bian, S.; Oian, C.; Du, G. *ACS Catal.* **2013**, *3*, 678–684.
- (202) Pecoraro, T. A.; Chianelli, R. R. *J. Catal.* **1981**, 1–16.
- (203) Sánchez-Delgado, R. *Organometallic Modeling of the Hydrodesulfurization and Hydrodenitrogenation Reactions*; Springer Netherlands, **2002**.
- (204) Abotsi, G. M. K.; Scaroni, A. W. *Fuel Process. Technol.* **1989**, *22*, 107–133.
- (205) Chianelli; Berhault; Torres *Catal. Today* **2009**, *147*, 12–12.
- (206) Eijsbouts; Mayo; Fujita *Appl. Catal. A* **2007**, *322*, 9–9.
- (207) Weber, T.; Prins, R.; van Santen, R. A. *Transitional Metal Sulphides*; Kluwer Academic Pub, 1998.
- (208) Eliel, E. L.; Krishnamurthy, S. *J. Org. Chem.* **1965**, *30*, 848–854..
- (209) Nagai, M.; Urimoto, H.; Uetake, K.; Sakikawa, N. *Bull. Chem. Soc. Jpn.* **1989**, *62*, 557–562.
- (210) Whalley, W. B.; Anderson, E. L.; Dugan, F.; Wilson, J. W.; Ullyot, G. E. *J. Am. Chem. Soc.* **1955**, *77*, 745–749.
- (211) Hauptmann, H.; Walter, W. F. *Chem. Rev.* **1962**, *62*, 347–404.
- (212) Topsoe, H.; Clausen, B. S.; Topsoe, N. Y.; Pedersen, E. *Ind. Eng. Chem. Fundam.* **1986**, *25*, 25–36.
- (213) Ho, *Catal. Today* **2004**, *98*, 16–16.
- (214) Vissers, J.; De Beer, V.; Prins, R. *J Chem Soc* **1987**.
- (215) Farag, H.; Whitehurst, D. D.; Sakanishi, K.; Mochida, I. *Catal. Today* **1999**, *50*, 9–17.
- (216) Duchet, J. C.; Van Oers, E. M.; De Beer, V.; Prins, R. *J. Catal.* **1983**.
- (217) (a) Vicic, D. A.; Jones, W. D. *Organometallics* **1998**, *17*, 3411–3413; (b) Torres-Nieto, J.; Brennessel, W. W.; Jones, W. D.; Garcia, J. J. *J. Am. Chem. Soc.* **2009**, *131*, 4120–4126.
- (218) Arévalo, A.; García, J. J. *Eur. J. Inorg. Chem.* **2010**.
- (219) Vicic, D. A.; Jones, W. D. *Organometallics* **1997**, *16*, 1912–1919.
- (220) Jones, W. D.; Chin, R. M. *J. Am. Chem. Soc.* **1994**.
- (221) Bianchini, C.; Jiménez, M. V.; Meli, A.; Moneti, S.; Patinec, V.; Vizza, F. *Organometallics* **1997**, *16*, 5696–5705..
- (222) Torres-Nieto, J.; Arévalo, A.; García, J. J. *Organometallics* **2007**, *26*, 2228–2233.
- (223) Herbst, K.; Monari, M.; Brorson, M. *Inorg. Chem.* **2002**, *41*, 1336–1338.

- (224) Angelici, R. J. *Bull. Soc. Chim. Belges* **2010**, *104*, 265–282.
- (225) Hernández, M.; Miralrio, G.; Arévalo, A.; Bernès, S.; García, J. J.; López, C.; Maitlis, P. M.; del Rio, F. *Organometallics* **2001**, *20*, 4061–4071.
- (226) Arévalo, A.; Bernès, S.; García, J. J.; Maitlis, P. M. *Organometallics* **1999**, *18*, 1680–1685.
- (227) Jones, W. D.; Chin, R. M. *J. Organomet. Chem.* **1994**.
- (228) Dullaghan, C. A.; Carpenter, G. B.; Sweigart, D. A.; Choi, D. S.; Lee, S. S.; Chung, Y. K. *Organometallics* **1997**, *16*, 5688–5695.
- (229) Zhang, X.; Dullaghan, C. A.; Watson, E. J.; Carpenter, G. B.; Sweigart, D. A. *Organometallics* **1998**, *17*, 2067–2075.
- (230) Myers, A. W.; Jones, W. D. *Organometallics* **1996**, *15*, 2905–2917.
- (231) Bianchini, C.; Jiménez, M. V.; Meli, A.; Moneti, S.; Vizza, F.; Herrera, V.; Sánchez-Delgado, R. A. *Organometallics* **1995**, *14*, 2342–2352.
- (232) Vicic, D. A.; Jones, W. D. *J. Am. Chem. Soc.* **1997**, *119*, 10855–10856.
- (233) Ogilvy, A. E.; Draganjac, M.; Rauchfuss, T. B.; Wilson, S. R. *Organometallics* **1988**, *7*, 1171–1177.
- (234) Gol'dfarb, Y. L.; Belen'kii, L. I. *Russ. Chem. Bull.* **1984**, *33*, 178–194.
- (235) Benaglia; Guizzetti; Pignataro *Coord. Chem. Rev.* **2008**, *252*, 21–21.
- (236) Chuit, C.; Corriu, R.; Reye, C.; Young, J. C. *Chem. Rev.* **1993**.
- (237) Fedorov, A.; Toutov, A. A.; Swisher, N. A.; Grubbs, R. H. *Chem. Sci.* **2013**, *4*, 1640–1645.
- (238) Fiorucci, A. R.; de Paula, L. R.; Neves, E. A.; Cavalheiro, É. T. G. *J. Chem. Eng. Data* **2002**, *47*, 1510–1513.
- (239) Studer, A.; Curran, D. P. *Angew. Chem. Int. Ed.* **2011**, *50*, 5018–5022.
- (240) For studies on Group I cation effects, see: Smithson, H.; Marianetti, C.; Morgan, D.; Van der Ven, A.; Predith, A.; Ceder, G. *Phys. Rev. B* **2002**, *66*, 144107 and references therein; (b) Solís-Casados, D.; Escobar, J.; Orozco, I. G.; Klimova, T. *Ind. Eng. Chem. Res.* **2011**, *50*, 2755–2761, and references therein.
- (241) Toulhoat, H.; Raybaud, P.; Kasztelan, S.; Kresse, G. *Catal. Today* **1999**.
- (242) Guo, L. J. *Phys. Chem. A* **2013**, *117*, 3458–3466.
- (243) Previtali, C. M. *Pure Appl. Chem.* **1995**, *67*, 127–134.
- (244) Riese, U.; Faza, N.; Massa, W.; Dehncke, K. *Angew. Chem. Int. Ed. Engl.* **1999**, *38*, 528–531.
- (245) Eisch, J. J. J.; Hallenbeck, L. E. L.; Han, K. I. K. *J. Am. Chem. Soc.* **1986**, *108*, 7763–7767.
- (246) Eisch, J. J.; Hallenbeck, L. E.; Han, K. I. *J. Org. Chem.* **1983**, *48*:18.

- (247) Klusener, P. A. A.; Brandsma, L.; Verkruissse, H. D.; Ragué Schleyer, von, P.; Friedl, T.; Pi, R. *Angew. Chem. Int. Ed. Engl.* **1986**, *25*, 465–466.
- (248) Knöpke, L. R.; Nemati, N.; Köckritz, A.; Brückner, A.; Bentrup, U. *ChemCatChem* **2010**, *2*, 273–280.
- (249) Bayram, E.; Linehan, J. C.; Fulton, J. L.; Roberts, J. A. S.; Szymczak, N. K.; Smurthwaite, T. D.; Özkar, S.; Balasubramanian, M.; Finke, R. G. *J. Am. Chem. Soc.* **2011**, *133*, 18889–18902.
- (250) Sattler, J. J. H. B.; Beale, A. M.; Weckhuysen, B. M. *CORD Conference Proceedings* **2013**, *15*, 12095–12103.
- (251) Deutsch, K. L.; Shanks, B. H. *Appl. Catal. A* **2012**, *447*-448, 144–150.
- (252) Choudhary, T. V.; Phillips, C. B. *Appl. Catal. A* **2011**, *397*, 1–12.
- (253) Ho, T. C. *Catal. Rev.* **1988**, *30*, 117–160.
- (254) Furimsky, E.; Massoth, F. E. *Catal. Rev.* **2005**, *47*, 297–489.
- (255) Fout, A.; Bailey, B. C.; Tomaszewski, J.; Mindiola, D. J. *J. Am. Chem. Soc.* **2007**, *129*, 12640–12641.
- (256) Bianchini, C.; Meli, A.; Vizza, F. *Eur. J. Inorg. Chem.* **2001**, *2001*, 43–68.
- (257) Roddy, D. J. *Biomass and Biofuels – Introduction*; Elsevier Ltd., 2012; Vol. 5, pp. 1–10.
- (258) Corma, A.; Iborra, S.; Velty, A. *Chem. Rev.* **2007**, *107*, 2411–2502.
- (259) Huber, G. W.; Iborra, S.; Corma, A. *Chem. Rev.* **2006**, *106*, 4044–4098.
- (260) Bu, Q.; Lei, H.; Zacher, A. H.; Wang, L.; Ren, S.; Liang, J.; Wei, Y.; Liu, Y.; Tang, J.; Zhang, Q.; Ruan, R. *Bioresour. Technol.* **2012**, *124*, 470–477.
- (261) Rodrigues Pinto, P. C.; Borges da Silva, E. A.; Rodrigues, A. E. in *Biomass Conversion: The Interface of Biotechnology, Chemistry and Materials Science*, Springer Berlin Heidelberg: Berlin, Heidelberg, **2012**; pp. 381–420.
- (262) Mullen, C. A.; Strahan, G. D.; Boateng, A. A. *Energy Fuels* **2009**, *23*, 2707–2718.
- (263) Ren, H.; Yu, W.; Salciccioli, M.; Chen, Y.; Huang, Y.; Xiong, K.; Vlachos, D. G.; Chen, J. G. *ChemSusChem* **2013**, *6*, 798–801.
- (264) Furimsky, E. *Appl. Catal. A* **2000**, *199*, 147–190.
- (265) Maercker, A. *Angew. Chem. Int. Ed. Engl.* **1987**, *26*, 972–989.
- (266) Kennedy, A. R.; Klett, J.; Mulvey, R. E.; Wright, D. S. *Science* **2009**, *326*, 706–708.
- (267) Dabo, P.; Cyr, A.; Lessard, J.; Brossard, L.; Menard, H. *Can. J. Chem.* **1999**, *77*, 1225–1229.
- (268) Wenkert, E.; Michelotti, E. L.; Swindell, C. S. *J. Am. Chem. Soc.* **1979**, *101*, 2246–2247.
- (269) Wenkert, E.; Michelotti, E. L.; Swindell, C. S.; Tingoli, M. *J. Org.*

- Chem.* **1984**, *49*, 4894–4899.
(270) Álvarez-Bercedo, P.; Martin, R. *J. Am. Chem. Soc.* **2010**, *132*, 17352–17353.
- (271) Yu, D.; Li, B.; Shi, Z. *Acc. Chem. Res.* **2010**, *43*, 1486–1495.
(272) Guan, B.-T.; Xiang, S.-K.; Wang, B.-Q.; Sun, Z.-P.; Wang, Y.; Zhao, K.-Q.; Shi, Z.-J. *J. Am. Chem. Soc.* **2008**, *130*, 3268–3269.
- (273) Sergeev, A. G.; Hartwig, J. F. *Science* **2011**.
- (274) For experimental papers on Ni-catalyzed aryl ether activation,
see: (a) Kelley, P.; Lin, S.; Edouard, G.; Day, M. W.; Agapie, T. *J. Am. Chem. Soc.* **2012**, *134*, 5480–5483; (b) Cornell, J.; Gomez-Bengoa, E.; Martin, R. *J. Am. Chem. Soc.* **2013**, *135*, 1997–2009.
- (275) For computational papers on Ni-catalyzed aryl ether activation,
see: (a) Quasdorf, K. W.; Antoft-Finch, A.; Liu, P.; Silberstein, A. L.; Komaromi, A.; Blackburn, T.; Ramgren, S. D.; Houk, K. N.; Snieckus, V.; Garg, N. K. *J. Am. Chem. Soc.* **2011**, *133*, 6352–6363; (b) Li, Z.; Zhang, S.-L.; Fu, Y.; Guo, Q.-X.; Liu, L. *J. Am. Chem. Soc.* **2009**, *131*, 8815.
- (276) Huang, J.-M.; Lin, Z.-Q.; Chen, D.-S. *Org. Lett.* **2012**, *14*, 22–25.
- (277) Gladysz, J. A.; Fulcher, J. G.; Togashi, S. *J. Org. Chem.* **1976**, *41*, 3647–3648.
- (278) Noujima, A.; Mitsudome, T.; Mizugaki, T.; Jitsukawa, K.; Kaneda, K. *Molecules* **2011**, *16*, 8209–8227.
- (279) Zhao; Prins *J. Catal.* **2004**, *222*, 13–13.
- (280) Laine, R. M. *Modeling Heterogeneous Catalysts with Homogeneous Catalysts: Modeling the Hydrodenitrogenation Reaction*; **1983**.
- (281) Weller, K. J.; Fox, P. A.; Gray, S. D.; Wigley, D. E. *Polyhedron* **1997**.
- (282) Weller, K. J.; Filippov, I.; Briggs, P. M.; Wigley, D. E. *Organometallics* **1998**, *17*, 322–329.
- (283) Bonanno, J. B.; Veige, A. S.; Wolczanski, P. T.; Lobkovsky, E. B. *Inorg. Chim. Acta* **2003**, *345*, 173–184.
- (284) Anthis, J. W.; Filippov, I.; Wigley, D. E. *Inorg. Chem.* **2004**, *43*, 716–724.
- (285) Tayebani, M.; Gambarotta, S.; Yap, G. P. A. *Angew. Chem. Int. Ed. Engl.* **1998**, *37*, 3002–3005.
- (286) Laine, R. M.; Thomas, D. W.; Cary, L. W. *J. Org. Chem.* **1979**, *44*, 4964–4966.
- (287) Jacob, J.; Jones, W. D. *J. Org. Chem.* **2003**, *68*, 3563–3568.
- (288) Sakanishi, K.; Ohira, M.; Mochida, I.; Okazaki, H.; Soeda, M. *J. Chem. Soc., Perkin Trans. 2* **1988**, 1769.
- (289) Adkins, H.; Coonradt, H. L. *J. Am. Chem. Soc.* **1941**, *63*, 1563–1570.
- (290) Borowski, A. F. A.; Vendier, L. L.; Sabo-Etienne, S. S.; Rozyczka-Sokolowska, E. E.; Gaudyn, A. V. A. *Dalton Trans.* **2012**, *41*, 14117–14125.

- (291) Prins; Egorova; Rothlisberger; Zhao; Sivasankar; Kukula *Catal. Today* **2006**, 111, 10–10.
- (292) Lewandowski, M.; Sarbak, Z. *Fuel* **2000**, 79, 487–495.
- (293) Maity, S. K.; Lemus, M.; Ancheyta, J. *Energy Fuels* **2011**, 25, 3100–3107.
- (294) McMurry, J. E.; Kees, K. L. *J. Org. Chem.* **1977**, 42, 2655–2656.
- (295) Burdon, J.; Price, R. C. *J. Chem. Soc., Chem. Commun.* **1986**, 893–894.
- (296) Taber, D. F.; Stachel, S. J. *Tetrahedron Lett.* **1992**, 33, 903–906.
- (297) Szmant, H. H. *Angew. Chem. Int. Ed. Engl.* **1968**, 7, 120–128.
- (298) Bashore, C. G.; Samardjiev, I. J.; Bordner, J.; Coe, J. W. *J. Am. Chem. Soc.* **2003**, 125, 3268–3272
- (299) Brewster, J. H. *J. Am. Chem. Soc.* **1954**, 76, 6364–6368.
- (300) Di Vona, M. L.; Floris, B.; Luchetti, L.; Rosnati, V. *Tetrahedron Lett.* **1990**, 31, 6081–6084.
- (301) Nakabayashi, T. *J. Am. Chem. Soc.* **1960**, 82, 3906–3908.
- (302) Nakabayashi, T. *J. Am. Chem. Soc.* **1960**, 82, 3909–3913.
- (303) Sakai, N.; Nagasawa, K.; Ikeda, R.; Nakaike, Y.; Konakahara, T. *Tetrahedron Lett.* **2011**, 52, 3133–3136.
- (304) Kogan, V.; Aizenshtat, Z.; Neumann, R. *Angew. Chem. Int. Ed.* **1999**, 38, 3331–3334.
- (305) Murry, J. E. *Chem. Rev.* **1989**, 89, 1513–1524.
- (306) Chauhan, B. P. S. B.; Rathore, J. S. J.; Bandoo, T. T. *J. Am. Chem. Soc.* **2004**, 126, 8493–8500.
- (307) Rahaim, R. J.; Maleczka, R. E. *Org. Lett.* **2011**, 13, 584–587.
- (308) Mitchell, R. H.; Lai, Y.-H. *Tetrahedron Lett.* **1980**, 21, 2637–2638.
- (309) Zuidema, D. R.; Williams, S. L.; Wert, K. J.; Bosma, K. J.; Smith, A. L.; Mebane, R. C. *Synt. Comm.* **2011**, 41, 2927–2931.
- (310) Chung, M.-K.; Qi, G.; Stryker, J. M. *Org. Lett.* **2006**, 8, 1491–1494.
- (311) Delaude; Demonceau; Noels *Coord. Chem. Rev.* **2004**, 248, 14–14.
- (312) Diéguez, H. R.; López, A.; Domingo, V.; Arteaga, J. F.; Dobado, J. A.; Herrador, M. M.; Quílez del Moral, J. F.; Barrero, A. F. *J. Am. Chem. Soc.* **2010**, 132, 254–259.
- (313) Kačík, F.; Veľková, V.; Šmíra, P.; Nasswettrová, A.; Kačíková, D.; Reinprecht, L. *Molecules* **2012**, 17, 9990–9999.
- (314) Bouvier-Brown, N. C.; Holzinger, R.; Palitzsch, K.; Goldstein, A. *H. J. Chrom. A* **2007**, 1161, 113–120.
- (315) Candy, J.-P.; Didillon, B.; Smith, E. L.; Shay, T. B.; Basset, J.-M. *J. Mol. Catal.* **1994**, 86, 179–204.
- (316) (a) Evans, D. F. *J. J. Chem. Soc.* **1959**, 2003–2005; (b) Live, D. H.; Chan, S. I. *Anal. Chem.* **1970**, 42, 791–792.; (c) Schubert, E. M. *J. Chem. Educ.* **1992**, 69, 62.
- (317) Eisch, J. J.; Dutta, S. *Organometallics* **2005**, 24, 3355–3358.
- (318) Gerdov, S. M.; Grishin, Y. K.; Roznyatovsky, V. A.; Ustyuk, Y.

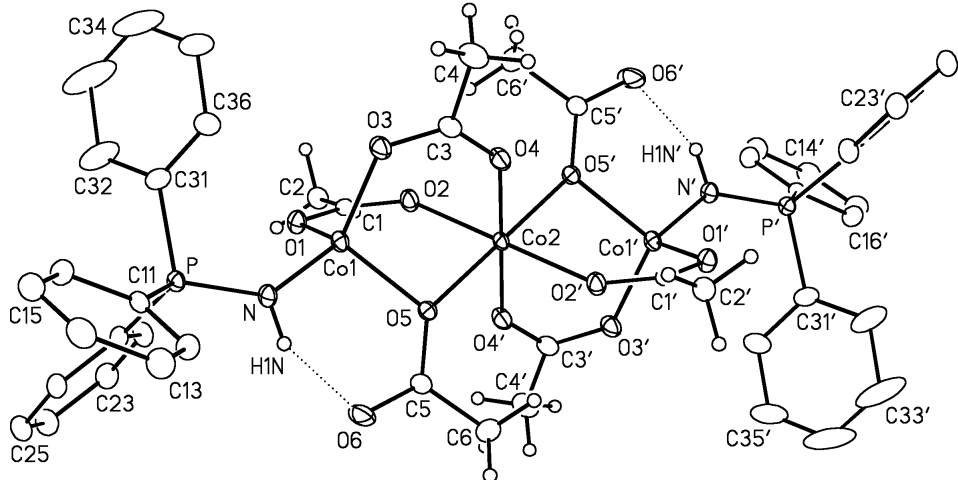
- A.; Kuchin, A. V.; Alekseev, I. N.; Frolova, L. L. *Russ. Chem. Bull.* **2005**, *54*, 1258–1265.
- (319) Gonçalves, J. A.; da Silva, M. J.; Piló-Veloso, D.; Howarth, O. W.; Gusevskaya, E. V. *J. Organomet. Chem.* **2005**, *690*, 2996–3003.
- (320) Spallek, M. J.; Stockinger, S.; Goddard, R.; Trapp, O. *Adv. Synth. Catal.* **2012**, *354*, 1466–1480.
- (321) Nador, F.; Moglie, Y.; Vitale, C.; Yus, M.; Alonso, F.; Radivoy, G. *Tetrahedron* **2010**, *66*, 4318–4325.
- (322) Yoshida, K.; Morimoto, I.; Mitsudo, K.; Tanaka, H. *Tetrahedron* **2008**, *64*, 5800–5807.
- (323) Lee, J.-H.; Caulton, K. G. *J. Organomet. Chem.* **2008**, *693*, 1664–1673.
- (324) Saraev, V. V.; Kraikivskii, P. B.; Vilms, A. I.; Zelinskii, S. N.; Yunda, A. Y.; Danilovtseva, E. N.; Kuzakov, A. S. *Kinet. Catal.* **2007**, *48*, 778–784.
- (325) Spielmann, J.; Harder, S. *Eur. J. Inorg. Chem.* **2008**, *2008*, 1480–1486.
- (326) Bramborg, A.; Linker, T. *Adv. Synth. Catal.* **2010**, *352*, 2195–2199..
- (327) Furukawa, S.; Kitagawa, S. *Inorg. Chem.* **2004**, *43*, 6464–6472.
- (328) Maegawa, T.; Takahashi, T.; Yoshimura, M.; Suzuka, H.; Monguchi, Y.; Sajiki, H. *Adv. Synth. Catal.* **2009**, *351*, 2091–2095.
- (329) Alacid, E.; Nájera, C. *Adv. Synth. Catal.* **2006**, *348*, 2085–2091..
- (330) Bei, X.; Hagemeyer, A.; Volpe, A.; Saxton, R.; Turner, H.; Guram, A. S. *J. Org. Chem.* **2004**, *69*, 8626–8633.
- (331) Zhao, B.; Lu, X. *Tetrahedron Lett.* **2006**, *47*, 6765–6768.
- (332) Díez-González, S.; Nolan, S. P. *Org. Prep. Proced. Int.* **2007**, *39*, 523–559.
- (333) Bart, S. C.; Lobkovsky, E.; Chirik, P. J. *J. Am. Chem. Soc.* **2004**, *126*, 13794–13807.
- (334) Konkol, M.; Kondracka, M.; Voth, P.; Spaniol, T. P.; Okuda, J. *Organometallics* **2008**, *27*, 3774–3784.
- (335) Oh, K.-B.; Kim, S.-H.; Lee, J.; Cho, W.-J.; Lee, T.; Kim, S. J. *Med. Chem.* **2004**, *47*, 2418–2421.
- (336) Kumar, V. K. R.; Gopidas, K. R. *Tetrahedron Lett.* **2011**, *52*, 3102–3105.
- (337) Lion, C. J.; Matthews, C. S.; Stevens, M. F. G.; Westwell, A. D. J. *Med. Chem.* **2005**, *48*, 1292–1295.
- (338) Bai, L.; Wang, J.-X. *Adv. Synth. Catal.* **2008**, *350*, 315–320.
- (339) Janarthanan, S.; Samuel, R. S.; Selvakumar, S.; Rajan, Y. C.; Jayaraman, D.; Pandi, S. *J. of Mat. Sci. and Tech.* **2011**, *27*, 271–274.
- (340) Gozzo, F. C.; Fernandes, S. A.; Rodrigues, D. C.; Eberlin, M. N.; Marsaioli, A. J. *J. Org. Chem.* **2003**, *68*, 5493–5499.

- (341) Meece, F. A.; Jayasinghe, C.; Histand, G.; Burns, D. H. *J. Org. Chem.* **2009**, *74*, 3156–3159.
- (342) Wang, C.; Piel, I.; Glorius, F. *J. Am. Chem. Soc.* **2009**, *131*, 4194–4195.
- (343) Zhang, J.; Zhang, Z.; Wang, Y.; Zheng, X.; Wang, Z. *Eur. J. Org. Chem.* **2008**, *2008*, 5112–5116.
- (344) Abraham, R. J.; Canton, M.; Griffiths, L. *Magn. Reson. Chem.* **2001**, *39*, 421–431.
- (345) Li, D.; Hopson, R.; Li, W.; Liu, J.; Williard, P. G. *Org. Lett.* **2008**, *10*, 909–911.
- (346) Yang, Q.; Ma, S.; Li, J.; Xiao, F.; Xiong, H. *Chem. Commun.* **2006**, *2495*.
- (347) Spielmann, J.; Buch, F.; Harder, S. *Angew. Chem. Int. Ed.* **2008**, *47*, 9434–9438.
- (348) Kitawaki, T.; Hayashi, Y.; Ueno, A.; Chida, N. *Tetrahedron* **2006**, *62*, 6792–6801.
- (349) Androsov, D. A.; Neckers, D. C. *J. Org. Chem.* **2007**, *72*, 1148–1152.
- (350) Manolikakes, G.; Muñoz Hernandez, C.; Schade, M. A.; Metzger, A.; Knochel, P. *J. Org. Chem.* **2008**, *73*, 8422–8436.
- (351) Prinsell, M. R.; Everson, D. A.; Weix, D. J. *Chem. Commun.* **2010**, *46*, 5743.
- (352) Arizaga, B.; de Leon, A.; Burgueño, N.; López, A.; Paz, D.; Martínez, N.; Lorenzo, D.; Dellacassa, E.; Bussi, J. *J. Chem. Technol. Biotechnol.* **2007**, *82*, 532–538.
- (353) Shoppee, C. W.; Henderson, G. N. *J. Chem. Soc., Perkin Trans. 1* **1975**, *765*.
- (354) Cano, R.; Yus, M.; Ramón, D. J. *Tetrahedron* **2011**, *67*, 8079–8085.
- (355) Galdi, N.; Izzo, L.; Oliva, L. *Organometallics* **2010**, *29*, 4434–4439.
- (356) Cao, L.; Ding, J.; Gao, M.; Wang, Z.; Li, J.; Wu, A. *Org. Lett.* **2009**, *11*, 3810–3813.
- (357) Fowley, L. A.; Lee, J. C.; Crabtree, R. H.; Siegbahn, P. E. M. *J. Organomet. Chem.* **1995**, *504*, 57–67.
- (358) Shaikh, N. S.; Junge, K.; Beller, M. *Org. Lett.* **2007**, *9*, 5429–5432.
- (359) Katritzky, A. R.; Lang, H.; Lan, X. *Tetrahedron*, **1993**, *49*, 7445–7454.
- (360) Kumar, A.; Maurya, R. A. *Tetrahedron Lett.* **2008**, *49*, 5471–5474.
- (361) Amatore, M.; Gosmini, C. *Chem. Commun.* **2008**, *5019*.
- (362) Avery, M. A.; Muraleedharan, K. M.; Desai, P. V.; Bandyopadhyaya, A. K.; Furtado, M. M.; Tekwani, B. L. *J. Med. Chem.* **2003**, *46*, 4244–4258.
- (363) Mirza-Aghayan, M.; Boukherroub, R.; Rahimifard, M. J.

- Organomet. Chem.* **2008**, *693*, 3567–3570.
(364) Rauniar, V.; Zhai, H.; Hall, D. G. *J. Am. Chem. Soc.* **2008**, *130*, 8481–8490.
(365) Wilsily, A.; Nguyen, Y.; Fillion, E. *J. Am. Chem. Soc.* **2009**, *131*, 15606–15607.
(366) Mondal, M.; Puranik, V. G.; Argade, N. P. *J. Org. Chem.* **2007**, *72*, 2068–2076.
(367) Tanaka, A.; Arai, Y.; Kim, S.-N.; Ham, J.; Usuki, T. *J. Asian Nat. Prod. Res.* **2011**, *13*, 290–296.
(368) Saa, J. M.; Dopico, M.; Martorell, G.; Garcia-Raso, A.; *J. Org. Chem.* **1990**, *55*, 991–995.
(369) Egami, H.; Katsuki, T. *J. Am. Chem. Soc.* **2007**, *129*, 8940–8941.
(370) Miyamoto, K.; Tada, N.; Ochiai, M. *J. Am. Chem. Soc.* **2007**, *129*, 2772–2773.
(371) Mino, T.; Hasegawa, T.; Shirae, Y.; Sakamoto, M.; Fujita, T. *J. Organomet. Chem.* **2007**, *692*, 4389–4396.
(372) Eißler, S.; Bogner, T.; Nahrwold, M.; Sewald, N. *Chem. Eur. J.* **2009**, *15*, 11273–11287.
(373) Belletire, J. L.; Spletzer, E. G. *Synt. Comm.* **1986**, *16*, 575–584.

Appendix

Crystallographic Information for Complex **13**. University of Alberta
Department of Chemistry Structure Determination Laboratory Report
#JMS0965r.



Perspective view of the $[\text{Co}_3(\text{OAc})_6(\text{HN}=\text{PPh}_3)_2]$ molecule showing the atom-labeling scheme. Non-hydrogen atoms are represented by Gaussian ellipsoids at the 20% probability level. Hydrogen atoms are shown with arbitrarily small thermal parameters except for phenyl group hydrogens, which are not shown. Primed atoms are related to unprimed ones via the crystallographic inversion center $(\frac{1}{2}, \frac{1}{2}, 0)$ upon which the Co_2 atom is located.

A. Crystal Data

formula	$\text{C}_{55}\text{H}_{58}\text{Co}_3\text{N}_2\text{O}_{12}\text{P}_2$
formula weight	1177.76
crystal dimensions (mm)	0.46 ' 0.19 ' 0.11
crystal system	monoclinic
space group	$I\bar{2}/a$ (an alternate setting of $C2/c$)
[No. 15])	
unit cell parameters ^a	
a (Å)	24.0364 (19)
b (Å)	8.5878 (7)
c (Å)	26.441 (2)
β (deg)	100.6036 (10)
V (Å ³)	5364.7 (7)
Z	4
r_{calcd} (g cm ⁻³)	1.458
μ (mm ⁻¹)	1.040

B. Data Collection and Refinement Conditions

diffractometer	Bruker D8/APEX II CCD ^b
radiation (λ [Å])	graphite-monochromated Mo K α
(0.71073)	
temperature (°C)	-100
scan type	w scans (0.3°) (20 s exposures)
data collection 2 q limit (deg)	52.88
total data collected	20881 (-30 ≤ h ≤ 30, -10 ≤ k ≤ 10, -33 ≤ l ≤ 33)
independent reflections	5515 ($R_{\text{int}} = 0.0295$)
number of observed reflections (NO)	4513 [$F_0^2 \geq 2s(F_0^2)$]
structure solution method	direct methods (<i>SHELXS-97^c</i>)
refinement method	full-matrix least-squares on F^2 (<i>SHELXL-97^c</i>)
absorption correction method indexed)	Gaussian integration (face-
range of transmission factors	0.8924–0.6473
data/restraints/parameters	5515 [$F_0^2 \geq -3s(F_0^2)$] / 4 ^d / 318
goodness-of-fit (S) ^e	1.068 [$F_0^2 \geq -3s(F_0^2)$]
final R indices ^f	
R_1 [$F_0^2 \geq 2s(F_0^2)$]	0.0520
wR_2 [$F_0^2 \geq -3s(F_0^2)$]	0.1516
largest difference peak and hole	1.849 and -1.095 e Å ⁻³

^aObtained from least-squares refinement of 9905 reflections with 5.00° < 2 q < 52.88°.

^bPrograms for diffractometer operation, data collection, data reduction and absorption correction were those supplied by Bruker.

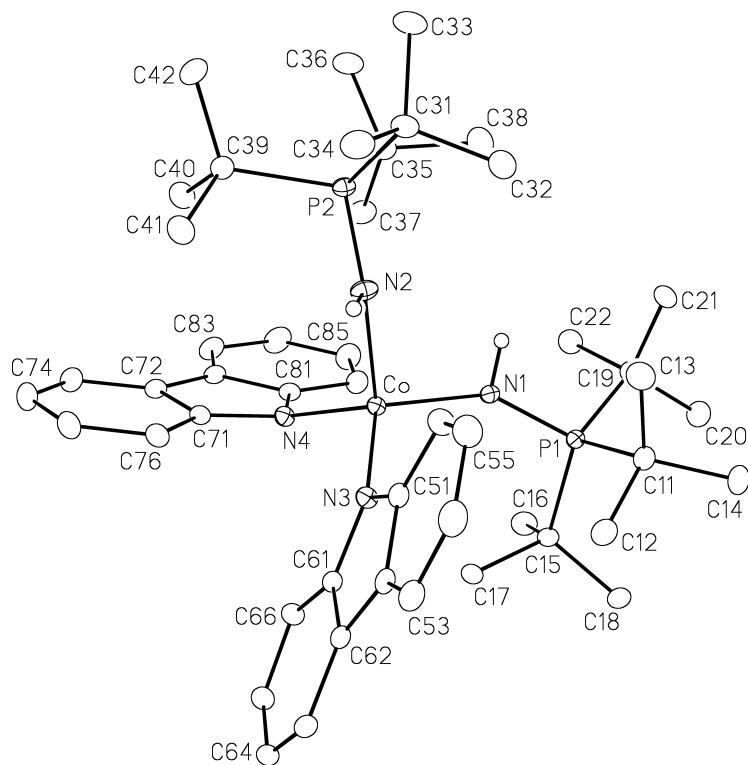
^cSheldrick, G. M. *Acta Crystallogr.* **2008**, A64, 112–122.

^dDistances involving the methyl carbon of the disordered solvent toluene molecule were given fixed idealized values during refinement: d(C1S–C7S) = 1.50(1) Å; d(C2S···C7S) = d(C6S···C7S) = 2.50(1) Å. The methyl carbon (C7S) was restrained to be coplanar with the atoms C1S, C2S, and C3S during refinement (i.e. by defining the C1S, C2S, C3S, and C7S atoms to be the vertices of a tetrahedron that was not to exceed a volume of 0.01 Å³). The ring carbons of the solvent toluene molecule were defined as a regular hexagon with d(C–C) = 1.39 Å and C–C–C angles of 120°.

^e $S = [\sum w(F_0^2 - F_C^2)^2/(n - p)]^{1/2}$ (n = number of data; p = number of parameters varied;
 $w = [s^2(F_0^2) + (0.0913P)^2 + 13.0782P]^{-1}$ where $P = [\text{Max}(F_0^2, 0) + 2F_C^2]/3$).

^f $R_1 = S||F_0|| - |F_C||/S|F_0|$; $wR_2 = [\sum w(F_0^2 - F_C^2)^2/\sum w(F_0^4)]^{1/2}$.

Crystallographic Information for Complex 17. University of Alberta
 Department of Chemistry Structure Determination Laboratory Report
 #JMS1064.



Perspective view of the $[\text{Co}(\text{HNPTBu}_3)_2(\text{carbazol-9-yl})_2]$ molecule showing the atom-labeling scheme. Non-hydrogen atoms are represented by Gaussian ellipsoids at the 20% probability level. Hydrogen atoms attached to nitrogens are shown with arbitrarily small thermal parameters; all other hydrogens are not shown.

Crystallographic Experimental Details

A. Crystal Data

formula	$\text{C}_{48}\text{H}_{72}\text{CoN}_4\text{P}_2$
formula weight	825.97
crystal dimensions (mm)	0.56 ' 0.41 ' 0.13
crystal system	monoclinic
space group	$P\bar{2}_1/n$ (an alternate setting of $P2_1/c$ [No. 14])
unit cell parameters ^a	
a (\AA)	13.7199 (10)
b (\AA)	19.1058 (14)
c (\AA)	17.8511 (13)
β (deg)	101.1329 (10)

V (Å ³)	4591.2 (6)
Z	4
ρ_{calcd} (g cm ⁻³)	1.195
μ (mm ⁻¹)	0.480
<i>B. Data Collection and Refinement Conditions</i>	
diffractometer	Bruker D8/APEX II CCD ^b
radiation (λ [Å]) (0.71073)	graphite-monochromated Mo Kα
temperature (°C)	-100
scan type	w scans (0.3°) (15 s exposures)
data collection 2 q limit (deg)	55.00
total data collected $-22 \leq l \leq 23$	40099 (-17 $\leq h \leq 17$, -24 $\leq k \leq 24$,
independent reflections	10511 ($R_{\text{int}} = 0.0244$)
number of observed reflections (NO)	9339 [$F_0^2 \geq 2s(F_0^2)$]
structure solution method (DIRDIF-2008 ^c)	Patterson/structure expansion
refinement method (SHELXL-97 ^d)	full-matrix least-squares on F^2
absorption correction method indexed)	Gaussian integration (face-
range of transmission factors	0.9381–0.7750
data/restraints/parameters	10511 / 0 / 496
goodness-of-fit (S) ^e [all data]	1.106
final R indices ^f	
R_1 [$F_0^2 \geq 2s(F_0^2)$]	0.0359
wR_2 [all data]	0.0957
largest difference peak and hole	0.384 and -0.359 e Å ⁻³

^aObtained from least-squares refinement of 8696 reflections with $4.66^\circ < 2q < 44.40^\circ$.

^bPrograms for diffractometer operation, data collection, data reduction and absorption correction were those supplied by Bruker.

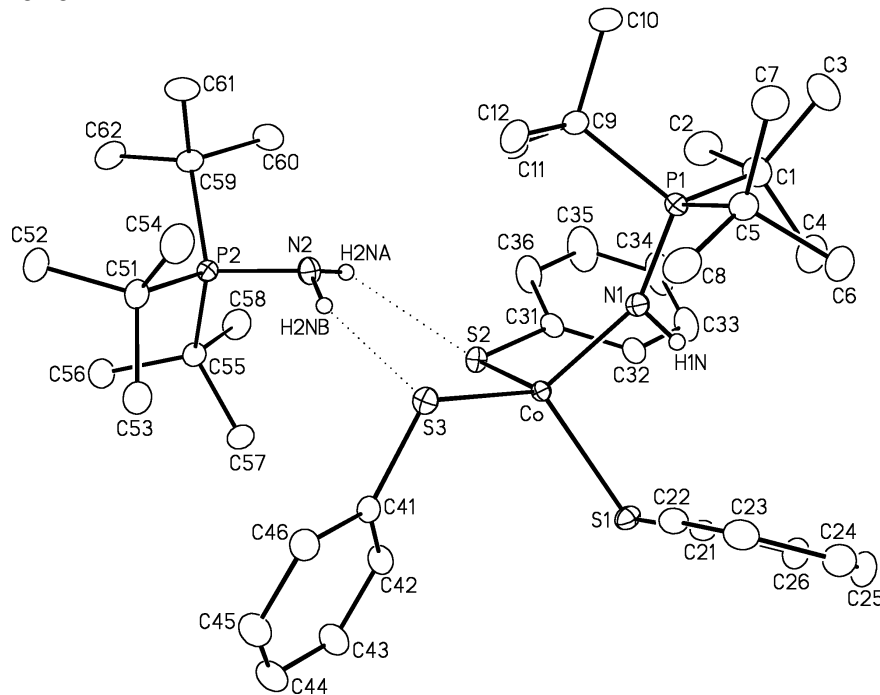
^cBeurskens, P. T.; Beurskens, G.; de Gelder, R.; Smits, J. M. M; Garcia-Granda, S.; Gould, R. O. (2008). The DIRDIF-2008 program system. Crystallography Laboratory, Radboud University Nijmegen, The Netherlands.

^dSheldrick, G. M. *Acta Crystallogr. A* **2008**, A64, 112–122.

^e $S = [\sum w(F_0^2 - F_C^2)^2/(n - p)]^{1/2}$ (n = number of data; p = number of parameters varied);
 $w = [s^2(F_0^2) + 0.0327P]^2 + 3.5022P]^{-1}$ where $P = [\text{Max}(F_0^2, 0) + 2F_C^2]/3$.

^f $R_1 = S||F_0| - |F_C||/S|F_0|$; $wR_2 = [\sum w(F_0^2 - F_C^2)^2/\sum w(F_0^4)]^{1/2}$.

Crystallographic Information for Complex **18**. University of Alberta
 Department of Chemistry Structure Determination Laboratory Report
 #JMS1070.



View of the $[t\text{Bu}_3\text{PNH}_2]^+$ cation and $[\text{Co}(\text{SPh})_3(\text{HNPT}\text{Bu}_3)]^-$ anion showing the atom-labeling scheme. Non-hydrogen atoms are represented by Gaussian ellipsoids at the 20% probability level. Hydrogen atoms are shown with arbitrarily small thermal parameters for the N–H and NH₂ groups, and are not shown for the phenyl and *t*-butyl groups.

Crystallographic Experimental Details

A. Crystal Data

formula	C ₄₆ H ₈₀ CoN ₂ OP ₂ S ₃
formula weight	894.17
crystal dimensions (mm)	0.43 ´ 0.15 ´ 0.04
crystal system	monoclinic
space group	P2 ₁ /n (an alternate setting of P2 ₁ /c [No. 14])
unit cell parameters ^a	
<i>a</i> (Å)	19.9262 (8)
<i>b</i> (Å)	12.0416 (5)
<i>c</i> (Å)	21.4175 (8)
<i>β</i> (deg)	102.4024 (5)
<i>V</i> (Å ³)	5019.1 (3)
<i>Z</i>	4

r_{calcd} (g cm ⁻³)	1.183
μ (mm ⁻¹)	0.564
<i>B. Data Collection and Refinement Conditions</i>	
diffractometer	Bruker D8/APEX II CCD ^b
radiation (λ [Å])	graphite-monochromated Mo K α
(0.71073)	
temperature (°C)	-100
scan type	w scans (0.3°) (20 s exposures)
data collection 2 q limit (deg)	53.34
total data collected	40191 (-25 ≤ h ≤ 25, -15 ≤ k ≤ 15, -26 ≤ l ≤ 26)
independent reflections	10547 ($R_{\text{int}} = 0.0615$)
number of observed reflections (NO)	7615 [$F_O^2 \geq 2s(F_O^2)$]
structure solution method	direct methods (<i>SHELXS-97^c</i>)
refinement method	full-matrix least-squares on F^2 (<i>SHELXL-97^c</i>)
absorption correction method indexed)	Gaussian integration (face-
range of transmission factors	0.9756–0.7947
data/restraints/parameters	10547 / 0 / 526
goodness-of-fit (S) ^d [all data]	1.014
final R indices ^e	
R_1 [$F_O^2 \geq 2s(F_O^2)$]	0.0399
w R_2 [all data]	0.0983
largest difference peak and hole	0.476 and -0.428 e Å ⁻³

^aObtained from least-squares refinement of 9944 reflections with 4.62° < 2 q < 46.24°.

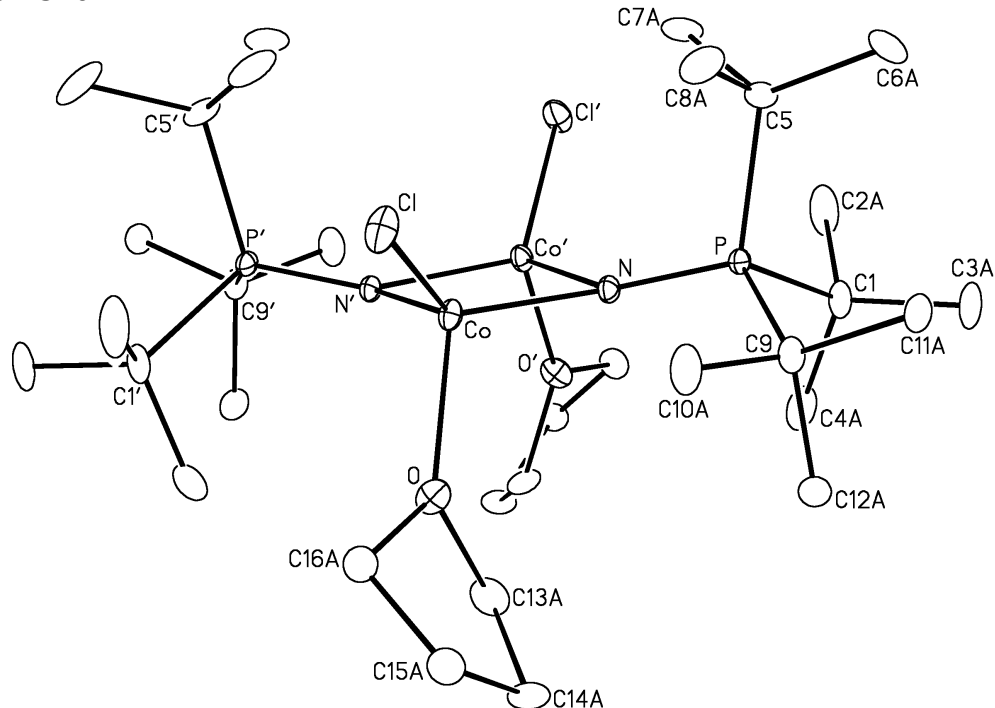
^bPrograms for diffractometer operation, data collection, data reduction and absorption correction were those supplied by Bruker.

^cSheldrick, G. M. *Acta Crystallogr.* **2008**, A64, 112–122.

^d $S = [Sw(F_O^2 - F_C^2)^2/(n - p)]^{1/2}$ (n = number of data; p = number of parameters varied; $w = [s^2(F_O^2) + (0.0365P)^2 + 3.0371P]^{-1}$ where $P = [\text{Max}(F_O^2, 0) + 2F_C^2]/3$).

^e $R_1 = S||F_O| - |F_C||/S|F_O|$; w $R_2 = [Sw(F_O^2 - F_C^2)^2/Sw(F_O^4)]^{1/2}$.

Crystallographic Information for Complex **24**. University of Alberta
 Department of Chemistry Structure Determination Laboratory Report
 #JMS1074.



Perspective view of the $[\text{Co}_2\text{Cl}_2(\text{THF})_2(\text{NP}^t\text{Bu}_3)_2]$ molecule showing the atom-labeling scheme. Primed atoms are related to unprimed ones by the crystallographic 2-fold rotation axis located at $(\frac{1}{2}, 0, \frac{1}{4})$. Only the major (75%) orientation of the disordered *t*-butyl groups is shown. Only one orientation of the disordered THF molecule is shown. Non-hydrogen atoms are represented by Gaussian ellipsoids at the 20% probability level. Hydrogen atoms are not shown.

Crystallographic Experimental Details

A. Crystal Data

formula	$\text{C}_{32}\text{H}_{70}\text{Cl}_2\text{Co}_2\text{N}_2\text{O}_2\text{P}_2$
formula weight	765.60
crystal dimensions (mm)	0.45 ' 0.10 ' 0.06
crystal system	monoclinic
space group	$\text{C}2/\text{c}$ (No. 15)
unit cell parameters ^a	
<i>a</i> (Å)	21.483 (5)
<i>b</i> (Å)	8.784 (2)
<i>c</i> (Å)	20.851 (5)
<i>b</i> (deg)	103.935 (3)
<i>V</i> (Å ³)	3819.0 (16)

Z	4
r_{calcd} (g cm ⁻³)	1.332
μ (mm ⁻¹)	1.122
B. Data Collection and Refinement Conditions	
diffractometer	Bruker D8/APEX II CCD ^b
radiation (λ [Å])	graphite-monochromated Mo K α
(0.71073)	
temperature (°C)	-100
scan type	w scans (0.3°) (20 s exposures)
data collection 2 q limit (deg)	52.94
total data collected	14867 (-26 ≤ h ≤ 26, -10 ≤ k ≤ 10, -26 ≤ l ≤ 26)
independent reflections	3938 ($R_{\text{int}} = 0.0263$)
number of observed reflections (NO)	3489 [$F_O^2 \geq 2s(F_O^2)$]
structure solution method	direct methods (<i>SHELXS-97^c</i>)
refinement method	full-matrix least-squares on F^2 (<i>SHELXL-97^c</i>)
absorption correction method	Gaussian integration (face-
indexed)	
range of transmission factors	0.9347–0.6299
data/restraints/parameters	3938 / 8 ^d / 262
goodness-of-fit (S) ^e [all data]	1.037
final R indices ^f	
R_1 [$F_O^2 \geq 2s(F_O^2)$]	0.0305
wR_2 [all data]	0.0820
largest difference peak and hole	0.641 and -0.459 e Å ⁻³

^aObtained from least-squares refinement of 9449 reflections with $4.88^\circ < 2q < 52.76^\circ$.

^bPrograms for diffractometer operation, data collection, data reduction and absorption correction were those supplied by Bruker.

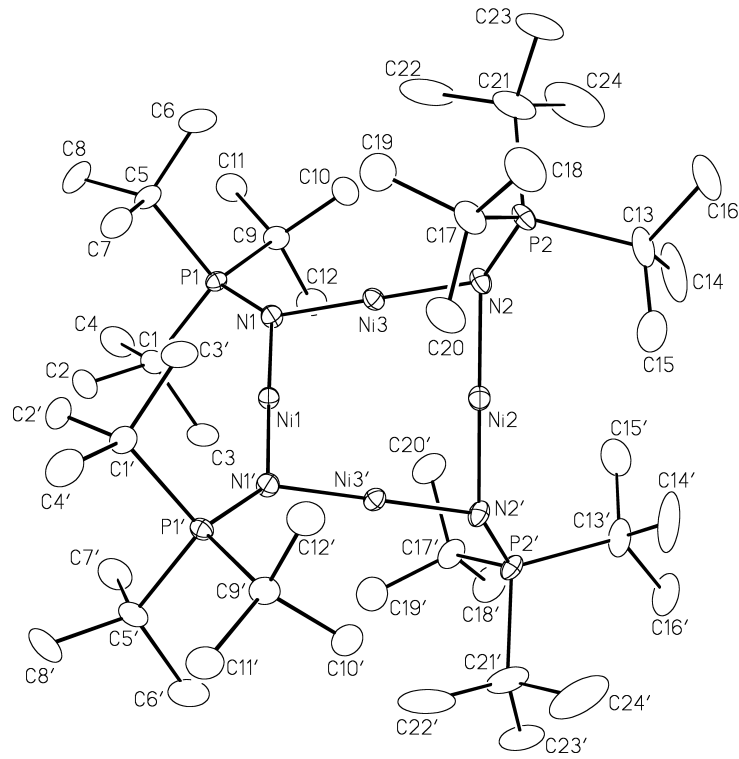
^cSheldrick, G. M. *Acta Crystallogr. 2008, A64*, 112–122.

^dThe C–C distances within the minor orientation for the two *tert*-butyl groups centered by carbon atoms C5 and C9 were restrained to be the same by use of the *SHELXL* SAME instruction. The O–C13B and O–C16B distances within the coordinated tetrahydrofuran molecule were restrained to be 1.430(4) Å.

^e $S = [Sw(F_O^2 - F_C^2)^2/(n - p)]^{1/2}$ (n = number of data; p = number of parameters varied; $w = [s^2(F_O^2) + (0.0411P)^2 + 5.6365P]^{-1}$ where $P = [\text{Max}(F_O^2, 0) + 2F_C^2]/3$).

^f $R_1 = S||F_O| - |F_C||/S|F_O|$; $wR_2 = [Sw(F_O^2 - F_C^2)^2/Sw(F_O^4)]^{1/2}$.

Crystallographic Information for Complex **26b**. University of Alberta
 Department of Chemistry Structure Determination Laboratory Report
 #JMS1111.



Perspective view of the $[\text{Ni}_4(\mu\text{-NP}^t\text{Bu}_3)_4]$ molecule showing the atom-labeling scheme. Non-hydrogen atoms are represented by Gaussian ellipsoids at the 20% probability level. Hydrogen atoms are not shown. Primed atoms are related to unprimed ones via the crystallographic twofold axis $(\frac{1}{2}, y, \frac{1}{4})$ passing through the Ni1 and Ni2 atoms.

Crystallographic Experimental Details

A. Crystal Data

formula	$\text{C}_{56}\text{H}_{124}\text{N}_4\text{Ni}_4\text{O}_2\text{P}_4$
formula weight	1244.31
crystal dimensions (mm)	0.24 ' 0.15 ' 0.06
crystal system	monoclinic
space group	$\text{C}2/\text{c}$ (No. 15)
unit cell parameters ^a	
<i>a</i> (Å)	23.4807 (17)
<i>b</i> (Å)	12.8848 (10)
<i>c</i> (Å)	23.8905 (18)
<i>b</i> (deg)	114.1930 (10)
<i>V</i> (Å ³)	6593.1 (9)
<i>Z</i>	4

r_{calcd} (g cm ⁻³)	1.254
μ (mm ⁻¹)	1.261
<i>B. Data Collection and Refinement Conditions</i>	
diffractometer	Bruker D8/APEX II CCD ^b
radiation (λ [Å])	graphite-monochromated Mo K α
(0.71073)	
temperature (°C)	-100
scan type	<i>w</i> scans (0.3°) (20 s exposures)
data collection 2 q limit (deg)	55.14
total data collected	28793 (-30 ≤ h ≤ 30, -16 ≤ k ≤ 16, -31 ≤ l ≤ 31)
independent reflections	7627 ($R_{\text{int}} = 0.0496$)
number of observed reflections (NO)	5698 [$F_O^2 \geq 2s(F_O^2)$]
structure solution method	direct methods (<i>SHELXS-97^c</i>)
refinement method	full-matrix least-squares on F^2 (<i>SHELXL-97^c</i>)
absorption correction method indexed)	Gaussian integration (face-
range of transmission factors	0.9327–0.7551
data/restraints/parameters	7627 / 11 ^d / 321
goodness-of-fit (S) ^e [all data]	1.105
final R indices ^f	
R_1 [$F_O^2 \geq 2s(F_O^2)$]	0.0649
wR_2 [all data]	0.1838
largest difference peak and hole	0.945 and -0.751 e Å ⁻³

^aObtained from least-squares refinement of 9039 reflections with 4.48° < 2 q < 49.68°.

^bPrograms for diffractometer operation, data collection, data reduction and absorption correction were those supplied by Bruker.

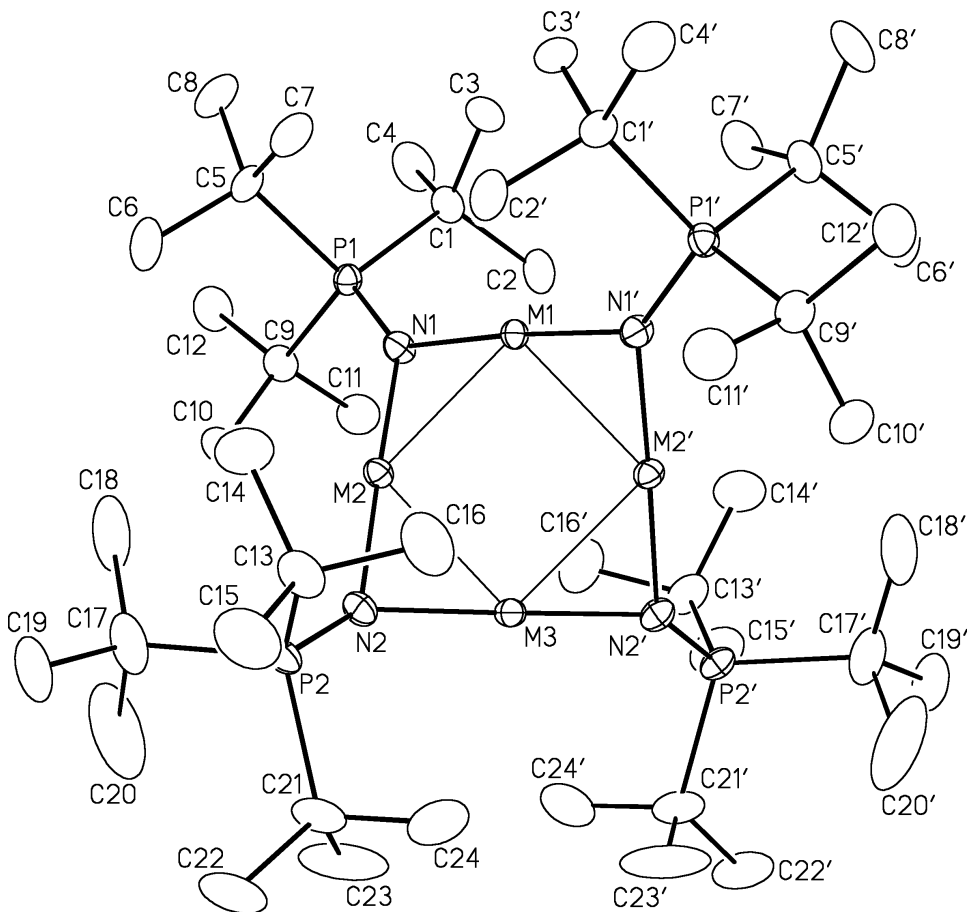
^cSheldrick, G. M. *Acta Crystallogr.* **2008**, A64, 112–122.

^dThe disordered solvent tetrahydrofuran molecules had the following restraints applied: O–C, 1.43(1) Å; C–C, 1.53(1) Å; O···C, 2.42(2) Å; C1SA/B···C4SA/B, 2.34(2) Å; C1SA/B···C3SA/B, C2SA/B···C4SA/B, 2.50(2) Å. An antibumping restraint of 2.00(1) Å was applied to H14B···H24C.

^e $S = [\sum w(F_O^2 - F_C^2)^2 / (n - p)]^{1/2}$ (n = number of data; p = number of parameters varied; $w = [s^2(F_O^2) + (0.0634P)^2 + 50.6126P]^{-1}$ where $P = [\text{Max}(F_O^2, 0) + 2F_C^2]/3$).

^f $R_1 = S||F_O| - |F_C||/S|F_O|$; $wR_2 = [\sum w(F_O^2 - F_C^2)^2 / \sum w(F_O^4)]^{1/2}$.

Crystallographic Information for Complex **26a**. University of Alberta
 Department of Chemistry Structure Determination Laboratory Report
 #JMS11a3.



Perspective view of the $[\text{Co}_{3.34}\text{Na}_{0.66}(\text{NPtBu}_3)_4]$ molecule showing the atom-labeling scheme. Atoms labeled as M were refined with a mixed occupancy of cobalt and sodium; see Table 2 footnotes for details. Primed atoms are related to unprimed ones by the 2-fold rotation axis at $(\frac{1}{2}, y, \frac{1}{4})$. Non-hydrogen atoms are represented by Gaussian ellipsoids at the 20% probability level. Hydrogen atoms are not shown.

Crystallographic Experimental Details

A. Crystal Data

formula	$\text{C}_{56}\text{H}_{124}\text{Co}_{3.34}\text{N}_4\text{Na}_{0.66}\text{O}_2\text{P}_4$
formula weight	1221.56
crystal dimensions (mm)	0.42 ' 0.27 ' 0.21
crystal system	monoclinic
space group	$\text{C}2/\text{c}$ (No. 15)
unit cell parameters ^a	

<i>a</i> (Å)	23.424 (2)
<i>b</i> (Å)	12.8863 (11)
<i>c</i> (Å)	23.816 (2)
<i>b</i> (deg)	114.2440 (10)
<i>V</i> (Å ³)	6554.8 (10)
<i>Z</i>	4
<i>r</i> _{calcd} (g cm ⁻³)	1.238
μ (mm ⁻¹)	0.975

B. Data Collection and Refinement Conditions

diffractometer	Bruker D8/APEX II CCD ^b
radiation (<i>l</i> [Å])	graphite-monochromated Mo Ka
(0.71073)	
temperature (°C)	-100
scan type	<i>w</i> scans (0.3°) (20 s exposures)
data collection 2 <i>q</i> limit (deg)	53.08
total data collected <i>I</i> ≤ 29)	6782 (-29 ≤ <i>h</i> ≤ 26, 0 ≤ <i>k</i> ≤ 16, 0 ≤
independent reflections	6931 (<i>R</i> _{int} = 0.0720)
number of observed reflections (<i>NO</i>)	5215 [$F_O^2 \geq 2s(F_O^2)$]
structure solution method	direct methods (<i>SHELXS-97</i> ^c)
refinement method (<i>SHELXL-97</i> ^c)	full-matrix least-squares on F^2
absorption correction method	multi-scan (<i>TWINABS</i>)
range of transmission factors	0.8206–0.6836
data/restraints/parameters	6931 / 20 ^d / 307
goodness-of-fit (<i>S</i>) ^e [all data]	1.048
final <i>R</i> indices ^f	
<i>R</i> ₁ [$F_O^2 \geq 2s(F_O^2)$]	0.0540
<i>wR</i> ₂ [all data]	0.1445
largest difference peak and hole	0.697 and -0.469 e Å ⁻³

^aObtained from least-squares refinement of 3087 reflections with 4.48° < 2*q* < 44.78°.

^bPrograms for diffractometer operation, data collection, data reduction and absorption correction were those supplied by Bruker. The crystal used for data collection was found to display non-merohedral twinning. Both components of the twin were indexed with the program *CELL_NOW* (Versioin 2008-2, Bruker AXS Inc., Madison, WI). The second twin component can be related to the first component by 180° rotation about the [0.418 0 1] axis in real space and about the [0 0 1] axis in reciprocal space. Integrated intensities for the reflections from the two components

were written into a *SHELXL*-97 HKLF 5 reflection file with the data integration program *SAINT* (version 7.68A), using all reflection data (exactly overlapped, partially overlapped and non-overlapped). The refined value of the twin fraction (*SHELXL*-97 BASF parameter) was 0.5002(12).

^cSheldrick, G. M. *Acta Crystallogr.* **2008**, *A64*, 112–122.

^dThe following distance restraints were applied to the disordered tetrahydrofuran solvent molecules: O–C, 1.46(1) Å; C–C, 1.52(1) Å; C1S…C4S, 2.38(1) Å; O1S…C2S, O1S…C3S, 2.42(1) Å; C1S…C3S, C2S…C4S, 2.54(1) Å.

^e $S = [Sw(F_O^2 - F_C^2)^2/(n - p)]^{1/2}$ (n = number of data; p = number of parameters varied; $w = [s^2(F_O^2) + (0.0772P)^2 + 6.3600P]^{-1}$ where $P = [\text{Max}(F_O^2, 0) + 2F_C^2]/3$).

^f $R_1 = S||F_O| - |F_C||/S|F_O|$; $wR_2 = [Sw(F_O^2 - F_C^2)^2/Sw(F_O^4)]^{1/2}$.